

Structural and Biochemical Studies on Three *Aspergillus fumigatus* Proteins That Present as Targets for Novel Antifungal Drugs

A thesis submitted for the degree of Doctor of Philosophy

Andrew C. Marshall

Department of Molecular and Cellular Biology,
School of Biological Sciences, The University of Adelaide

June 2018

Table of Contents

Thesis Summary.....	i
Statement of Declaration.....	ii
Acknowledgements.....	iii
Chapter 1: <i>Aspergillus fumigatus</i> and the Need for New Antifungals.....	1
1.1. <i>Aspergillus fumigatus</i> Infections.....	2
1.2. Incidence of Invasive Aspergillosis and Associated Mortality Rates.....	3
1.3. Limitations of Current Treatment Options	4
1.4. The Rise in Antifungal Resistance.....	6
1.5. Potential Targets for New Antifungals	7
Chapter 2: Using a Structural Genomics Approach to Provide a Foundation for Antifungal Drug Discovery.....	9
2.1. Structural Genomics.....	10
2.2. Aims and Scope of the Current Project.....	11
Chapter 3: Structural Genomics-Based Identification of Candidates for Novel <i>A. fumigatus</i> Drug Targets	13
3.1. Target Selection	14
3.2. Parallel Cloning and Screening for Heterologous Expression and Solubility	16
Chapter 4 (Publication): Structure of <i>Aspergillus fumigatus</i> Cytosolic Thiolase: Trapped Tetrahedral Reaction Intermediates and Activation by Monovalent Cations.....	19
Statement of Authorship	20
Supporting Information.....	39
Chapter 5 (Publication): Structure of the Sliding Clamp from the Fungal Pathogen <i>Aspergillus fumigatus</i> (AfumPCNA) and Interactions with Human p21.....	53
Statement of Authorship	54
Chapter 6 (Manuscript Submitted): <i>Aspergillus fumigatus</i> Thioredoxin Reductase: Structure, Mechanism, and Inhibition	75
Statement of Authorship	76
Supplementary Information	99
Chapter 7: Discussion and Future Directions	107
7.1. Structural Characterisation of Promising Targets for New Antifungals.....	108
7.2. Future Directions for Three Targets that were the Focus of the Current Study	108

7.2.1. Cytosolic Thiolase	108
7.2.2. Proliferating Cell Nuclear Antigen	109
7.2.3. Thioredoxin Reductase	109
7.3. Additional Targets for Future Investigation	110
7.3.1 The Master Regulator of the UPR: IreA	110
7.3.2. Chitin Synthases	111
7.3.3. The β -Oxidation Pathway	113
7.4. Concluding Remarks.....	114
Appendices.....	115
Appendix 1 – PCR Primer Sequences for Preliminary Targets.....	116
Appendix 2 – Small-Scale Protein Expression and Solubility Testing Protocol.....	118
Appendix 3 – Protein Purification and Preliminary Crystallisation Screening for the <i>A. fumigatus</i> IreA Luminal Domain.....	119
Appendix 4 – Co-crystallisation of <i>AfTrxR</i> in Complex with EbSe: Preliminary Results	120
Bibliography (for Chapters 1, 2, 3 and 7).....	121

Included Publications:

Marshall, A.C., Bond, C.S., and Bruning, J.B. (2018) Structure of *Aspergillus fumigatus* Cytosolic Thiolase: Trapped Tetrahedral Reaction Intermediates and Activation by Monovalent Cations. *ACS Catalysis* 8: 1973–1989.

Marshall, A.C., Kroker, A.J., Murray, L.A.M., Gronthos, K., Rajapaksha, H., Wegener, K.L., and Bruning, J.B. (2017) Structure of the sliding clamp from the fungal pathogen *Aspergillus fumigatus* (AfumPCNA) and interactions with Human p21. *The FEBS Journal* 284, 985–1002.

Marshall, A.C., Hossain, M.A., Arentz, G., Hoffman, P., Coad, B.R., and Bruning, J.B. (2018) *Aspergillus fumigatus* thioredoxin reductase: structure, mechanism and inhibition. *Antimicrobial Agents and Chemotherapy* (under consideration).

Thesis Summary

The increasing use of aggressive immunosuppressive regimes over the last half-century has been accompanied by an increased incidence of opportunistic invasive fungal infections, with *Aspergillus fumigatus* emerging as one of the main etiologic agents. *A. fumigatus* is now the major airborne fungal pathogen and is a pathogen to be feared; it is difficult to diagnose early and accurately, a detailed understanding of the factors regulating its growth and pathogenesis is lacking, and invasive infections are associated with high mortality rates, longer hospital stays and high treatment costs. In addition, the number of antifungals effective against it is limited and resistance is increasing, highlighting the need for the characterisation of novel targets for new antifungals. A detailed knowledge of the structure of a protein is essential for understanding its underlying molecular mechanism and enabling structure-based drug design. This dissertation reports the application a structural genomics-style approach to a pilot set of proteins that are involved in a range of processes essential for the growth, cellular homeostasis and survival of *A. fumigatus* in the human host. Following on from preliminary experiments to identify proteins amenable to study by X-ray crystallography, three *A. fumigatus* proteins were selected for comprehensive structural and biochemical characterisation:

(1) Crystal structures of cytosolic thiolase (afCT), which catalyses the first step in isoprenoid synthesis, were solved to resolutions between 1.7 and 2.25 Å. One of these crystals trapped two previously unobserved tetrahedral reaction intermediates, providing the first direct structural observation of the full thiolase reaction cycle. Unexpectedly, afCT is more similar structurally and biochemically to human mitochondrial thiolase II (hT2) than it is to human cytosolic thiolase (hCT). Here it is shown that, like hT2, afCT is strongly activated by monovalent cations, with a preference for K⁺ ions. Additionally, structural comparisons and *in silico* docking experiments suggest that afCT has a substrate specificity more similar to hT2 than hCT.

(2) The structure of proliferating cell nuclear antigen (AfumPCNA), which is essential for DNA replication and repair, was solved to 2.6 Å. Strong structural similarities between AfumPCNA and human PCNA at their main protein-protein interaction site suggest that the structural basis by which PCNA functions is conserved. Consistent with this, it is shown herein that the PCNA-interacting peptide of the human tumour-suppressor protein p21 binds AfumPCNA with only ten-fold lower affinity than for hPCNA, presenting AfumPCNA as a target for potential peptide-based antifungals.

(3) Thioredoxin reductase (AfTrxR) catalyses the transfer of reducing equivalents from NADPH to a number of important biosynthetic and redox-active enzymes. The structure of AfTrxR was solved to 3.2 Å, and shows high structural similarity to bacterial, plant and yeast TrxRs. It is also shown herein that ebselen (EbSe), a small drug-like molecule, is a nanomolar inhibitor of AfTrxR *in vitro* and a potent inhibitor of *A. fumigatus* growth. Further investigation by mass spectrometry revealed that EbSe interacts covalently with a redox-active cysteine at the AfTrxR catalytic site. *In silico* docking experiments were used to define key enzyme-inhibitor interactions that will be important to consider when designing potent and specific antifungal drugs targeting TrxR in the future.

Statement of Declaration

I certify that this work contains no material which has been accepted for the award of any other degree or diploma in my name, in any university or other tertiary institution and, to the best of my knowledge and belief, contains no material previously published or written by another person, except where due reference has been made in the text. In addition, I certify that no part of this work will, in the future, be used in a submission in my name, for any other degree or diploma in any university or other tertiary institution without the prior approval of the University of Adelaide and where applicable, any partner institution responsible for the joint-award of this degree.

I acknowledge that copyright of published works contained within this thesis resides with the copyright holder(s) of those works.

I also give permission for the digital version of my thesis to be made available on the web, via the University's digital research repository, the Library Search and also through web search engines, unless permission has been granted by the University to restrict access for a period of time.

I acknowledge the support I have received for my research through the provision of an Australian Government Research Training Program Scholarship.

8th June, 2018

Acknowledgements

First to my supervisor, John. For introducing me to protein crystallography and the wonders of structural biology. For demonstrating how to be simultaneously passionate and pragmatic, and for always being hilarious, regardless of the grant situation.

To past and present members of the Bruning and Booker labs. For good friendships, good advice and endless entertainment. Special thanks to Alice and Bec for the time you've spent proofreading, answering questions and making the lab a fun place to work and study.

To my family. For your support and encouragement, for instilling in me a passion to ask *why*, and for being interested in this (or at least pretending to be).

To Anna, my wife. For your love, support and patience with me through everything – I'd be a total wreck without you.

To the Creator, above all, thank you for giving us hearts to love, minds to think, and a world to explore.

Chapter 1:

Aspergillus fumigatus and the Need for New Antifungals

1.1. *Aspergillus fumigatus* Infections

The filamentous fungus *Aspergillus fumigatus* (**Figure 1**) is found worldwide. It is a saprophyte, usually feeding on decaying organic matter, and disseminates via the production of microscopic spores, called conidia (McCormick et al., 2010). Spores are ubiquitous and constantly inhaled by humans. *Aspergillus* infections are therefore most commonly respiratory (**Figure 2**). Infections that involve mycelial growth in the body are classified as allergic bronchopulmonary aspergillosis (ABPA), aspergilloma, or invasive aspergillosis (IA) (Latge, 1999). ABPA is most common in patients with asthma or cystic fibrosis and causes death by respiratory failure if left untreated. Aspergilloma, or “fungus ball”, is characterised by a mass of spherical mycelial growth in the airways. Although usually asymptomatic, it can cause internal bleeding, haemoptysis, and death (Latge, 1999). IA is common in immunocompromised hosts such as hematopoietic stem cell (HSC) and solid-organ transplant recipients, or patients with haematological malignancy, acute leukaemia or AIDS (Gallien et al., 2008; Latge, 1999). Cases of severe IA caused by *A. fumigatus* are reported in immunocompetent patients, albeit rarely (Chen et al., 2011). General symptoms are variable and include fever, chest pain, cough, malaise, weight loss, dyspnoea, haemoptysis, neurological deficit, and meningitis (Gallien et al., 2008; Latge, 1999). Although most often pulmonary, infections of the bronchi, sinuses, and dissemination to the brain and other organs are also common (Gallien et al., 2008; Latge, 1999). Early diagnosis of *A. fumigatus* infections is difficult and there is a need for more accurate and sensitive diagnostic methods (Steinbach, 2013).

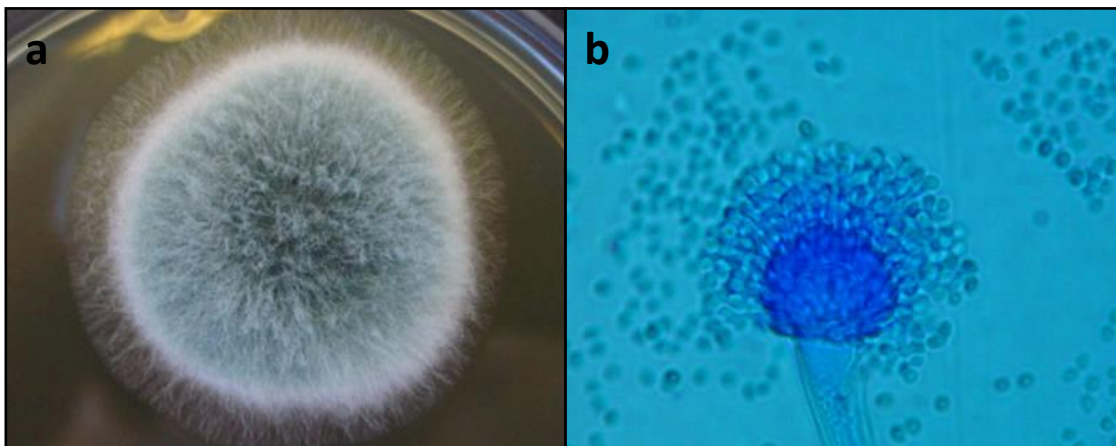


Figure 1: (a) *A. fumigatus* after 4 days growth on malt extract agar. (b) An *A. fumigatus* conidial head with spores (1000x magnification). Images reproduced from The Aspergillus Website (<http://www.asperweb.co.uk>).

Alveolar macrophages are the major host immune cells involved in the initial response to *Aspergillus* infection, clearing fungal conidia from the lungs via phagocytosis and production of reactive oxygen species (ROS). Neutrophils recruited during inflammation play a major role in phagocytosis of hyphae and can also ingest conidia missed by macrophages (Latge, 1999; McCormick et al., 2010). They respond to infection by production of ROS, antimicrobial proteases and neutrophil extracellular traps (NETs) (Espinosa and Rivera, 2016). Administration of corticosteroids – which inhibit killing of conidia by macrophages, inflammation, and recruitment of neutrophils – has been identified as a risk factor for the development of IA (Upton et al., 2007). Neutropenia has also been correlated with an increased

risk of developing IA and failure of treatment (Gallien et al., 2008; Latge, 1999). Another factor that complicates treatment is angioinvasion and occlusion of blood vessels by *A. fumigatus*, often making delivery of anti-fungal drugs to the site of infection difficult (Steinbach, 2013).

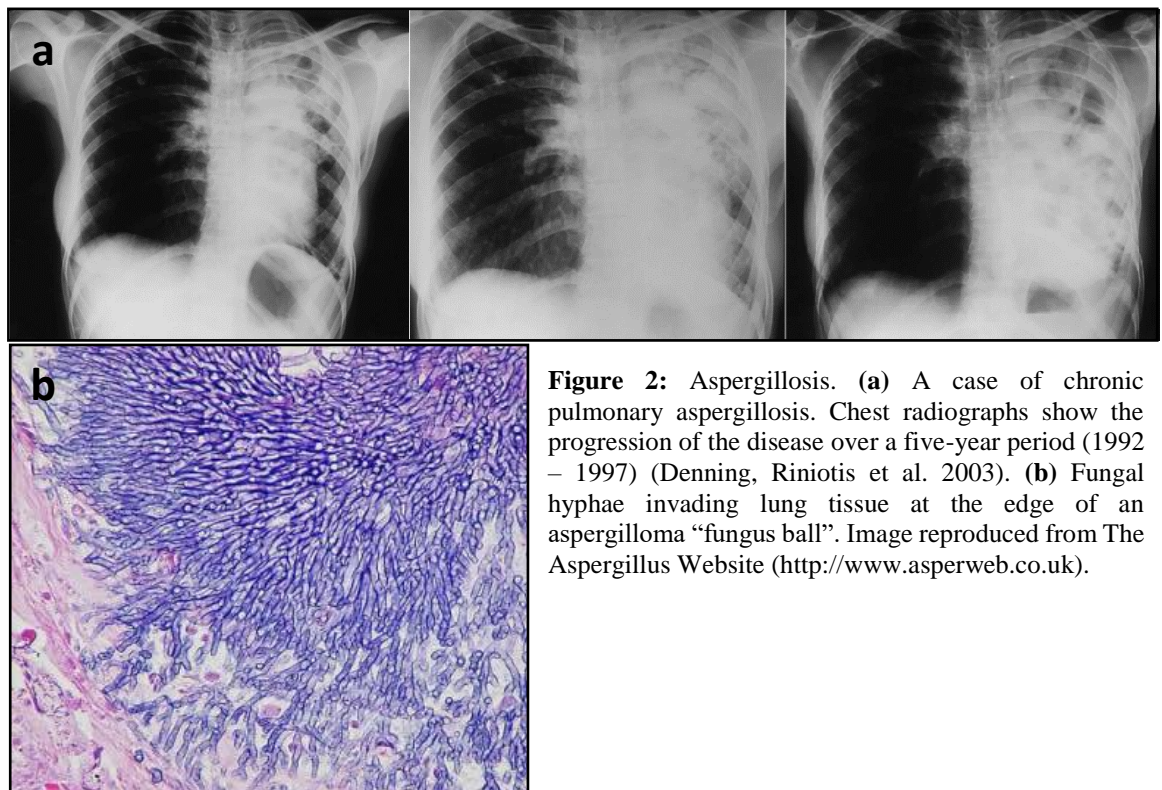


Figure 2: Aspergillosis. (a) A case of chronic pulmonary aspergillosis. Chest radiographs show the progression of the disease over a five-year period (1992 – 1997) (Denning, Riniotis et al. 2003). (b) Fungal hyphae invading lung tissue at the edge of an aspergilloma “fungus ball”. Image reproduced from The Aspergillus Website (<http://www.asperweb.co.uk>).

1.2. Incidence of Invasive Aspergillosis and Associated Mortality Rates

The incidence of IA is difficult to estimate due to a historical lack of consistency in surveillance and case definition (Warnock, 2007). A 2005 review reported that the mean incidence of IA in transplant recipients varied from 0.7 to 11% depending on the type of transplant, with mortality rates of 63 to 100% (Singh and Paterson, 2005). It is generally recognised, however, that *Aspergillus* infections have become increasingly common in the last few decades. This can be attributed to considerable progress in the areas of cancer treatment and transplantation, with a concomitant rise in the number of immunocompromised patients. Aside from cancer remission or transplant failure, the leading cause of death for these patients is infection, in which *A. fumigatus* is a major player (Latge, 2001; Steinbach, 2013). Indeed, IA is one of the most hazardous and common mould infections in immunocompromised patients (Gallien et al., 2008) and the most common cause of death due to lung infection in HSC transplant patients (Walsh et al., 2008).

The mortality rate associated with IA is variable, and depends on the patient’s underlying medical conditions, the site of infection, and antifungal therapy. All the same, it remains unacceptably high. A systematic review of literature from 1995 to 2000 revealed an overall IA case-fatality rate of 58%, with rates for HSC transplant patients and those with central nervous system (CNS) or disseminated aspergillosis of 86.7% and 88.1%, respectively (Lin et

al., 2001). CNS aspergillosis is associated with particularly high mortality rates (Gallien et al., 2008; Schwartz et al., 2005). A large study at a single US centre demonstrated that, of over 400 HSC transplant patients with IA from 1990 to 2004, 90.9% died after being diagnosed with IA, with approximately one third of deaths considered to be attributable to IA (Upton et al., 2007).

1.3. Limitations of Current Treatment Options

There are four classes of antifungal agents that have *in vitro* antifungal activity against *Aspergillus* species: polyenes, echinocandins, allylamines and triazoles (Hadrich et al., 2012; Qiao et al., 2008). These all target components of the fungal cell wall or cell membrane, directly or indirectly (**Figure 3**).

Amphotericin B is a broad-spectrum **polyene** antifungal that interacts with ergosterol, the main fungal cell membrane sterol, and was the standard treatment for *Aspergillus* infections for decades. It binds to ergosterol directly to form transmembrane channels, thereby increasing the permeability of the membrane to monovalent cations (Bolard, 1986; Latge, 1999). It also results in depletion of cellular energy reserves by inhibiting proton ATPase pumps and decreases the integrity of the cell membrane by causing oxidative damage to lipids (Latge, 1999; Qiao et al., 2008). However, more recent research has suggested that amphotericin B primarily kills fungal cells via ergosterol binding *per se*, and that channel formation is a complimentary secondary antifungal mechanism (Gray et al., 2012). Its insolubility in water

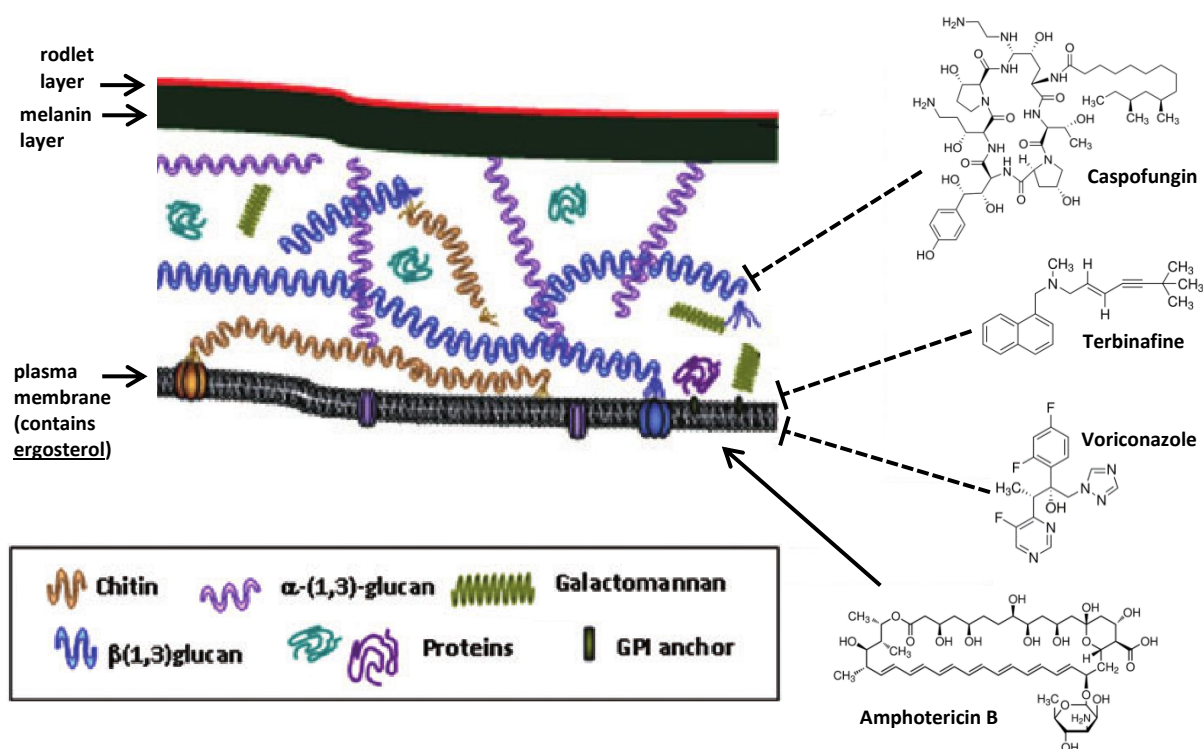


Figure 3: Cartoon representation of the putative organisation of the cell wall of a fungal conidium (adapted from Latge, 2010). On the right are representatives of current anti-*Aspergillus* drug classes and their targets. Echinocandins (casposfungin) inhibit β -(1,3)-glucan synthesis, azoles (voriconazole) and allylamines (terbinafine) inhibit ergosterol synthesis, and polyenes (amphotericin B) bind ergosterol directly in the membrane. All chemical structures were reproduced from Sigma-Aldrich® (<http://www.sigmaaldrich.com>).

means that it must be mixed with detergent to be bioavailable. High patient toxicity commonly results in severe side effects; the most notable is acute renal failure, which is associated with a high mortality rate in itself (Bates et al., 2001; Gallien et al., 2008; Herbrecht et al., 2002). Lipid formulations are less toxic, but more expensive (Chowdhry and Marshall, 2008; Latge, 1999). It is only available as an intravenous formulation, often resulting in infusion reactions (Chowdhry and Marshall, 2008; Herbrecht et al., 2002).

Echinocandins – including caspofungin and micafungin – target the major subunit of glucan synthase, encoded by the *FKS1* gene (Arendrup et al., 2009). They inhibit synthesis of the essential fungal cell wall component, β -(1,3)-glucan, and are fungistatic against *Aspergillus spp.* Adverse side-effects include rash and hepatotoxicity (Chowdhry and Marshall, 2008; Rocha et al., 2007).

Terbinafine, the main **allylamine** antifungal, inhibits squalene epoxidase, which is encoded by the *ergA* gene in *A. fumigatus* and is involved early in the ergosterol biosynthesis pathway. Its inhibition results in depletion of ergosterol and accumulation of squalene, resulting in fungal cell death (Alcazar-Fuoli and Mellado, 2012; Rocha et al., 2006; Ryder, 1992).

Triazole antifungals target lanosterol 14- α -demethylase, a cytochrome P450 enzyme and the product of the *cyp51A* gene (also known as *erg11*). Triazole drugs act by competing with oxygen for binding to the iron atom occupying the haem group at the *cyp51A* active site (Hadrich et al., 2012). This prevents the synthesis of ergosterol resulting in the accumulation of intermediate sterols, altered membrane fluidity, accumulation of intracellular unsaturated fatty acids and phospholipids, and inhibition of fungal growth (Latge, 1999; Lelièvre et al., 2013). Triazoles are selective for fungal over human cytochrome P450, thereby reducing toxicity to the patient. Despite this, effective treatment options may be restricted due to interactions with other common drugs that modulate P450 metabolism. Triazoles effective against *A. fumigatus* include voriconazole, itraconazole and posaconazole; however, the latter two are only available in oral formulations, limiting their use in ICU (Chowdhry and Marshall, 2008; Latge, 1999). Common adverse side-effects associated with azole therapy are hepatotoxicity, psychosis and temporary visual disturbances including altered colour perception, hallucinations, and episodes of confusion (Chowdhry and Marshall, 2008; Herbrecht et al., 2002).

Triazoles are the main class of antifungal for the treatment of IA. Voriconazole is the preferred agent for first-line IA therapy, as it has been shown to be more effective and have less severe side-effects than amphotericin B (Herbrecht et al., 2002). Current guidelines for the treatment of IA from the Infectious Diseases Society of America recommend voriconazole and posaconazole for primary treatment and prophylaxis, respectively, in most cases. Liposomal amphotericin B, posaconazole, itraconazole, caspofungin or micafungin are recommended for salvage therapy in cases where infection is refractory to voriconazole (Patterson et al., 2016; Walsh et al., 2008). No allylamines have been approved for clinical use in the treatment of IA (Alcazar-Fuoli and Mellado, 2012; Hadrich et al., 2012). The benefit of using combinations of currently available drugs has been shown to be limited, highlighting the need for the development of new therapies with novel targets (Steinbach, 2013; Upton et al., 2007).

1.4. The Rise in Antifungal Resistance

The rise in *A. fumigatus* infections has been accompanied by a rise in cases of resistance to current antifungal medications (Hadrich et al., 2012; Qiao et al., 2008). It is well recognised that *A. fumigatus* can acquire resistance to triazoles – the main class of antifungal used against it. Resistance was first identified in the clinic in 1997 (Chryssanthou, 1997; Denning et al., 1997b), and although cases were rare for the following decade, its incidence has increased dramatically in recent years (Lelièvre et al., 2013; Vermeulen et al., 2013). Azole resistance has now been reported in Australia, Canada, China, Columbia, India, Tanzania, USA and across Europe (Hadrich et al., 2012; Verweij et al., 2016). Current evidence suggests that resistance may be acquired in the clinic due to the selective pressure associated with long-term antifungal therapy, or in the environment due to widespread use of azole fungicides in agriculture (Lelièvre et al., 2013; Vermeulen et al., 2013). A UK study (**Figure 4a**) showed that, of 519 clinical *A. fumigatus* isolates from 1992 to 2007, 7% were resistant to itraconazole, and of these, 65% and 74% were cross-resistant to voriconazole and posaconazole, respectively. The earliest example of azole-resistance was seen in 1999, with a significant increase in frequency after 2004; the incidence of azole-resistant isolates in 2007 was 17% (Howard et al., 2009). Similar results have been reported in the Netherlands: the overall frequency of patients from 1994 to 2007 harbouring an itraconazole resistant *A. fumigatus* isolate was 2.6%, increasing steadily after 1999. In most cases, itraconazole resistant isolates showed cross-resistance to other azole antifungals (Snelders et al., 2009). A more recent follow up study by the same group showed that this trend has persisted, with the prevalence of azole-resistant *A. fumigatus* increasing from 4.3% in 2008 to 10.1% in 2010 (D. Versteeg et al., 2012) (**Figure 4b**). Results of a study at an institution in the USA showed that triazole resistance increased after institutional use of itraconazole began, and that some itraconazole resistant isolates also showed decreased susceptibilities to voriconazole, caspofungin or amphotericin B (Balajee et al., 2004). Resistance is most often mediated by mutations in the

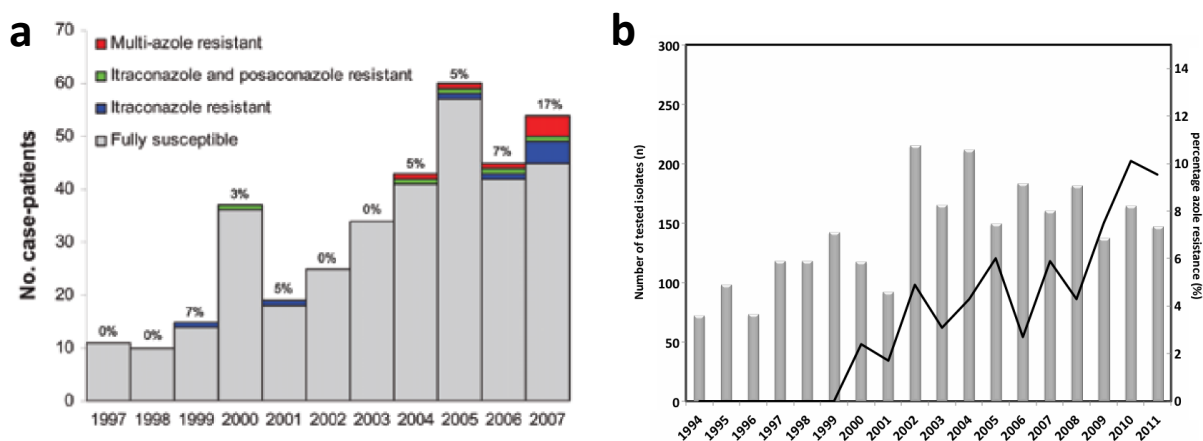


Figure 4: Resistance of *A. fumigatus* to azole antifungals is increasing. **(a)** Data from a UK study showing the incidence of azole resistant *A. fumigatus* isolates (total percentage indicated above each column) in patients from 1997 to 2007. Resistance was probably acquired during or after azole therapy. Figure reproduced from Howard *et al.* (2009). **(b)** A Dutch study showing the number of patients with a confirmed *A. fumigatus* infection (grey bars; left axis) and the percentage from which an itraconazole resistant *A. fumigatus* strain was isolated (black line; right axis) from 1994 to 2011. Resistance probably originated in the environment due to selective pressure from triazole fungicides used in agriculture (Snelders *et al.*, 2009). Figure reproduced from Versteeg *et al.* (2012).

cyp51A gene or its regulatory elements, resulting in structural modifications that preclude azole binding or increase gene expression (Hadrich et al., 2012; Lelièvre et al., 2013). Cross-resistance to azoles is common and depends on the specific amino acid substitution conferred by mutations in *cyp51A* (Arendrup et al., 2008). Other non-*cyp51A*-related resistance mechanisms have also been observed (Vermeulen et al., 2013). For example, drug resistance has also been associated with an overexpression of efflux pumps, of which *A. fumigatus* has many (Lelièvre et al., 2013). Multiazole-resistant *A. fumigatus* has been associated with high mortality in patients with IA (van der Linden et al., 2011). Unsurprisingly, a correlation between azole resistance and treatment failure in a murine model of IA has also been demonstrated (Denning et al., 1997a). Drugs that are effective against filamentous fungi are limited, and those of the azole class are the only ones that can be administered orally (Lelièvre et al., 2013), therefore the recent increase in resistance to these drugs is of great concern.

Regarding the other available antifungal drug classes, resistance of *A. fumigatus* to polyenes or echinocandins is rare. However, it has been suggested that reduction in plasma membrane ergosterol content or overproduction of enzymes that neutralise oxidative stress could possibly confer resistance to amphotericin B (Qiao et al., 2008). In addition, rare cases of resistance to echinocandins, which have only more recently become available for clinical use, have been reported (Arendrup et al., 2008; Balajee et al., 2004; Madureira et al., 2007). Although the exact mechanism has not yet been determined, increased *FKSI* expression and growth rate have been associated with a caspofungin resistant clinical *A. fumigatus* isolate (Arendrup et al., 2008).

Although the main cause of IA is *A. fumigatus*, other *Aspergillus* species are also commonly implicated in the disease (Walsh et al., 2008). Many species show intrinsic resistance or variable susceptibility to currently available antifungal drugs. For example, *A. terreus* shows intrinsic resistance to amphotericin B (Hadrich et al., 2012). This further highlights the need for a broader range of antifungal treatment options.

1.5. Potential Targets for New Antifungals

Despite the increasing incidence of IA, limited treatment options, and rise in antifungal resistance, the characterisation of novel targets for antifungals effective against *A. fumigatus* has been lacking in recent years. Being a saprophyte, *A. fumigatus* does not require a human host to complete its life cycle. Therefore, there is an absence of selective pressure to facilitate development in the human body. This is consistent with the lack of true virulence factors identified by single-gene deletion strategies, and indicates that *A. fumigatus* virulence involves numerous factors that make this fungus particularly hazardous to the immunocompromised host. The virulence of *A. fumigatus* has been suggested to be multifactorial, attributed to the ability of conidia to penetrate deep into the lower alveolar airways, effectively evade or resist host defence mechanisms, readily adapt to the host environment, and invade host tissue (Abad et al., 2010; Latge, 1999; Steinbach, 2013). The functions of various proteins key to several different pathways, for example: calcineurin, a protein phosphatase involved in stress response; IreA, an endoplasmic reticulum stress sensor; LaeA, a master regulator of secondary metabolite production and development; and *srbA*, a putative transcription factor essential for hypoxic adaptation, have all been shown to be significantly correlated with virulence

(McCormick et al., 2010; Steinbach, 2013). Thermotolerance is a factor that has also been shown to contribute to virulence (Abad et al., 2010; McCormick et al., 2010). These findings suggest that a more promising approach to antifungal development may be to target key components of important regulatory pathways rather than specific putative virulence factors.

Uncovering proteins that are essential for the growth and virulence of *A. fumigatus* is only the first step in identifying new antifungal targets. Indeed, it must be shown that the protein in question is also ‘druggable’, such that bioavailable molecules can bind to and modulate the function of the protein to give the desired therapeutic outcome (Steinbach, 2013). To this end, high resolution structural information is invaluable.

Chapter 2:

Using a Structural Genomics Approach
to Provide a Foundation for Antifungal
Drug Discovery

2.1. Structural Genomics

Detailed macromolecular structural information is invaluable for understanding the fundamental mechanisms that underlie biological processes. This information is important not only for gaining a detailed understanding of the basic biology of an organism, but also in facilitating the rational design of therapeutics targeted to specific components of a process – two outcomes that are often intrinsically linked (Ennifar, 2013; Zheng et al., 2015). In the past, the selection of a particular protein for structural characterisation has typically followed from the prior study and characterisation of its function by traditional biochemical and molecular biology methods. The advent of technologies for efficient large scale heterologous protein production, purification and structure determination, in addition to large scale sequencing projects making available whole-genome sequence data, has made a less biased approach possible – where structural characterisation of proteins often occurs prior to elucidation of their function (Anderson, 2009; Weigelt, 2010).

The field of Structural Genomics (SG) has thus emerged in the last fifteen years or so as an approach to address two broad goals: (1) To expand our knowledge of protein fold space by determining structures for proteins with novel sequences, therefore providing structural templates for all proteins; and (2) To systematically determine the structures of all proteins from a particular organism in order to understand the basic molecular mechanisms that occur within, providing a foundation for applied biomedical research, with a particular focus on drug discovery. SG programs have included international consortiums and large projects in the USA, Europe and Japan (Anderson, 2009; Grabowski et al., 2016; Weigelt, 2010). These have so far contributed approximately 12% of all structures deposited in the Protein Data Bank (PDB) (Grabowski et al., 2016), with SG projects accounting for nearly a quarter of novel structures of human proteins currently available (Weigelt, 2010).

The general approach taken by a SG program involves first the selection of a large number of protein targets that will be studied in parallel, cloning of these into vectors for heterologous expression, small-scale testing for soluble protein, large scale protein expression and purification, followed by crystallisation, X-ray diffraction, and finally structure solution. For proteins for which structures can be solved, enzyme assays or other biochemical studies are established, and the molecular mechanisms that underlie their functions are characterised at an atomic level by co-crystallisation and structure solution with natural ligands. Following this, co-crystallisation with known inhibitors or those identified by screening facilitates the identification and optimisation of lead compounds for novel drugs.

A structure-guided approach to drug discovery is particularly valuable for optimisation of lead compounds to increase affinity and specificity for a target, leading to the development of antimicrobial drugs against specific pathogenic organisms. Even though the proteins selected for characterisation in a SG project are often not validated drug targets, the approach makes available structures for many proteins that can then be further studied to validate them as potential drug targets, and also increases the knowledge of the pathogen under investigation. Many pathogens have been the subject of SG projects, including viruses, pathogenic protozoa, bacteria and malaria (Anderson, 2009; Li et al., 2014; Musa et al., 2009; Weigelt, 2010).

An example of a large and successful SG project is the Tuberculosis Structural Genomics Consortium (TBSGC – <http://www.webtb.org>), which commenced in 2000 and is the subject

of numerous reviews (Arora et al., 2011; Chim et al., 2011; Ehebauer and Wilmanns, 2011; Ioerger and Sacchettini, 2009; Musa et al., 2009). This collaboration includes approximately 100 different research groups in 15 countries and its focus is to solve the structures of biologically important *Mycobacterium tuberculosis* proteins, with a strong emphasis on providing a foundation for structure-based drug discovery efforts. So far over one third of *M. tuberculosis* protein structures currently deposited in the PDB are attributed to members of the TBSGC – equal to over 250 structures. This has led to an enhanced understanding of proteins involved in important metabolic pathways and those associated with virulence, pathogenesis and persistent infection. In addition, misannotations in the genome have been corrected, and new potential drug targets have been identified and structurally characterised, allowing for screening of inhibitors and identification of potential drug leads (Lin et al., 2006).

The sequence of the entire *Aspergillus fumigatus* genome has been made publicly available (Nierman et al., 2005), making possible the cloning of any particular gene of interest for heterologous expression. At the commencement of the current project, there were 91 structures of *A. fumigatus* proteins deposited in the PDB, representing only 36 unique proteins – a very small number compared to other important human pathogens. Applying a SG approach to the study of this important opportunistic pathogen would provide valuable structural information and is expected to uncover avenues for the development of drugs that exploit new targets. The SG projects discussed above are often multidisciplinary and involve large laboratories or consortiums of many different laboratories in addition to well established processes for large-scale parallel screening of targets followed by structure solution. This kind of project obviously falls outside the scope of a single PhD project. Despite this, it is possible to use the same approach on a much smaller scale.

2.2. Aims and Scope of the Current Project

The current project therefore applies the same structure-based approach with the aim of characterising important proteins from *A. fumigatus*, beginning with a pilot set of proteins that have a broad range of functions and are of particular importance to the survival and growth of the organism within the human host. Specifically, a list of almost twenty proteins involved in essential cellular processes were selected for parallel investigation, with the aim of solving crystal structures and performing further biochemical characterisation of two or three of these. Parallel cloning and screening of a large number of protein targets for expression, solubility and crystallisation at the outset pre-empts the bottleneck that often occurs at the crystallisation step, and is an efficient way to ensure that useful structural information, with supporting biochemical data, is gained within the timeframe of a single PhD project. This information will be valuable for gaining a better understanding of the fundamental biochemistry that governs essential processes within this important opportunistic pathogen, and provide a foundation for the rational design of drugs to modulate these processes.

Chapter 3:

Structural Genomics-Based

Identification of Candidates for Novel *A.*

fumigatus Drug Targets

3.1. Target Selection

The genome of *A. fumigatus* consists of eight chromosomes and contains 9,926 predicted genes (Nierman et al., 2005). An initial set of eighteen proteins were selected for this study (**Table 1**). These are all involved in essential processes such as stress response, synthesis of cell wall or membrane components, cellular metabolism, or DNA replication, and each fulfil at least two of the following criteria:

- Essential for growth and/or virulence
- Has prior validation as a drug target or predicted ‘druggable’ potential
- Lacks a human homologue
- Structures of homologues are unavailable
- Is predicted to be soluble

These criteria are similar to those used by the Center for Structural Genomics of Infectious Diseases (Anderson, 2009).

To increase the probability of successfully obtaining soluble recombinant protein, truncations of all eight chitin synthases (ChS) contained in the *A. fumigatus* genome were constructed to include only the putative catalytic ChS domain; that is, all predicted transmembrane regions and other domains (such as the myosin motor-like domains of CSMA and CSMB) were excluded (see **Table 1** for truncations). Protein secondary structure predictions (Phyre2 server (Kelley and Sternberg, 2009)) and alignment to previous truncations of a fungal ChS successfully expressed in *E. coli* (Magellan et al., 2010) were used as guides for designing appropriate truncations. Two truncations of the endoplasmic reticulum stress sensor, IreA, were designed to include either the core ER luminal domain or the dual catalytic cytosolic domain. The positions of these truncations were informed by previously solved *S. cerevisiae* and human Ire1 crystal structures (Ali et al., 2011; Credle et al., 2005; Lee et al., 2008; Zhou et al., 2006). All other targets were cloned as full length wild type proteins.

Table 1: Preliminary set of *A. fumigatus* proteins chosen for structural characterisation.

Gene	NCBI Reference	Protein Truncation(s)	Protein name(s) and function	Essential?	References
<i>IreA</i>	XM_744829.1	A101-G453 (luminal domain) G702-E1146 (cytosolic domain)	Protein kinase and ribonuclease Ire1/IreA. Endoplasmic reticulum stress sensor and mediator of the Unfolded Protein Response.	Under specific conditions	(Feng et al., 2011; Krishnan and Askew, 2014)
<i>GFAI</i>	XM_745432.1	None. (Full length protein)	Glutamine-fructose-6-phosphate amino-transferase. First step in chitin biosynthetic pathway.	Yes	(Hu et al., 2007)
<i>ERG10</i>	XM_742114.1	None.	Type II thiolase/acetyl-CoA acetyl-transferase/acetoacetyl-CoA thiolase. First step in mevalonate pathway.	Yes	(Hiser et al., 1994; Hu et al., 2007)
<i>TRR1</i>	XM_746439.1 (*updated: MG551986)	None.	Thioredoxin reductase. Cell redox homeostasis.	Yes	(Hu et al., 2007)
<i>HEM15</i>	XM_748768.1	None.	Mitochondrial ferrochelatase. Heme biosynthesis.	Yes	(Hu et al., 2007)
<i>ChSA</i>	XM_744229.1	H163-S545	Chitin synthase A. Synthesis of chitin – a major structural component of the fungal cell wall.	No	(Muszkieta et al., 2014)
<i>ChSB</i>	XM_741511.1	A281-S703	Chitin synthase B. Synthesis of chitin.	No	(Muszkieta et al., 2014)
<i>ChSC</i>	XM_743170.1	H160-S525	Chitin synthase C. Synthesis of chitin.	No	(Muszkieta et al., 2014)
<i>ChSD</i>	XM_747537.1	T100-R396	Chitin synthase D. Synthesis of chitin.	No	(Muszkieta et al., 2014)
<i>ChSF</i>	XM_742271.1	H635-T1019	Chitin synthase F. Synthesis of chitin.	No	(Muszkieta et al., 2014)
<i>ChSG</i>	XM_749091.1	A141-G562	Chitin synthase G. Synthesis of chitin.	No	(Muszkieta et al., 2014)
<i>CSMA</i>	XM_750584.1	L1231-S1564	Chitin synthase E/Myosin motor-like domain-containing chitin synthase A. Synthesis of chitin.	No	(Muszkieta et al., 2014)
<i>CSMB</i>	XM_750583.1	Q1054-G1405	Myosin motor-like domain-containing chitin synthase B. Synthesis of chitin.	No	(Muszkieta et al., 2014)
<i>ACD</i>	XM_747761.1	None.	Acyl-CoA dehydrogenase. Catalyses 1 st step in β -oxidation pathway (fatty acid catabolism).	unknown	(Kretschmer et al., 2012)
<i>ECH</i>	XM_750305.1	None.	Enoyl-CoA hydratase. Catalyses 2 nd step in β -oxidation pathway.	unknown	(Kretschmer et al., 2012)
<i>3HACD</i>	XM_743258.2	None.	3-hydroxyacyl-CoA dehydrogenase. Catalyses 3 rd step in β -oxidation pathway.	unknown	(Kretschmer et al., 2012)
<i>KATI</i>	XM_747542.1	None.	3-ketoacyl-CoA thiolase. Catalyses 4 th step in β -oxidation pathway.	unknown	(Kretschmer et al., 2012)
<i>PCNA</i>	XM_745146.1 ([†] afu1g04900)	None.	Proliferating Cell Nuclear Antigen/Sliding clamp. Hub protein for DNA replication/repair enzymes and cell cycle regulators.	unknown (likely)	(Moldovan et al., 2007)

*See Chapter 6, Materials and methods.

[†]Updated sequence available at www.aspergillusgenome.org. See Chapter 5, Materials and methods.

3.2. Parallel Cloning and Screening for Heterologous Expression and Solubility

The protein coding sequence for each target was PCR amplified from *A. fumigatus* strain af293 (Nierman et al., 2005) cDNA (a gift from Assoc. Prof. James Fraser, School of Chemistry and Molecular Biosciences, University of Queensland) and cloned into Gateway® pDONR™221 Vector (Invitrogen™) with a Tobacco Etch Virus (TEV) protease cleavage site at the 5' end to facilitate proteolytic removal of any N-terminal tag used during protein purification (see **Appendix 1**). These open reading frames (ORFs) were then subcloned via Gateway® recombination sites into vectors of choice for expression of protein in *Escherichia coli*, and confirmed using the Sanger sequencing service provided by the Australian Genome Research Facility (Plant Genomics Centre, Urrbrae, SA). The pVP16 vector (Center for Eukaryotic Structural Genomics) was used as a default first choice for expression of recombinant protein with an N-terminal maltose binding protein (MBP) and hexahistidine tag to enhance solubility and facilitate purification by affinity chromatography. These constructs were then tested for protein expression in BL21(λDE3) *E. coli* cells, solubility, and binding to Ni²⁺-NTA resin on a small scale (10 mL cultures; see **Appendix 2** for protocol), before selecting those for which the highest yield of soluble protein was obtained for large scale culture (3 - 10 L). This follows a similar standard approach as that taken by the TBSGC (Chim et al., 2011; Ioerger and Sacchettini, 2009).

All targets were successfully over-expressed as MBP-fusion proteins (**Figure 5**), with the exception of the IreA cytosolic domain (IreA.CD), which, when over-expressed, may have been toxic to the cells, as indicated by their highly reduced growth rate (observed in two separate experiments). CSMB, ChSA, ChSB, ChSC, ChSG, GFA1 and HEM15 all exhibited low solubility or appeared to be degraded easily. ChSD appeared to be partially soluble, but at least 50% degraded. CSMA and ChSF showed the greatest solubility and stability of all the ChS catalytic domains, albeit with some observable degradation. The IreA luminal domain (IreA.LD), TRR1, ERG10, 3HACD, ACD, ECH and KAT1 were all highly soluble and bound well to the Ni-NTA resin. Due to time constraints, it was not feasible to pursue structural analyses of all of these soluble targets within the current project. It is unknown which, if any, of the four enzymes of the β-oxidation pathway (ACD, ECH, 3HACD and KAT1; see **Table 1**) are important for fungal pathogenesis. This is further complicated by the multiplicity of β-oxidation genes contained in the *A. fumigatus* genome, as illustrated by the multiple putative KATs annotated (see **Chapter 4, Figure S1**), posing the possibility of functional redundancy. Indeed, previous genomic analyses have indicated that *A. fumigatus* possesses complete β-oxidation pathways in both mitochondria and peroxisomes (Shen and Burger, 2009). It was therefore concluded that a structural and biochemical analysis of the complete β-oxidation pathway of *A. fumigatus* constitutes a separate study, which is discussed further in **Chapter 7**, but is outside of the scope of the current study.

Therefore, following from positive results for the small-scale tests, the IreA luminal domain (IreA), thioredoxin reductase (TRR1) and cytosolic thiolase (ERG10) were selected, in addition to PCNA (PCNA), for large scale protein purification and crystallisation screening. All of these proteins have been shown to be, or are very likely to be, essential for *A. fumigatus* growth or virulence (see **Table 1**). For *A. fumigatus* PCNA, a well-established protocol for the purification of human PCNA (previously developed by Dr. John Bruning) was used (see

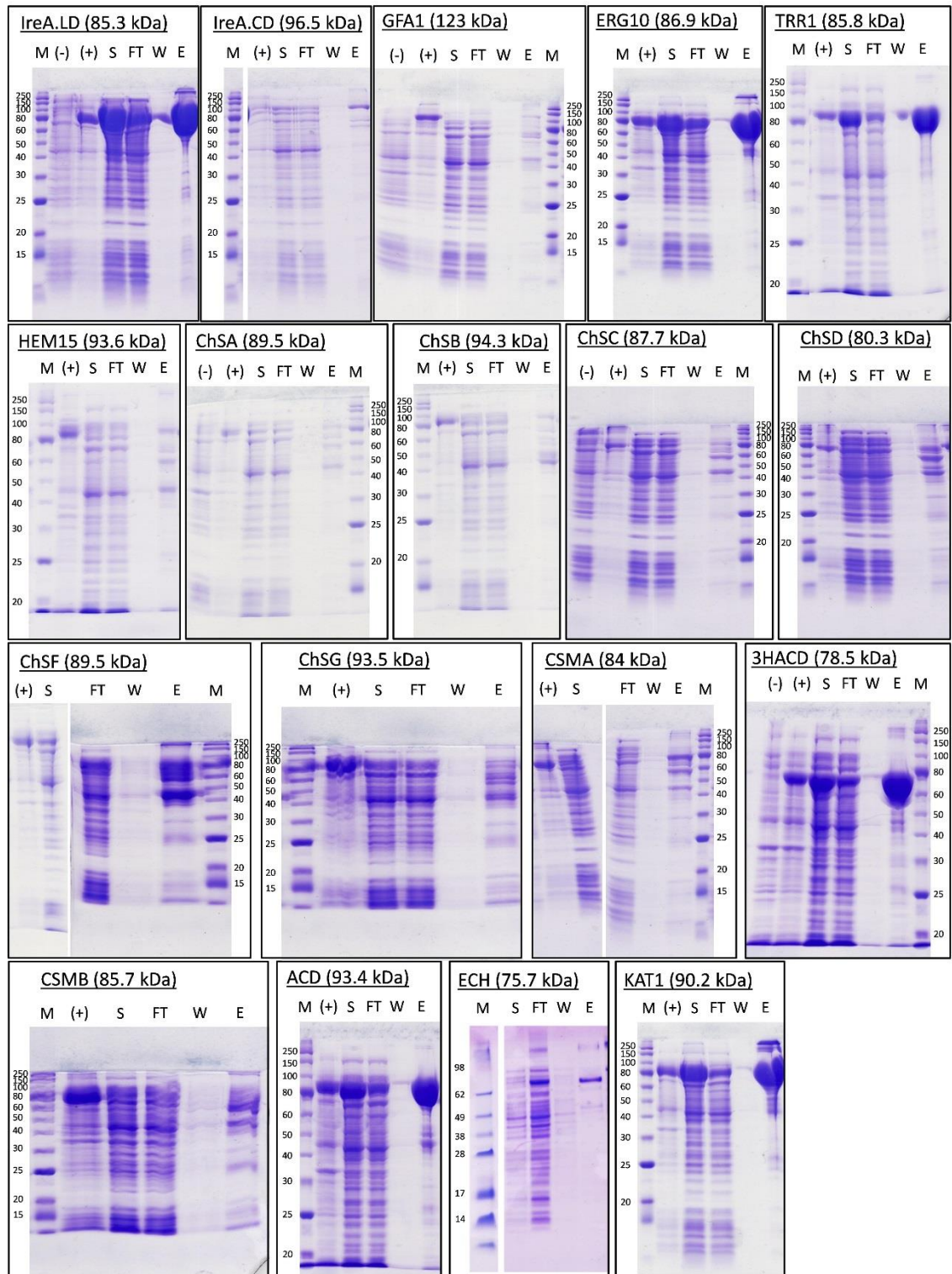


Figure 5. SDS-PAGE analysis of small-scale *E. coli* expression, solubility and Ni-NTA resin binding tests for preliminary 6xhis-MBP tagged *A. fumigatus* targets. (-), whole cell sample taken pre-induction; (+), whole cell sample taken post-induction; FT, unbound fraction; W, 10 mM imidazole wash; E, elution (500 mM imidazole); M, protein size standards. Expected protein molecular weight (including 6xhis-MBP tag) is indicated above each gel. The molecular weight of the protein standards is indicated in kDa.

Chapter 5, Materials and methods), bypassing any small-scale testing. All four of these proteins were successfully purified to homogeneity from *E. coli* culture, with sufficient yields to facilitate extensive crystallisation screening. Crystal structures were solved and supporting biochemical and/or biophysical data were collected for cytosolic thiolase (afCT; see **Chapter 4**), PCNA (AfumPCNA; see **Chapter 5**) and thioredoxin reductase (AfTrxR; see **Chapter 6**). A large (12 mg) homogenous IreA.LD protein sample was also successfully obtained. However, growth of diffraction-quality crystals has thus far been unsuccessful (see **Appendix 3**).

Chapter 4 (Publication):

Structure of *Aspergillus fumigatus*

Cytosolic Thiolase: Trapped Tetrahedral
Reaction Intermediates and Activation
by Monovalent Cations

Statement of Authorship

Title of Paper	Structure of <i>Aspergillus fumigatus</i> Cytosolic Thiolase: Trapped Tetrahedral Reaction Intermediates and Activation by Monovalent Cations.
Publication Status	<input checked="" type="checkbox"/> Published <input type="checkbox"/> Accepted for Publication <input type="checkbox"/> Submitted for Publication <input type="checkbox"/> Unpublished and Unsubmitted work written in manuscript style
Publication Details	Andrew C. Marshall, Charles S. Bond and John B. Bruning. (2018) <i>ACS Catalysis</i> 8: 1973–1989.

Principal Author

Name of Principal Author (Candidate)	Andrew C. Marshall		
Contribution to the Paper	Performed purification of recombinant protein, enzymology, X-ray data collection, processing, solution of crystal structures and interpretation, and prepared manuscript.		
Overall percentage (%)	80		
Certification:	This paper reports on original research I conducted during the period of my Higher Degree by Research candidature and is not subject to any obligations or contractual agreements with a third party that would constrain its inclusion in this thesis. I am the primary author of this paper.		
Signature		Date	12/12/17

Co-Author Contributions

By signing the Statement of Authorship, each author certifies that:

- i. the candidate's stated contribution to the publication is accurate (as detailed above);
- ii. permission is granted for the candidate to include the publication in the thesis; and
- iii. the sum of all co-author contributions is equal to 100% less the candidate's stated contribution.

Name of Co-Author	Charles S. Bond		
Contribution to the Paper	Advised X-ray data collection strategy and assisted with interpretation of crystallographic data and manuscript preparation.		
Signature		Date	

Name of Co-Author	John B. Bruning		
Contribution to the Paper	Managed project, and assisted with crystallography, data interpretation and manuscript preparation. Corresponding author.		
Signature		Date	12.12.2017

Please cut and paste additional co-author panels here as required.

Structure of *Aspergillus fumigatus* Cytosolic Thiolase: Trapped Tetrahedral Reaction Intermediates and Activation by Monovalent Cations

Andrew C. Marshall,[†] Charles S. Bond,[‡] and John B. Bruning^{*,†,§}

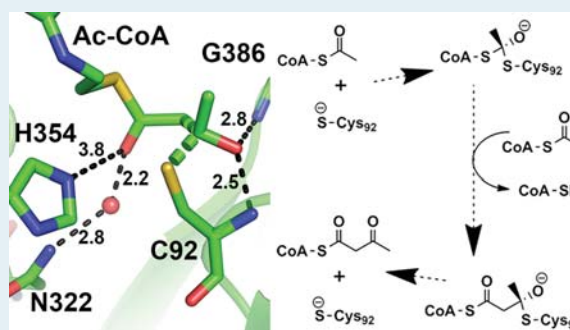
[†]Institute for Photonics and Advanced Sensing (IPAS), School of Biological Sciences, The University of Adelaide, Adelaide, South Australia 5005, Australia

[‡]School of Molecular Sciences, The University of Western Australia, Crawley, Western Australia 6009, Australia

Supporting Information

ABSTRACT: Cytosolic thiolase (CT) catalyzes the reversible Claisen condensation of two molecules of acetyl-CoA to produce acetoacetyl-CoA. The reaction cycle proceeds via a ping-pong mechanism involving an acetylated enzyme intermediate and two separate oxyanion holes which stabilize negatively charged reaction intermediates. This is the initial step in the synthesis of ergosterol in the prominent fungal pathogen *Aspergillus fumigatus* and is essential for the growth and survival of the organism. Here, we present crystal structures of *A. fumigatus* CT in liganded and apo forms and in a complex with different monovalent cations. Careful observation of the electron density at the active sites of two different afCT structures crystallized in the presence of acetyl-CoA shows that our crystals have trapped various stages of the thiolase catalytic cycle, including two tetrahedral reaction intermediates that have previously eluded structural characterization. Unexpectedly, we have also shown that afCT is activated by monovalent cations, a biochemical property previously thought to apply only to the mitochondrial biosynthetic thiolase, with a preference for potassium ions. Structures of fungal CT provide valuable insight into the thiolase reaction cycle and allosteric activation of members of this class of enzymes by monovalent cations.

KEYWORDS: biosynthetic thiolase, acetoacetyl-CoA, Claisen condensation, tetrahedral reaction intermediate, monovalent cation activation



INTRODUCTION

Ergosterol is the main fungal cell-membrane sterol; it is essential for fungal cell viability and survival and is lacking in host cell membranes, making it an attractive antifungal target. Antifungals targeting ergosterol are central to the treatment of invasive aspergillosis (IA), a debilitating condition caused by *Aspergillus* spp. associated with high morbidity and mortality rates and has had an increasing incidence in recent decades.^{1–5} First-line anti-*Aspergillus* drugs target ergosterol, either directly in the membrane or by inhibiting its synthesis. Amphotericin B binds ergosterol directly, disrupting membrane function.^{6–8} Although it has been used to treat IA for over four decades, it has largely been superseded by the azole class of antifungals due to its poor side-effect profile.⁹ Triazole antifungals target 14- α -lanosterol demethylase (*ERG11*), inhibiting ergosterol synthesis at the conversion of lanosterol to C14-demethyl-lanosterol. Voriconazole is currently recommended for first-line treatment of IA in most cases.¹⁰ Unfortunately, triazole antifungals are also associated with significant side effects, including liver toxicity, psychosis, and visual disturbances.^{9,11}

More importantly, the past two decades have seen an alarming increase in the incidence of azole-resistant isolates of *A. fumigatus*—the main causative agent of IA—worldwide. Azole-resistant strains of *A. fumigatus* have emerged both in the clinic and in the environment and are associated with poorer treatment outcomes.^{12–14}

Because of its essential role in fungal growth and relevance to the action of currently available antifungals, the biosynthesis of ergosterol is an essential area of study to improve current antifungals or uncover new targets in the synthetic pathway. In *A. fumigatus*, squalene is converted to ergosterol via approximately 12 distinct enzymes.¹⁵ Squalene is produced from mevalonate, the precursor for all isoprenoids, which include many important organic molecules such as sterols (including ergosterol), quinones, polyprenyl alcohols, heme A, and the post-translational prosthetic groups farnesyl and

Received: August 25, 2017

Revised: January 9, 2018

Published: January 25, 2018

geranylgeranyl.^{16,17} Mevalonate is produced in the cytosol from acetyl-CoA (Ac-CoA) via three catalytically independent steps (Figure 1). The first step is catalyzed by an acetoacetyl-CoA (AcAc-CoA) thiolase (ACAT). Therefore, synthesis of ergosterol, and all other sterols, starts with cytosolic ACAT.

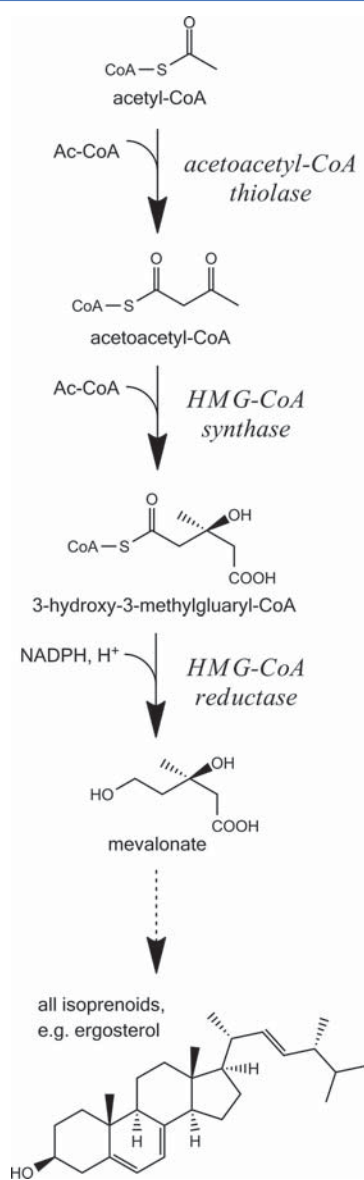


Figure 1. Production of mevalonate in the cytosol, involving three steps starting with the condensation of two molecules of acetyl-CoA by acetoacetyl-CoA thiolase (ACAT). Mevalonate is the precursor for all isoprenoids, including ergosterol, for which the chemical structure is shown (bottom).

Thiolases are ubiquitous enzymes involved in the transfer of acyl groups between acyl-CoA derivatives. There are two functional classes: type I thiolases, referred to as 3-ketoacyl-CoA thiolases (KAT), and type II thiolases, which are referred to as acetoacetyl-CoA thiolases (ACAT) or acetyl-CoA acetyltransferases.^{18,19} ACATs studied thus far are typically

homotetramers, while KATs are homotetramers or homodimers. KATs can accept acyl-CoA derivatives with a variety of chain lengths and are localized to mitochondria or peroxisomes, where they are involved in β -oxidation of fatty acids.¹⁸ ACATs are cytosolic, mitochondrial, or peroxisomal²⁰ and are specific for short-chain acyl-CoA substrates (C2–C4), catalyzing the formation or degradation of AcAc-CoA from Ac-CoA. Although the degradative reaction is entropically favored, high cellular concentrations of Ac-CoA derived from cellular catabolism along with rapid turnover of AcAc-CoA by the next enzyme in the pathway are postulated to drive the reaction in the biosynthetic direction.^{21–25} ACATs are therefore often referred to as biosynthetic thiolases. While cytosolic ACAT is essential for sterol synthesis, mitochondrial ACAT is essential for ketone body metabolism.^{26–28} In addition, mammalian mitochondrial ACAT (referred to in the literature as T2) differs from its cytosolic counterpart (referred to simply as cytosolic thiolase, CT) with regard to its substrate specificity and dependence on ions for activity. Unlike CT, T2 has been shown to turn over 2-methylacetoacetyl-CoA, implicating it in isoleucine catabolism.^{27,28} Also, T2 has K^+ and Cl^- ion binding sites near its active site and its catalytic activity is increased severalfold in the presence of K^+ ions, whereas the activities of bacterial and mammalian CTs studied thus far are ion independent.^{29,30} K^+ -dependent stimulation of thiolase activity is used as a tool for diagnosis of human T2 deficiency, a well-characterized disorder presenting with episodes of acute ketoacidosis, caused by mutations in the gene encoding for T2.^{27,31,32}

The cytosolic ACAT catalytic cycle has been studied in detail in the bacterium *Zoogloea ramigera*^{22,24,33–37} and involves the sequential binding of two Ac-CoA molecules to a single catalytic pocket (Figure 2). Upon binding of the first Ac-CoA, the acetyl group is transferred from the CoA to the catalytic cysteine, Cys89, forming an acetylated protein intermediate (Figure 2, stages 1–4). His348 is postulated to deprotonate Cys89, activating it for nucleophilic attack on the carbonyl of the acetyl moiety. Another Ac-CoA then binds and a Claisen condensation reaction occurs, involving transfer of the acetyl group from the enzyme, forming AcAc-CoA (Figure 2, stages 5–8). Cys378 is the active site base, abstracting a proton from C2 of the second acetyl moiety, activating it for nucleophilic attack on the carbonyl of the first acetyl moiety.^{34,37} In both acetyl-transfer reactions, the reaction must proceed via a tetrahedral intermediate associated with a negative charge on the acetyl oxygen atom, which is stabilized by two separate oxyanion holes (OAH). OAH1 is formed by $N\epsilon 2$ of His348 and a conserved catalytic water molecule and is involved in both steps of the catalytic cycle, while OAH2 is formed by peptide backbone nitrogen atoms of Cys89 and Gly380 and is only involved in the second step. The catalytic water is involved in forming OAH1 stabilized by a hydrogen bond to Asn316, an interaction shown to be essential for efficient catalysis.³⁷

The Claisen condensation reaction catalyzed by ACATs is a fundamental first step in the construction of carbon skeletal frameworks, essential for energy storage and normal cellular function in both prokaryotes and eukaryotes. There is also evidence to suggest that ACATs play a central role in cellular stress response. Bacterial ACAT catalyzes the first step in the synthesis of polyhydroxyalkanoates (PHA), the major energy and carbon storage molecules in many bacteria, important for survival under conditions of nutrient limitation or stress.^{25,38} Bacterial ACAT activity is inhibited by CoA, a negative feedback loop that is hypothesized to sense the metabolic state

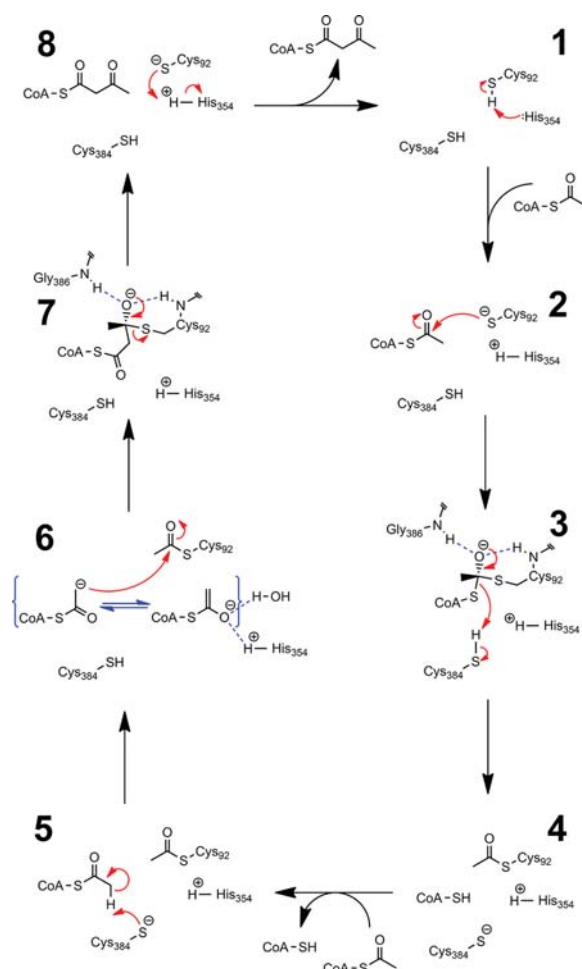


Figure 2. Catalytic cycle of ACAT. Residue numbers refer to *A. fumigatus* cytosolic ACAT (afCT). Cys92, His354, Cys384, and Gly386 of afCT correspond to Cys89, His348, Cys378, and Gly380 of *Z. ramigera* cytosolic ACAT (bCT), respectively (see text). Arrows indicate the progress of the reaction in the biosynthetic direction. Oxyanion hole 1 (OAH1) is formed by the side chain of His354 and a water molecule (referred to as Wat_{cat1} herein); OAH2 is formed by backbone N atoms of Cys92 and Gly386. Note that the thioester oxygen atom of the tetrahedral intermediate formed at stage 3 is drawn occupying OAH2. This is consistent with the structural evidence contained herein and challenges the previous understanding of the reaction mechanism, where it was thought that this tetrahedral intermediate was stabilized by OAH1.³⁶

of the cell.³⁹ Soto et al.⁴⁰ showed that expression of alfalfa cytosolic ACAT is upregulated under conditions of cold or salinity stress and also that overexpression of alfalfa cytosolic ACAT in bacteria increased bacterial stress resistance. Importantly, they showed that plant ACAT is also inhibited by CoA. It therefore follows that isoprenoid production is dependent on intracellular CoA concentrations. CoA is released from the citric acid cycle under optimal growth conditions, but this pathway is inhibited under conditions of oxidative stress.^{39,41,42} It has therefore been suggested that, when CoA concentrations are high (during optimal conditions), thiolase activity is low and so the rate-limiting step is the third step in the pathway, catalyzed by HMG-CoA reductase (Figure 1);

however, when CoA concentrations are low, thiolase activity is high and the first step, catalyzed by cytosolic ACAT, becomes the rate-limiting step.⁴⁰ Thus, it has been proposed that, upon encountering conditions of stress, many organisms alter their metabolism from the TCA cycle to the PHA or mevalonate pathways to provide highly reduced molecules for the antioxidant response.^{40,43} In agreement with this, in eukaryotes, consumption of Ac-CoA for lipogenesis is inhibited when the intracellular ATP concentration is low (cAMP concentration is high)⁴⁴—as would be the case when the citric acid cycle is inhibited. Under these conditions, conversion of Ac-CoA to malonyl-CoA—the rate-limiting step in lipogenesis—is inhibited by AMP-activated protein kinase (AMPK). This would increase the Ac-CoA concentration, increasing thiolase activity in the synthetic direction. Indeed, inactivation of the AMPK homologue in yeast resulted in decreased cytosolic Ac-CoA concentrations and reduced overall fitness and resistance to stress.⁴⁵ All of these observations suggest that cytosolic ACAT plays a key role in the cellular response to environmental stress in both prokaryotes and eukaryotes.

In fungi, *S. cerevisiae* cytosolic ACAT is the product of a single gene, *ERG10*, and is essential for viability in the absence of exogenous mevalonate.⁴⁶ Similarly, *Candida tropicalis* cytosolic ACAT null mutant is auxotrophic for mevalonate.²⁰ Unsurprisingly, *ERG10* has also been shown to be essential for growth in *A. fumigatus*,⁴⁷ presenting cytosolic ACAT as a potential target for novel antifungals. Despite its importance to fungal cell growth and survival, there have been no structural studies on a fungal ACAT until now. Here, we present the X-ray crystal structure of cytosolic ACAT from *A. fumigatus* (afCT), representing the first structure of a fungal type II thiolase. To our surprise, afCT is more similar to human mitochondrial ACAT (hT2) than to human cytosolic ACAT (hCT) with regard to its primary sequence, substrate binding pocket, accommodation of K⁺ and Cl⁻ ions, and dependence on K⁺ for activity. We have also investigated the enzyme's monovalent cation preference, with observations that challenge the current paradigm regarding activation of T2 by K⁺ but not Na⁺. Perhaps most importantly, our crystals have trapped several different catalytic site configurations, including both tetrahedral reaction intermediates of the thiolase reaction cycle, allowing us to clearly interpret the reaction mechanism of this enzyme for the first time in *A. fumigatus*, with implications for all members of the thiolase family.

EXPERIMENTAL SECTION

Reagents. Dithiothreitol was purchased from Apollo Scientific Ltd.; all other reagents were purchased from Sigma-Aldrich. CoA and AcAc-CoA stock concentrations were determined using Ellman's test⁴⁸ in 0.1 mM EDTA and 100 mM potassium phosphate pH 7.0. Protein purification columns were purchased from Bio-Rad Laboratories Pty., Ltd.

Sequence Analysis. A phylogenetic tree was generated by the "Simple Phylogeny" tool on the EMBL-EBI Web site using a Clustal omega multiple sequence alignment of ACATs from a range of species; the Interactive Tree of Life web-based tool⁴⁹ was used to generate Figure S1. Peroxisomal target signal sequences were predicted using the "Target Signal Predictor" web-based program.⁵⁰ Mitochondrial targeting peptide sequences were predicted using TargetP.⁵¹ A Clustal omega multiple sequence alignment of select ACATs was uploaded to the ESPript 3.0 server⁵² to produce Figure S2.

Protein Purification. The *A. fumigatus* cytosolic ACAT (afCT) DNA sequence (NCBI accession: XM_742114.1) was amplified from af293 cDNA (a generous gift from Dr. James Fraser, University of Queensland), cloned into pET-57-DEST via Gateway technology (Invitrogen), and recombinant afCT was then overexpressed in a 3 L culture of *E. coli* BL21(λ DE3) overnight at 16 °C in shake flasks. Cells were then resuspended in buffer (20 mM Tris pH 8.0, 0.5 M NaCl, 10% glycerol, 10 mM imidazole, 5 mM β -mercaptoethanol) and lysed by mechanical disruption. Clarified cell lysate was subjected to Ni²⁺-affinity chromatography twice, with a TEV digest in between to remove the hexahistidine and NusA tags. afCT protein was then purified to >95% (as assessed by SDS-PAGE) by anion-exchange chromatography (using an ENrich Q5 \times 50 Column; Bio-Rad) and dialyzed overnight at 4 °C to 10 mM NaCl, 1 mM DTT, and 10 mM Tris pH 8.0. Protein was concentrated to approximately 8 mg/mL, flash-cooled in liquid nitrogen, and stored at –80 °C.

Enzyme Assays. The activity of the purified enzyme in the degradative direction was assessed in vitro at 25 °C by the Mg²⁺ assay essentially as described⁵³ (Table 1). In the standard assay,

Table 1. Kinetic Parameters of *A. fumigatus* Cytosolic ACAT (afCT) (This Study), Human Cytosolic ACAT (hCT),⁷⁴ Rat Liver Cytosolic ACAT (rCT),⁵³ Human Mitochondrial ACAT (hT2),³⁰ and *Z. ramigera* Cytosolic ACAT (bCT)³⁷ with Acetoacetyl-CoA as the Substrate

enzyme	conditions ^b	K_m (μ M)	k_{cat} (s ⁻¹)	k_{cat}/K_m (s ⁻¹ μ M ⁻¹)
afCT ^a	low salt ^c	42 \pm 19	7 \pm 2	0.17
	100 mM NaCl	8 \pm 2	33 \pm 3	4.1
	100 mM KCl	8 \pm 2	100 \pm 10	13
hCT ⁷⁴	low salt	ND ^d	~170	ND
rCT ⁵³	50 mM KCl	33	ND	ND
hT2 ³⁰	40 mM NaCl	8 \pm 2	7.4 \pm 0.2	0.93
	40 mM KCl	4 \pm 0.6	21 \pm 1	5.3
bCT ³⁷	low salt	24 \pm 5	813 \pm 125	34

^aAll data for the current study were collected in triplicate, with uncertainty expressed as standard error. ^bAll assays were done in the thiolytic direction using the Mg²⁺ method under similar conditions, but with various [salt]. ^cSalts included in the standard conditions for the current study are 20 mM MgCl₂, 50 mM Tris-HCl (pH 8.1), and approximately 0.08 mM NaCl (from protein storage buffer). ^dNot determined.

the reaction was started by the addition of 300 ng of afCT to 50 mM Tris-HCl pH 8.1, 20 mM MgCl₂, 42 μ M CoA, and 7.5 μ M AcAc-CoA. The initial decrease in absorbance at 303 nm was then used to determine the rate of conversion of AcAc-CoA to Ac-CoA. The extinction coefficient for the Mg²⁺-AcAc-CoA enolate complex under these conditions was determined to be 16000 M⁻¹ cm⁻¹, similar to that previously reported.^{29,54} The k_{cat} and apparent K_m values for AcAc-CoA were determined by varying the concentration of AcAc-CoA from 0 to 38 μ M. The addition of either NaCl or KCl substantially increased the reaction rate, with maximum activity achieved at approximately 100 mM KCl. Therefore, K_m and k_{cat} values were also determined in the presence of 100 mM NaCl or 100 mM KCl, with the addition of 200 or 100 ng of afCT, respectively, to commence the reaction. To investigate the relationship between monovalent cation (MVC) ionic radius and activation of thiolase, chloride salts of other group I cations (Li, Rb, and Cs), as well as ammonium, were also tested at 100 mM in the

standard assay, with the addition of 200 ng of afCT to commence the reaction. All data were collected in triplicate, unless otherwise indicated, and fit in GraphPad Prism (v7).

Protein Crystallization. All protein crystallization experiments were performed at 16 °C using the vapor-diffusion method. afCT apo crystals grew as plates in 20% polyethylene glycol 3350 and 0.2 M KF to a maximum size of approximately 400 \times 400 μ m in 3 days in hanging drop format, with 4 μ L drops (2 μ L of the protein sample plus 2 μ L of the reservoir solution) and 0.5 mL reservoir volume. In the same way, crystals of afCT in complex with rubidium or cesium were grown in 20% polyethylene glycol 3350 and 0.15 M RbCl or 20% polyethylene glycol 3350 and 0.15 M CsCl, respectively. Crystals of afCT in complex with substrate were obtained by the addition of 5 mM Ac-CoA to 8 mg/mL purified protein immediately prior to setting up crystallization screens. Crystals grew as approximately 200–300 μ m rods after 3 days under two different conditions: 23% polyethylene glycol 3350, 0.2 M (NH₄)₂SO₄, 0.1 M Bis-Tris pH 6.5, and 0.2 M KCl in hanging drop format, with 2 μ L drops (1 μ L protein plus 1 μ L reservoir) and 0.5 mL reservoir volume; 25% polyethylene glycol 3350, 0.2 M (NH₄)₂SO₄, and 0.1 M Bis-Tris pH 6.5 in sitting drop format, with 2 μ L drops and 75 μ L reservoir volume.

Data Collection and Refinement. Data collection and refinement statistics are presented in Table S1 in the Supporting Information. Diffraction data were collected at 100 K at the Australian Synchrotron (MX1 beamline),⁵⁵ using mother liquor supplemented with 16% glycerol as cryoprotectant. Each data set consists of 360 frames collected at 1° intervals with 1° oscillation. All data were collected at an X-ray energy of 13000 eV, except for additional data sets collected at 8500 or 15350 eV for Cs⁺- and Rb⁺-containing crystals, respectively, to maximize anomalous signals. Data sets were processed using iMosflm,⁵⁶ and structures were solved by molecular replacement (MR) using PhaserMR.⁵⁷ Human mitochondrial ACAT (hT2) (PDB code: 2IBY) was used as the initial search model for MR; the first afCT structure was then used as the search model for subsequent afCT structures. Atomic coordinates were refined using phenix.refine⁵⁸ with iterative cycles of rebuilding in Coot,⁵⁹ with anisotropic B-factor refinement restricted to automatically defined torsion-liberation-screw (TLS) groups⁶⁰ and Rb⁺ and Cs⁺ ions individually, where applicable. The final models have good geometry statistics, with greater than 97% of peptide bonds within the favored region of the Ramachandran plot. The only Ramachandran outlier occurs at Val91 of all apo afCT structures and subunit C of afCT+AcCoA+NH₄⁺. phenix-maps⁶¹ was used to calculate anomalous difference maps, using data to 3.0 or 3.3 Å for afCT+Cs⁺_{anom} and afCT+Rb⁺_{anom} data sets, respectively. Anomalous difference Fourier maps for Rb⁺ and Cs⁺ ions, in addition to isomorphous difference maps derived from comparisons between data from crystals grown in the presence of KCl and those grown in the presence of RbCl or CsCl, were used to identify MVC binding sites. Atomic coordinates and structure factors for all models have been deposited in the RCSB Protein Data Bank (<https://www.rcsb.org/>) with the accession codes 6ARF, 6ARG, 6ARL, 6ARR, 6ART, 6AQP, and 6ARE (see Table S1).

Molecular Docking. Docking of (2S)-methylacetoacetyl-CoA and (2R)-methylacetoacetyl-CoA separately to the substrate binding site of the D subunit of afCT + AcCoA + K⁺ was performed manually, guided by the bound CoA

molecule in the crystal structure. This was then followed by global optimization of side chains and annealing of the peptide backbone (20 iterations) using ICM Molsoft (v3.8-6a).⁶²

Structure Visualization. Electrostatic surface representations were colored using electrostatic potential maps calculated by the APBS tool⁶³ in UCSF Chimera.⁶⁴ Atomic charges were first assigned using PDB 2PQR.⁶⁵ All other molecular graphics images were produced using PyMOL (v1.8.6.0) with all stereoviews produced using cross-eye stereo mode.⁶⁶ All chemical diagrams were drawn using ChemDraw Ultra (v12.0).

RESULTS

Sequence Analysis. Protein sequences of animal, plant, fungal, and bacterial thiolases were compared to provide insight into the evolution and function of *A. fumigatus* thiolases. A phylogenetic analysis can be found in Figure S1. *A. fumigatus* has genome annotations for four putative KATs and two putative ACATs.⁶⁷ Previous comparative genomic analyses of fungal species, along with *Aspergillus nidulans* gene deletion studies, have shown that, while yeasts such as *Saccharomyces* spp. and *Candida* spp. appear to have lost a mitochondrial β -oxidation pathway, retaining only a peroxisomal pathway, most fungi (including *Aspergillus* spp.) possess both mitochondrial and peroxisomal pathways.^{68–70} Shen et al.⁷⁰ showed that two of the four KATs in the *A. fumigatus* genome are likely localized to the mitochondria and the other two to the mitochondria or peroxisome. Interestingly, all four KATs from *A. fumigatus* cluster with plant, yeast, and human peroxisomal KATs, while human and fly mitochondrial KATs cluster separately. This suggests differences in the evolution of thiolase subcellular localization between lower eukaryotes and higher eukaryotes and is also consistent with the fact that fungi lack a mitochondrial trifunctional enzyme (TFE) homologue, involved in the type II β -oxidation pathway in higher eukaryotes.⁷⁰

ACATs from all species cluster together, separate from the KATs. Both *A. fumigatus* ACAT sequences were analyzed for predicted mitochondrial targeting peptide (mTP) and peroxisomal targeting signal (PTS) sequences. One ACAT possesses neither a predicted PTS nor mTP, and the other contains an N-terminal mTP, consistent with their respective clustering with yeast and plant cytosolic ACATs or human and fly mitochondrial ACATs (Figure S1). *A. fumigatus* cytosolic ACAT is homologous to *S. cerevisiae* cytosolic ACAT (NCBI accession: NP_015297.1), the product of the *ERG10* gene (NCBI Gene ID: 856079).⁴⁶ Intriguingly, in comparison to ACATs from higher eukaryotes, cytosolic ACATs from plant and fungi are more similar in terms of amino acid sequence to mitochondrial ACATs than to cytosolic ACATs. The crystal structure of human mitochondrial ACAT (hT2) revealed a K^+ binding site that stabilizes the substrate binding pocket and the catalytic histidine, providing a structural basis for its activation by K^+ ions.³⁰ In addition, a Cl^- ion was observed at the dimer interface, also stabilizing active site residues. *A. fumigatus* cytosolic ACAT—referred to simply as cytosolic thiolase (afCT) herein—has a higher sequence identity to hT2 (49.6%) than it does to human cytosolic ACAT (hCT) (44.3%). Upon closer inspection of the multiple sequence alignment of fungal, human, and bacterial ACATs (Figure S2), all the residues that differentiate hT2 from hCT (and bacterial ACAT (bCT)) with regard to Cl^- binding are conserved in afCT (Lys90, Asn385, and Gly389 with residue numbers referring to afCT), and most of the residues involved in

coordination of the K^+ in hT2 are well conserved in afCT (most notably, Tyr187). In addition, Phe325 of hT2, which has been suggested to be a key determinant for the broader substrate specificity of T2 over CT, is also conserved in afCT (Phe294). Interestingly, most of these residues are also conserved in yeast and *A. thaliana* cytosolic ACATs, consistent with the clustering of ACATs from fungi and plant with hT2, separately from hCT and bCT (Figure S1).

Enzyme Kinetics. Recombinant afCT was purified to homogeneity and assessed for AcAc-CoA thiolase activity in the degradative direction using the Mg^{2+} method (see the Experimental Section). When the assay was performed in the standard protein buffer (low [salt]), thiolase activity was very low, with a turnover rate much lower than for mammalian and bacterial ACATs, and a higher K_m for AcAc-CoA (Table 1). The high sequence similarity between afCT and hT2, particularly in regions associated with ion binding, prompted us to determine whether the catalytic activity of afCT is modulated by K^+ ions in the same way as for hT2. afCT activity was markedly increased in the presence of KCl, with maximum activity achieved at a KCl concentration of approximately 100 mM. Addition of 100 mM KCl caused a 5-fold decrease in the K_m value for AcAc-CoA and increased the k_{cat} value by 14-fold. afCT catalytic efficiency was also enhanced in the presence of NaCl; addition of 100 mM NaCl resulted in the same decrease in K_m for AcAc-CoA and a 5-fold increase in k_{cat} to a value similar to the k_{cat} value of hT2 in the presence of KCl, but still 3-fold lower than the k_{cat} value of afCT in the presence of KCl (Table 1). This was unexpected, as it is currently accepted that T2 is activated by K^+ but not Na^+ ions.^{29,30} Addition of 100 mM choline chloride resulted in no increase in afCT activity in the standard assay (Figure 3), showing that activation of afCT

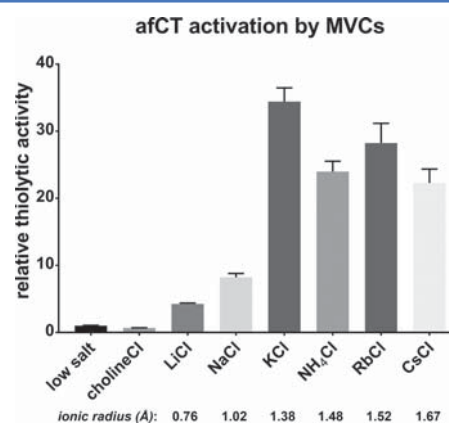


Figure 3. Activation of afCT by monovalent cations (MVC). Addition of 100 mM chloride salts of ammonium or all common alkali-metal ions (100 mM) increased afCT activity relative to the case when no additional salt was added to the standard assay conditions (see Experimental Section; “low salt” denotes approximately 0.08 mM NaCl from protein storage buffer). Addition of 100 mM choline chloride resulted in no increase in enzyme activity, showing that activation cannot be attributed to an increase in the Cl^- concentration or an increase in the ionic strength. The ionic radius of each MVC (coordination number 6) is shown (values are from the Database of Ionic Radii (<http://abulafia.mt.ic.ac.uk/shannon/>),⁹⁶ NH_4^+ ionic radius is from Sidey⁹⁷). Enzyme activity values are the mean of four separate experiments (except for NH_4Cl ; $n = 3$). Error bars represent standard error of the mean.

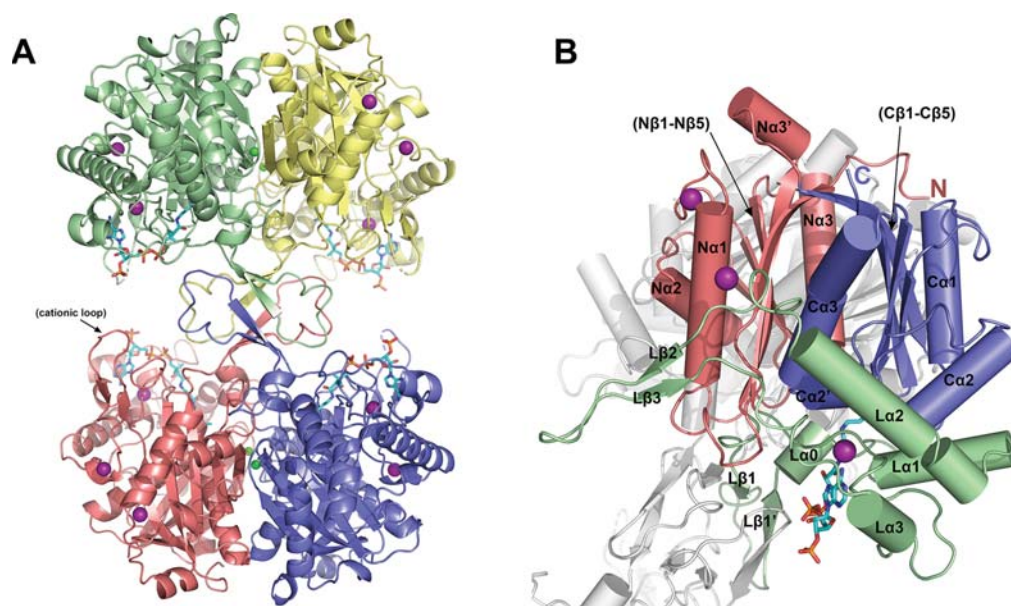


Figure 4. Cartoon representations of the three-dimensional structure of afCT showing CoA (cyan sticks), K^+ ion (purple spheres), and Cl^- ion (green spheres) binding sites: (A) tetrameric arrangement, with each subunit colored differently; (B) subunit tertiary structure, with α -helices (solid cylinders) and β -strands (arrows) labeled according to Modis and Wierenga²⁴ and the NTD, loop domain, and CTD colored red, green, and blue, respectively. Other subunits are colored white.

by NaCl is specific and is not simply a result of increasing ionic strength. It also rules out the possibility that activation is due to Cl^- ions rather than Na^+ ions. The MVC preference of afCT was investigated further by testing the effect of other monovalent cations (MVC) on afCT activity. Addition of chloride salts of all five common alkali-metal ions, or ammonium, increased the thiolytic reaction rate to some degree (Figure 3). Li^+ and Na^+ increased afCT activity 4-fold and 8-fold, whereas K^+ , NH_4^+ , Rb^+ , and Cs^+ all increased afCT activity greater than 20-fold relative to low salt conditions, with the greatest activity observed in the presence of K^+ (34-fold increase). This suggests that afCT possesses a site(s) that accommodates MVCs with an optimal ionic radius of that of K^+ (1.38 Å, where the coordination number is 6) but is promiscuous for other MVCs also.

Thiolase Structure. X-ray crystal structures of afCT were solved by molecular replacement using data to resolutions of 1.70–2.25 Å. Structures were solved in apo and liganded forms in complexes with different MVCs. Data processing and refinement statistics can be accessed in Table S1 in the Supporting Information. Occupancy refinement was performed for all ions, ligands, and residues with alternate conformations. For liganded structures, atoms of CoA were defined as a group separate from each individual acetyl group for refinement of group occupancies. Residues 1–398 could be confidently modeled into the electron density for all subunits in all structures (including Gly0—the remnant of the TEV protease cleavage site), except for N-terminal residues 1–3 for subunits A of afCT+ K^+ , afCT+ Rb^+ , and afCT+ Cs^+ and residues 211–214 of the cationic loop for most subunits across all structures. afCT crystallized in space group $P2_1$ in all cases, with four protein molecules per asymmetric unit, representing the biological tetramer (Figure 4A). The tetramer exhibits noncrystallographic 222 symmetry and is comprised of two tight dimers arranged head to head, with one dimer rotated

approximately 45° with respect to the other, such that residues of the cationic loop (including basic residues Arg212 and Lys214) point toward the CoA binding pocket of the opposing subunit (Figure 4A). Each subunit is essentially identical (RMSD across all α -carbons is 0.15–0.29 Å) and is composed of an N-terminal domain (NTD), a loop domain, and a C-terminal domain (CTD) (Figure S2 and Figure 4B). Residues of N β 2 and Na2, including their extended connecting loop (Asn59 to Asn68), along with N β 3 and Na3 of the NTD, contribute most of the interface between tight dimers. L β 1 and La1 of the loop domain and C β 1 of the CTD make up the remaining interface surface. The interface surface areas between directly opposite subunits (i.e., A and C or B and D) and diagonally opposite subunits (i.e., A and D or B and C) are approximately 344 and 758 Å², respectively. This is significantly less than the dimer interface surface area (i.e., between A and B or C and D), which is approximately 2494 Å². For all afCT structures, the average B factor of one dimer is approximately double that of the opposing dimer (see Table S1), indicating that the weaker tetramerization interaction allows for a degree of flexibility between the two tight dimers. This has been observed previously for other tetrameric thiolases,^{24,36,71} but its functional significance remains unknown.

The cagelike tetramerization motif is typical of biosynthetic thiolases and has been described in detail previously.²⁴ It is composed of residues His127 to Met148 of the loop domain (Figure S2). This loop extends away from the subunit core, allowing Tyr138, at the distal end of the loop, to form part of the entrance to the pantetheine binding tunnel leading to the thiolase active site of the diagonally opposite subunit and fill a hydrophobic pocket on its surface formed by Ile147, Met148, Leu152, and Leu255. L β 1 (residues 127–129) and L β 1' (residues 141–144) form an antiparallel β -sheet that is partially continuous with the equivalent β -sheet of both its dimeric partner and of the subunit diagonally opposite, such that a small

distorted β -barrel is formed. Twelve leucine residues, Leu129, Leu132, and Leu143 from each subunit, point inwardly to form the hydrophobic core of the cage. Four salt bridges formed between Arg133 and Asp145 of dimeric partners at the top and bottom of the cage stabilize the structure. Also contained within the loop domain is the cationic loop (residues 203–221), which extends into the intertetramer space toward the substrate binding site of the opposing subunit (Figure 4). A highly conserved arginine at the N-terminus (Arg14) appears to be responsible for anchoring the cationic loop to the NTD via electrostatic interactions with highly conserved acidic residues at either end of the cationic loop sequence (Glu202 and Asp222) (see Figure S2). The importance of these interactions was highlighted by a deletion mutation of the residue preceding Asp222 identified in hT2 from a T2-deficient patient.³¹

The NTD and CTD share a $\beta\alpha\beta\alpha\beta\beta$ topology, with the loop domain inserted between the final two β -strands of the NTD, a secondary structural topology well conserved among thiolases.^{19,24} Each terminal domain is composed of a central mixed β -sheet, flanked by helices on either side. These domains are rotated approximately 180° with respect to one another and pack face to face such that N α 3 and C α 3 are at the center, sandwiched between the β -sheets (Figure 4B).

Comparison to ACATs from Other Species. The afCT monomer has a tertiary structure very similar to those of hCT, hT2, and *Z. ramigera* ACAT (bCT), with average RMSD values across all C-alphas of 1.20–1.34 Å, respectively (Figure S3A). Superposition of dimers gives similar RMSD values (1.20–1.37 Å). Inclusion of the whole tetramer in this superposition demonstrates a degree of variation regarding the relative position of the second dimer (Figure S3B). This signifies a departure from exact 222 symmetry, consistent with the flexible nature of the tetramerization motif, and has been discussed in detail previously.⁷¹

The main differences between afCT and the other cytosolic ACATs (hCT and bCT) concern residues at the dimerization interface and substrate binding pocket, corresponding to regions that differentiate hCT from hT2, and have been shown to be involved in binding of K⁺ and Cl⁻ ions in hT2.³⁰

Binding of Monovalent Cations near the Substrate Binding Pocket. To probe for MVC binding sites, crystals of afCT were grown in the presence of K⁺, Rb⁺, or Cs⁺ ions. Anomalous difference Fourier maps for Rb⁺ and Cs⁺ ions (Figure S4), in addition to isomorphous difference maps derived from comparisons between data from crystals grown in KCl and those grown in RbCl or CsCl, were used to identify MVC binding sites. Average anomalous difference map peak heights are given in Table 2 (Tables S2 and S3 give anomalous and $F_o - F_c$ peak heights for all Cs⁺ and Rb⁺ sites, respectively). Thirteen binding sites were identified for Rb⁺ and 15 for Cs⁺. All of the Rb⁺ binding sites correspond to Cs⁺ binding sites, with the two extra Cs⁺ ions present at low occupancy (approximately 50%) at sites distant from the active site,

Table 2. Average Rb and Cs Anomalous Peak Heights (RMSD Units, σ) for Data Collected at Different Wavelengths

element	8500 eV data	13000 eV data	15350 eV data
Rb	NA ^a	4.5	13.2
Cs	23.5	11.9	NA

^aNot applicable.

implying that they are likely to be crystallization artifacts. Of the 13 MVC sites common to the Rb⁺ and Cs⁺ structures, one of these is part of a crystal contact, consistently present at low occupancy (approximately 50%), indicating that it is also likely to be a crystallization artifact.

On the basis of these results, 13 K⁺ ions were modeled at the sites common to the Rb⁺ and Cs⁺ structures, in both the apo (afCT+K⁺) and liganded (afCT+AcCoA+K⁺) structures, for which the crystallization conditions contained K⁺. The K⁺ ions are in the same position in each subunit of the tetramer and form similar coordination bonds. For the latter structure, K⁺ modeled into MVC binding sites refined to occupancies of between 43 and 97%. The crystallization conditions for this structure contained equal concentrations of K⁺ and NH₄⁺ ions; therefore, given the high activity of afCT observed in the presence of K⁺ or NH₄⁺ and their similar ionic radii (1.38 and 1.48 Å, respectively), it is likely that they would compete for the same binding sites, explaining the lower occupancy of K⁺ at MVC sites in this structure (Table S4). In addition, a structure of liganded afCT in the presence of only NH₄⁺ (afCT+Ac-CoA+NH₄⁺) was obtained, for which NH₄⁺ ions were modeled in all cation binding sites for which there was appropriate electron density (10 sites). Disregarding the MVC site that is part of a crystal contact, each subunit has the same three MVC binding sites (Figure 4). Two are positioned at the C-terminal ends of separate surface-exposed helices and coordinated by three or four water molecules and three carbonyl oxygens of adjacent residues within surface-exposed loops. The other is situated near the adenosine binding pocket (Figure 5). On the basis of proximity to the substrate binding pocket, coordination by protein atoms, and average occupancy and B factors for Cs⁺, Rb⁺, K⁺, and NH₄⁺ in all structures (see Tables S2–S4), the last of these three binding sites is most likely to be relevant to the modulation of thiolase activity in vivo.

This site is homologous to the K⁺ binding site of hT2,³⁰ with approximate octahedral coordination by six oxygen atoms. The K⁺ is coordinated by one water molecule (Wat_{MVC}; 2.7 Å) and five protein atoms: the backbone carbonyl oxygens of Ala249 (3.3 Å), Pro250 (2.7 Å), Ser252 (2.6 Å), and Val350 (2.8 Å) along with the hydroxyl oxygen of Tyr187 (2.8 Å) (Figure 5). Ion coordination at this site is essentially identical in liganded and apo afCT structures, aside from a small shift in Wat_{MVC} (~0.7 Å), facilitating the formation of a hydrogen bond (3.0 Å) to the adenine base (N7) of CoA in the liganded structure. Similarly, K⁺ coordinations at this site are essentially identical for afCT and hT2, with the only significant difference being a 0.6 Å shift of the coordinated water closer to the position of the bound CoA molecule, caused by the substitution of Pro254 (afCT) for Thr285 (hT2) (Figure S5). It has been previously suggested that, for hT2, coordination of a K⁺ ion at this position helps to rigidify the adenine binding pocket and stabilize the C β –C α 3 loop, which contains the catalytic histidine.³⁰ Ala249, Pro250, Ser252, and Tyr187 of afCT all make direct contact with bound CoA substrate and are contained within regions of the loop domain that contribute most of the residues involved in substrate binding. Val350 is part of a short helix (Ca2') immediately preceding the loop containing the catalytic histidine, His354 (Figure 5).

The mean length of coordination bonds (across all subunits) for K⁺, Rb⁺, and Cs⁺ ions bound at this position are 2.86, 2.96, and 3.12 Å, respectively. These values correspond very well to mean six-coordinate M⁺–O²⁻ complex bond lengths determined previously of 2.828, 2.989, and 3.124 Å, respectively.⁷²

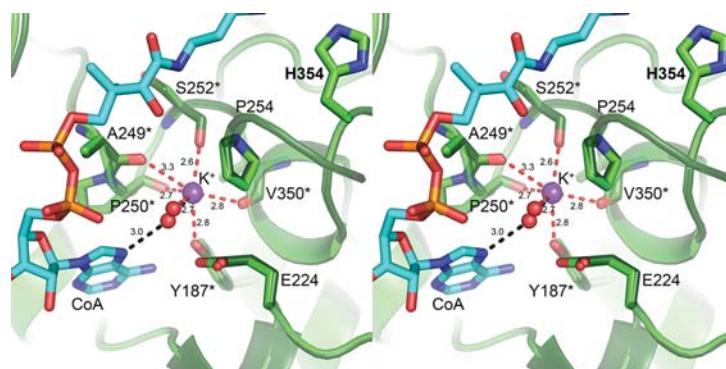


Figure 5. Stereoview of the monovalent cation binding site adjacent to the substrate binding pocket of afCT. The K^+ (purple sphere) is coordinated by adenosine pocket residues and Val350 (marked with asterisks), which is in the loop preceding the catalytic histidine (His354). Coordination bond (red dashes) lengths are shown (Å). apo (light green) and liganded afCT (dark green) are superposed, showing that the positions of the K^+ and surrounding residues are unaltered by ligand binding, but Wat_{MVC} (red sphere) shifts closer to CoA (cyan) in order to mediate hydrogen bonding from K^+ to CoA(N7A) (black dashes).

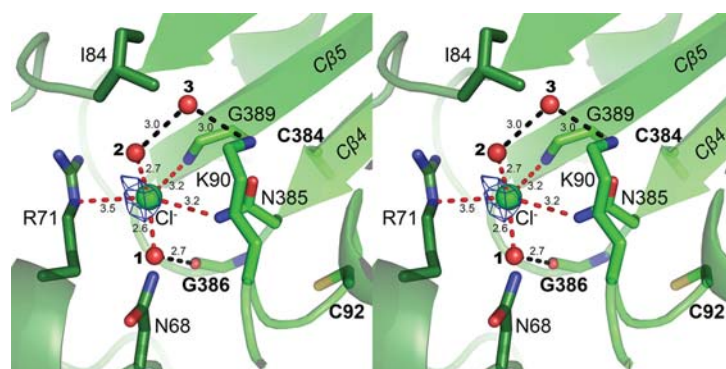


Figure 6. Stereoview of the Cl^- binding site at the dimerization interface of afCT with key residues labeled. Catalytic residues are labeled in bold type. Main chain atoms are hidden for all residues except Gly386 and Gly389. Opposing subunits of the tight dimer are colored different shades of green. The Cl^- ion (green sphere) is coordinated by three protein atoms and two waters (red spheres) near the thiolase catalytic site. Lengths of coordination bonds (red dashes) and water-mediated hydrogen bonds (black dashes) to residues adjacent to the catalytic site are displayed in Å. Wat_{CL1} , Wat_{CL2} , and Wat_{CL3} are numbered. An anomalous difference map calculated from data collected at 8500 eV is shown for the Cl^- as a blue mesh contoured at 3σ . Residues 85–86 were excluded from the foreground for clarity.

Superposition of these three apo structures shows that substitution of K^+ for Rb^+ or Cs^+ has no effect on the position of any of the coordinating atoms except for Wat_{MVC} , which shifts away from the MVC as the radius of the ion increases (Figure S6). This increases the distance between the relative positions of Wat_{MVC} in apo and liganded structures. For example, in the Cs^+ -bound structure, Wat_{MVC} is shifted 2.0 Å from the position it occupies when it forms a hydrogen bond with the adenine (N7) in the liganded structure. K^+ sits in the same plane as the coordinating oxygens of Tyr187, Ala249, Ser252, and Val350; however, due to their size, both Rb^+ and Cs^+ shift out of this plane, such that Cs^+ is positioned 0.5 Å closer to the substrate binding site. This less ideal coordination geometry, accompanied by the shift of Wat_{MVC} away from its substrate-interacting position, provides a molecular explanation for why K^+ is better able to stimulate afCT activity in comparison to these larger MVCs. Conversely, the planar geometry of K^+ with four coordinating ligands suggests that the site is larger than ideal for smaller MVCs; Octahedral Li^+-O^{2-} and Na^+-O^{2-} complexes have average bond lengths of 2.178 and 2.441 Å, respectively.⁷² Therefore, although the MVC site

of afCT can accommodate all common alkali-metal ions, its size is ideal for coordination of K^+ .

Calculation of an electrostatic potential surface map shows a strong negative charge at the MVC binding pocket, largely contributed by Glu224 (Figure S7A). In the absence of MVCs, electrostatic repulsion would exist between this negatively charged region and the pyrophosphate of CoA. MVC binding would increase the positive electrostatic potential of the adenosine binding pocket, increasing its affinity for the negatively charged phosphate groups of CoA. For hCT, a water molecule occupies a position similar to the K^+ of afCT and hT2 (Figure S7C). This water molecule is coordinated by only five oxygens: three backbone carbonyl oxygens (corresponding to Ala249, Ser252, and Val350 of afCT) and two other waters. The major differences between afCT and hCT regarding this pocket are the substitution of Tyr187 for Gln186 and Glu224 for Phe221. The significance of Tyr187, which provides a K^+ coordinating oxygen, is highlighted by its conservation across fungal ACATs and hT2 (Figure S2). A glutamine is present at this position for both hCT and bCT, which is too far from the K^+ site to donate a coordinating oxygen. Glu224, which carries the closest negative charge to the

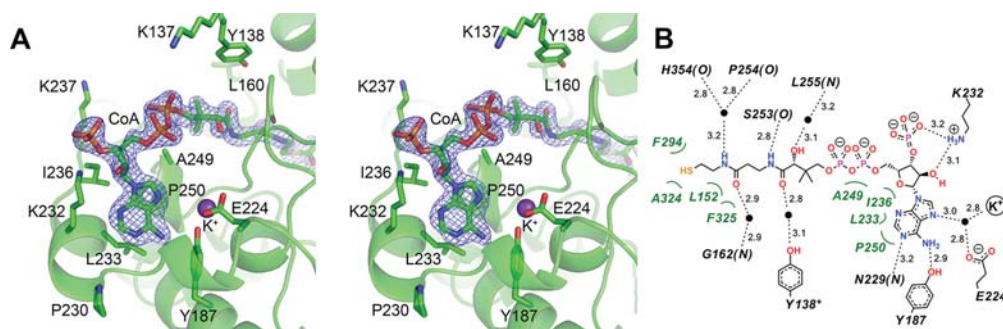


Figure 7. Mode of CoA binding. (A) Stereoview of CoA substrate bound to afCT. Key residues are shown as sticks. A $2mF_o-DF_c$ composite omit map (blue mesh) contoured at 1.0σ is shown for the CoA molecule. The K^+ is represented by a purple sphere. (B) Two-dimensional schematic of interactions between afCT and bound CoA. Hydrogen bonds are indicated by dashed lines, and van der Waals contacts are indicated by solid curved lines. Waters involved in water-mediated hydrogen bonds are shown as black circles. All interacting residues are from the same subunit, except for Tyr138 (marked with an asterisk), which protrudes for the tetramerization loop of the diagonally opposite subunit.

K^+ (4.4 Å), is conserved in hT2 but substituted for a phenylalanine or tyrosine in hCT or bCT, respectively, decreasing the negative electrostatic potential of the pocket (Figure S7B).

Chloride Ion Binding Site. Residues that were identified to make contacts with the Cl^- ion in hT2 are conserved in afCT (Figure S2). This prompted us to model Cl^- ions at these sites for afCT. In addition, small anomalous difference peaks for data collected at 8500 eV (Table S1, afCT+Cs⁺_{anom} data set) provided further validation that these Cl^- ions were modeled correctly (Figure 6). There are two identical Cl^- binding sites at each dimer interface (one for every subunit), within approximately 10 Å of the thiolase active site (Figure 6). The Cl^- is positioned between two basic residues—Arg71 from one monomer, and Lys90 from the dimeric partner—and is coordinated by five atoms, Arg71 (N ϵ ; 3.5 Å), Asn385 (N δ_2 ; 3.2 Å), Gly389 (N; 3.3 Å), Wat_{CL1} (2.6 Å), and Wat_{CL2} (2.7 Å), consistent with a recent survey of PDB structures indicating that 5 is the preferred coordination number for Cl^- within proteins.⁷³ Even though it is not involved in catalysis directly, this Cl^- stabilizes the catalytic site via both direct and water-mediated hydrogen bonds to catalytic residues and residues adjacent. Aside from forming a coordination bond with Asn385—which is flanked on either side by catalytic residues Cys384 and Gly386—the Cl^- interacts with Gly386(O) via Wat_{CL1}, and Lys90(N ζ) via Wat_{CL2} and Wat_{CL3}. Comparison with the structure of hT2 shows that Ala102 and P118 of hT2 are substituted for Asn68 and Ile84 in afCT, respectively (Figure S8A). The effect of these two substitutions is to widen the afCT Cl^- binding pocket slightly, allowing one extra water molecule in comparison to hT2 and shifting the Cl^- by 1.6 Å, so that it is closer to Arg71 and the C β 4–C β 5 active site loop (containing Cys384, Asn385, and Gly386). In addition, the afCT site much more solvent accessible than the hT2 site. The Cl^- is connected to bulk solvent via a chain of waters leading to Gly156 on the surface of the protein. For hT2, this residue is Tyr188, which disrupts this chain of waters. Interestingly, of all the ACAT sequences compared in Figure S2, afCT is the only one without an aromatic residue at this position.

Regarding the region corresponding to the Cl^- binding site, the dimerization interfaces of hCT and bCT are much more hydrophobic in comparison to afCT and hT2. Although Arg71 is highly conserved, Lys90, Asn385, and Gly389 are all substituted for hydrophobic residues, Met90, Ile384, and

Met388 in hCT, with the last of these occupying the space of the Cl^- and Wat_{CL2} in the afCT structure (Figure S8B).

Mode of CoA Binding. In addition to forming the tetramerization motif, the loop domain contains most of the residues that are important for substrate binding. Average *B* factors for protein atoms of liganded structures are much lower than for the apo structures (Table S1), indicating that substrate binding stabilizes the polypeptide. The CoA binding site can be conceptually divided into two pockets: the 3'-phosphoadenosine binding pocket and the pantetheine binding pocket. Both pockets open into the intertetramer space. Loop domain residues 224–237 and 249 to 250, along with Tyr187, form the 3'-phosphoadenosine binding pocket (Figure 7A). Of note are five basic residues within 10 Å of the phosphate groups of CoA: Lys232 and Lys237 of the subunit in question, Lys137 of the diagonally opposite subunit, and Arg212 and Lys214 of the cationic loop (residues 203–221), which extend into the intertetramer space from the opposing subunit (note that the side chains of Arg212 and Lys214 are unstructured in almost all structures; however, the proximity of the peptide backbone affords the possibility that they interact with the 3'-phosphate of CoA). Similar positioning of basic residues in tetrameric ACATs from other species has been suggested to facilitate electrostatic interactions with CoA to aid substrate capture.^{24,74} One of these basic residues—Lys232—forms a salt bridge with the 3'-phosphate of CoA. Despite possessing numerous hydrogen bond donors and acceptors, there are only three other hydrogen bonds made directly between CoA and protein atoms: Tyr187 (OH) to adenosine (N6) (2.9 Å), Asn229 (N) to adenosine (N1) (3.2 Å), and Ser253 (O) to pantetheine (N8) (2.8 Å) (Figure 7B). All other hydrogen bonds are mediated by surrounding water molecules, including the Wat_{MVC}-mediated interaction with K^+ , mentioned previously. A similar lack of direct bonding has been noted previously for bCT, which possesses only one direct hydrogen bond between protein and substrate.²⁴ All residues that interact with bound substrate are from the same subunit, with the exception of Tyr138, which protrudes from the tetramerization loop of the diagonally opposite subunit, forming part of the entrance of the pantetheine binding tunnel and participating in a water-mediated hydrogen bond with pantetheine (O9) (Figure 7). Interestingly, of the ACAT sequences compared in Figure S2, this tyrosine is only conserved in hT2. Ala249 and Pro250, which both provide oxygen atoms for coordination of the K^+ ,

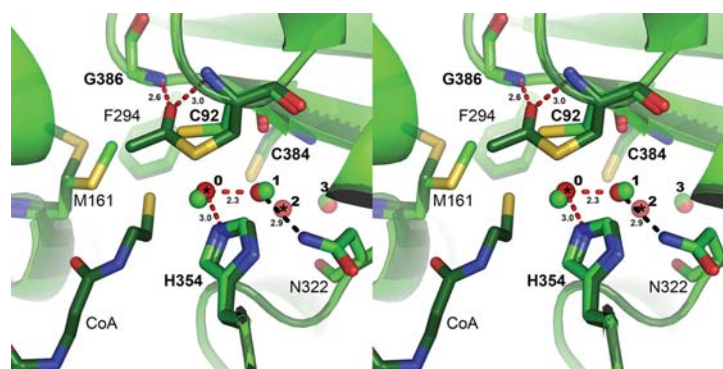


Figure 8. afCT catalytic site shown in stereoview. Superposition of afCT liganded (dark green) and apo (light green) structures shows that ligand binding induces changes in the side chain conformations of Cys92 and Met161. Cys92 is acetylated in the liganded structure. Key residues are labeled and key waters represented by spheres: colored red in the liganded structure and light green in the apo structure. Positions of $\text{Wat}_{\text{cat}1}$, $\text{Wat}_{\text{cat}2}$, and $\text{Wat}_{\text{cat}3}$ are labeled 1, 2, and 3. $\text{Wat}_{\text{cat}1}$ shifts into OAH1 in the absence of an occupying acetyl group (i.e., from Ac-CoA); this position is labeled 0. Asterisks indicate alternate conformations for waters modeled in the liganded structure (see text). OAHs 1 and 2 are indicated in the liganded structure by hydrogen bonds (red dashes; measurements are in Å) to $\text{Wat}_{\text{cat}1}$ (position 0) and Ac-Cys92, respectively. When it occupies position 1, $\text{Wat}_{\text{cat}1}$ is stabilized by a hydrogen bond from Asn322 (black dashes).

contact the adenosine of CoA. The pyrophosphate is less than 3.5 Å from Ala249, such that the CoA molecule bends around Ala249 at this point. Pro250 packs against the adenine rings (<3.7 Å). Leu233 and Ile236 also contribute van der Waals interactions with the adenine and ribose groups, respectively. For hT2, similar van der Waals interactions are facilitated by corresponding residues: Ala280, Ala281, Val264, and Leu267. Residues 227–230 of the $L\beta 3$ – $L\alpha 3$ loop, which wrap around the bound adenine in afCT, are shifted approximately 2 Å away from the interdimer space relative to the same region of hT2 (Figure S9A). This is largely caused by the substitution of Phe261 in hT2 for Pro230 in afCT and results in a similar small shift in the adenosine (~1 Å) deeper into the protein. Despite this, the overall structure of the adenosine binding pocket and key interactions are highly conserved between afCT and hT2.

Unlike hT2, the adenine binding pocket is much less conserved between afCT and other cytosolic ACATs. hCT and bCT contain a small uncharged residue (Ala230 of hCT) at the position corresponding to Lys232 of afCT and therefore lack this salt bridge to the 3'-phosphate of the adenosine. Both also contain one extra residue in the $L\beta 3$ – $L\alpha 3$ loop (220–229 of afCT)—His224 of hCT and His221 of bCT—which packs down against the surface of the protein away from the bound CoA, resulting in a significant rearrangement of this loop relative to the afCT structure (Figure S9B). This allows the preceding arginine (hCT Arg223, bCT Arg220) to stack against the adenine rings of CoA—an interaction that is absent from both afCT and hT2 structures.

Aside from Ser252 and Ser253, the pantetheine pocket leading to the catalytic site is lined exclusively by hydrophobic residues: Met122, Leu152, Met161, Gly162, Ala239, Phe240, Pro254, and Leu255 of the loop domain and Phe294, Ala324, Phe325, and Ile356 of the CTD. These residues are highly conserved across fungal, bacterial, human, and plant ACATs (Figure S2), with the notable exceptions of Ala239, Pro254, and Phe294. In addition, Leu160, which is positioned approximately 7 Å away from the pantetheine at the tunnel entrance, is substituted for a histidine in hT2 (His192), hCT (His159), and bCT (His156), which contacts the pantetheine of the bound substrate (Figure S9A,B). The area occupied by this histidine is replaced by a water molecule in afCT, mediating a hydrogen-

bonding interaction between pantetheine (OS) and Gly162 (N) (Figure 7B). Ala239 is conserved for bCT but substituted for Tyr237 in hCT (Figure S9B). This tyrosine provides more surface area for van der Waals interaction with the pantetheine moiety but does not appear to significantly alter the relative position of the bound substrate. Pro254 is near the K^+ binding site and is substituted for a glycine in both hCT and bCT, probably to allow for the extra bulk of the aromatic residue that occupies the space of Glu224 near the K^+ site mentioned earlier.

Accommodation of 2-Methylacetoacetyl-CoA by afCT. In addition to catalyzing the synthesis and degradation of AcAc-CoA, T2 catalyzes the last reaction in the isoleucine degradation pathway, where 2-methylacetoacetyl-CoA is converted to propionyl-CoA and Ac-CoA in the mitochondria.²⁷ Human T2 deficiency results in accumulation of isoleucine degradation metabolites. Substitution of afCT Phe294 for methionine in both hCT and bCT is the only major difference between these enzymes at their catalytic sites. Phe294 is conserved in hT2 (Phe325) and has been linked to the broader substrate specificity of hT2 in comparison to hCT. The Phe325-Pro326 dipeptide of hT2 expands the catalytic cavity relative to hCT (for which the corresponding sequence is Met293-Gly294), allowing it to accommodate the larger branched chain substrate, 2-methylacetoacetyl-CoA.³⁰ bCT has been shown to have no activity toward 2-methylacetoacetyl-CoA.²⁵ Strikingly, Phe294 is conserved across all ACAT sequences compared in Figure S2, except for hCT and bCT, for which it is substituted for a methionine. Specifically, the Phe-Pro dipeptide is conserved in both mitochondrial ACATs (*A. fumigatus* mACAT and hT2); both hCT and bCT contain Met-Gly, and all other cytosolic ACATs contain a Phe-Thr dipeptide at this position. In addition, afCT Asn332 is conserved across all these ACATs except for hCT and bCT, which both contain an aliphatic residue at this position (Figure S2). The N δ 2 atom of Asn332 (hT2 Asn363) forms a hydrogen bond (2.9 Å) with the backbone O atom of Thr295 (hT2 Pro326) and is possibly important for anchoring the preceding phenylalanine to allow room for the extra methyl group of this branched chain substrate.

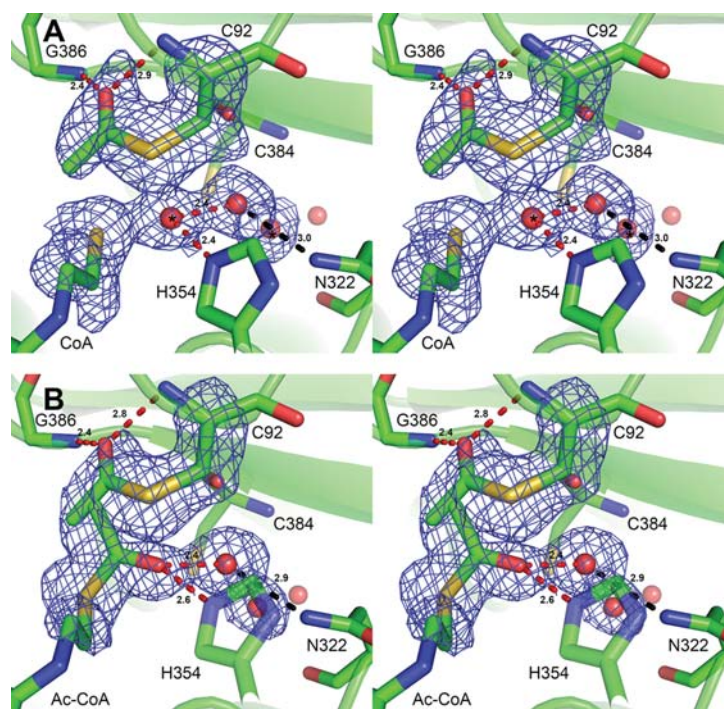


Figure 9. Stages 2 and 4 of the thiolase reaction cycle trapped in afCT crystal structures. Images are shown in stereoview. Polder maps (blue mesh) are shown for the Cys92 side chain, the sulfur and adjacent carbon of CoA, acetyl groups, and waters in position 0, 1, or 2 of the water trail. Maps are contoured at 3.0σ . Waters with alternate conformations are marked with asterisks. Hydrogen bonds of OAHs are indicated by red dashes. The hydrogen bond from Asn322 stabilizing Wat_{cat1} is colored black. Units of measurement are Å. (A) Catalytic site of afCT+AcCoA+ K^+ subunit D demonstrates the conformation of Ac-Cys92 occupying OAH2 with CoA bound. Wat_{cat1} partially occupies OAH1. (B) Catalytic site of afCT+AcCoA+ K^+ subunit C shows the position of the acetyl group both before and after the first acetyl-transfer reaction as alternate conformations of Ac-CoA (occupying OAH1) and Ac-Cys92 (occupying OAH2). His354 (foreground) is shown as transparent sticks.

A simple molecular docking experiment suggests that afCT can indeed accommodate 2-methylacetoacetyl-CoA, requiring only a minor (20°) rotation of Phe294 away from substrate. This places Phe294 in a position almost identical with that observed for the corresponding phenylalanine (Phe325) in the structure of hT2 in complex with CoA (PDB: 2IBY).³⁰ The extra methyl group is in van der Waals contact with the phenyl ring of Phe294, and the thioester and 3-keto O atoms are positioned in OAHs 1 and 2, respectively (Figure S10). This is consistent with the results of a similar docking experiment performed for hT2.³⁰ These results potentially implicate afCT in isoleucine metabolism; however, further investigation is needed to confirm this and clarify its biological significance.

Catalytic Site. The catalytic residues—Cys92, His354, Cys384 and Gly386—are contained in three loops, $\text{N}\beta 3\text{-N}\alpha 3$, $\text{C}\beta 3\text{-C}\alpha 3$, and $\text{C}\beta 4\text{-C}\beta 5$, in the interior of each subunit (Figure 8). Conserved glycines (95, 357, and 360) of the two central helices ($\text{N}\alpha 3$ and $\text{C}\alpha 3$) allow them to pack very close to one another, positioning the catalytic site at the N-terminal ends of two long helices, taking advantage of helix dipoles to decrease the pK_a of active site cysteines and assist with stabilization of negatively charged species formed during the thiolase catalytic cycle (Figure 2).⁷⁵ In addition, Asn322, which is part of the signature NEAF motif of thiolases located in the $\text{C}\beta 2\text{-C}\alpha 2$ loop (corresponding to Asn316 of bCT), stabilizes a catalytic water (Wat_{cat1}) via a hydrogen bond. Wat_{cat1} and His354 ($\text{Ne}2$) form OAH1. The peptide backbone nitrogens of Cys92 and Gly386 form OAH2. Cys92, which serves as the nucleophile in

the first acetyl transfer (Figure 2, stage 2), is contained within a 3_{10} -helix at the N-terminal end of $\text{N}\alpha 3$, a strained conformation observed previously for other thiolases,^{36,74} stabilized by hydrogen bonds between Ser94 (OH) and the peptide backbone of Lys90 and Val91. Val91 is the only Ramachandran outlier in any of the structures. It is only present consistently in afCT apo structures, suggesting that this strained peptide conformation is “relieved” during the thiolase reaction cycle.

For both liganded structures (afCT+AcCoA+ K^+ and afCT+AcCoA+ NH_4^+), CoA could be modeled into all active sites with an occupancy of 76% or greater. Ligand binding induces no large conformational changes in protein structure; RMSD values between apo and liganded afCT are 0.24 or 0.67 Å across *Cas* of a single subunit or the entire tetramer, respectively. The only notable changes occur at the active site, regarding the side chain conformations of Met161 and Cys92 (Figure 8). $S\delta$ of Met161 is shifted 2.6 Å away from the active site center upon ligand binding to allow room for the pantetheine of CoA. Binding of CoA also induces a small shift in the position of Cys92 ($S\gamma$), 1.4 Å toward the side chain of His354. It is postulated that this shift facilitates the deprotonation of Cys92 ($S\gamma$) by His354 ($\text{Ne}2$), allowing Cys92 to act as the nucleophile in the first acetyl transfer.³⁵ Once bound, the sulfur of CoA is then positioned only 4.1 Å away from Met161 ($S\delta$), 4.0 Å from Cys92 ($S\gamma$), and 5.4 Å from Cys384 ($S\gamma$). Positioning of CoA (S) near sulfur atoms at the thiolase active site is important for high affinity binding of substrate.⁷⁶

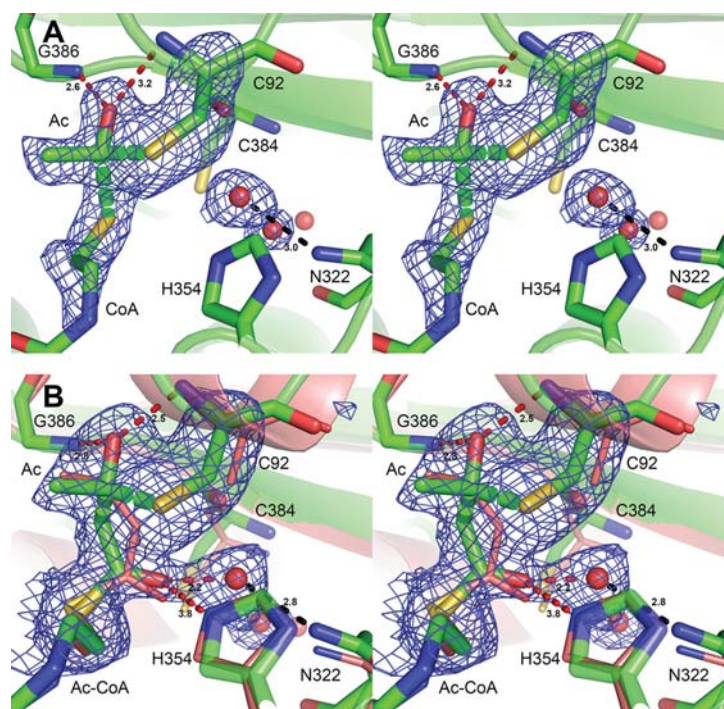


Figure 10. Both tetrahedral reaction intermediates of the thiolase reaction cycle trapped in afCT crystal structures. Images are shown in stereoview. Polder maps (blue mesh) are shown for the Cys92 side chain, the sulfur and adjacent carbon of CoA, acetyl groups, and waters in position 1 or 2 of the water trail. Maps are contoured at 3.0σ and 2.5σ for (A) and (B), respectively. The hydrogen bond from Asn322 stabilizing $\text{Wat}_{\text{cat}1}$ is colored black. Units of measurement are Å. (A) Catalytic site of afCT+AcCoA+ NH_4^+ subunit D shows the covalent tetrahedral intermediate formed during the first acetyl-transfer step, stabilized by OAH2. Dashed sticks indicate bonds that are formed or broken during this stage of the thiolase reaction cycle. (B) Catalytic site of afCT+AcCoA+ NH_4^+ subunit C shows the covalent tetrahedral intermediate formed during the second acetyl-transfer step. The first acetyl group is stabilized by OAH2, and the second (Ac-CoA) occupies OAH1. Superposition with AcAc-CoA bound to bCT (Cys98Ala) (narrow salmon sticks; PDB: 1M1O) shows that the intermediate is positioned in a way similar to that for AcAc-CoA, as expected.

Approximately 15 ordered water molecules are displaced by substrate binding; 9 from the adenosine pocket and 6 from the pantetheine pocket. In addition, there is a chain of 3 water molecules that begins at the active site and penetrates further into the interior of the protein. This includes $\text{Wat}_{\text{cat}1}$, which, along with His354 ($\text{Ne}2$), forms OAH1. In contrast, for both hCT and bCT this chain of waters includes approximately 10 waters, forming a hydrogen-bonding network that extends through a narrow cavity between $C\beta 2$ and $C\alpha 2$ through to solvent at the back side of the protein.^{35,74} It has been suggested that this water network may modulate the electrostatic environment of the catalytic site, promoting catalysis and may explain the lower catalytic efficiency of T2 (which lacks this network) in comparison to hCT and bCT.³⁷ In both afCT and hT2 structures, only the first two or three waters of the network are present, closest to the catalytic site. Comparison of the sequences and crystal structures of afCT and hT2 with hCT and bCT indicates that substitution of several residues within $C\alpha 2$ may account for the narrowing of this cavity, disallowing the presence of water molecules (Figure S11). Ser326, Val327, and Leu330 of afCT pack against $L\alpha 1$ and $L\alpha 2$ and are all larger than the equivalent residues of hCT, which are all alanine residues. These three $C\alpha 2$ residues are on the side of the helix opposite to $C\beta 2$, shifting the helix closer to $C\beta 2$. Another $C\alpha 2$ residue, Asn332, is conserved in all ACATs except hCT and bCT (where it is substituted for an aliphatic residue; Figure S2) and forms hydrogen bonds with backbone atoms of $C\alpha 1$

(Thr295 and Ala299), also drawing $C\alpha 2$ closer to $C\beta 2$ (Figure S11). In addition, Tyr182 occupies what would be the entrance to the cavity at the surface of the protein.

Although both liganded structures share similar global folds ($C\alpha$ -RMSD of tetramers: 0.66 Å), notable differences in the electron density present in the catalytic sites of the enzyme prompted us to model the atomic composition at each active site of the tetramer in both structures separately using Polder maps to both reduce model bias and enhance weak density that may be masked by bulk solvent.⁷⁷ The observed density indicates that Cys92 is modified such that OAH2 is occupied, and at least one acetyl group is present in every active site. Given that CoA occupies every active site, and there is density for at least one acetyl group, there are seven different configurations of atoms possible, corresponding to stages 2–8 of the reaction cycle shown in Figure 2. The electron density suggests that we have trapped multiple reaction intermediates.

For five of the eight active sites, CoA and an acetylated Cys92 (Ac-Cys92) corresponded to the electron density (Figure 9A), with the occupancy of the acetyl group between 63 and 76%, in agreement with the occupancy of the corresponding bound CoA molecule. OAH2 is occupied by the acetyl carbonyl oxygen, with hydrogen bonds to Cys92 (N) (2.9 Å) and Gly386 (N) (2.4 Å). This represents stage 4 of the reaction cycle, after acetyl transfer from the first Ac-CoA to Cys92. For biosynthetic thiolase, the rate-limiting steps in both biosynthetic and degradative directions are those involving

deacetylation of the active site cysteine;³⁵ therefore, it is unsurprising that this is the most commonly observed active site configuration. In all these cases there is additional density observed in OAH1. This space is occupied by a water molecule in the apo structure (afCT+K⁺), in which the second water is absent from the water chain that begins with Wat_{cat1} (Figure 8). This suggests that Wat_{cat1} shifts forward into OAH1, accompanied by a shift in the adjacent water (Wat_{cat2}) from position 2 in the water chain to the original position of Wat_{cat1} (position 1), leaving position 2 vacant, as observed for the apo structure. To reflect this, for the liganded structure, a water molecule was modeled with two alternate conformations: (1) occupying position 2 of the water chain (Wat_{cat2}) or (2) occupying OAH1 (Figures 8 and 9A). Subsequent refinement resulted in occupancies of approximately 50% at both positions. The position of the thioester O atom of Ac-Cys92 (occupying OAH2) that we observe conflicts with previous structural studies on bCT.^{24,35,36} This is discussed further in the subsequent section.

Additional electron density present between the sulfur atoms of CoA and Cys92 in one of the afCT+AcCoA+K⁺ active sites promoted us to model a second acetyl group, as Ac-CoA (Figure 9B). This clashed with Ac-Cys92 and therefore was modeled as an alternate conformation, corresponding simultaneously to stages 2 and 4 of the reaction cycle (Figure 2)—immediately before and after the first acetyl transfer. For stage 2, the thioester O of Ac-CoA occupies OAH1, with hydrogen bonds to Wat_{cat1} (2.4 Å) and His354 (Nε2) (2.6 Å). This stabilizes the partial negative charge present on this oxygen, increasing the electrophilicity of the adjacent C1 atom. Cys92 (Sγ) is very close to C1 of the acetyl group (2.3 Å), poised for nucleophilic attack. For stage 4, the carbonyl O of Ac-Cys92 occupies OAH2 in the same way as for the active sites with CoA and Ac-Cys92 described above.

Tetrahedral Intermediates Trapped for Both Acetyl-Transfer Reactions. For a single active site of the afCT+AcCoA+NH₄⁺ structure, there is strong density connecting C1 of Ac-Cys92 to the sulfur of CoA. The shape of the density indicates that Cys92 (Sγ), the acetyl group, and CoA (S) adopt a tetrahedral geometry (Figure 10A). Therefore, covalent bonds were defined from the acetyl group C1 atom to both Cys92 (Sγ) and CoA (S). This represents the tetrahedral intermediate formed during acetyl transfer from Ac-CoA to Cys92 (Figure 2, stage 3). The negatively charged thioester O atom is positioned in OAH2, stabilized by hydrogen bonds to Cys92 (N) (3.2 Å) and Gly386 (N) (2.6 Å). While the conformation of this Cys92-Ac-CoA tetrahedral intermediate is well justified by the electron density, it is inconsistent with the previous suggestion that the first acetyl transfer proceeds via a tetrahedral intermediate stabilized by OAH1.³⁶ No density is observed in OAH1, suggesting that the S atom of CoA—which is approximately 0.6 Å closer to Cys92 (Sγ) than for the active sites containing CoA and Ac-Cys92—prevents Wat_{cat1} from shifting into OAH1, as observed for the CoA+Ac-Cys92 active sites (Figure 9A).

For the remaining active site of afCT+AcCoA+NH₄⁺ there is continuous density occupying both OAHs and connecting CoA (S) to Cys92 (Sγ). This was explained well by modeling an acetyl group in OAH2 covalently linked via C1 to both Cys92 (Sγ) and C2 of a bound Ac-CoA molecule (Figure 10B). This configuration represents the tetrahedral intermediate that occurs during the second acetyl transfer—from Cys92 to Ac-CoA—to form AcAc-CoA (Figure 2, stage 7). The negative

charge present at the thioester O atom of the first acetyl group is stabilized by OAH2, with hydrogen bonds of 2.5 and 2.8 Å to Cys92 (N) and Gly386 (N), respectively. The thioester O atom of Ac-CoA partially occupies OAH1 but is farther away from His354 (Nε2) (3.8 Å) and closer to Wat_{cat1} (2.2 Å) in comparison to its position immediately prior to the first acetyl transfer (stage 2) shown in Figure 9B. Superposition of this catalytic site with the structure of bCT in complex with AcAc-CoA (the active site cysteine—Cys89—was mutated to serine) (PDB: 1M1O)³⁶ shows that the acetyl groups of the tetrahedral intermediate occupy positions similar to those of the reaction product, AcAc-CoA, as expected (Figure 10B).

DISCUSSION

Implications for the Thiolase Catalytic Cycle. Crystal structures representing all five different acetyl-group configurations of the catalytic site have been determined previously for *Z. ramigera* ACAT (bCT) (stages 1,³⁵ 2,³⁶ 4,²⁴ 5³⁵ and 8³⁶ of the reaction cycle shown in Figure 2); however, a crystal structure of an ACAT in complex with a tetrahedral reaction intermediate (Figure 2; stage 3 or 7) has not been reported until now. Here we present structures of *A. fumigatus* cytosolic ACAT (afCT) in complex with both tetrahedral reaction intermediates previously predicted to form during each of the acetyl-transfer reactions. Different active sites of the crystallized tetrameric enzyme trapped substrates/intermediates at different stages of the reaction cycle are depicted in Figure 2, including (1) Ac-Cys92+CoA (stage 4), (2) a site containing alternate conformations of Cys92+Ac-CoA as well as Ac-Cys92+CoA (stages 2 and 4, respectively), (3) Cys92-Ac-CoA tetrahedral intermediate (stage 3), and (4) Cys92-Ac-CoA tetrahedral intermediate (stage 7). These last two structures complete the structural repertoire of all stable intermediates that occur during the thiolase reaction cycle, allowing us to observe with direct experimental structural evidence the full reaction mechanism for the first time.

Regarding the first acetyl-transfer reaction (Figure 2; stages 1–4), our structural data show that Ac-CoA binds with the thioester O atom occupying OAH1 (Figure 9B) and that, upon nucleophilic attack of Cys92 (Sγ) on the electrophilic C1 atom, the acetyl group rotates into OAH2, where the negative charge on the thioester O atom of the tetrahedral intermediate is stabilized by hydrogen bonds to the backbone N atoms of Cys92 and Gly386 (Figure 10A). After acetyl transfer, the thioester O of Ac-Cys92 remains in OAH2 (Figure 9A). This sequence of events conflicts with previous studies which have suggested that, during acetyl transfer, the thioester oxygen atom of the acetyl group occupies OAH1 and only shifts to OAH2 upon binding of a second Ac-CoA.³⁶ This previous conclusion was based on the interpretation of four structures of bCT: (1) a C89A mutant bCT in complex with Ac-CoA (stage 2) showing that the acetyl group binds in OAH1 (PDB: 1M3Z),³⁶ (2) the acetylated enzyme (Ac-Cys89) in complex with CoA (stage 4) showing that the thioester O atom points away from OAH2 and is positioned between CoA (S) and Cys378 (O) (PDB: 1QFL),²⁴ (3) the unliganded acetylated enzyme (between stages 4 and 5) showing that the thioester O atom partially occupies OAH1 while the C2 atom occupies OAH2 (PDB: 1M4S),³⁶ and (4) the acetylated enzyme in complex with Ac-CoA (stage 5) showing that binding of the second Ac-CoA shifts the thioester O atom of Ac-Cys89 into OAH2 (PDB: 1DM3).³⁵ Of these structures, 1 and 4 are consistent with our interpretation of afCT structures. We suggest that the electron

density observed at the active sites of bCT structures 2 and 3 was insufficient to accurately interpret the orientation of the acetyl group. Therefore, on the basis of the structures presented herein, for which there is strong, readily interpretable density, we propose that the tetrahedral intermediate formed during the first acetyl-transfer reaction is stabilized by OAH2, as indicated by the reaction scheme shown in Figure 2 (stage 3).

Regarding the Claisen condensation reaction represented by the second tetrahedral intermediate (Figure 10B), the nucleophilic character of C2 of the second acetyl group (Ac-CoA) is imparted by proton abstraction by Cys384 (S γ).³⁴ This C2 is 4.8 Å from Cys384 (S γ): too far for proton abstraction, suggesting that proton abstraction and nucleophilic attack are discrete steps, consistent with previous biochemical studies indicating that C–H bond cleavage is separate from C–C bond formation^{25,34} and that OAH1 is critical for the stabilization of the enolate ion formed after proton abstraction has occurred³⁷ (Figure 2, stage 6).

Enzyme Activation by MVCs. We have shown that, like hT2, the catalytic efficiency of afCT is greatly increased by K⁺. Numerous examples of MVC-activated enzymes have been documented; all those characterized thus far have a preference for either Na⁺ or K⁺.^{78–80} Na⁺-activated enzymes, such as thrombin⁸¹ and β -galactosidase, are generally poorly activated by smaller (Li⁺) or larger (K⁺, Rb⁺, Cs⁺) MVCs. K⁺-activated enzymes, such as kinases^{82–84} and molecular chaperones,⁸⁵ are generally also activated partially by NH₄⁺ and Rb⁺ but not by Li⁺, Na⁺, or Cs⁺.⁷⁸ MVC-activated enzymes are classified into two broad categories.⁷⁹ Type I MVC activation involves direct contact between the MVC and substrate, and the requirement for MVCs is usually absolute. This is typified by enzymes involved in phosphoryl transfer reactions, such as kinases, which require both a divalent metal ion and a MVC. The MVC is required for ATP binding and polarization of phosphate groups and sometimes stabilization of the active conformation of the protein. Type II activated enzymes have a basal level of activity that is enhanced by specific binding of MVC(s) to a site(s) distal to the active site. For example, Na⁺ binding to thrombin induces subtle conformational changes that propagate through the protein to the active site to promote catalysis.⁸⁶ A contrasting example is the DNA mismatch repair protein MutL, in which a MVC is bound very close to its substrate binding site and forms a water-mediated hydrogen bond with the α -phosphate of ATP.⁸⁷ Like afCT, MutL also exhibits a broad MVC specificity; although it has a preference for Na⁺, it is also activated by K⁺, Rb⁺, and Cs⁺. Given that the MVC is not in direct contact with substrate and the requirement for MVCs is not absolute, afCT can be clearly classified as a type II activated enzyme.

We suggest that the MVC bound by afCT activates the enzyme in two ways: (1) by increasing affinity for substrate via a water-mediated hydrogen bond and stabilization of the adenosine binding loop and (2) by stabilization of the loop containing the catalytic histidine (His354). Interestingly, the $k_{\text{cat}}/K_{\text{m}}$ value of afCT was markedly increased by addition of either Na⁺ or K⁺. Both decreased the K_{m} value for AcAc-CoA equally, but the k_{cat} value was 3-fold higher for K⁺ than for Na⁺. Assuming the rate of catalysis is much slower than that of substrate binding, this indicates that both ions increase substrate affinity similarly, but K⁺ is more effective at promoting catalysis. Further biochemical studies are required to confirm this. It is known that ACATs can turn over AcAc-pantetheine with only slightly lower catalytic efficiency than for AcAc-

CoA,^{21,23} indicating that the adenosine part of CoA is not required for substrate binding. Comparison of the kinetic properties of afCT using CoA substrate versus pantetheine substrate would be valuable for delineating relative contributions of effects 1 and 2 to enhancing its catalytic efficiency. In addition, determination of the structure of the enzyme in the absence of MVCs and in complex with Na⁺, followed up by mutagenesis studies, is anticipated to provide further insight into the allosteric activation of afCT (and T2) by MVCs.

To our knowledge, ACATs are a unique example of a class of enzymes which includes members that are specifically activated by MVCs and members that are ion independent, while otherwise maintaining a highly conserved overall structure. From our structural comparisons, we suggest that the structural determinants which differentiate K⁺-activated ACATs (afCT and hT2) from ion-independent ACATs (hCT and bCT) involve very few residues. These include Tyr187 (afCT), which is a glutamine in both hCT and bCT, and Glu224, which is an aromatic residue in hCT and bCT. A previously reported clinical mutation in hT2 indicates the importance of Tyr187 (hT2 Tyr219): biochemical characterization of hT2-(Tyr219His) showed that this mutation abolished enzyme activity.³¹ Glu224 confers a strong negative charge to facilitate electrostatic attraction of K⁺ to the MVC coordination site (Figure S7A). In addition to these two residues, the L β 3–L α 3 loop, which forms the outside of the adenosine binding pocket, is one residue longer in these ion-independent ACATs. This additional histidine (hCT His224) causes a structural rearrangement, allowing a cation– π interaction between the preceding basic residue (hCT Arg223) and the adenine rings of CoA (Figure S9B). It is interesting to note that this basic residue is conserved in K⁺-activated ACATs (afCT Lys226), but the conformation of the L β 3–L α 3 loop precludes it from contacting the substrate.

Insights into Other Species. Surprisingly, afCT is more like hT2 than hCT or bCT in terms of primary sequence, structure of key elements surrounding the active site, and biochemical properties. Discrimination of mitochondrial ACAT from cytosolic ACAT based on activation by K⁺—as demonstrated for mammalian tissues²⁹—clearly does not apply for fungi. It is interesting to note that *A. thaliana* cytosolic ACAT is also more similar to hT2 and afCT than to hCT and bCT in terms of overall sequence identity (Figure S1) and conservation of key residues involved in substrate specificity and binding of K⁺ and Cl[–] (Figure S2). It is therefore possible that the biochemical properties of plant ACATs also conflict with the current paradigm differentiating mitochondrial and cytosolic ACATs and that bacterial and mammalian cytosolic ACATs are the exception regarding nonactivation by K⁺. Further bioinformatic and biochemical studies are anticipated to elucidate the extent to which MVC activation of ACATs is conserved across all domains of life. To our knowledge, there are no published data showing that the activity of T2 is independent of Na⁺ ions. The similarity between the ion binding sites of hT2 and afCT along with the MVC promiscuity that afCT exhibits leads us to suggest that the accepted notion that T2 is activated by K⁺ but not Na⁺²⁹ may need to be revisited. That is, although K⁺ is the preferred activating MVC, afCT—and therefore probably T2—are not strictly selective for K⁺ and thus do not adhere to a strict dichotomy of activation by K⁺ but not Na⁺.

■ CONCLUDING REMARKS

We have solved the first structure of a fungal type II thiolase, both in apo form and in complex with substrate. The different catalytic site configurations trapped in the crystals of afCT provide the first direct experimental observations of the structures of the tetrahedral intermediates formed during the thiolase reaction cycle. We have also shown that, unexpectedly, afCT possesses specific ion binding sites and is activated by MVCs in a way similar to that for hT2. Future work focusing on the comparison of key structural features of ion-dependent and ion-independent thiolases is anticipated to provide further structural rationales for the allosteric ion activation of this class of enzymes.

Biosynthetic thiolases catalyze the first step in the synthesis of highly reduced organic molecules in both prokaryotes and eukaryotes that are essential for energy storage and maintenance of normal cellular function, presenting them as potential drug targets. In addition, for many years much biotechnological research has focused on microbial metabolic engineering for the large-scale biosynthesis of biodegradable plastics such as polyhydroxyalkanoates,^{88–91} high-value isoprenoid-based natural products,¹⁶ and production of biofuels from renewable sources^{92–95}—all processes for which biosynthetic thiolases play a central role. Thus, the detailed structural investigation of ACATs, such as presented herein, is anticipated to inform both the rational design of antimicrobial drugs and the advancement of biotechnological applications for industrial, commercial, and biomedical fields in the future.

■ ASSOCIATED CONTENT

Supporting Information

The Supporting Information is available free of charge on the ACS Publications website at DOI: 10.1021/acscatal.7b02873.

X-ray crystallographic data collection and structure refinement statistics (Table S1), map peak heights for anomalous data and $F_o - F_c$ data, and atomic properties for all modeled Cs⁺ and Rb⁺ ions (Tables S2 and S3), atomic properties for all modeled K⁺ and NH₄⁺ ions (Table S4), and Figures S1–S11 as described in the text (PDF)

■ AUTHOR INFORMATION

Corresponding Author

*J.B.B.: tel, +61 (08) 8313-5218; fax, +61 (08) 8313-4362; e-mail, john.bruning@adelaide.edu.au.

ORCID

John B. Bruning: 0000-0002-6919-1824

Author Contributions

A.C.M., purification of enzyme, enzymology, manuscript preparation, crystallography; C.S.B., crystallography, manuscript preparation, and intellectual contribution; J.B.B., crystallography, management of project, manuscript preparation, and intellectual contribution.

Notes

The authors declare no competing financial interest.

■ ACKNOWLEDGMENTS

This research was undertaken on the MX1 beamline at the Australian Synchrotron, part of ANSTO.

■ REFERENCES

- (1) Ben-Ami, R.; Lewis, R. E.; Kontoyiannis, D. P. *Br. J. Haematol.* **2010**, *150*, 406–417.
- (2) Bitar, D.; Lortholary, O.; Le Strat, Y.; Nicolau, J.; Coignard, B.; Tattevin, P.; Che, D.; Dromer, F. *Emerging Infect. Dis.* **2014**, *20*, 1149–55.
- (3) Lin, S. J.; Schranz, J.; Teutsch, S. M. *Clin. Infect. Dis.* **2001**, *32*, 358–66.
- (4) McNeil, M. M.; Nash, S. L.; Hajjeh, R. A.; Phelan, M. A.; Conn, L. A.; Plikaytis, B. D.; Warnock, D. W. *Clin. Infect. Dis.* **2001**, *33*, 641–7.
- (5) Yoon, H. J.; Choi, H. Y.; Kim, Y. K.; Song, Y. J.; Ki, M. *Epidemiol. Health* **2014**, *36*, e2014017.
- (6) Bolard, J. *Biochim. Biophys. Acta, Rev. Biomembr.* **1986**, *864*, 257–304.
- (7) Ermishkin, L. N.; Kasumov, K. M.; Potzeluyev, V. M. *Nature* **1976**, *262*, 698–9.
- (8) Gray, K. C.; Palacios, D. S.; Dailey, I.; Endo, M. M.; Uno, B. E.; Wilcock, B. C.; Burke, M. D. *Proc. Natl. Acad. Sci. U. S. A.* **2012**, *109*, 2234–9.
- (9) Chowdhry, R.; Marshall, W. L. *J. Intensive Care Med.* **2008**, *23*, 151–8.
- (10) Patterson, T. F.; Thompson, G. R., 3rd; Denning, D. W.; Fishman, J. A.; Hadley, S.; Herbrecht, R.; Kontoyiannis, D. P.; Marr, K. A.; Morrison, V. A.; Nguyen, M. H.; Segal, B. H.; Steinbach, W. J.; Stevens, D. A.; Walsh, T. J.; Wingard, J. R.; Young, J. H.; Bennett, J. E. *Clin. Infect. Dis.* **2016**, *63*, e1–e60.
- (11) Herbrecht, R.; Denning, D. W.; Patterson, T. F.; Bennett, J. E.; Greene, R. E.; Oestmann, J. W.; Kern, W. V.; Marr, K. A.; Ribaud, P.; Lortholary, O.; Sylvester, R.; Rubin, R. H.; Wingard, J. R.; Stark, P.; Durand, C.; Caillot, D.; Thiel, E.; Chandrasekar, P. H.; Hodges, M. R.; Schlamm, H. T.; Troke, P. F.; de Pauw, B. N. *Engl. J. Med.* **2002**, *347*, 408–15.
- (12) Howard, S. J.; Cerar, D.; Anderson, M. J.; Albarrag, A.; Fisher, M. C.; Pasqualotto, A. C.; Laverdiere, M.; Arendrup, M. C.; Perlin, D. S.; Denning, D. W. *Emerging Infect. Dis.* **2009**, *15*, 1068–76.
- (13) Snelders, E.; Melchers, W. J.; Verweij, P. E. *Future Microbiol.* **2011**, *6*, 335–47.
- (14) van der Linden, J. W.; Snelders, E.; Kampinga, G. A.; Rijnders, B. J.; Mattsson, E.; Debets-Ossenopp, Y. J.; Kuijper, E. J.; Van Tiel, F. H.; Melchers, W. J.; Verweij, P. E. *Emerging Infect. Dis.* **2011**, *17*, 1846–54.
- (15) Alcazar-Fuoli, L.; Mellado, E. *Front. Microbiol.* **2013**, *3*, 439.
- (16) Chemler, J. A.; Yan, Y. J.; Koffas, M. A. G. *Microb. Cell Fact.* **2006**, *5*, 20.
- (17) Kirby, J.; Keasling, J. D. *Annu. Rev. Plant Biol.* **2009**, *60*, 335–55.
- (18) Kunau, W. H.; Dommès, V.; Schulz, H. *Prog. Lipid Res.* **1995**, *34*, 267–342.
- (19) Mathieu, M.; Modis, Y.; Zeelen, J. P.; Engel, C. K.; Abagyan, R. A.; Ahlberg, A.; Rasmussen, B.; Lamzin, V. S.; Kunau, W. H.; Wierenga, R. K. *J. Mol. Biol.* **1997**, *273*, 714–28.
- (20) Kanayama, N.; Ueda, M.; Atomi, H.; Tanaka, A. *J. Bacteriol.* **1998**, *180*, 690–8.
- (21) Davis, J. T.; Moore, R. N.; Imperiali, B.; Pratt, A. J.; Kobayashi, K.; Masamune, S.; Sinskey, A. J.; Walsh, C. T.; Fukui, T.; Tomita, K. *J. Biol. Chem.* **1987**, *262*, 82–9.
- (22) Davis, J. T.; Chen, H. H.; Moore, R.; Nishitani, Y.; Masamune, S.; Sinskey, A. J.; Walsh, C. T. *J. Biol. Chem.* **1987**, *262*, 90–6.
- (23) Gehring, U.; Lynen, F. In *The Enzymes*; Paul, D. B., Ed.; Academic Press: Cambridge, MA, 1972; Vol. 7, pp 391–405.
- (24) Modis, Y.; Wierenga, R. K. *Structure* **1999**, *7*, 1279–90.
- (25) Masamune, S.; Walsh, C. T.; Sinskey, A. J.; Peoples, O. P. *Pure Appl. Chem.* **1989**, *61*, 303–312.
- (26) Fukao, T.; Song, X. Q.; Mitchell, G. A.; Yamaguchi, S.; Sukegawa, K.; Orii, T.; Kondo, N. *Pediatr. Res.* **1997**, *42*, 498–502.
- (27) Korman, S. H. *Mol. Genet. Metab.* **2006**, *89*, 289–99.
- (28) Middleton, B.; Bartlett, K. *Clin. Chim. Acta* **1983**, *128*, 291–305.
- (29) Middleton, B. *Biochem. J.* **1973**, *132*, 717–30.

- (30) Haapalainen, A. M.; Merilainen, G.; Pirila, P. L.; Kondo, N.; Fukao, T.; Wierenga, R. K. *Biochemistry* **2007**, *46*, 4305–21.
- (31) Sakurai, S.; Fukao, T.; Haapalainen, A. M.; Zhang, G.; Yamada, K.; Lilliu, F.; Yano, S.; Robinson, P.; Gibson, M. K.; Wanders, R. J.; Mitchell, G. A.; Wierenga, R. K.; Kondo, N. *Mol. Genet. Metab.* **2007**, *90*, 370–8.
- (32) Zhang, G. X.; Fukao, T.; Rolland, M. O.; Zabet, M. T.; Renom, G.; Touma, E.; Kondo, M.; Matsuo, N.; Kondo, N. *Pediatr. Res.* **2004**, *56*, 60–4.
- (33) Thompson, S.; Mayerl, F.; Peoples, O. P.; Masamune, S.; Sinskey, A. J.; Walsh, C. T. *Biochemistry* **1989**, *28*, 5735–42.
- (34) Palmer, M. A.; Differding, E.; Gamboni, R.; Williams, S. F.; Peoples, O. P.; Walsh, C. T.; Sinskey, A. J.; Masamune, S. *J. Biol. Chem.* **1991**, *266*, 8369–75.
- (35) Modis, Y.; Wierenga, R. K. *J. Mol. Biol.* **2000**, *297*, 1171–82.
- (36) Kursula, P.; Ojala, J.; Lambeir, A. M.; Wierenga, R. K. *Biochemistry* **2002**, *41*, 15543–56.
- (37) Merilainen, G.; Poikela, V.; Kursula, P.; Wierenga, R. K. *Biochemistry* **2009**, *48*, 11011–25.
- (38) Kadouri, D.; Jurkevitch, E.; Okon, Y.; Castro-Sowinski, S. *Crit. Rev. Microbiol.* **2005**, *31*, 55–67.
- (39) Senior, P. J.; Dawes, E. A. *Biochem. J.* **1973**, *134*, 225–38.
- (40) Soto, G.; Stritzler, M.; Lisi, C.; Alleva, K.; Pagano, M. E.; Ardila, F.; Mozzicafreddo, M.; Cuccioloni, M.; Angeletti, M.; Ayub, N. D. *J. Exp. Bot.* **2011**, *62*, S699–711.
- (41) Baxter, C. J.; Redestig, H.; Schauer, N.; Reipsilber, D.; Patil, K. R.; Nielsen, J.; Selbig, J.; Liu, J.; Fernie, A. R.; Sweetlove, L. J. *Plant Physiol.* **2006**, *143*, 312–25.
- (42) Godon, C.; Lagniel, G.; Lee, J.; Buhler, J. M.; Kieffer, S.; Perrot, M.; Boucherie, H.; Toledano, M. B.; Labarre, J. *J. Biol. Chem.* **1998**, *273*, 22480–9.
- (43) Fox, A. R.; Soto, G.; Mozzicafreddo, M.; Garcia, A. N.; Cuccioloni, M.; Angeletti, M.; Salerno, J. C.; Ayub, N. D. *Gene* **2014**, *533*, 5–10.
- (44) Pietroccola, F.; Galluzzi, L.; Bravo-San Pedro, J. M.; Madeo, F.; Kroemer, G. *Cell Metab.* **2015**, *21*, 805–821.
- (45) Zhang, M.; Galdieri, L.; Vancura, A. *Mol. Cell. Biol.* **2013**, *33*, 4701–4717.
- (46) Hiser, L.; Basson, M. E.; Rine, J. *J. Biol. Chem.* **1994**, *269*, 31383–9.
- (47) Hu, W.; Sillaots, S.; Lemieux, S.; Davison, J.; Kauffman, S.; Breton, A.; Linteau, A.; Xin, C.; Bowman, J.; Becker, J.; Jiang, B.; Roemer, T. *PLoS Pathog.* **2007**, *3*, e24.
- (48) Riddles, P. W.; Blakeley, R. L.; Zerner, B. *Anal. Biochem.* **1979**, *94*, 75–81.
- (49) Letunic, I.; Bork, P. *Nucleic Acids Res.* **2016**, *44*, W242–5.
- (50) Glover, J. R.; Andrews, D. W.; Subramani, S.; Rachubinski, R. A. *J. Biol. Chem.* **1994**, *269*, 7558–63.
- (51) Emanuelsson, O.; Nielsen, H.; Brunak, S.; von Heijne, G. *J. Mol. Biol.* **2000**, *300*, 1005–16.
- (52) Robert, X.; Gouet, P. *Nucleic Acids Res.* **2014**, *42*, W320–4.
- (53) Middleton, B. *Biochem. J.* **1974**, *139*, 109–21.
- (54) Middleton, B.; Tubbs, P. K. *Biochem. J.* **1972**, *126*, 27–34.
- (55) McPhillips, T. M.; McPhillips, S. E.; Chiu, H. J.; Cohen, A. E.; Deacon, A. M.; Ellis, P. J.; Garman, E.; Gonzalez, A.; Sauter, N. K.; Phizackerley, R. P.; Soltis, S. M.; Kuhn, P. *J. Synchrotron Radiat.* **2002**, *9*, 401–406.
- (56) Leslie, A. G. W.; Powell, H. R. In *Evolving Methods for Macromolecular Crystallography*; Read, R. J., Sussman, J. L., Eds.; Springer: Dordrecht, The Netherlands, 2007; Vol. 245, pp 41–51.
- (57) McCoy, A. J.; Grosse-Kunstleve, R. W.; Adams, P. D.; Winn, M. D.; Storoni, L. C.; Read, R. J. *J. Appl. Crystallogr.* **2007**, *40*, 658–674.
- (58) Afonine, P. V.; Grosse-Kunstleve, R. W.; Echols, N.; Headd, J. J.; Moriarty, N. W.; Mustyakimov, M.; Terwilliger, T. C.; Urzhumtsev, A.; Zwart, P. H.; Adams, P. D. *Acta Crystallogr., Sect. D: Biol. Crystallogr.* **2012**, *68*, 352–67.
- (59) Emsley, P.; Lohkamp, B.; Scott, W. G.; Cowtan, K. *Acta Crystallogr., Sect. D: Biol. Crystallogr.* **2010**, *66*, 486–501.
- (60) Winn, M. D.; Isupov, M. N.; Murshudov, G. N. *Acta Crystallogr., Sect. D: Biol. Crystallogr.* **2001**, *57*, 122–33.
- (61) Adams, P. D.; Afonine, P. V.; Bunkoczi, G.; Chen, V. B.; Davis, I. W.; Echols, N.; Headd, J. J.; Hung, L. W.; Kapral, G. J.; Grosse-Kunstleve, R. W.; McCoy, A. J.; Moriarty, N. W.; Oeffner, R.; Read, R. J.; Richardson, D. C.; Richardson, J. S.; Terwilliger, T. C.; Zwart, P. H. *Acta Crystallogr., Sect. D: Biol. Crystallogr.* **2010**, *66*, 213–221.
- (62) Abagyan, R.; Totrov, M.; Kuznetsov, D. *J. Comput. Chem.* **1994**, *15*, 488–506.
- (63) Baker, N. A.; Sept, D.; Joseph, S.; Holst, M. J.; McCammon, J. A. *Proc. Natl. Acad. Sci. U. S. A.* **2001**, *98*, 10037–10041.
- (64) Huang, C. C.; Couch, G. S.; Pettersen, E. F.; Ferrin, T. E. In *Pacific Symposium on Biocomputing 1996*, Vol. 1, 724.
- (65) Dolinsky, T. J.; Nielsen, J. E.; McCammon, J. A.; Baker, N. A. *Nucleic Acids Res.* **2004**, *32*, W665–W667.
- (66) *The PyMOL Molecular Graphics System, Version 1.8*; Schrodinger, LLC, 2015.
- (67) Nierman, W. C.; Pain, A.; Anderson, M. J.; Wortman, J. R.; Kim, H. S.; Arroyo, J.; Berriman, M.; Abe, K.; Archer, D. B.; Bermejo, C.; Bennett, J.; Bowyer, P.; Chen, D.; Collins, M.; Coulsen, R.; Davies, R.; Dyer, P. S.; Farman, M.; Fedorova, N.; Fedorova, N.; Feldblyum, T. V.; Fischer, R.; Fosker, N.; Fraser, A.; Garcia, J. L.; Garcia, M. J.; Goble, A.; Goldman, G. H.; Gomi, K.; Griffith-Jones, S.; Gwilliam, R.; Haas, B.; Haas, H.; Harris, D.; Horiuchi, H.; Huang, J.; Humphray, S.; Jimenez, J.; Keller, N.; Khouri, H.; Kitamoto, K.; Kobayashi, T.; Konzack, S.; Kulkarni, R.; Kumagai, T.; Lafon, A.; Latge, J. P.; Li, W.; Lord, A.; Lu, C.; Majoros, W. H.; May, G. S.; Miller, B. L.; Mohamoud, Y.; Molina, M.; Monod, M.; Mouyna, I.; Mulligan, S.; Murphy, L.; O’Neil, S.; Paulsen, I.; Penalva, M. A.; Perteu, M.; Price, C.; Pritchard, B. L.; Quail, M. A.; Rabinowitsch, E.; Rawlins, N.; Rajandream, M. A.; Reichard, U.; Renauld, H.; Robson, G. D.; Rodriguez de Cordoba, S.; Rodriguez-Pena, J. M.; Ronning, C. M.; Rutter, S.; Salzberg, S. L.; Sanchez, M.; Sanchez-Ferrero, J. C.; Saunders, D.; Seeger, K.; Squares, R.; Squares, S.; Takeuchi, M.; Tekai, F.; Turner, G.; Vazquez de Aldana, C. R.; Weidman, J.; White, O.; Woodward, J.; Yu, J. H.; Fraser, C.; Galagan, J. E.; Asai, K.; Machida, M.; Hall, N.; Barrell, B.; Denning, D. W. *Nature* **2005**, *438*, 1151–6.
- (68) Cornell, M. J.; Alam, I.; Soanes, D. M.; Wong, H. M.; Hedeler, C.; Paton, N. W.; Rattray, M.; Hubbard, S. J.; Talbot, N. J.; Oliver, S. G. *Genome Res.* **2007**, *17*, 1809–22.
- (69) Maggio-Hall, L. A.; Keller, N. P. *Mol. Microbiol.* **2004**, *54*, 1173–85.
- (70) Shen, Y. Q.; Burger, G. *Funct. Integr. Genomics* **2009**, *9*, 145–51.
- (71) Ithayaraja, M.; Janardan, N.; Wierenga, R. K.; Savithri, H. S.; Murthy, M. R. *Acta Crystallogr., Sect. F: Struct. Biol. Commun.* **2016**, *72*, 534–44.
- (72) Gagne, O. C.; Hawthorne, F. C. *Acta Crystallogr., Sect. B: Struct. Sci., Cryst. Eng. Mater.* **2016**, *72*, 602–625.
- (73) Carugo, O. *BMC Struct. Biol.* **2014**, *14*, 7.
- (74) Kursula, P.; Sikkila, H.; Fukao, T.; Kondo, N.; Wierenga, R. K. *J. Mol. Biol.* **2005**, *347*, 189–201.
- (75) Hol, W. G.; van Duijnen, P. T.; Berendsen, H. J. *Nature* **1978**, *273*, 443–6.
- (76) Merilainen, G.; Schmitz, W.; Wierenga, R. K.; Kursula, P. *FEBS J.* **2008**, *275*, 6136–48.
- (77) Liebschner, D.; Afonine, P. V.; Moriarty, N. W.; Poon, B. K.; Sobolev, O. V.; Terwilliger, T. C.; Adams, P. D. *Acta Crystallogr., Sect. D: Struct. Biol.* **2017**, *73*, 148–157.
- (78) Page, M. J.; Di Cera, E. *Physiol. Rev.* **2006**, *86*, 1049–92.
- (79) Gohara, D. W.; Di Cera, E. *J. Biol. Chem.* **2016**, *291*, 20840–20848.
- (80) Di Cera, E. *J. Biol. Chem.* **2006**, *281*, 1305–8.
- (81) Prasad, S.; Wright, K. J.; Banerjee Roy, D.; Bush, L. A.; Cantwell, A. M.; Di Cera, E. *Proc. Natl. Acad. Sci. U. S. A.* **2003**, *100*, 13785–90.
- (82) Jurica, M. S.; Mesecar, A.; Heath, P. J.; Shi, W.; Nowak, T.; Stoddard, B. L. *Structure* **1998**, *6*, 195–210.
- (83) Larsen, T. M.; Benning, M. M.; Rayment, L.; Reed, G. H. *Biochemistry* **1998**, *37*, 6247–55.

- (84) Machius, M.; Chuang, J. L.; Wynn, R. M.; Tomchick, D. R.; Chuang, D. T. *Proc. Natl. Acad. Sci. U. S. A.* **2001**, *98*, 11218–23.
- (85) Viitanen, P. V.; Lubben, T. H.; Reed, J.; Goloubinoff, P.; O'Keefe, D. P.; Lorimer, G. H. *Biochemistry* **1990**, *29*, 5665–71.
- (86) Niu, W.; Chen, Z.; Bush-Pelc, L. A.; Bah, A.; Gandhi, P. S.; Di Cera, E. J. *Biol. Chem.* **2009**, *284*, 36175–85.
- (87) Hu, X. J.; Machius, M.; Yang, W. *FEBS Lett.* **2003**, *544*, 268–273.
- (88) Keshavarz, T.; Roy, I. *Curr. Opin. Microbiol.* **2010**, *13*, 321–6.
- (89) Urtuvia, V.; Villegas, P.; Gonzalez, M.; Seeger, M. *Int. J. Biol. Macromol.* **2014**, *70*, 208–13.
- (90) Wang, Y.; Yin, J.; Chen, G. Q. *Curr. Opin. Biotechnol.* **2014**, *30*, 59–65.
- (91) Mozejko-Ciesielska, J.; Kiewisz, R. *Microbiol. Res.* **2016**, *192*, 271–82.
- (92) Choi, Y. J.; Lee, S. Y. *Nature* **2013**, *502*, 571–4.
- (93) d'Espaux, L.; Mendez-Perez, D.; Li, R.; Keasling, J. D. *Curr. Opin. Chem. Biol.* **2015**, *29*, 58–65.
- (94) Kim, S.; Jang, Y. S.; Ha, S. C.; Ahn, J. W.; Kim, E. J.; Lim, J. H.; Cho, C.; Ryu, Y. S.; Lee, S. K.; Lee, S. Y.; Kim, K. J. *Nat. Commun.* **2015**, *6*, 8410.
- (95) Sheppard, M. J.; Kunjapur, A. M.; Prather, K. L. *Metab. Eng.* **2016**, *33*, 28–40.
- (96) Shannon, R. D. *Acta Crystallogr., Sect. A: Cryst. Phys., Diffraction, Theor. Gen. Crystallogr.* **1976**, *32*, 751–767.
- (97) Sidey, V. *Acta Crystallogr., Sect. B: Struct. Sci., Cryst. Eng. Mater.* **2016**, *72*, 626–633.

Supporting Information

Structure of *Aspergillus fumigatus* Cytosolic Thiolase: Trapped Tetrahedral Reaction Intermediates and Activation by Monovalent Cations.

Andrew C. Marshall^a, Charles S. Bond^b, and John B. Bruning^{a,1}

^aInstitute for Photonics and Advanced Sensing (IPAS), School of Biological Sciences, The University of Adelaide, Adelaide, South Australia 5005, Australia.

^bSchool of Molecular Sciences, The University of Western Australia, Crawley, Western Australia, 6009, Australia.

¹To whom correspondence should be addressed. John B. Bruning, The University of Adelaide, School of Biological Sciences, University of Adelaide, Adelaide, SA 5005, Australia, Tel.: +61 (08) 8313-5218; Fax: +61 (08) 8313-4362; E-mail: john.bruning@adelaide.edu.au

SUPPORTING TABLES

Table S1. X-ray diffraction data collection and refinement statistics.

	afCT+K ⁺ (PDB: 6ARF)	afCT+Rb ⁺ (PDB: 6ARG)	afCT+Rb ⁺ (PDB: 6ARL)	afCT+Cs ⁺ (PDB: 6ARR)	afCT+Cs ⁺ (PDB: 6ART)	afCT+AcCoA+K ⁺ (PDB: 6AQP)	afCT+AcCoA+NH ₄ ⁺ (PDB: 6ARE)
Data collection^a							
Space group	P2 ₁	P2 ₁	P2 ₁	P2 ₁	P2 ₁	P2 ₁	P2 ₁
Cell dimensions							
<i>a</i> , <i>b</i> , <i>c</i> (Å)	71.44, 105.41, 110.42	71.26, 105.37, 110.26	71.25, 105.44, 110.28	71.41, 105.27, 110.45	71.37, 105.29, 110.43	71.37, 106.98, 111.09	71.36, 106.59, 110.84
α , β , γ (°)	90.00, 108.74, 90.00	90.00, 108.69, 90.00	90.00, 108.78, 90.00	90.00, 108.61, 90.00	90.00, 108.60, 90.00	90.00, 104.18, 90.00	90.00, 104.27, 90.00
Wavelength (Å)	0.9537	0.9537	0.8077	0.9537	1.4586	0.9537	0.9537
Resolution (Å)	36.3–1.70 (1.73–1.70) ^b	36.2–1.78 (1.81–1.78) ^b	56.8–1.90 (1.93–1.90) ^b	56.9–1.82 (1.85–1.82) ^b	67.46–2.25 (2.30–2.25) ^b	48.10–1.80 (1.83–1.80) ^b	31.5–1.75 (1.78–1.75) ^b
<i>R</i> _{merge}	0.133 (1.819)	0.168 (1.675)	0.184 (1.155)	0.230 (2.151)	0.104 (0.351)	0.127 (0.868)	0.385 (1.971)
<i>R</i> _{rim}	0.056 (0.830)	0.071 (0.775)	0.080 (0.544)	0.090 (0.885)	0.041 (0.159)	0.053 (0.376)	0.152 (0.793)
<i>CC(1/2)</i>	0.997 (0.329)	0.991 (0.342)	0.987 (0.560)	0.993 (0.314)	0.997 (0.926)	0.996 (0.702)	0.968 (0.368)
<i>I</i> / σ <i>I</i>	9.7 (0.9)	9.2 (1.0)	9.1 (1.6)	8.3 (1.0)	16.4 (5.0)	11.6 (2.1)	4.1 (1.0)
Completeness (%)	99.9 (99.0)	98.8 (96.6)	97.6 (93.2)	99.9 (99.4)	99.7 (95.6)	95.9 (90.4)	99.6 (99.0)
Redundancy	6.5 (5.7)	6.4 (5.5)	6.0 (5.1)	7.4 (6.8)	7.3 (5.8)	6.2 (5.6)	7.3 (7.1)
Refinement							
Resolution (Å)	36.3–1.70	36.2–1.78	52.7–1.90	56.9–1.82	56.9–2.25	47.9–1.80	31.3–1.75
No. reflections	168972	144843	121256	137982	73451	149491	160889
<i>R</i> _{work} / <i>R</i> _{free}	0.1653 / 0.2000	0.1819 / 0.2199	0.2012 / 0.2411	0.1772 / 0.2086	0.1522 / 0.1927	0.1746 / 0.2190	0.1944 / 0.2315
No. atoms							
Protein	11457	11429	11424	11428	11394	11472	11466
Ligand/ion ^c	47	35	35	37	37	211	215
Water	1569	1625	1500	1430	1100	2606	1362
<i>B</i> -factors							
Protein	41.1	32.2	31.0	32.6	34.4	19.5	18.6
(chain A, B, C, D) ^d	(63.1, 52.7, 25.4, 23.7) ^d	(48.5, 41.8, 19.9, 18.7)	(46.9, 41.3, 19.2, 18.3)	(51.3, 45.1, 18.6, 17.7)	(53.6, 46.4, 20.0, 19.0)	(25.3, 30.2, 13.7, 12.8)	(14.1, 13.4, 23.3, 28.0)
Ligand/ion	42.7	31.1	37.2	32.7	34.5	35.3	43.2
Water	42.9	37.5	34.9	35.9	33.2	34.7	25.8
RMS deviations							
Bond lengths (Å)	0.007	0.007	0.007	0.008	0.007	0.006	0.008
Bond angles (°)	0.81	0.85	0.86	0.84	0.83	0.85	0.98

^a Data was collected from a single crystal for each structure. ^b Values in parentheses are for highest-resolution shell. ^c ‘‘Ligand/ion’’ includes atoms of CoA, acetyl groups, and glycerol, and Cl⁻, K⁺, Rb⁺ and Cs⁺ ions. ^d *B*-factor values in parentheses are mean values for protein atoms in chains A, B, C and D, respectively.

Table S2. Cs⁺ sites. Anomalous (Anom) peak heights, isomorphous difference map (Fo-Fo) peak heights and atomic properties for all ordered Cs⁺ ions in the afCT+Cs⁺ structure. Listed values refer to subunits A, B, C and D, respectively. MVC binding sites are listed above each column, labeled as the closest coordinating residue (except for the site near the substrate binding pocket; labeled “CoA pocket”).

	CoA pocket	Val44	Asp200	Asn274 ^c	Asp314
Anom @ 8500 eV (σ)	25, 29, 41, 43	15, 12, 23, 27	20, 20, 28, 36	na ^d , na, na, 16	na, na, 11, 8
Anom @ 13000 eV (σ)	13, 14, 21, 22	7, 7, 13, 15	9, 9, 14, 17	na, na, na, 7	na, na, 8, 4
Fo-Fo ^a (σ)	25, 30, 59, 67	18, 9, 33, 35	18, 19, 35, 43	na, na, na, 23	na, na, 18, 11
Occupancy (%) ^b	97, 99, 95, 99	84, 80, 66, 73	92, 91, 80, 79	na, na, na, 48	na, na, 55, 57
B-factor (\AA^2) ^b	55, 46, 17, 15	75, 90, 26, 26	73, 66, 26, 21	na, na, na, 27	na, na, 43, 73
Occupancy/B-factor ^b	1.8, 2.1, 5.7, 6.6	1.1, 0.9, 2.6, 2.8	1.3, 1.4, 3.1, 3.9	na, na, na, 1.8	na, na, 1.3, 0.8

^a Fo-Fo is Fo(afCT+Cs⁺) minus Fo(afCT+K⁺), with all data collected @ 13000 eV. ^b For data collected @ 13000 eV. ^c At interface with symmetry-mate. ^d Not applicable.

Table S3. Rb⁺ sites. Anomalous (Anom) peak heights, isomorphous difference map (Fo-Fo) peak heights and atomic properties for all ordered Rb⁺ ions in the afCT+Rb⁺ structure. Listed values refer to subunits A, B, C and D, respectively. MVC binding sites are listed above each column, labeled as the closest coordinating residue (except for the site near the substrate binding pocket; labeled “CoA pocket”).

	CoA pocket	Val44	Asp200	Asn274 ^c
Anom @ 15350 eV (σ)	15, 17, 20, 20	8, 7, 14, 13	11, 12, 14, 17	na, na, na, 6
Anom @ 13000 eV (σ)	5, 4, 6, 6	3, 3, 5, 4	3, 4, 5, 6	na, na, na, 4
Fo-Fo ^a (σ)	16, 18, 28, 35	9, 6, 20, 18	11, 13, 23, 25	na, na, na, 9
Occupancy (%) ^b	85, 96, 94, 97	82, 94, 69, 76	87, 90, 79, 85	na, na, na, 58
B-factor (\AA^2) ^b	41, 41, 18, 17	66, 89, 20, 24	65, 52, 20, 20	na, na, na, 49
Occupancy/B-factor ^b	2.1, 2.4, 5.1, 5.8	1.2, 1.1, 3.4, 3.2	1.3, 1.7, 4.0, 4.3	na, na, na, 1.2

^a Fo-Fo is Fo(afCT+Rb⁺) minus Fo(afCT+K⁺), with all data collected @ 13000 eV. ^b For data collected @ 13000 eV. ^c At interface with symmetry-mate.

Table S4. Atomic properties of all ordered K⁺ ions at MVC binding sites in afCT+K⁺ and afCT+AcCoA+K⁺ structures and NH₄⁺ ions in the afCT+AcCoA+NH₄⁺ structure. Listed values refer to subunits A, B, C and D, respectively. MVC binding sites are listed above each column, labeled as the closest coordinating residue (except for the site near the substrate binding pocket; labeled “CoA pocket”).

<i>afCT+K⁺</i>	CoA pocket	Val44	Asp200	Asn274 ^b
Occupancy (%)	76, 94, 100, 100	96, 100, 91, 82	100, 100, 91, 90	na, na, na, 50
B-factor (\AA^2)	39, 43, 23, 19	69, 78, 24, 22	69, 58, 21, 21	na, na, na, 37
Occupancy/B-factor	1.9, 2.2, 4.3, 5.3	1.4, 1.3, 3.8, 3.8	1.5, 1.7, 4.4, 4.3	na, na, na, 1.4
<i>afCT+AcCoA+K⁺</i> ^a				
Occupancy (%)	58, 49, 54, 43	84, 97, 70, 82	82, 84, 85, 77	na, na, na, na
B-factor (\AA^2)	25, 29, 12, 10	25, 39, 12, 18	24, 26, 14, 10	na, na, na, na
Occupancy/B-factor	2.3, 1.7, 4.4, 4.2	3.4, 3.1, 5.9, 7.8	3.4, 2.5, 5.7, 4.5	na, na, na, na
<i>afCT+AcCoA+NH₄⁺</i>				
Occupancy (%)	100, 100, 100, 90	na, 100, 100, na	100, 100, 88, 100	na, na, na, na
B-factor (\AA^2)	9, 6, 15, 18	na, 33, 39, na	22, 19, 22, 32	na, na, na, na
Occupancy/B-factor	11, 17, 6.8, 5.1	na, 3.0, 2.5, na	4.6, 5.3, 4.1, 3.2	na, na, na, na

^a Crystallization condition contained NH₄⁺ ions also. ^b At interface with symmetry-mate.

SUPPORTING FIGURES

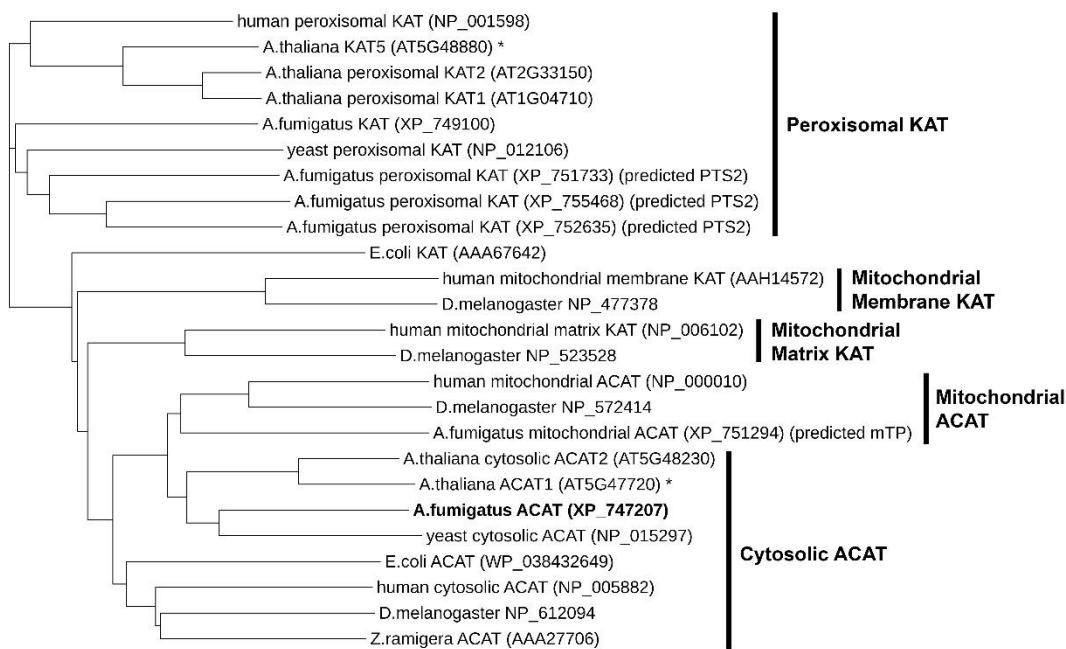


Figure S1. Phylogenetic tree of all thiolase protein sequences from *Aspergillus fumigatus*, *Saccharomyces cerevisiae*, *Arabidopsis thaliana*, Human, *Drosophila melanogaster*, *Escherichia coli* and *Zoogloea ramigera*. NCBI accession numbers are shown for all sequences except *A. thaliana*, for which sequences were obtained from The Arabidopsis Information Resource (TAIR, www.arabidopsis.org). The subcellular location of all *A. thaliana* thiolases has been experimentally determined¹; proteins with both cytosolic and peroxisomal isoforms are marked with an asterisk.

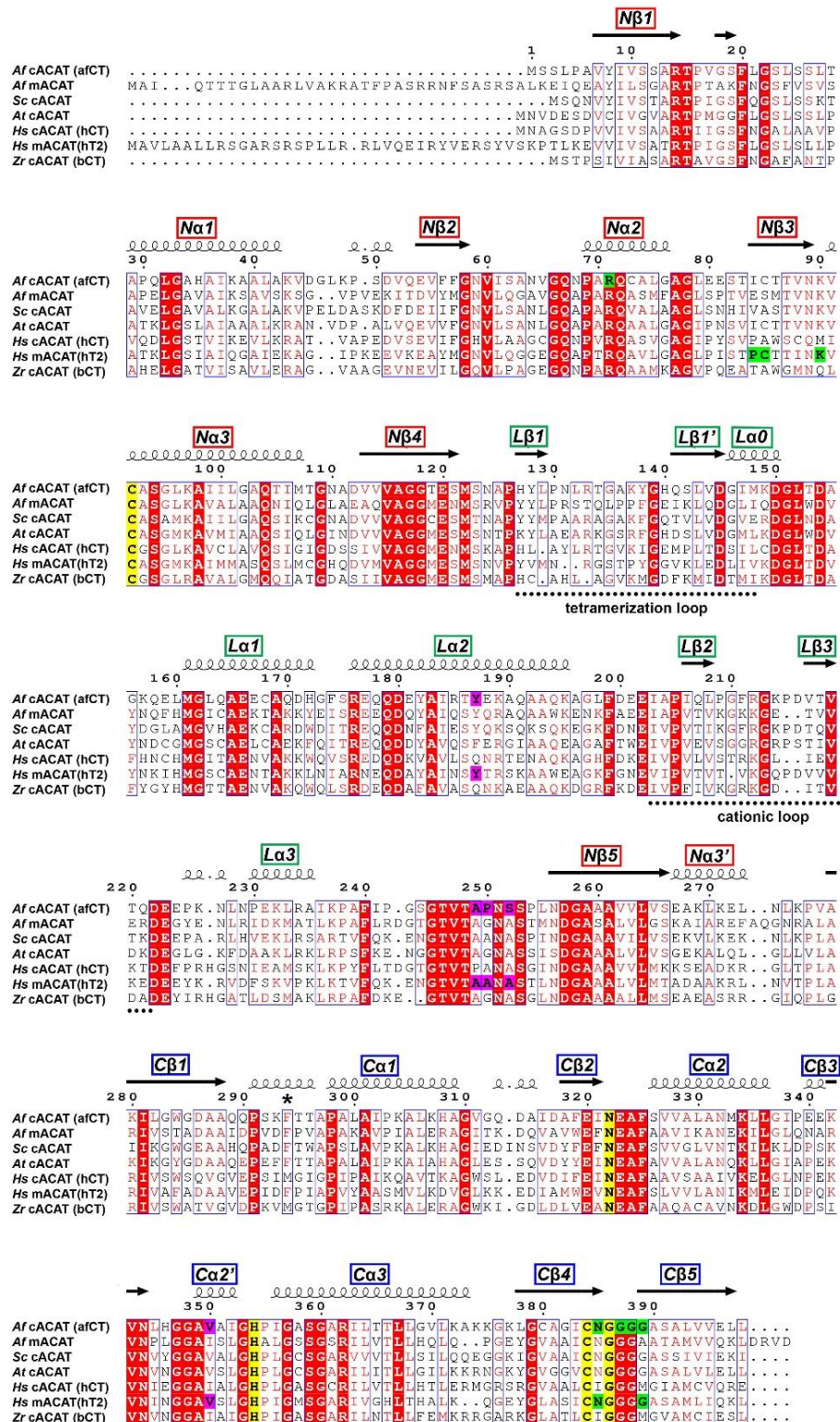


Figure S2. Multiple sequence alignment of cytosolic and mitochondrial acetoacetyl-CoA thiolases (cACAT and mACAT) from *Aspergillus fumigatus* (*Af*), *Saccharomyces cerevisiae* (*Sc*), *Arabidopsis thaliana* (*At*), *Homo sapiens* (*Hs*) and *Zoogloea ramigera* (*Zr*). Conserved sequences are outlined by blue boxes: Strictly conserved residues are white text on a red background, highly similar residues are red text. Catalytic residues are highlighted yellow. Residues of afCT or hT2 highlighted green or magenta are involved in binding Cl⁻ or K⁺ ions, respectively. Phe294, involved in substrate specificity, is marked with an asterisk. Secondary structural elements of afCT (shown above the sequence - β -strands: arrows, α -helices: large coils, 3_{10} -helices: tight coils) are labeled according to the nomenclature adopted for the first crystal structure of a tetrameric ACAT². Element labels for the NTD, loop domain and CTD are colored red, green and blue, respectively. (Sequence accession numbers: *Af* cACAT - XP_747207.1, *Af* mACAT - XP_751294.1, *Sc* cACAT - NP_015297.1, *At* cACAT - AT5G48230.1, *Hs* cACAT - NP_005882.2, *Hs* mACAT - NP_000010.1, *Zr* cACAT - AAA27706.1)

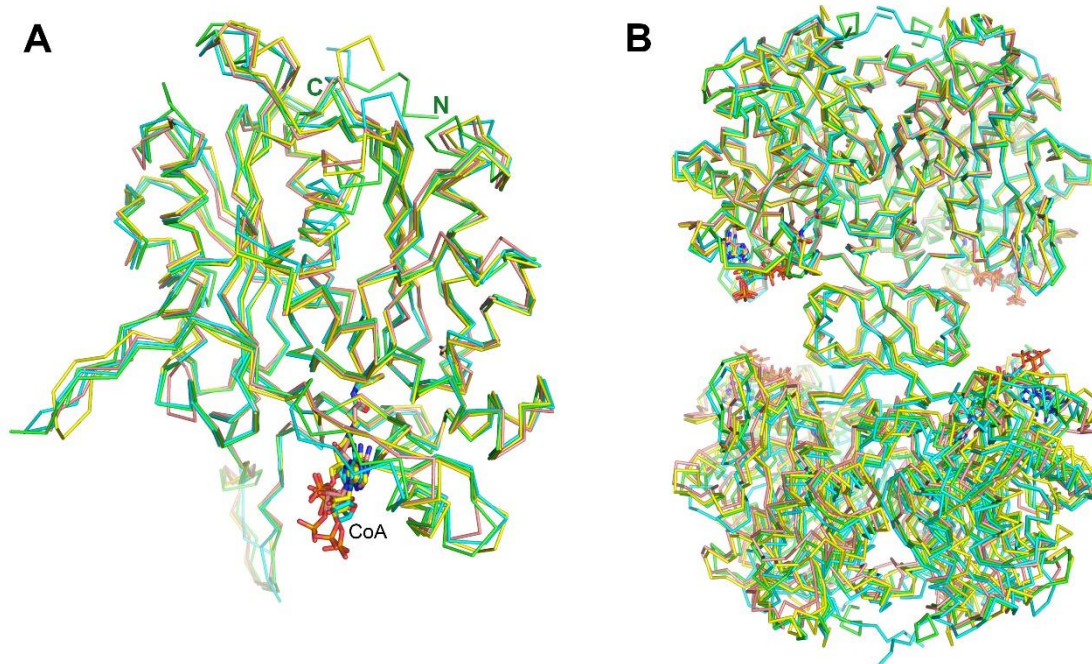


Figure S3. Comparison of afCT (green – this study), hCT (yellow – 1WL4), hT2 (cyan – 2IBY) and bCT (salmon – 1QFL) structures. α -carbons are traced as ribbons and CoA molecules are shown as sticks. **(A)** Single subunit superposition. The N- and C-termini of afCT are labeled. **(B)** Tetramers. Only the top tight dimer of each was used for the superposition, showing the variation in orientation of the second tight dimer.

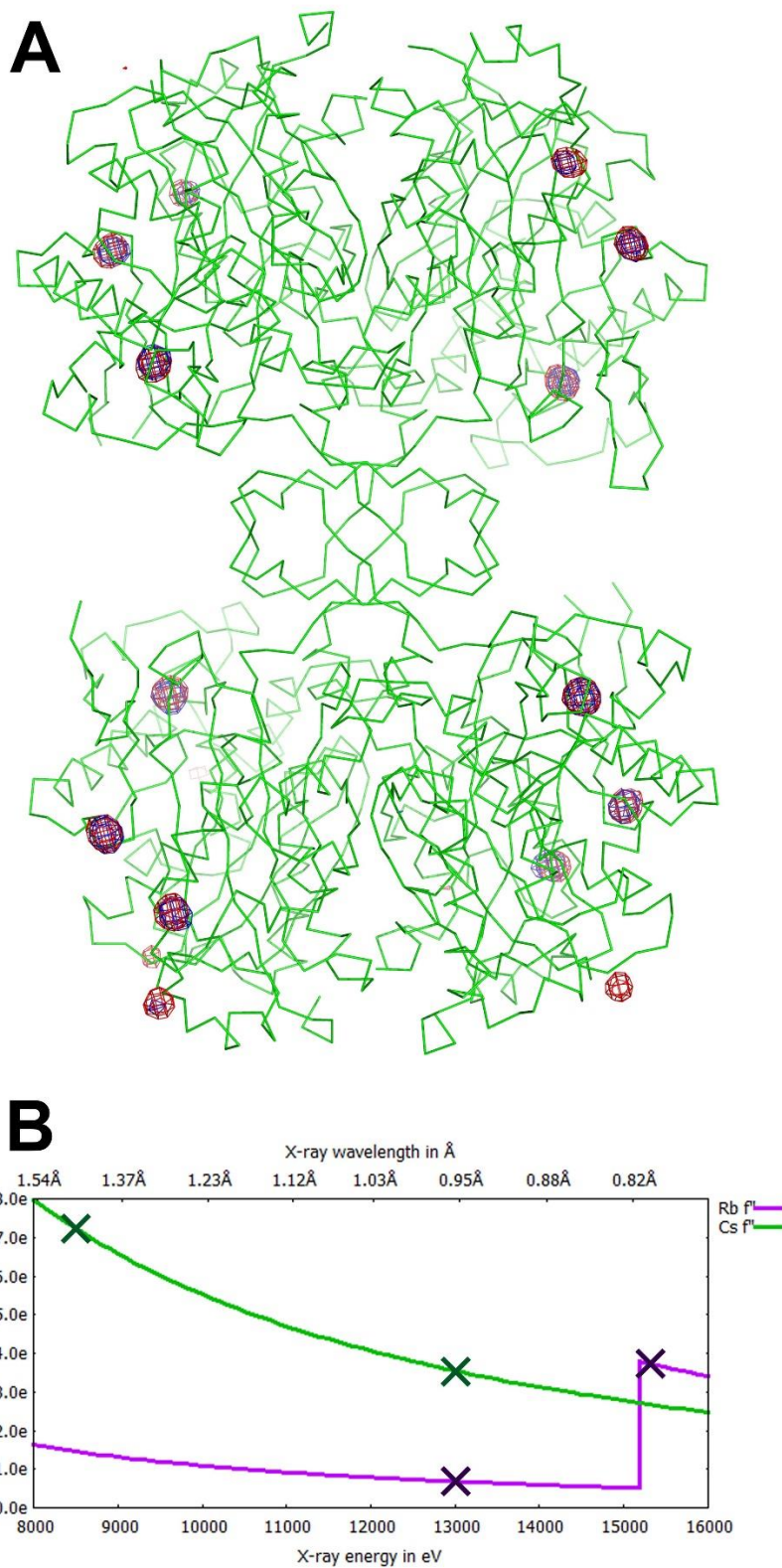


Figure S4. Monovalent cation binding sites of afCT. **(A)** Superposition of anomalous difference maps for afCT+Rb⁺_{anom} (15350 eV) (blue mesh) and afCT+Cs⁺_{anom} (8500 eV) (red mesh) datasets contoured at 4.5 and 5.5 σ , respectively. afCT is shown as green ribbons. **(B)** Relationship of X-ray energy to theoretical anomalous signal strength (f'') for Rb and Cs (data from <http://skuld.bmsc.washington.edu/scatter>³, plotted using Gnuplot v5.0.6). Datasets were collected at X-ray energies indicated by the crosses; average anomalous peak heights for data collected at each wavelength are listed in Table 2.

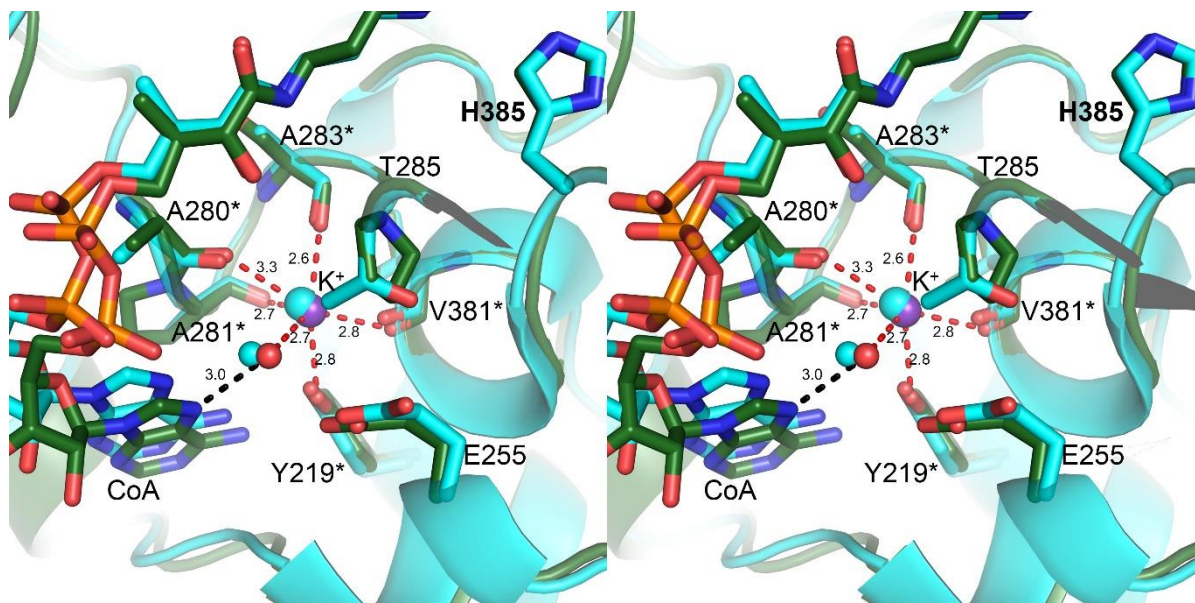


Figure S5. Superposition of afCT+AcCoA+K⁺ (dark green) with hT2 (cyan; also bound to CoA; PDB: 2IBY) shows that their K⁺-binding sites are almost identical. The K⁺ of afCT (purple sphere) is shown with coordination bonds (red dashes, lengths in Å); Wat_{MVC} is shown as a red sphere. Both the K⁺ and coordinating water of hT2 (large and small cyan spheres) are shifted only very slightly relative to those of the afCT structure. Residue labels refer to hT2. K⁺ coordinating residues are indicated by asterisks.

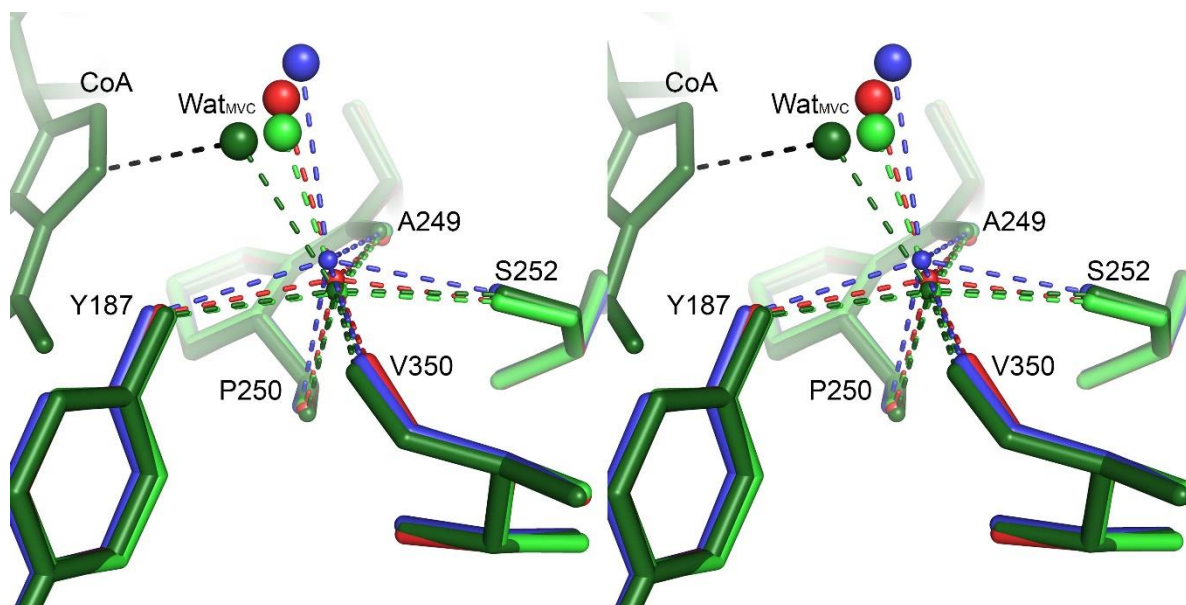


Figure S6. The MVC binding site of afCT is an ideal size to accommodate K⁺ ions. Superposition of afCT+K⁺ (light green), afCT+Rb⁺ (red) and afCT+Cs⁺ (blue) (all elements for each individual structure are colored the same) shows that the larger the radius of the cation (K⁺ < Rb⁺ < Cs⁺; shown as tiny spheres for clarity), the further it shifts out of the plane formed by the coordinating oxygen atoms of Tyr187, Ala249, Ser252 and Val350, simultaneously pushing Wat_{MVC} (larger spheres) further away from its position in afCT+AcCoA+K⁺ (dark green).

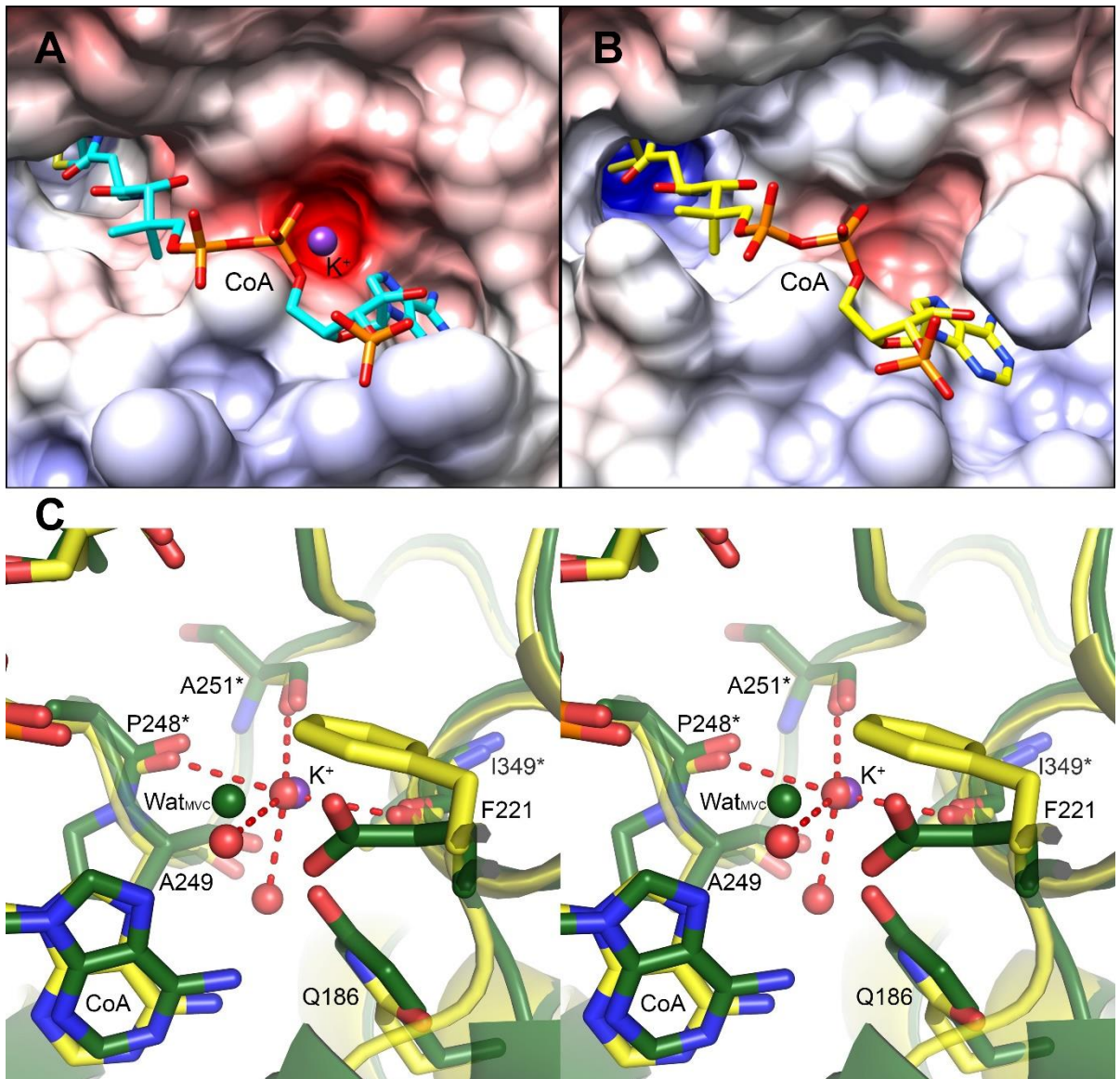


Figure S7. Space-filling representations of afCT and hCT colored by electrostatic potential (gradient: -9 to +9, red to blue). CoA is shown as sticks. **(A)** afCT: The K^+ ion (purple sphere) binding site is a pocket with a strong negative charge close to the adenosine of CoA. **(B)** hCT: The region surrounding the adenosine binding pocket is much less negatively charged than for afCT, largely due to the substitution of Glu224 (afCT) for Phe221 (hCT). **(C)** Superposition of afCT+AcCoA+ K^+ (dark green) with hCT (yellow; PDB: 1WL4) shows that, in the hCT structure, a water molecule (red spheres) is coordinated (red dashes) at the homologous site to the K^+ (purple sphere) of afCT. Wat_{MVC} of afCT is shown as a dark green sphere. Residue labels refer to hCT, with those that coordinate the water marked with an asterisk.

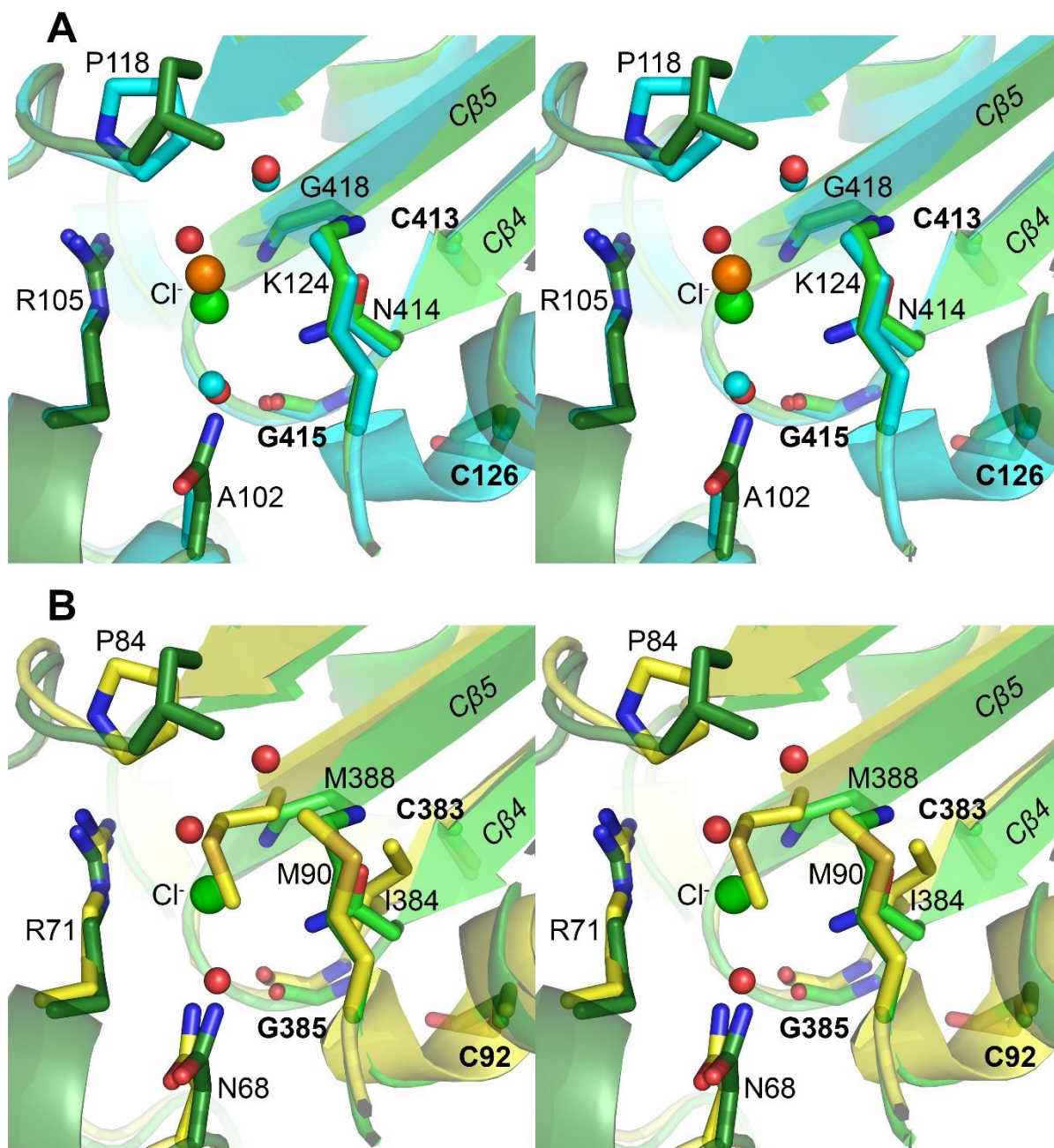


Figure S8. Comparison of the Cl⁻ binding site of afCT with corresponding regions of hT2 and hCT shown in stereo view. **(A)** Superposition of afCT (green) and hT2 (cyan) Cl⁻ binding sites. The hT2 site accommodates one less water (cyan spheres) and the Cl⁻ (orange) is shifted further from the Cβ4-Cβ5 loop. Residues labels refer to hT2. **(B)** Superposition of afCT (green) with hCT (yellow). Met388 of hCT occupies the space corresponding to the Cl⁻ in afCT. Residues labels refer to hCT.

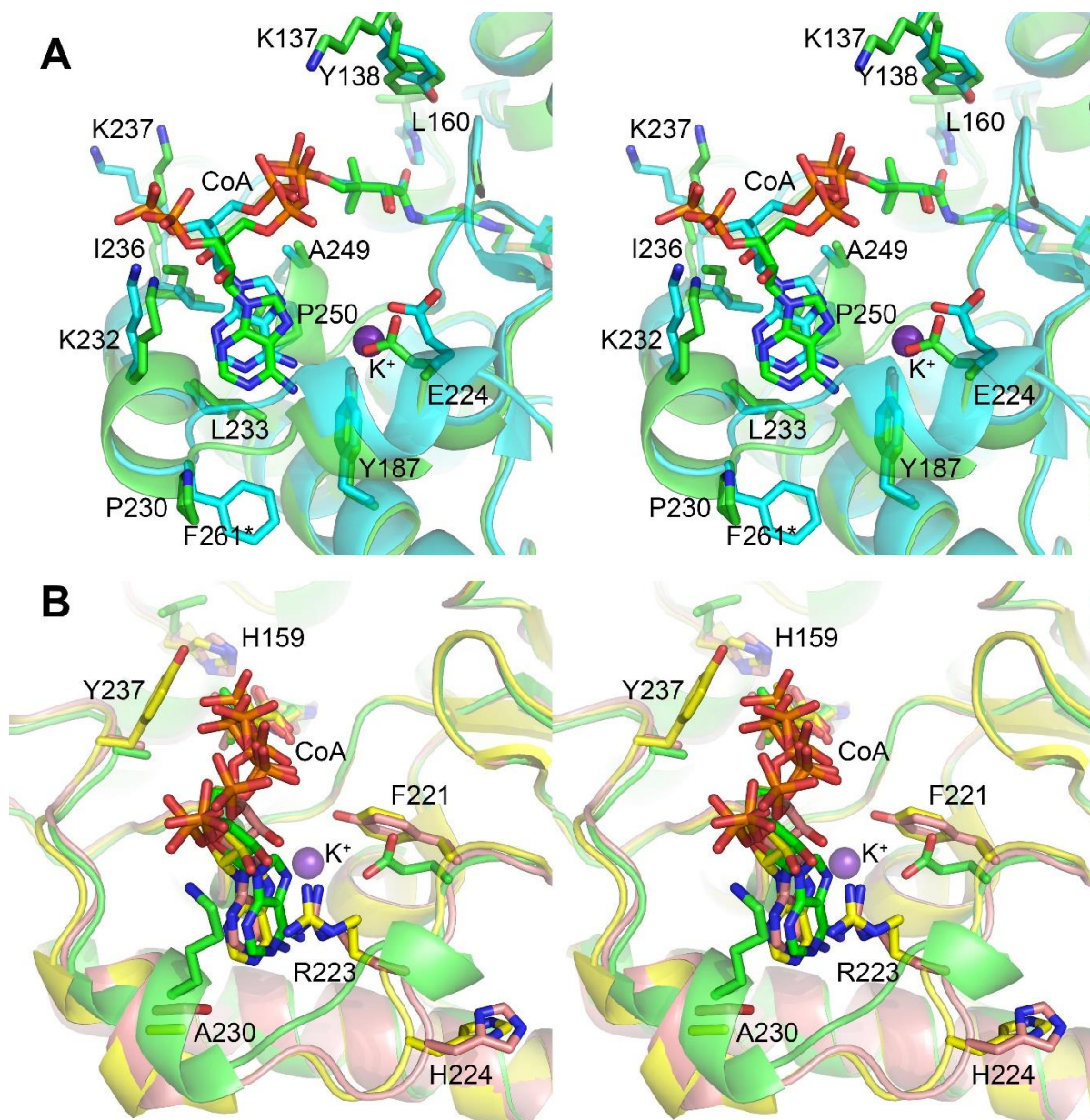


Figure S9. Comparison of the substrate binding sites of afCT, hT2, hCT and bCT shown in stereo view. **(A)** Superposition of the adenosine binding pockets of afCT (green) and hT2 (cyan; PDB: 2IBY). Labels always refer to afCT residues discussed in the text, except for Phe261 of hT2 (marked with an asterisk), which shifts the position of the L β 3-L α 3 loop relative to afCT. The K⁺ is represented by a purple sphere. **(B)** Superposition of the adenosine binding pockets of afCT (green), hCT (yellow; PDB: 1WL4) and bCT (salmon; PDB: 1QFL). Residues that represent key differences (see text) are shown as sticks. Residue labels refer to hCT.

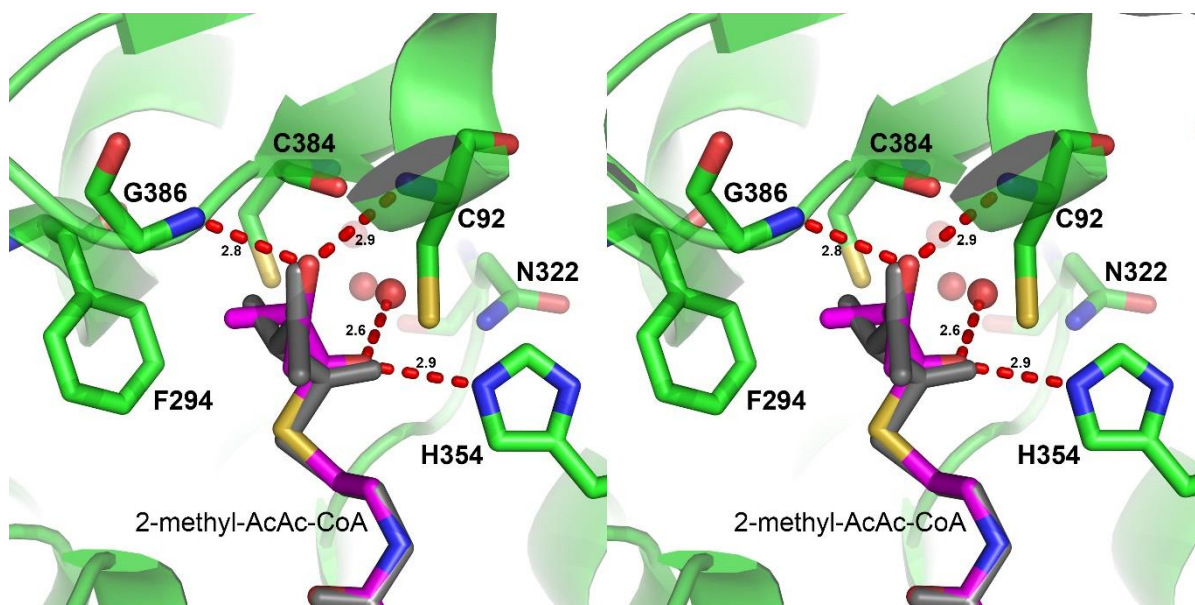


Figure S10. Stereo view of 2-methylacetoacetyl-CoA (sticks: carbon atoms of *S*-enantiomer are magenta; for clarity, all atoms of *R*-enantiomer are grey) docked *in silico* to the active site of afCT. Key residues are shown as sticks, and waters as red spheres. The 2-methyl moiety of both enantiomers make van der Waals contact with the phenyl ring of Phe294. Thioester and 3-keto oxygens of the substrate occupy oxyanion holes formed by His354 (N ϵ 2) and Wat_{cat1} (OAH1), and Cys92 (N) and Gly386 (N) (OAH2). Red dashes indicate hydrogen bonds; distances are in Å.

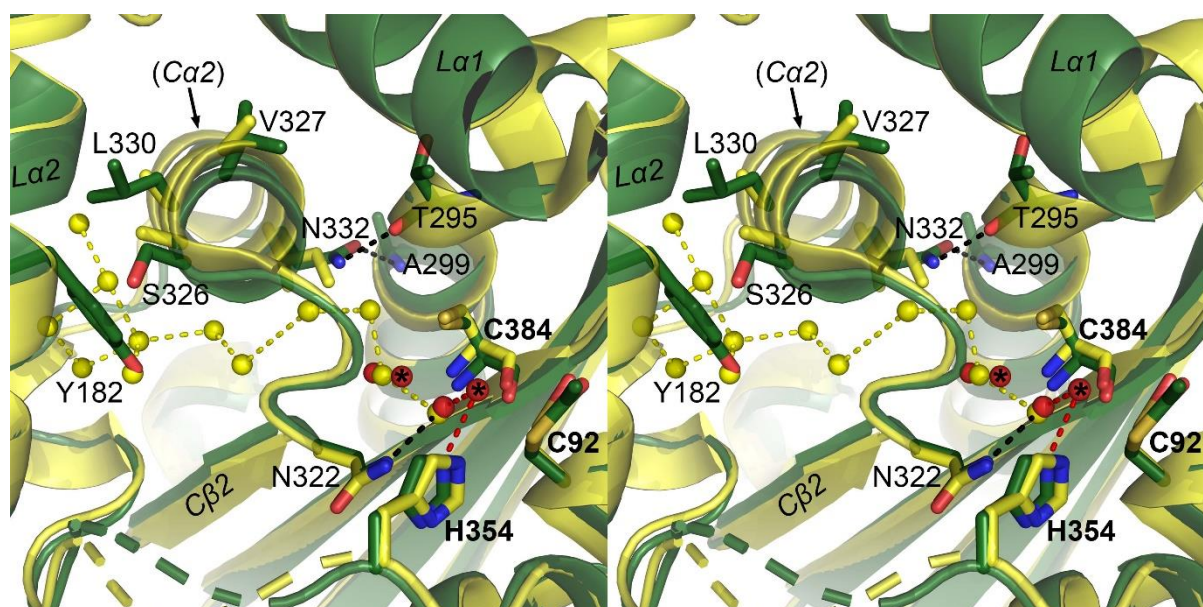


Figure S11. Superposition of hCT (yellow; PDB: 1WL4) and afCT (dark green) shows that afCT possesses only the first three waters (red spheres) of the water trail present in hCT (yellow spheres). Waters with alternate locations are marked with asterisks. La1, La2, C β 2 and Ca2 are labeled in italics. Residues discussed in the text are labeled, with catalytic residues in bold; all labels refer to afCT residues. Cys92 is acetylated for afCT and oxidized for hCT. Hydrogen bonds (dashes) are shown for the hCT water trail (yellow), OAH1 (red), stabilization of Wat_{cat1} by Asn322 (black) and the sidechain of Asn322 with backbone atoms of Ca1 (black). Note that, for clarity, Ca2' was omitted from the models shown (dashed cartoon representation; foreground). Figure shown in cross-eye stereo view.

References for Supporting Information

- (1) Carrie, C.; Murcha, M. W.; Millar, A. H.; Smith, S. M.; Whelan, J. *Plant Mol. Biol.* **2007**, *63*, 97–108.
- (2) Modis, Y.; Wierenga, R. K. *Structure* **1999**, *7*, 1279–90.
- (3) Cromer, D. T.; Liberman, D. A. *Acta Crystallogr. Sect. A* **1981**, *37*, 267–268.

Chapter 5 (Publication):

Structure of the Sliding Clamp from the
Fungal Pathogen *Aspergillus fumigatus*
(AfumPCNA) and Interactions with
Human p21

Statement of Authorship

Title of Paper	Structure of the sliding clamp from the fungal pathogen <i>Aspergillus fumigatus</i> (AfumPCNA) and interactions with Human p21
Publication Status	<input checked="" type="checkbox"/> Published <input type="checkbox"/> Accepted for Publication <input type="checkbox"/> Submitted for Publication <input type="checkbox"/> Unpublished and Unsubmitted work written in manuscript style
Publication Details	Andrew C. Marshall, Alice J. Kroker, Lauren A.M. Murray, Kahlia Gronthos, Harinda Rajapaksha, Kate L. Wegener and John B. Bruning. The FEBS Journal 284 (2017) 985–1002

Principal Author

Name of Principal Author (Candidate)	Andrew C. Marshall
Contribution to the Paper	Performed protein purification and crystallisation, data processing, structure solution and interpretation, and prepared figures and manuscript.
Overall percentage (%)	40
Certification:	This paper reports on original research I conducted during the period of my Higher Degree by Research candidature and is not subject to any obligations or contractual agreements with a third party that would constrain its inclusion in this thesis. I am the primary author of this paper.
Signature	Date 12/12/17

Co-Author Contributions

By signing the Statement of Authorship, each author certifies that:

- i. the candidate's stated contribution to the publication is accurate (as detailed above);
- ii. permission is granted for the candidate to include the publication in the thesis; and
- iii. the sum of all co-author contributions is equal to 100% less the candidate's stated contribution.

Name of Co-Author	Alice J. Kroker*
Contribution to the Paper	Performed gene cloning, purification guidance, and helped prepare and evaluate manuscript, particularly in regards to placing the data in a broader biological context. (*Andrew C. Marshall and Alice J. Kroker contributed equally to this work.)
Signature	Date 18/12/17

Name of Co-Author	Lauren A.M. Murray
Contribution to the Paper	Helped with protein purification and crystallisation trials.
Signature	Date 11/12/17


Name of Co-Author	Kahlia Gronthos		
Contribution to the Paper	Helped with protein purification and crystallisation trials.		
Signature		Date	12/12/17

Name of Co-Author	Harinda Rajapaksha		
Contribution to the Paper	Performed molecular dynamics simulations.		
Signature		Date	11/12/17

Name of Co-Author	Kate L. Wegener		
Contribution to the Paper	Performed peptide binding studies, and assisted with manuscript preparation.		
Signature		Date	12/12/17

Name of Co-Author	John B. Bruning		
Contribution to the Paper	Conceived and managed project, and helped with data processing, structure solution, and preparation of manuscript and figures. Corresponding author.		
Signature		Date	12-12-2017

Structure of the sliding clamp from the fungal pathogen *Aspergillus fumigatus* (AfumPCNA) and interactions with Human p21

Andrew C. Marshall^{1,*}, Alice J. Kroker^{1,*}, Lauren A.M. Murray¹, Kahlia Gronthos¹, Harinda Rajapaksha², Kate L. Wegener¹ and John B. Bruning¹ 

¹ School of Biological Sciences, The University of Adelaide, South Australia, Australia

² Department of Biochemistry and Genetics, La Trobe Institute for Molecular Life Science, La Trobe University, Bundoora, Australia

Keywords

Aspergillus; p21; PCNA; PIP-box; sliding clamp

Correspondence

J. B. Bruning, School of Biological Sciences, Adelaide, South Australia, Australia
Fax: +61 (08) 8313-4362
Tel: +61 (08) 8313-5218
E-mail: john.bruning@adelaide.edu.au

*These authors contributed equally

(Received 14 November 2016, revised 16 January 2017, accepted 2 February 2017)

doi:10.1111/febs.14035

The fungal pathogen *Aspergillus fumigatus* has been implicated in a drastic increase in life-threatening infections over the past decade. However, compared to other microbial pathogens, little is known about the essential molecular processes of this organism. One such fundamental process is DNA replication. The protein responsible for ensuring processive DNA replication is PCNA (proliferating cell nuclear antigen, also known as the sliding clamp), which clamps the replicative polymerase to DNA. Here we present the first crystal structure of a sliding clamp from a pathogenic fungus (*A. fumigatus*), at 2.6 Å. Surprisingly, the structure bears more similarity to the human sliding clamp than other available fungal sliding clamps. Reflecting this, fluorescence polarization experiments demonstrated that AfumPCNA interacts with the PCNA-interacting protein (PIP-box) motif of human p21 with an affinity (K_d) of 3.1 μM . Molecular dynamics simulations were carried out to better understand how AfumPCNA interacts with human p21. These simulations revealed that the PIP-box bound to AfumPCNA forms a secondary structure similar to that observed in the human complex, with a central 3_{10} helix contacting the hydrophobic surface pocket of AfumPCNA as well as a β -strand that forms an antiparallel sheet with the AfumPCNA surface. Differences in the 3_{10} helix interaction with PCNA, attributed to residue Thr131 of AfumPCNA, and a less stable β -strand formation, attributed to residues Gln123 and His125 of AfumPCNA, are likely causes of the over 10-fold lower affinity of the p21 PIP-box for AfumPCNA as compared to hPCNA.

Database

The atomic coordinates and structure factors for the *Aspergillus fumigatus* sliding clamp can be found in the RCSB Protein Data Bank (<http://www.rcsb.org>) under the accession code 5TUP.

Introduction

In recent decades, an increase in the number of treatment regimens involving immunosuppressant therapies has been associated with a rise in the incidence of invasive nosocomial fungal infections worldwide [1–3]. Aside from transplant failure or cancer relapse, the

primary cause of death for immunocompromised patients is infection, and various species of fungi, particularly *Candida* and *Aspergillus* spp., play a major role [4]. The saprophytic filamentous fungus *Aspergillus fumigatus* is abundant in the environment, and the

Abbreviations

Afum, *Aspergillus fumigatus*; IDCL, interdomain connector loop; PCNA, proliferating cell nuclear antigen; PIP, PCNA-interacting protein.

most common cause of invasive fungal infection in immunocompromised patients [5,6]. Typically found feeding on decaying organic matter, it plays a crucial role in the recycling of carbon and nitrogen [7,8]. *Aspergillus fumigatus* spores, called conidia, are ubiquitous and thus inhaled on a daily basis [9]. Conidia are usually cleared efficiently from the lungs by the innate immune system, but in specific cases they may germinate and cause infection [10]. Infection is most often pulmonary, but infections of the bronchi, sinus, and dissemination to the brain and other organs are also common. Susceptibility to invasive infection is closely linked to the immune status of the host; individuals at highest risk are those with hematological malignancies, particularly acute leukemia, and transplant patients [7,11]. Although morbidity and mortality are usually associated with invasive aspergillosis (IA) in immunocompromised patients, an even larger number of patients are affected by chronic or allergic conditions caused by *Aspergillus* spp. [12]. Occurrence of IA in otherwise immunocompetent patients is atypical, but has been reported following influenza [13,14] in ICU patients without hematological malignancy [15] and in otherwise healthy individuals [16,17]. *Aspergillus fumigatus* conidia are small enough to reach the lower airways and are readily internalized by alveolar epithelial cells, where they are able to evade host immune cells and to initiate systemic infection [18]. The low sensitivity of current microbiological and histopathological methods, along with a lack of consistency in surveillance and case definition, has made estimation of the incidence of IA in the past difficult and has probably lead to an underestimation of the true disease burden [19,20]. However, it is generally recognized that the incidence of invasive fungal infections is increasing, with the major contributors shifting from *Candida* spp. to *Aspergillus* spp. [19,21]. Central nervous system aspergillosis is a particularly devastating condition associated with a very poor prognosis and mortality rates of approximately 90% [11,12,17,22,23]. In addition, IA is the most common cause of death due to lung infection in hematopoietic stem cell transplant (HSCT) patients [23]. A multicenter prospective survey of 23 institutions in the US reported an incidence of invasive fungal infections in HSCT patients of 0.9%–13.2%. IA was the most common condition, with *A. fumigatus* by far the most prevalent species implicated. Overall 1-year survival rates for all autologous and allogeneic HSCT patients included in the study were 87% and 64%, respectively, but dropped to 25.4% when including only those who contracted aspergillosis [19]. IA is also common in solid organ transplant recipients, with an associated mortality of

approximately 22% [12]. In particular, lung transplant recipients exhibit invasive fungal infections in up to 19% of cases, with the majority of infections caused by *A. fumigatus* [24–26].

Despite the availability and widespread use of antifungals active against *A. fumigatus* for many years, the mortality rate remains unacceptably high. The major drugs approved for the treatment of IA target components of the cell membrane: amphotericin B, and azole antifungals including voriconazole, itraconazole, posaconazole, and more recently, isavuconazole [27]. Amphotericin B is associated with severe side effects, the most notable being severe kidney and liver toxicity, and has been largely superseded by the azole antifungals, although these are also often associated with significant side effects [28,29]. Current aspergillosis management guidelines from the Infectious Diseases Society of America recommend voriconazole for primary therapy in almost all cases, and posaconazole for prophylaxis [12]. The last 15 years or so have seen an alarming increase in the incidence of azole-resistant *A. fumigatus* strains that appear to have originated both in the environment—due to the widespread use of azole antifungals in agriculture—and in the clinic. Azole resistance is a major cause of treatment failure [30–34]. In addition, as the incidence of *Aspergillus* infection increases and species identification methods advance, more related species are added to the list that cause disease. These have differing antifungal susceptibilities and have been associated with negative clinical outcomes, highlighting the need for improved diagnostic protocols and a broader range of antifungal options [6,35]. Expanding our basic knowledge of the essential biological processes of this important fungal pathogen is crucial to further advances in medical treatment, and the development of new antifungal drugs with novel targets. One process that presents as a therapeutic target for many diseases is DNA replication and repair.

Proliferating cell nuclear antigen (PCNA) tethers proteins to DNA in cellular processes including DNA replication, DNA repair, and cell cycle control [36]. It is a member of the sliding clamp family of proteins, found in all three domains of life. Despite a lack of sequence homology between them [37], all sliding clamps share a pseudo sixfold symmetry arising from six structurally similar domains [38,39], and have a high level of structural conservation. In archaea and eukaryotes, the sliding clamp is trimeric [37,39,40]. PCNA subunits from different species are able to interact to form a trimer; the PCNA subunit from *Saccharomyces pombe* is able to interact with both *Drosophila melanogaster* and human PCNA subunits,

suggesting that interactions between PCNA subunits, and important residues in the interaction interface, are evolutionarily conserved [41]. PCNA alone has no intrinsic enzymatic activity but functions by fully encircling DNA and sliding freely. Through this topological interaction it is able to control and coordinate the access of proteins to DNA, particularly at the DNA replication fork. PCNA has been described as a 'tool belt', referring to its ability to interact with numerous and varied proteins [42,43]. These proteins are interchangeable, allowing for the 'belt' to hold different 'tools' depending on its current role within the cell. The majority of proteins that interact with PCNA contain a PCNA-interacting protein (PIP)-box peptide motif [36] which binds a hydrophobic cavity present on each monomer in the trimeric ring and forms an antiparallel β -sheet with the interdomain connector loop (IDCL) of PCNA. This allows for the binding of up to three such proteins to PCNA at one time [44]. This hydrophobic PIP-box-binding pocket is present in all eukaryotic sliding clamps; a comparable pocket is also present in bacterial sliding clamps, although there are significant differences in the pockets and binding peptides between eukaryotes and bacteria [45]. The PIP-box was first defined by Warbrick *et al.*, using a yeast two-hybrid screen followed by alanine scanning to identify key residues involved in the interaction of the tumor-suppressor protein p21 with PCNA, and its ability to inhibit SV40 DNA replication. It has been suggested that drugs based on the PIP-box of p21, either as derivatives or peptide mimetics, could have therapeutic uses in down-regulating DNA replication [41,44]. Small molecules that act as competitive inhibitors of the PCNA-PIP-box interaction have also been identified and proposed as novel anticancer therapeutics [46]. In addition, small molecules [47–49], natural compound derivatives [50], peptides [51], peptide mimetics [45,52], and cyclic peptides [53] that target the function of the bacterial sliding clamp have all been presented as novel antimicrobials. Despite its integral role in cell growth and survival, PCNA has not yet been investigated as a target for novel antifungal drugs.

Here we present the first crystal structure of a sliding clamp from a pathogenic fungus. We have solved the X-ray crystal structure of PCNA from *A. fumigatus* (AfumPCNA) to 2.6Å resolution. The structure reveals a trimeric ring-shaped fold similar to other eukaryotic sliding clamps. Interestingly, the overall structure is more similar to the human sliding clamp than that from *Saccharomyces cerevisiae* (yPCNA). Fluorescence polarization experiments with AfumPCNA and the

PIP-box from human p21 demonstrate a K_d of 3 μ M, providing evidence that AfumPCNA interacts with proteins at the replication fork through a conserved PIP-box mechanism similar to the human system, rather than the prokaryotic systems which do not employ use of the PIP-box system for protein-protein interactions. We have employed molecular dynamics simulations with AfumPCNA and the human p21 PIP-box to better understand the interactions. This revealed that the secondary structure of the PIP-box motif is similar in its interactions with AfumPCNA as with hPCNA. However, differences in the 3_{10} helix interaction cavity and the IDCL as well as a decreased ability to form a beta-strand conformation are likely to contribute to the lower affinity of p21 for AfumPCNA rather than hPCNA.

Results

Identification of PCNA from *Aspergillus fumigatus*

The *A. fumigatus* protein sequence was identified using the Aspergillus Genome Database and confirmed by means of multiple sequence alignment with PCNA from other species, as shown in Fig. 1. Analysis of the amino acid sequence of PCNA from several different sequences, as shown in Table 1, reveals that PCNA from *A. fumigatus* is most similar to *A. thaliana* (56.9%) and *D. melanogaster* (56.6%), followed very closely by human PCNA (53.9%). It is interesting to note that, in terms of PCNA sequence, the fungus *A. fumigatus* is more closely related to the higher order eukaryotes than to the yeast *S. cerevisiae* (49.6%). Previous studies have shown evolutionary drift of PCNA between the yeast and pathogenic fungi such as AfumPCNA. In eukaryotic species, the N- and C-terminal domains of each subunit are connected via an extended loop (residues 118 to 134) known as the interdomain connector loop (IDCL), which is necessary for interaction with the PIP-box-containing peptides [44]. Evolutionary drift among the PCNA molecules of Fungi is perhaps most notable in the IDCL. Zamir *et al.* [54] compared the IDCL of PCNA from numerous different fungal species and found that variation in just 4 of the 12 IDCL residues analyzed appeared to allow segregation of the different species into two distinct groups, as indicated in Fig. 1. Chimera-based protein-protein binding experiments in which the IDCL of fungal species were interchanged among the PCNA molecules and affinity for PIP-box-containing proteins was measured, demonstrated that

the IDCLs of the two groups of fungi could not be interchanged without significant loss of affinity. IDCL sequences from Group I fungal species (including *S. cerevisiae*) were incompatible with IDCL sequences from Group II species (including *A. fumigatus*) suggesting large evolutionary drift among the fungal species. However, to date no structural information has been available to explain these differences.

X-ray crystal structure of PCNA from *Aspergillus fumigatus*

To gain a better understanding of AfumPCNA structure and mechanism, AfumPCNA was purified and crystallized in space group P2₁. The AfumPCNA structure was solved to a resolution of 2.6 Å by means of molecular replacement. Data processing and

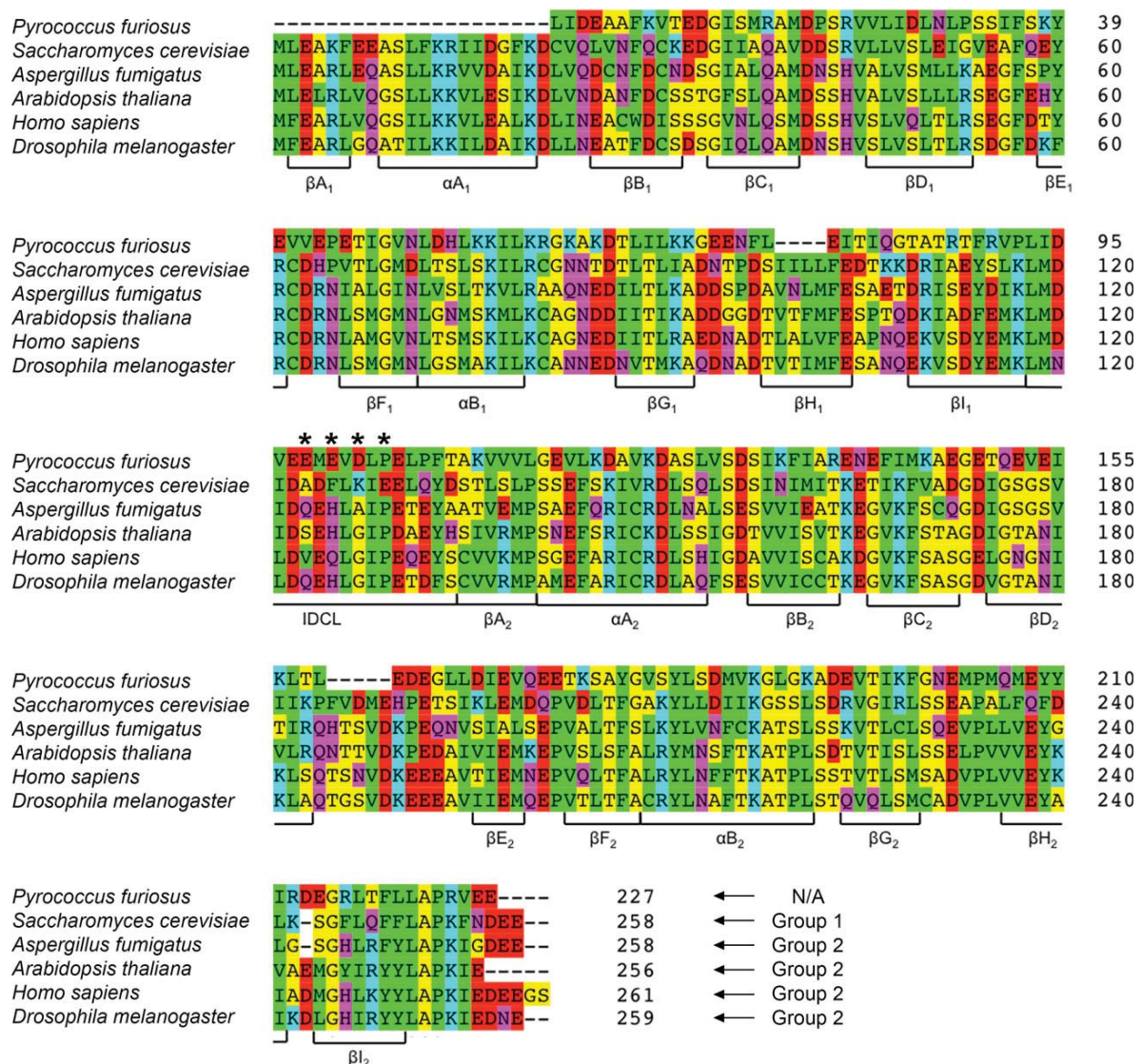


Fig. 1. Sequence alignment of the PCNA protein sequence from six different organisms. Residues are colored according to the following scheme [54]; nonpolar residues are yellow (GAST), polar residues are magenta (NQH), hydrophobic residues are green (CVILPFYMW), negatively charged residues are red (DE), positively charged residues are blue (KR). α -helices and β -sheets are labeled as they were described for the structure of *Saccharomyces cerevisiae* PCNA [37]. The IDCL is labeled as defined by Gulbis *et al.* [44]. The four residues within the IDCL identified by Zamir *et al.* [54] as segregating fungal species into two distinct groups are marked above by asterisks. The IDCL from *Pyrococcus furiosus* does not clearly belong to either group, as indicated.

Table 1. Percent identity (PIM scores) for PCNA amino acid sequence compared between six different organisms.

	<i>Pyrococcus furiosus</i>	<i>Saccharomyces cerevisiae</i>	<i>Aspergillus fumigatus</i>	<i>Arabidopsis thaliana</i>	Human	<i>Drosophila melanogaster</i>
<i>P. furiosus</i>	100.00	26.11	23.45	24.34	25.99	25.55
<i>S. cerevisiae</i>	26.11	100.00	49.61	40.00	35.66	36.05
<i>A. fumigatus</i>	23.45	49.61	100.00	56.86	53.88	56.59
<i>A. thaliana</i>	24.34	40.00	56.86	100.00	65.23	62.11
Human	25.99	35.66	53.88	65.23	100.00	71.04
<i>D. melanogaster</i>	25.55	36.05	56.59	62.11	71.04	100.00

Table 2. Data collection and refinement statistics.

	AfumPCNA ^a
Data collection	
Space group	P 2 ₁
Cell dimensions	
<i>a</i> , <i>b</i> , <i>c</i> (Å)	56.95, 103.37, 79.2
α , β , γ (°)	90.00, 96.60, 90.00
Resolution (Å)	78.68–2.60 (2.72–2.60) ^b
<i>R</i> _{merge}	0.189 (2.018)
<i>R</i> _{pim}	0.076 (0.837)
<i>CC</i> (1/2)	0.994 (0.330)
<i>I</i> / σ <i>I</i>	7.2 (1.0)
Completeness (%)	99.5 (96.7)
Redundancy	7.1 (6.6)
Refinement	
Resolution (Å)	44.02–2.602
No. reflections	28 050
<i>R</i> _{work} / <i>R</i> _{free}	0.1970 / 0.2571
No. atoms	
Protein	5634
Water	205
<i>B</i> -factors	
Protein	74
Water	61
RMS deviations	
Bond lengths (Å)	0.004
Bond angles (°)	0.978

^aData collected from 1 crystal.^bValues in parentheses are for highest-resolution shell.

refinement statistics can be found in Table 2 and a reduced model bias stereo figure of representative electron density can be seen in Fig. 2. The asymmetric unit is composed of three subunits that form a ring-shaped trimer that is representative of DNA sliding clamps from other species (Fig. 3). Subunits of the trimer show high structural similarity, with RMSD values between subunits ranging from 0.89 Å to 0.97 Å (calculated over 254 C α atoms) and total surface areas of 12375 Å², 12297 Å², and 12446 Å², giving an average surface area per subunit of 12373 Å². Subunits are composed of four α -helices and 18 β -strands arranged

into two domains of nearly identical topology, connected by an IDCL (Fig. 3A). Each domain consists of two adjacent α -helices covered on one side by two antiparallel β -sheets of four or five strands each. Each β -sheet is continuous with the β -sheet of the adjacent domain, such that six, nine-stranded β -sheets surround the trimeric ring: three cross the domain interface within each subunit and three cross the interface between each subunit (Fig. 3B). The AfumPCNA trimer therefore has a pseudo sixfold rotational symmetry, with the axis of symmetry running through the center of the ring. The subunits pack to form the trimer leaving a central cavity of approximately 30 Å—a diameter which would allow nonspecific interactions with DNA.

Atomic interactions of the AfumPCNA subunit interface

Proliferating cell nuclear antigen oligomerizes via an interface that is conserved among all three subunit–subunit interfaces (Figs 3B and 4). The subunit–subunit interfaces involve the interaction of β I1 and α B1 of the N-terminal domain with β D2 and α A2 of the C-terminal domain. The peripheral β -strands of each domain (β I1 and β D2) form an antiparallel β -sheet such that the β -sheet is continuous across the subunit interface. For the following discussion, we refer to the interface between subunits A and C, unless otherwise specified.

The interface surface area is 687.2 Å²; similar to the corresponding interfaces of both hPCNA and yPCNA (697.6 Å² and 654.1 Å², respectively), and involving 11 hydrogen bonds (Fig. 4A) and one salt bridge (Fig. 4B). Eight hydrogen bonds between peptide backbone atoms of residues 109 to 117 (β I1) and 175 to 183 (β D2) have distances ranging from 2.28 Å to 3.40 Å, and define the antiparallel β -sheet (Fig. 4A). The remaining three hydrogen bonds are weak (distance > 3.6 Å) and are between Lys77 (NZ) and Ala153 (O), Thr108 (N) and Gln193 (OE1), and Asp115 (OD2) and Ser177 (OG). Arg110, contained in

β I1, forms a salt bridge with Glu143 from α A2 (Fig. 4B). The core of the interface is hydrophobic, centered around Tyr114, and is composed of α B1 residues Val78 and Ala81, β I1 residues Tyr114 and Ile116, α A2 residues Leu151 and Leu154, and β D2 residues Ile175 and Val180 (Fig. 4B).

The subunit interface is highly conserved among species, with comparisons to hPCNA and yPCNA revealing very similar surface areas and interacting

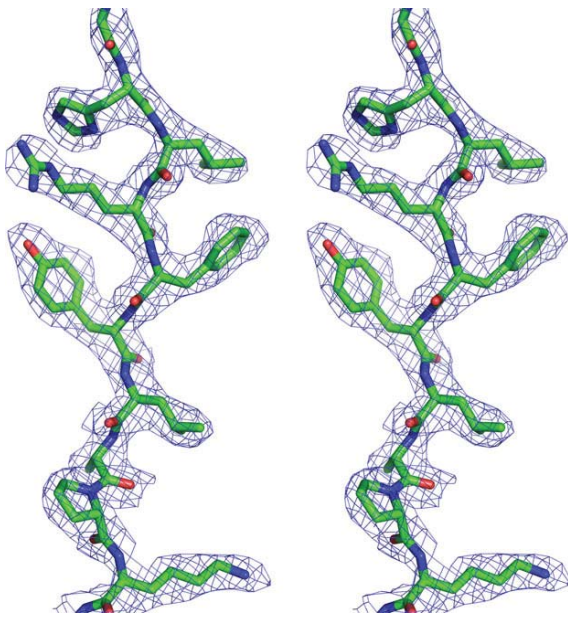


Fig. 2. Representative electron density. Wall-eye stereo image of a reduced model bias feature-enhanced map [68] contoured at 1.5σ encompassing residues Gly244 to Lys253 of AfumPCNA.

residues. All of the hydrophobic residues at the interface core are conserved in human and yeast PCNA, and each interface involves a similar number of hydrogen bonds. The most conspicuous nonconservative substitution is at position 153 of α A2, which is an alanine, histidine, or glutamine in AfumPCNA, hPCNA, and yPCNA, respectively. However, this substitution for bulkier residues in both hPCNA and yPCNA appears to have very little effect on the conformation of other interface residues, but may contribute to a slightly larger interaction surface. The only other significant nonconservative substitution at the subunit interface is a glutamine residue in AfumPCNA (Gln83), which is glycine in hPCNA. This permits the side chain of Arg146, which points to solvent in AfumPCNA (Fig. 4B), to contact α B1 of the opposing subunit of hPCNA, forming a hydrogen bond with Lys80 (O) (2.97Å). The hPCNA interface includes a salt bridge at the end of the β -strand, involving Lys117 and Glu174, which is absent in both AfumPCNA and yPCNA. Lys117 is conserved in fungal PCNA, but residue 174 is an aspartate residue, which lacks the conformational flexibility required to form an electrostatic interaction with Lys117. The salt bridge between residues 110 and 143 is conserved in AfumPCNA, with the variation that 110 is an arginine rather than a lysine. In yPCNA, Arg110 also forms a salt bridge, but partners with Asp150 rather than Glu143. Interestingly, both Glu143 and Asp150 are conserved and in similar positions in both fungal PCNA structures, suggesting that Arg110 may be able to form a salt bridge with either of these residues. This is confirmed in AfumPCNA upon inspection of the interface between subunits B and C, where indeed an

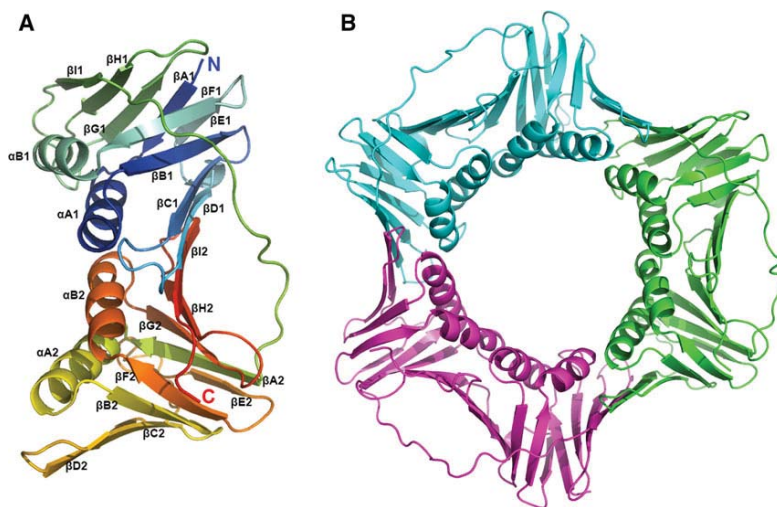


Fig. 3. Structure of the AfumPCNA. Depicted are ribbon diagrams of AfumPCNA. (A) Single subunit of AfumPCNA. (B) AfumPCNA trimer colored by subunit.

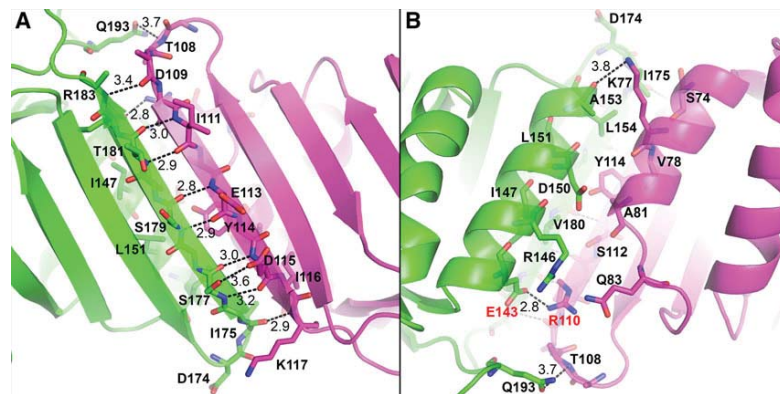


Fig. 4. Subunit-subunit interface of AfumPCNA. AfumPCNA is shown in ribbons with interacting residues shown as sticks. Subunit A is shown in magenta, while subunit B is shown in green. (A) Subunit-subunit interface of the β -sheet region. (B) Subunit-subunit interface of the α -helix region.

Arg110–Asp150 salt bridge is present, rather than the Arg110–Glu143 salt bridge of the interface between subunits A and C. Furthermore, at the remaining interface (A–B), the side chain of Arg110 is disordered in the electron density, consistent with conformational flexibility at this position. In contrast, the shorter side chain of Lys110 of hPCNA precludes it from forming a salt bridge with Asp150, limiting interaction to Glu143.

Comparison of AfumPCNA to the yeast and human PCNA

AfumPCNA shows high overall structural similarity to both the human and yeast PCNA crystal structures (Fig. 5), with average RMSD values across all subunits of 1.51Å and 1.53Å, respectively. Despite this, variation in the sequence of the IDCL results in structural changes that may affect interactions with binding partners. Interestingly, the IDCL of AfumPCNA showed more similarity to the human IDCL rather than the yeast IDCL, implying the AfumPCNA surface may interact with interacting partners by means of a human type PIP-box. The IDCL (residues 118–134) stretches across the outside of seven of the nine strands of the core β -sheet in each subunit (Fig. 6A). It is stabilized by a number of interactions with both backbone atoms and side chains protruding from the underlying sheet, including hydrogen bonds between Met119 (N) and Gly69 (O) (2.94Å), Gln123 (NE2) and Asp29 (OD2) (2.70Å), and Leu126 (O) and Gln38 (NE2) (3.32Å). The hydroxyl group of Tyr133 also forms two separate water-mediated hydrogen bonds with Pro234 (O) and Try249 (OH). In addition, Ile128 packs against hydrophobic residues Leu47 and Tyr249, and Tyr133 sits in a hydrophobic pocket formed by Cys228, Val233, Leu236, and Tyr249.

These interactions are conserved in hPCNA, with the notable exception of Gln123. A valine is present at

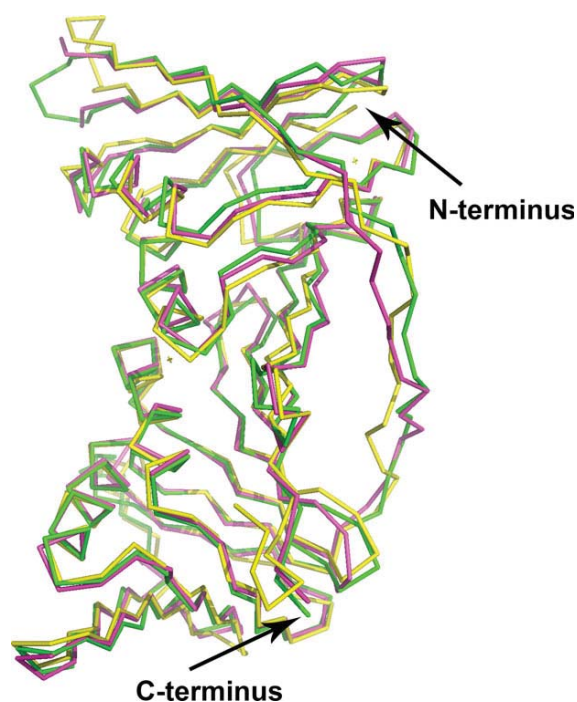


Fig. 5. Superimposition of PCNA subunits from different species. PCNA subunits are depicted in wire format. AfumPCNA is depicted in green (5TUP), hPCNA is depicted in magenta (PDB: 1AXC), and yPCNA is depicted in yellow (PDB: 1PLO) [37,44].

this position of the IDCL in hPCNA, precluding any hydrogen bonding interaction with Asp29. This aspartate residue has been shown to be involved in binding p21 (and other PIP-box peptides with antiparallel β -strand interaction) [44,55]. Therefore, the sequestering of this hydrogen bond acceptor by Gln123 in AfumPCNA may result in differences in binding specificity and affinity for PIP-box-containing peptides. This difference at position 123 is accompanied by the most evident conformational difference in the IDCL

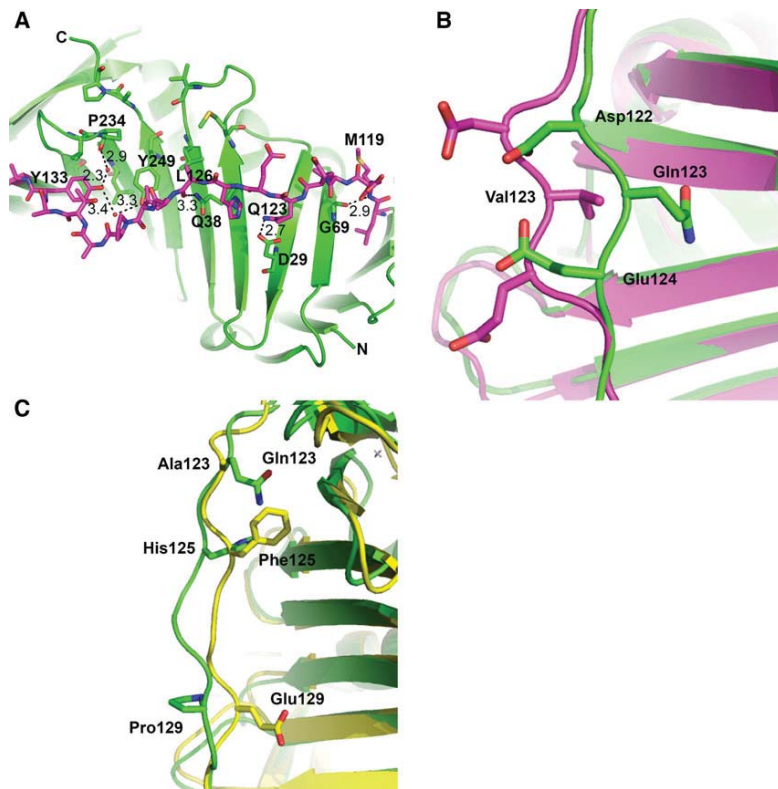


Fig. 6. Details of the AfumPCNA IDCL. (A) Interactions of the AfumPCNA IDCL. AfumPCNA is shown in green ribbons with the IDCL highlighted as magenta sticks. (B) Superimposition of AfumPCNA (green) with unliganded hPCNA (magenta; PDB: 1W60) [56]. (C) Superimposition of AfumPCNA (green) with yPCNA (yellow; PDB: 1PLO) [37].

between human and AfumPCNA; relative to Val123 of unliganded hPCNA (PDB: 1W60) [56], Gln123(C α) is shifted 4.14 Å toward the surface of PCNA and results in a concomitant shift of adjacent residues Asp122 and Glu124 in the same direction (Fig. 6B).

Inspection of the IDCL from *S. cerevisiae* PCNA (yPCNA) [37] reveals conformational differences with AfumPCNA (Fig. 6C). These differences are due to substitutions at His125 and Pro129, two of the four IDCL residue positions that have been used to separate fungal species into two separate evolutionary families (Fig. 1) [54]. However, this region of the yPCNA structure is involved in a number of crystal contacts, which may also contribute to conformational differences in the IDCL. Interestingly, despite the presence of a hydrophobic residue at position Ala123, similar to hPCNA, the position of the IDCL in this region (122 to 124) is more similar to that of AfumPCNA, which contains a glutamine residue at this position (Gln123), as shown in Fig. 6C. Phe125 of yPCNA participates in hydrophobic interactions that have a similar effect on the position of IDCL residues 122 to 124 as the hydrogen bond between the side chains of Gln123 and Asp29 of AfumPCNA. The side chain of Phe125 packs onto the underlying β -sheet via hydrophobic

interaction with Ile36 (Ala36 in AfumPCNA), drawing residues 124 to 127 of the IDCL an average of ~ 1.1 Å closer to the underlying β -sheet (Fig. 6C). Phe125 of yPCNA partially occupies the space of Asp29 of both AfumPCNA and hPCNA. This is reflected by the conformation of the side chain of Gln29 of yPCNA, which is shifted ~ 3.8 Å away from the IDCL backbone relative to Asp29 of AfumPCNA, potentially precluding it from acting as a hydrogen-bonding partner for PIP-box-containing peptides. The proline at position 129 in AfumPCNA is Glu129 in yPCNA (Fig. 6C). This substitution induces a different conformation of the IDCL and markedly alters the position of this residue, allowing it to pack ~ 3.7 Å closer to the underlying β -sheet, facilitated by an additional weak hydrogen bond between Glu129 (OE1) and Gln247 (NE2) (3.5 Å). This increased flexibility also allows Glu130 to occupy the space of Gln131 in hPCNA, which has been shown to form a hydrogen bond with the Tyr151 side chain hydroxyl group of the p21 peptide [44]. AfumPCNA contains a Thr (Thr131) at this position, a considerably shorter side chain which would require extension of PCNA toward the PIP-box for hydrogen bond formation as compared to the human structure.

Proliferating cell nuclear antigen residues (AfumPCNA residue numbers) Met40, Val45, Leu47, Leu126, Ile128, Pro129, Tyr133, Pro234, Tyr249, Ala251, and Pro252 form a hydrophobic pocket that is 'plugged' by the conserved 3_{10} helix of the PIP-box. This interaction has been shown to be essential for high-affinity binding of PIP-box-containing peptides [55]. Strikingly, these residues are 100% conserved between hPCNA and AfumPCNA highlighting the conserved nature of this interaction. Comparison of these with the hydrophobic pocket of yPCNA reveals only minor differences, with the only nonconserved substitution being position 129 in the IDCL, as previously mentioned.

Proliferating cell nuclear antigen residues of the C terminus that have been shown to interact with PIP-box peptides include Ala252, Pro253, and Ile255 of hPCNA and Ala251, Pro252, Lys253, and Phe254 of yPCNA [37,44]. These are conserved in AfumPCNA, suggesting their importance in mediating PCNA-PIP interactions across fungi and mammals. The six C-terminal residues of hPCNA (256 to 261) are disordered in the PCNA:p21-peptide structure. This includes four charged residues which have been suggested to closely associate with the charged residues at the N terminus of the p21 peptide via poorly ordered ionic interactions. The final four residues of AfumPCNA and yPCNA (both 255 to 258) are undefined in the electron density of these structures and include three charged residues, one aspartate and two glutamine residues, suggesting the conservation of this poorly ordered ionic interaction with binding peptides.

AfumPCNA binds p21 peptide with high affinity

To determine if the AfumPCNA interacts with its partners by means of a PIP-box, we determined the affinity of AfumPCNA for a peptide derived from the cyclin-dependent kinase inhibitor protein p21, previously shown to have the highest known affinity for hPCNA [55]. AfumPCNA binding to a canonical human p21 PIP-box motif was determined by incubating FITC-labeled p21 peptide (N-139 GRKRRQTSM TDFYHSKRRLIFS 160-C) with increasing concentrations of AfumPCNA, and measuring the changes in fluorescence polarization. Figure 7 contains the dose-response curves for the fluorescence binding. A K_d value of $3.1 \pm 0.1 \mu\text{M}$ was determined in PBS using similar conditions to Bozza *et al.* [57] (Fig. 7B). These authors determined the affinity of hPCNA to the same peptide in these conditions to be 342 nM. Thus, using similar buffer conditions, the p21 interaction for hPCNA is only 10-fold higher in affinity than the

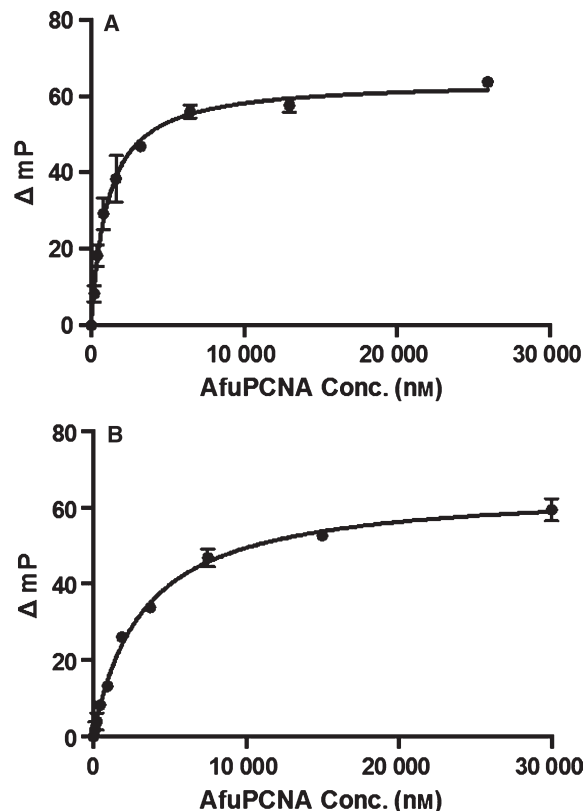


Fig. 7. Fluorescence polarization binding curves. Determination of the binding affinity of AfumPCNA for N-terminally FITC-labeled human p21 peptide in (A) 20 mM Tris with 10% glycerol and (B) PBS, pH 7.4 (full details of buffer conditions are given in the Materials and methods). Curves represent single experiments, where each data point is the mean of triplicate samples and error bars represent the standard deviation. Each experiment was repeated three times.

interaction with AfumPCNA. In experiments using Tris buffer (Fig. 7A), the K_d was determined to be $1.0 \pm 0.1 \mu\text{M}$, indicating that removal of salt strengthens the AfumPCNA/p21 interaction. Electrostatic contacts play a role in hPCNA/p21 complex formation, with salt bridges stabilizing the intermolecular β -sheet (hPCNA Asp29 to p21 Arg154, and hPCNA residues Asp122 and Glu124, to p21 Arg155). These hPCNA residues are conserved in AfumPCNA suggesting the intermolecular electrostatic interactions may be maintained, consistent with the FP data.

Deciphering the interaction of p21 with AfumPCNA by molecular dynamics simulation

Given our finding that AfumPCNA interacts with the human p21 peptide with high affinity, we performed

molecular dynamics simulations to better define the interactions of AfumPCNA with p21 as well as identify the structural basis for the lower affinity interaction with AfumPCNA versus hPCNA. The molecular dynamics simulation was carried out for a total of 50 ns using the AfumPCNA trimer bound to one p21 peptide per subunit. The simulation was stable over the entire time frame as indicated by the RMSD versus time (plotted by secondary structure) depicted in Fig. 8, and the overall structural trajectory is shown in Fig. 9. Two movies of the simulation can be found in the Supporting Information section (Movies S1 and S2).

The molecular dynamics simulation revealed that, although the core binding mode of the p21 peptide to PCNA is largely conserved between human and *A. fumigatus*, a number of differences are present that may contribute to a lower peptide-protein affinity for the *A. fumigatus* protein. The interaction of p21 with AfumPCNA, much like with hPCNA, can be conceptually divided into interactions of the p21 N terminus, 3_{10} helix, and C terminus, the latter of which forms an antiparallel β -sheet with the IDCL of PCNA.

The interaction of the p21 peptide N-terminal residues with the AfumPCNA C terminus was maintained throughout the simulation. Similar to the interactions of p21 with hPCNA, interactions of the N terminus of p21 include a system of hydrogen bonds: a hydrogen bond from p21 Arg143 main chain oxygen atom to Ile255 main chain nitrogen atom and from Gln144 side chain to Ser44 main chain oxygen atom (Fig. 10A). Unlike the p21 interaction with hPCNA, the side chain of Thr145 does not make a hydrogen bond with AfumPCNA and is instead rotated away from the surface of AfumPCNA making no intermolecular contacts by means of the side chain atoms.

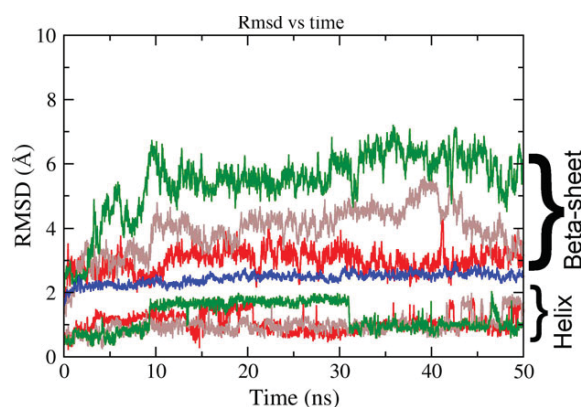


Fig. 8. Molecular dynamics RMSD versus time binned by secondary structure. AfumPCNA is shown as blue, while the p21 peptides are shown in green, red, and brown.

The p21 3_{10} helix that plugs a hydrophobic pocket on PCNA was stable throughout the duration of the simulation, reflecting the high conservation of residues that form the pocket (including residues Met40, Val45, Leu47, Leu126, Ile128, Pro129, Tyr133, Pro234, Tyr249, Ala251, and Pro252). Tyr151 is one of the key residues for high-affinity interaction of p21 with hPCNA [58], due to the side chain hydroxyl proton forming a hydrogen bond to the side chain nitrogen atom of Gln131. This interaction was predicted to be lost in AfumPCNA, due to the substitution of Gln for Thr at this position (Thr131 of AfumPCNA). The simulations showed this held true for two of the three peptide-PCNA interactions, but interestingly, a hydrogen bond between Thr131 (side chain hydroxyl) and p21 peptide Tyr151 (side chain hydroxyl) is present in the remaining peptide interaction, but requires Tyr151 to shift approximately 2.7Å toward the core of the protein. Of the three p21 peptides bound to the PCNA trimer, the peptide which forms the hydrogen bond between Thr131 and Tyr151 also adheres to a well-formed antiparallel β -strand, while the two peptides with unstable β -strand formation are correlated with a loss of hydrogen bonding capacity between these residues (Fig. 10B). From this it can be deduced that at least part of the lower affinity of p21 for AfumPCNA can be attributed to the lessened ability of p21 to hydrogen bond with AfumPCNA residue Thr131, which is intricately linked to the β -strand conformation of the peptide. In addition, AfumPCNA contains a larger and less hydrophobic surface cavity (124Å^3 in hPCNA/p21 versus 235Å^3 in AfumPCNA/p21) capable of promoting interaction with the 3_{10} helix (Fig. 10C,D); both of these effects can partly be attributed to the presence of Thr131 in the AfumPCNA structure rather than Gln131 as seen in the hPCNA structure.

The antiparallel β -sheet formed between the p21 peptide C terminus and residues 121–127 of the AfumPCNA IDCL is maintained throughout the simulation for one of the three peptides, partially maintained for another, but has completely dissociated in the case of the remaining peptide (Figs 9 and 10B). The formation of the β -strand conformation of p21 in the AfumPCNA-bound simulation only occurs with significant rearrangement of the IDCL as compared to the human p21-bound IDCL. The disruption of this interaction is consistent with the observation that Asp123 of the IDCL sequesters the electrostatic interaction to Arg156 in the AfumPCNA crystal structure, precluding the formation of hydrogen bonds to Asp29 from Arg156 of p21 that aid in anchoring the C-terminal half of the peptide to the surface of hPCNA

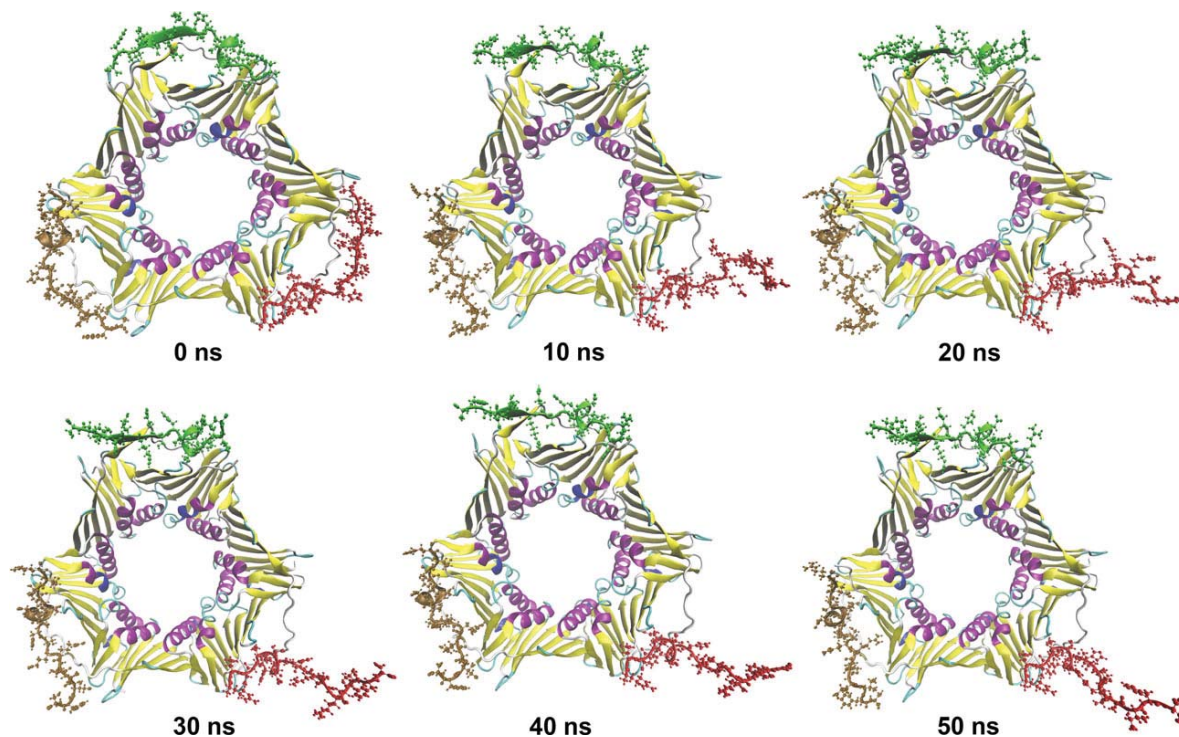


Fig. 9. Molecular dynamics simulation trajectory over time at 10-ns intervals. Displayed is a ribbon diagram of AfumPCNA (colored by secondary structure) with p21 peptides shown as sticks (green, red, and brown).

(Fig. 10E). Furthermore, His125 of AfumPCNA obstructs β -sheet by formation of a favorable side chain hydrogen bond with the His152 side chain of p21, forcing the peptide in a conformation that is too distant from the surface of AfumPCNA to form the tight hydrogen bonds of a β -sheet as seen in the human structure (Fig. 10E).

It is interesting to note that, while the interaction between the central 3_{10} -helical plug and the AfumPCNA hydrophobic pocket is very stable, the polar interactions between the N-terminal and C-terminal peptide residues and the PCNA C terminus and IDCL, respectively, appear to be mutually exclusive. This is shown by the observation that the loss of intermolecular hydrogen bonding at the C-terminal half of the p21 peptide is accompanied by an increase in the number of hydrogen bonds between the N terminus of the peptide and C terminus of AfumPCNA (Fig. 11C). In fact, the only peptide for which the conformation of the peptide's N terminus and 3_{10} helix (residues 143 to 151) is almost identical to that of the hPCNA-p21 peptide structure is the one that has completely lost the β -sheet interaction at the C-terminal end of the peptide. On the other hand, extensive hydrogen bonding involving the C-terminal region of the peptide is

accompanied by a decrease in hydrogen bonding at the N terminus of the peptide (Fig. 11A,B). Regarding the peptide for which the β -strand in the C-terminal region of the peptide is well maintained, the 3_{10} helix is forced into a more α -helical conformation by interaction with Thr131; a peptide conformation which favors C-terminal β -strand formation, but disfavors interactions between the N-terminal region and the C terminus of AfumPCNA.

Discussion

Here we present the first crystal structure of PCNA from *A. fumigatus* as well as the first crystal structure of PCNA from a pathogenic fungus. Interestingly, the structure of the AfumPCNA is more structurally related to human PCNA than the previously reported *S. cerevisiae* PCNA. Furthermore, we also demonstrated that AfumPCNA interacts with high affinity with a human PIP-box, implying that PCNA-interacting proteins from the pathogen *A. fumigatus* are likely to interact with AfumPCNA by means of a conserved PIP-box similar to that of the human sequence. Given that p21 interacts with AfumPCNA with 10-fold lower affinity than its human counterpart, we performed

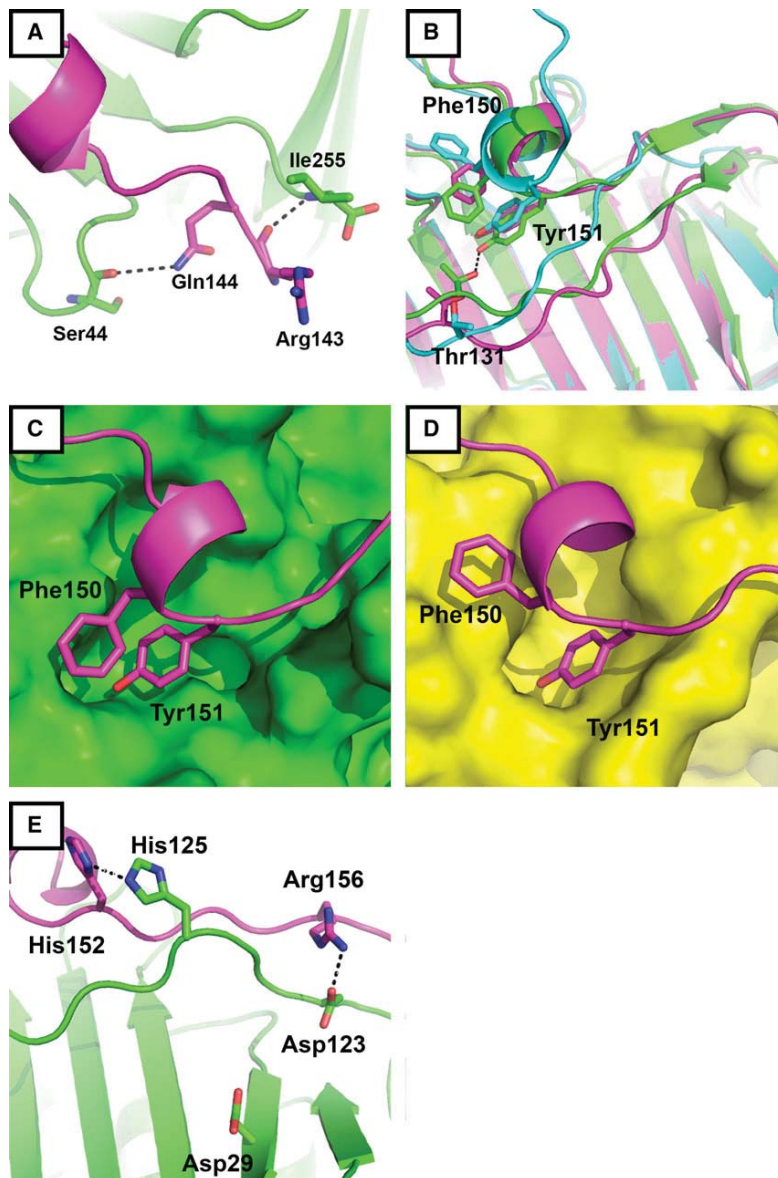


Fig. 10. Interactions of AfumPCNA with the p21 peptide as determined by molecular dynamics. (A) Interactions of the p21 N terminus (magenta) with PCNA (green). (B) Interactions of the conserved Tyr151 of p21 with Thr131 of AfumPCNA. Shown is a superimposition of each PCNA subunit (differentiated by color: cyan, green, and magenta) bound to p21. (C) Surface representation of AfumPCNA (green) bound to p21 (magenta sticks). (D) Surface representation of hPCNA (yellow) [44] bound to p21 (magenta) (PDB: 1AXC). (E) Interactions of the C terminus of p21 (magenta) with AfumPCNA (green).

molecular dynamics simulations to uncover fundamental structural differences in the AfumPCNA surface that can account for these differences in affinity. Our MD revealed differences in the IDCL of AfumPCNA that likely contribute to this difference in affinity, including residues Asp29, His125, Asp123, and Thr131.

Previous studies focusing on human PCNA have suggested that a key factor for determining the affinity of a protein for PCNA is the primary sequence of its PIP-box [55,59]. Therefore, further investigation into native partners of *A. fumigatus* PCNA, with a

focus on their PIP-box sequences, could uncover determinants of high-affinity binding. It has also been suggested that, evolutionarily speaking, natural PCNA-interacting proteins are not optimized for high affinity, but rather that affinity is finely tuned to allow for rapid and appropriate exchange of partners to allow the cell to adapt promptly to changing environmental conditions [55,60]. This affords the possibility that artificial PIP-box sequences could be designed that have a greater affinity for PCNA than the highest affinity native PIP-box-containing proteins. Indeed, using the p21 PIP-box sequence to

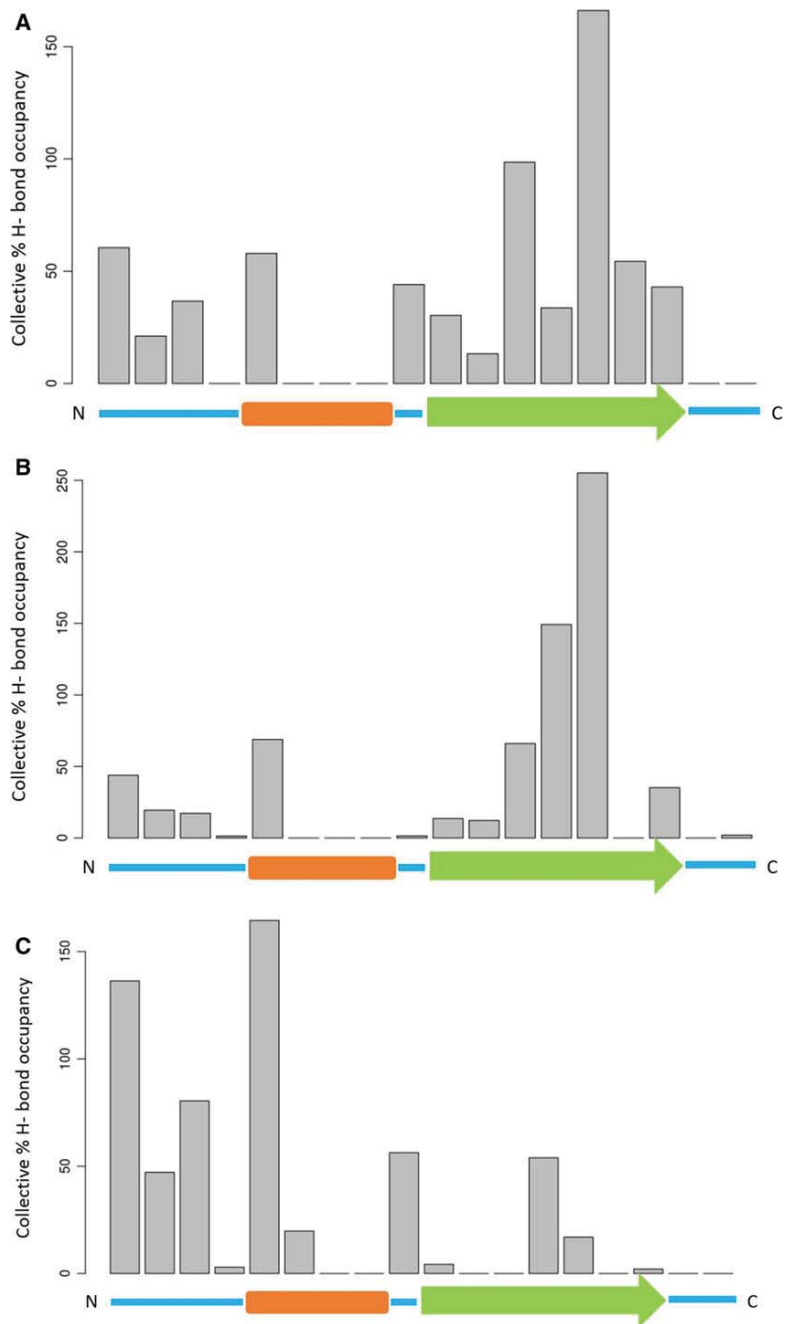


Fig. 11. Frequency of intermolecular hydrogen bonds between residues of the p21 peptide and AfumPCNA during the MD trajectory. 'Collective % H-bond occupancy' (y-axis) denotes the proportion of time that a hydrogen bond exists between a specific p21 peptide residue and PCNA over the course of the MD simulation. Note that this value may be > 100% if there are multiple hydrogen bond donors or acceptors implicated in either the peptide residue or PCNA. (A) Hydrogen bonds of subunit A. (B) Hydrogen bonds of subunit B. (C) Hydrogen bonds of subunit C.

guide the design of high-affinity peptide mimetics that target hPCNA for the treatment of cancer is the subject of ongoing investigation. In the same way, we expect that the details of the PCNA–peptide interaction interface presented in the current study will be useful for guiding the synthesis of high-affinity peptides which could, in turn, guide the design of stable,

high-affinity peptide mimetics that bind tightly to AfumPCNA, halting DNA replication, thereby preventing fungal cell growth. In addition, the differences between the peptide interaction surfaces of hPCNA and AfumPCNA highlighted here may afford specificity of antifungal peptides toward the fungal PCNA over its human homolog.

Materials and methods

Protein expression and purification

The AfumPCNA coding sequence was PCR amplified from *A. fumigatus* strain af293 cDNA using primers (a) 5'-CCC GGGCATATGTTGGAAGCAGACTAG-3' and (b) 5'-GG GCCCGGATCCTTACTCCTCATCTCCGATC-3' and cloned into the pMCSG19 vector using BamHI and NdeI restriction sites. Sequencing revealed that the sequence coding for AfumPCNA included 117 extra nucleotides at the 5' end when compared to the sequence deposited in the NCBI database (Accession [XM_745146](#)) [61] but was identical to the ORF sequence available at [www.aspergillusgenome.org](#) (afu1g04900) (accessed 23 May 2016), indicating an error in the original annotation. AfumPCNA was overexpressed in *Escherichia coli* BL21(DE3) shake-flask culture by the addition of 0.5 mM IPTG when the culture reached log-phase, and incubated at 16 °C for approximately 18 h. Cell pellets were resuspended in 20 mM Tris pH 7.5, 20 mM NaCl, 0.5 mM EDTA, 2 mM DTT, and stored at -80 °C until required.

Cells were lysed by high-pressure disruption and insoluble debris was removed by centrifugation before purification of the protein from the crude lysate, as follows. Lysate was loaded onto a 5 mL Unosphere Q column (Bio-Rad, Hercules, CA, USA) and eluted using a linear NaCl gradient (20 to 700 mM). Fractions containing AfumPCNA were pooled and brought up to 1.5M (NH₄)₂SO₄ by the dropwise addition of 3 M (NH₄)₂SO₄ before incubating overnight at 4 °C with gentle stirring. Precipitate was then cleared by centrifugation; supernatant was loaded onto a 5 mL HiTrap Phenyl FF column (GE) and eluted using a reverse linear salt gradient (1.5 to 0M (NH₄)₂SO₄, 20 to 0 mM NaCl). AfumPCNA fractions were pooled and dialyzed with 20 mM Tris pH 7.5, 50 mM NaCl, and 2 mM DTT overnight at 4 °C. Dialyzed protein was concentrated to 10 mL and passed through a HiPrep Sephacryl 26/60 S-300 column (GE) equilibrated in 20 mM Tris pH 7.5, 50 mM NaCl, and 2 mM DTT. AfumPCNA fractions were then pooled and dialyzed against 20 mM Tris pH 7.5, 20 mM NaCl, and 2 mM DTT overnight at 4 °C. Dialyzed protein was loaded onto a 1 mL Enrich Q column (Bio-Rad) and eluted using a linear NaCl gradient (20 to 500 mM). AfumPCNA fractions were pooled and dialyzed with 20 mM Tris pH 7.5, 2 mM DTT, and 10% glycerol overnight at 4 °C, concentrated to approximately 10 mg·mL⁻¹ and subjected to crystallization trials immediately.

Crystallization, data collection, and structure determination

Protein crystallization was carried out by vapor diffusion in sitting-drop format at 16 °C. Crystals grew as small plates in 0.2 M KCl, 20% PEG 3350, and diffracted X-rays to

2.6 Å using the MX-1 beamline at the Australian Synchrotron [62]. Data were collected at 100 K using 1° oscillations at a wavelength of 0.9537 Å. The AfumPCNA data were processed in space group P2₁ using iMosflm and solved by molecular replacement using phaserMR [63] with a homology model built using chainsaw [23]. The *Litopenaeus vannamei* PCNA crystal structure (PDB: [4CS5](#)) [64] was used as a template for the homology model. The structure was refined by iterations of manual rebuilding using Coot [65] and refinement using phenix.refine [66]. Groups for TLS parameterization [67] were defined automatically using phenix.refine and used for refinement as this improved refinement statistics. For the final rounds of refinement, NCS restraints were imposed along with optimization of X-ray/stereochemistry weight to improve the stereochemistry of the final model. The final rebuild was performed using a feature-enhanced map (FEM) generated using phenix [68]. The final structure contained 0.66% Ramachandran outliers with 99.34% of the residues contained in the most favored and allowed regions. Coordinates were deposited in the PDB, accession code [5TUP](#).

P21 peptide binding assay using fluorescence polarization

Fluorescence polarization assays were carried out on a PerkinElmer Victor X5 2030 Multilabel Reader, using 100 nM N-terminally FITC-labeled human P21 peptide (N-139 GRKRRQTSMTDFYHSKRRLIFS 160-C) as the labeled ligand, and increasing concentrations of AfumPCNA (0.2–26 μM). Experiments were performed at room temperature, in either buffer 1: 20 mM Tris (pH 7.5) with 10% glycerol, or buffer 2: phosphate-buffered saline (137 mM NaCl, 2.7 mM KCl, 1.5 mM KH₂PO₄, 8.1 mM Na₂HPO₄, pH 7.4). Each buffer also contained 2 mM DTT, 0.01% triton, 1 mM EDTA, and 1xCOMPLETE protease inhibitors.

Data were fit to the following equation:

$$\Delta FP = FP_{\max} * \frac{(L_T + K_d + R_T)}{\sqrt{(L_T + K_d + R_T)^2 - 4L_T R_T}} - \frac{4L_T R_T}{2L_T}$$

where ΔFP is the measured change in fluorescence polarization, FP_{max} is the maximum change in polarization of the labeled ligand upon saturation, L_T is the ligand concentration, R_T is the protein concentration, and K_d is the dissociation constant for the interaction. Each experiment consisted of triplicate samples, and experiments were repeated three times to obtain a mean K_d value, and standard deviation.

Molecular dynamics simulations

The p21 peptide was docked onto the AfumPCNA-binding surface of one subunit using the ICMPro (Molsoft) software

suite [69]. The trimeric complex of AfumPCNA–p21 was constructed using hPCNA as a guide after aligning individual AfumPCNA–p21 complexes with the hPCNA trimer. Molecular dynamics simulation of p21 peptide bound to the AfumPCNA was conducted using NAMD 2.9 [70]. PCNA and peptide complex was parameterized with the CHARMM27 force field [71] and solvated using the solvate plugin of VMD [72]. After neutralization, 150 mM NaCl was added to the solvated system using the autoionize plugin of VMD. Prior to the simulation, the system was equilibrated to NPT ensemble for a period of 2 ns. Then the production simulation was carried out for a period of 50 ns. During the simulation, a 12 Å cutoff was used for nonbonded short-range interactions, and long-range electrostatics were treated with the particle-mesh Ewald method [73]. Temperature and pressure were maintained at 310K and 101.3 kPa using Langevin thermostat and the Langevin piston. The time step used was 1 fs. Trajectories were saved at every 20 ps. Data analysis and the visualization of the simulation were carried out by the VISUAL MOLECULAR DYNAMICS package [72].

Acknowledgements

We thank La Trobe University Comprehensive Protein Platform for providing infrastructure and expertise. We thank the beamline scientists of the Australian Synchrotron for help with data collection. The Australian Synchrotron CAP8221 in part funded this work.

Author contributions

AJK performed gene cloning, purification guidance, and helped prepare manuscript. ACM performed protein purification and crystallization, data processing, structure solution, and prepared figures and manuscript. KG and LM helped purify protein and crystallization trials. K LW performed binding studies, and assisted with manuscript preparation. HR carried out MD simulations. JBB conceived and managed project, and helped with data processing, structure solution, and preparation of manuscript and figures.

References

- Bitar D, Lortholary O, Le Strat Y, Nicolau J, Coignard B, Tattevin P, Che D & Dromer F (2014) Population-based analysis of invasive fungal infections, France, 2001–2010. *Emerg Infect Dis* **20**, 1149–1155.
- McNeil MM, Nash SL, Hajjeh RA, Phelan MA, Conn LA, Plikaytis BD & Warnock DW (2001) Trends in mortality due to invasive mycotic diseases in the United States, 1980–1997. *Clin Infect Dis* **33**, 641–647.
- Yoon HJ, Choi HY, Kim YK, Song YJ & Ki M (2014) Prevalence of fungal infections using National Health Insurance data from 2009–2013, South Korea. *Epidemiol Health* **36**, e2014017.
- Steinbach WJ (2013) Are we there yet? Recent progress in the molecular diagnosis and novel antifungal targeting of *Aspergillus fumigatus* and invasive aspergillosis. *PLoS Pathog* **9**, e1003642.
- Ben-Ami R, Lewis RE & Kontoyiannis DP (2010) Enemy of the (immunosuppressed) state: an update on the pathogenesis of *Aspergillus fumigatus* infection. *Br J Haematol* **150**, 406–417.
- Sugui JA, Kwon-Chung KJ, Juvvadi PR, Latge JP & Steinbach WJ (2015) *Aspergillus fumigatus* and related species. *Cold Spring Harb Perspect Med* **5**, a019786.
- Latge JP (1999) *Aspergillus fumigatus* and aspergillosis. *Clin Microbiol Rev* **12**, 310–350.
- Mullins J, Harvey R & Seaton A (1976) Sources and incidence of airborne *Aspergillus fumigatus* (Fres). *Clin Allergy* **6**, 209–217.
- Hospenthal DR, Kwon-Chung KJ & Bennett JE (1998) Concentrations of airborne *Aspergillus* compared to the incidence of invasive aspergillosis: lack of correlation. *Med Mycol* **36**, 165–168.
- McCormick A, Loeffler J & Ebel F (2010) *Aspergillus fumigatus*: contours of an opportunistic human pathogen. *Cell Microbiol* **12**, 1535–1543.
- Gallien S, Fournier S, Porcher R, Bottero J, Ribaud P, Sulahian A, Socie G & Molina JM (2008) Therapeutic outcome and prognostic factors of invasive aspergillosis in an infectious disease department: a review of 34 cases. *Infection* **36**, 533–538.
- Patterson TF, Thompson GR 3rd, Denning DW, Fishman JA, Hadley S, Herbrecht R, Kontoyiannis DP, Marr KA, Morrison VA, Nguyen MH *et al.* (2016) Practice guidelines for the diagnosis and management of Aspergillosis: 2016 Update by the Infectious Diseases Society of America. *Clin Infect Dis* **63**, e1–60.
- Abad A, Fernandez-Molina JV, Bikandi J, Ramirez A, Margareto J, Sendino J, Hernando FL, Ponton J, Garaizar J & Rementeria A (2010) What makes *Aspergillus fumigatus* a successful pathogen? Genes and molecules involved in invasive aspergillosis *Revista iberoamericana de micologia* **27**, 155–182.
- Wauters J, Baar I, Meersseman P, Meersseman W, Dams K, De Paep R, Lagrou K, Wilmer A, Jorens P & Hermans G (2012) Invasive pulmonary aspergillosis is a frequent complication of critically ill H1N1 patients: a retrospective study. *Intensive Care Med* **38**, 1761–1768.
- Meersseman W, Vandecasteele SJ, Wilmer A, Verbeken E, Peetermans WE & Van Wijngaerden E (2004) Invasive aspergillosis in critically ill patients without malignancy. *Am J Respir Crit Care Med* **170**, 621–625.
- Chen CH, Ho C, Liu HC, Tsung TT & Hung TT (2011) Spontaneous empyema necessitatis caused by

- Aspergillus fumigatus* in an immunocompetent patient. *JRSM Short Rep* **2**, 25.
- 17 Siddiqui K, Douglas M, Carey M & Benamer H (2008) A case of invasive aspergillosis in a patient with no identifiable immunodeficiencies. *Libyan J Med* **3**, 49–51.
 - 18 Escobar N, Ordonez SR, Wosten HA, Haas PJ, de Cock H & Haagsman HP (2016) Hide, keep quiet, and keep low: properties that make *Aspergillus fumigatus* a successful lung pathogen. *Front Microbiol* **7**, 438.
 - 19 Kontoyiannis DP, Marr KA, Park BJ, Alexander BD, Anaissie EJ, Walsh TJ, Ito J, Andes DR, Baddley JW, Brown JM *et al.* (2010) Prospective surveillance for invasive fungal infections in hematopoietic stem cell transplant recipients, 2001–2006: overview of the Transplant-Associated Infection Surveillance Network (TRANSNET) Database. *Clin Infect Dis* **50**, 1091–1100.
 - 20 Warnock DW (2007) Trends in the epidemiology of invasive fungal infections. *Nihon Ishinkin Gakkai zasshi* **48**, 1–12.
 - 21 Groll AH, Shah PM, Mentzel C, Schneider M, Just-Nuebling G & Huebner K (1996) Trends in the postmortem epidemiology of invasive fungal infections at a university hospital. *J Infect* **33**, 23–32.
 - 22 Lin SJ, Schranz J & Teutsch SM (2001) Aspergillosis case-fatality rate: systematic review of the literature. *Clin Infect Dis* **32**, 358–366.
 - 23 Walsh TJ, Anaissie EJ, Denning DW, Herbrecht R, Kontoyiannis DP, Marr KA, Morrison VA, Segal BH, Steinbach WJ, Stevens DA *et al.* (2008) Treatment of aspergillosis: clinical practice guidelines of the Infectious Diseases Society of America. *Clin Infect Dis* **46**, 327–360.
 - 24 Arthurs SK, Eid AJ, Deziel PJ, Marshall WF, Cassivi SD, Walker RC & Razonable RR (2010) The impact of invasive fungal diseases on survival after lung transplantation. *Clin Transplant* **24**, 341–348.
 - 25 Doligalski CT, Benedict K, Cleveland AA, Park B, Derado G, Pappas PG, Baddley JW, Zaas DW, Harris MT & Alexander BD (2014) Epidemiology of invasive mold infections in lung transplant recipients. *Am J Transplant* **14**, 1328–1333.
 - 26 Neofytos D, Fishman JA, Horn D, Anaissie E, Chang CH, Olyaei A, Pfaller M, Steinbach WJ, Webster KM & Marr KA (2010) Epidemiology and outcome of invasive fungal infections in solid organ transplant recipients. *Transplant Infect Dis* **12**, 220–229.
 - 27 Hadrich I, Makni F, Neji S, Abbas S, Cheikhrouhou F, Trabelsi H, Sellami H & Ayadi A (2012) Invasive aspergillosis: resistance to antifungal drugs. *Mycopathologia* **174**, 131–141.
 - 28 Chowdhry R & Marshall WL (2008) Antifungal therapies in the intensive care unit. *J Intensive Care Med* **23**, 151–158.
 - 29 Kim A, Nicolau DP & Kuti JL (2011) Hospital costs and outcomes among intravenous antifungal therapies for patients with invasive aspergillosis in the United States. *Mycoses* **54**, e301–e312.
 - 30 Albataineh MT, Sutton DA, Fothergill AW & Wiederhold NP (2016) Update from the Laboratory: clinical identification and susceptibility testing of fungi and trends in antifungal resistance. *Infect Dis Clin North Am* **30**, 13–35.
 - 31 Lelièvre L, Groh M, Angebault C, Maherault AC, Didier E & Bournoux ME (2013) Azole resistant *Aspergillus fumigatus*: an emerging problem. *Médecine et Maladies Infectieuses* **43**, 139–145.
 - 32 van der Linden JW, Snelders E, Kampinga GA, Rijnders BJ, Mattsson E, Debets-Ossenkopp YJ, Kuijper EJ, Van Tiel FH, Melchers WJ & Verweij PE (2011) Clinical implications of azole resistance in *Aspergillus fumigatus*, The Netherlands, 2007–2009. *Emerg Infect Dis* **17**, 1846–1854.
 - 33 Vermeulen E, Lagrou K & Verweij PE (2013) Azole resistance in *Aspergillus fumigatus*: a growing public health concern. *Curr Opin Infect Dis* **26**, 493–500.
 - 34 Verweij PE, Chowdhary A, Melchers WJ & Meis JF (2016) Azole resistance in *Aspergillus fumigatus*: can we retain the clinical use of mold-active antifungal azoles? *Clin Infect Dis* **62**, 362–368.
 - 35 Lamoth F (2016) *Aspergillus fumigatus*-related species in clinical practice. *Front Microbiol* **7**, 683.
 - 36 Moldovan GL, Pfander B & Jentsch S (2007) PCNA, the maestro of the replication fork. *Cell* **129**, 665–679.
 - 37 Krishna TS, Kong XP, Gary S, Burgers PM & Kuriyan J (1994) Crystal structure of the eukaryotic DNA polymerase processivity factor PCNA. *Cell* **79**, 1233–1243.
 - 38 Maga G & Hubscher U (2003) Proliferating cell nuclear antigen (PCNA): a dancer with many partners. *J Cell Sci* **116**, 3051–3060.
 - 39 Matsumiya S, Ishino Y & Morikawa K (2001) Crystal structure of an archaeal DNA sliding clamp: proliferating cell nuclear antigen from *Pyrococcus furiosus*. *Protein Sci* **10**, 17–23.
 - 40 Shamoo Y & Steitz TA (1999) Building a replisome from interacting pieces: sliding clamp complexed to a peptide from DNA polymerase and a polymerase editing complex. *Cell* **99**, 155–166.
 - 41 Warbrick E, Lane DP, Glover DM & Cox LS (1995) A small peptide inhibitor of DNA replication defines the site of interaction between the cyclin-dependent kinase inhibitor p21WAF1 and proliferating cell nuclear antigen. *Current Biol* **5**, 275–282.
 - 42 De Biasio A & Blanco FJ (2013) Proliferating cell nuclear antigen structure and interactions: too many partners for one dancer? *Advances Protein Chem Struct Biol* **91**, 1–36.
 - 43 Freudenthal BD, Gakhar L, Ramaswamy S & Washington MT (2010) Structure of monoubiquitinated PCNA and implications for translesion synthesis and

- DNA polymerase exchange. *Nat Struct Mol Biol* **17**, 479–484.
- 44 Gulbis JM, Kelman Z, Hurwitz J, O'Donnell M & Kuriyan J (1996) Structure of the C-terminal region of p21(WAF1/CIP1) complexed with human PCNA. *Cell* **87**, 297–306.
- 45 Wolff P, Olieric V, Briand JP, Chaloin O, Dejaegere A, Dumas P, Ennifar E, Guichard G, Wagner J & Burnouf DY (2011) Structure-based design of short peptide ligands binding onto the *E. coli* processivity ring. *J Med Chem* **54**, 4627–4637.
- 46 PUNCHIHewa C, Inoue A, Hishiki A, Fujikawa Y, Connelly M, Evison B, Shao Y, Heath R, Kuraoka I, Rodrigues P *et al.* (2012) Identification of small molecule proliferating cell nuclear antigen (PCNA) inhibitor that disrupts interactions with PIP-box proteins and inhibits DNA replication. *J Biol Chem* **287**, 14289–14300.
- 47 Georgescu RE, Yurieva O, Kim SS, Kuriyan J, Kong XP & O'Donnell M (2008) Structure of a small-molecule inhibitor of a DNA polymerase sliding clamp. *Proc Natl Acad Sci USA* **105**, 11116–11121.
- 48 Yin Z, Wang Y, Whittell LR, Jergic S, Liu M, Harry E, Dixon NE, Kelso MJ, Beck JL & Oakley AJ (2014) DNA replication is the target for the antibacterial effects of nonsteroidal anti-inflammatory drugs. *Chem Biol* **21**, 481–487.
- 49 Yin Z, Whittell LR, Wang Y, Jergic S, Liu M, Harry EJ, Dixon NE, Beck JL, Kelso MJ & Oakley AJ (2014) Discovery of lead compounds targeting the bacterial sliding clamp using a fragment-based approach. *J Med Chem* **57**, 2799–2806.
- 50 Kling A, Lukat P, Almeida DV, Bauer A, Fontaine E, Sordello S, Zaburanyi N, Herrmann J, Wenzel SC, Konig C *et al.* (2015) Antibiotics. Targeting DnaN for tuberculosis therapy using novel griselimycins. *Science (New York, NY)* **348**, 1106–1112.
- 51 Wolff P, Amal I, Olieric V, Chaloin O, Gygli G, Ennifar E, Lorber B, Guichard G, Wagner J, Dejaegere A *et al.* (2014) Differential modes of peptide binding onto replicative sliding clamps from various bacterial origins. *J Med Chem* **57**, 7565–7576.
- 52 Wijffels G, Johnson WM, Oakley AJ, Turner K, Epa VC, Briscoe SJ, Polley M, Liepa AJ, Hofmann A, Buchardt J *et al.* (2011) Binding inhibitors of the bacterial sliding clamp by design. *J Med Chem* **54**, 4831–4838.
- 53 Kjelstrup S, Hansen PM, Thomsen LE, Hansen PR & Lobner-Olesen A (2013) Cyclic peptide inhibitors of the beta-sliding clamp in *Staphylococcus aureus*. *PLoS One* **8**, e72273.
- 54 Zamir L, Zaretsky M, Fridman Y, Ner-Gaon H, Rubin E & Aharoni A (2012) Tight coevolution of proliferating cell nuclear antigen (PCNA)-partner interaction networks in fungi leads to interspecies network incompatibility. *Proc Natl Acad Sci USA* **109**, E406–E414.
- 55 Bruning JB & Shamoo Y (2004) Structural and thermodynamic analysis of human PCNA with peptides derived from DNA polymerase-delta p66 subunit and flap endonuclease-1. *Structure* **12**, 2209–2219.
- 56 Kontopidis G, Wu SY, Zheleva DI, Taylor P, McInnes C, Lane DP, Fischer PM & Walkinshaw MD (2005) Structural and biochemical studies of human proliferating cell nuclear antigen complexes provide a rationale for cyclin association and inhibitor design. *Proc Natl Acad Sci USA* **102**, 1871–1876.
- 57 Bozza WP, Yang K, Wang J & Zhuang Z (2012) Developing peptide-based multivalent antagonists of proliferating cell nuclear antigen and a fluorescence-based PCNA binding assay. *Anal Biochem* **427**, 69–78.
- 58 Kroker AJ & Bruning JB (2015) p21 exploits residue Tyr151 as a tether for high-affinity PCNA binding. *Biochemistry* **54**, 3483–3493.
- 59 De Biasio A, Campos-Olivas R, Sanchez R, Lopez-Alonso JP, Pantoja-Uceda D, Merino N, Villate M, Martin-Garcia JM, Castillo F, Luque I *et al.* (2012) Proliferating cell nuclear antigen (PCNA) interactions in solution studied by NMR. *PLoS One* **7**, e48390.
- 60 Fridman Y, Gur E, Fleishman SJ & Aharoni A (2013) Computational protein design suggests that human PCNA-partner interactions are not optimized for affinity. *Proteins* **81**, 341–348.
- 61 Nierman WC, Pain A, Anderson MJ, Wortman JR, Kim HS, Arroyo J, Berriman M, Abe K, Archer DB, Bermejo C *et al.* (2005) Genomic sequence of the pathogenic and allergenic filamentous fungus *Aspergillus fumigatus*. *Nature* **438**, 1151–1156.
- 62 McPhillips TM, McPhillips SE, Chiu HJ, Cohen AE, Deacon AM, Ellis PJ, Garman E, Gonzalez A, Sauter NK, Phizackerley RP *et al.* (2002) Blu-Ice and the Distributed Control System: software for data acquisition and instrument control at macromolecular crystallography beamlines. *J Synchrotron Radiat* **9**, 401–406.
- 63 McCoy AJ, Grosse-Kunstleve RW, Adams PD, Winn MD, Storoni LC & Read RJ (2007) Phaser crystallographic software. *J Appl Crystallogr* **40**, 658–674.
- 64 Carrasco-Miranda JS, Lopez-Zavala AA, Arvizu-Flores AA, Garcia-Orozco KD, Stojanoff V, Rudino-Pinera E, Briebe LG & Sotelo-Mundo RR (2014) Crystal structure of the shrimp proliferating cell nuclear antigen: structural complementarity with WSSV DNA polymerase PIP-box. *PLoS One* **9**, e94369.
- 65 Emsley P & Cowtan K (2004) Coot: model-building tools for molecular graphics. *Acta Crystallogr D Biol Crystallogr* **60**, 2126–2132.
- 66 Afonine PV, Grosse-Kunstleve RW, Echols N, Headd JJ, Moriarty NW, Mustyakimov M, Terwilliger TC,

- 1 Urzhumtsev A, Zwart PH & Adams PD (2012)
2 Towards automated crystallographic structure
3 refinement with phenix.refine. *Acta Crystallogr D Biol*
4 *Crystallogr* **68**, 352–367.
- 5 67 Winn MD, Isupov MN & Murshudov GN (2001) Use
6 of TLS parameters to model anisotropic displacements
7 in macromolecular refinement. *Acta Crystallogr D Biol*
8 *Crystallogr* **57**, 122–133.
- 9 68 Afonine PV, Moriarty NW, Mustyakimov M, Sobolev
10 OV, Terwilliger TC, Turk D, Urzhumtsev A & Adams
11 PD (2015) FEM: feature-enhanced map. *Acta*
12 *Crystallogr D Biol Crystallogr* **71**, 646–666.
- 13 69 Abagyan R & Totrov M (1994) Biased probability
14 Monte Carlo conformational searches and electrostatic
15 calculations for peptides and proteins. *J Mol Biol* **235**,
16 983–1002.
- 17 70 Phillips JC, Braun R, Wang W, Gumbart J,
18 Tajkhorshid E, Villa E, Chipot C, Skeel RD, Kale L &
19 Schulten K (2005) Scalable molecular dynamics with
20 NAMD. *J Comput Chem* **26**, 1781–1802.
- 21 71 MacKerell AD, Bashford D, Bellott M, Dunbrack RL,
22 Evanseck JD, Field MJ, Fischer S, Gao J, Guo H, Ha
23 S *et al.* (1998) All-atom empirical potential for
24 molecular modeling and dynamics studies of proteins.
25 *J Phys Chem B* **102**, 3586–3616.
- 26 72 Humphrey W, Dalke A & Schulten K (1996)
27 VMD: visual molecular dynamics. *J Mol Graph* **14**,
28 27–28.
- 29 73 Darden TA & Pedersen LG (1993) Molecular
30 modeling: an experimental tool. *Environ Health*
31 *Perspect* **101**, 410–412.

Supporting information

Additional Supporting Information may be found online in the supporting information tab for this article:

Movie S1. 50 ns molecular dynamics simulation of AfumPCNA with p21 PIP-box with camera view adjacent to PIP-box-binding surface.

Movie S2. 50 ns molecular dynamics simulation of AfumPCNA with p21 PIP-box with camera view adjacent to central DNA cavity.

Chapter 6 (Manuscript Submitted):

Aspergillus fumigatus Thioredoxin

Reductase: Structure, Mechanism, and
Inhibition

Statement of Authorship

Title of Paper	Aspergillus fumigatus thioredoxin reductase: structure, mechanism and inhibition	
Publication Status	<input type="checkbox"/> Published <input checked="" type="checkbox"/> Submitted for Publication	<input type="checkbox"/> Accepted for Publication <input type="checkbox"/> Unpublished and Unsubmitted work written in manuscript style
Publication Details	Andrew C. Marshall, Mohammed A. Hossain, Georgia Arentz, Peter Hoffman, Bryan R. Coad, and John B. Bruning. (submitted)	

Principal Author

Name of Principal Author (Candidate)	Andrew C. Marshall	
Contribution to the Paper	Performed purification of proteins, enzymology, X-ray data collection, processing, structure solution and interpretation, <i>in silico</i> molecular docking experiments, and manuscript preparation.	
Overall percentage (%)	80	
Certification:	This paper reports on original research I conducted during the period of my Higher Degree by Research candidature and is not subject to any obligations or contractual agreements with a third party that would constrain its inclusion in this thesis. I am the primary author of this paper.	
Signature		Date 12/12/17

Co-Author Contributions

By signing the Statement of Authorship, each author certifies that:

- i. the candidate's stated contribution to the publication is accurate (as detailed above);
- ii. permission is granted for the candidate to include the publication in the thesis; and
- iii. the sum of all co-author contributions is equal to 100% less the candidate's stated contribution.

Name of Co-Author	Mohammed A. Hossain	
Contribution to the Paper	Microbiology, antifungal susceptibility testing.	
Signature		Date 11/11/2018

Name of Co-Author	Georgia Arentz	
Contribution to the Paper	Performed mass spectrometry and assisted with data interpretation.	
Signature		Date 11/12/2017

Name of Co-Author	Peter Hoffman		
Contribution to the Paper	Assisted with mass spectrometry data interpretation.		
Signature		Date	17/1/2018

Name of Co-Author	Bryan R. Coad		
Contribution to the Paper	Antifungal susceptibility testing, data interpretation, manuscript preparation.		
Signature		Date	11/12/2017

Name of Co-Author	John B. Bruning		
Contribution to the Paper	Crystallography, management of project, manuscript preparation, and intellectual contribution. Corresponding author.		
Signature		Date	12-12-2017

Aspergillus fumigatus thioredoxin reductase: structure, mechanism, and inhibition

Andrew C. Marshall¹, Mohammed A. Hossain², Georgia Arentz⁴, Peter Hoffmann⁴, Bryan R. Coad^{2,3}, and John B. Bruning^{1,*}

¹ Institute for Photonics and Advanced Sensing (IPAS), School of Biological Sciences, The University of Adelaide, Adelaide, South Australia 5005, Australia.

² Future Industries Institute, University of South Australia, Mawson Lakes, South Australia, Australia.

³ School of Agriculture, Food & Wine, The University of Adelaide, Adelaide, South Australia 5005.

⁴ Adelaide Proteomics Centre, School of Biological Sciences, University of Adelaide, Adelaide, SA, Australia; Institute for Photonics and Advanced Sensing (IPAS), University of Adelaide, Adelaide, SA, Australia

*To whom correspondence should be addressed. John B. Bruning, School of Biological Sciences, Adelaide, South Australia, Australia, Tel.: +61 (08) 8313-5218; Fax: +61 (08) 8313-4362; E-mail: john.bruning@adelaide.edu.au

ABSTRACT: *Aspergillus fumigatus* infections are associated with high mortality rates and high treatment costs. Limitations of available antifungals and increasing antifungal resistance highlight the need for new antifungals. Thioredoxin reductase (TrxR) is essential for maintaining redox homeostasis and presents as a promising target for novel antifungals. We show that ebselen (2-phenyl-1,2-benzoselenazol-3(2H)-one) is a potent inhibitor of *A. fumigatus* TrxR ($K_i = 0.22 \mu\text{M}$) and inhibits growth of the fungus with an MIC of 1-2 $\mu\text{g/mL}$. Mass spectrometry analysis demonstrates that ebselen interacts covalently with a catalytic cysteine of TrxR, Cys148. We also present the X-ray crystal structure of *A. fumigatus* TrxR, and use *in silico* modeling of the enzyme-inhibitor complex to outline key molecular interactions, providing a scaffold for future design of specific and potent anti-*Aspergillus* drugs that target TrxR.

In recent years, considerable progress in the areas of cancer treatment and transplantation, with a concomitant rise in the number of immunocompromised patients, has been accompanied by an increased incidence of invasive fungal infections (2-5). The main contributors are *Candida* spp. and *Aspergillus* spp., with a recent trend towards the latter as the most common cause of invasive fungal infection (6, 7). *Aspergillus fumigatus* is one of the most prevalent airborne fungal species in the environment; spores are ubiquitous and constantly inhaled by humans (2). Normally spores are cleared easily by the innate immune system; however, in the case of an immunocompromised host they can germinate and cause infection (8). *A. fumigatus* is by far the most common etiologic agent of invasive aspergillosis (IA), frequently causing life-threatening infections in immunocompromised patients such as transplant recipients, those with hematological malignancies, particularly acute leukemia, and AIDS patients (2, 3, 9). IA is now the main contributor to mortality due to lung infection in bone-marrow transplant patients (10). *A. fumigatus* infection is difficult to diagnose early and accurately, and knowledge of the details of its growth, host-interactions and pathogenesis is lacking. In addition, the number of antifungals effective against it is limited and resistance is on the rise (11-14).

There are three classes of antifungals used to treat *A. fumigatus* infections: azoles, polyenes and echinocandins, all targeting components of the cell wall or cell membrane (15). All three drug classes are associated with significant side-effects (11). Amphotericin B, a polyene, has been used to treat IA for over four decades, but has been largely superseded by azole antifungals due its poor side-effect profile (11, 16). In particular, acute renal failure associated with amphotericin B treatment has contributed to longer hospital stays and higher mortality rates (17). Current practice guidelines by the Infectious Diseases Society of America for the management of IA recommend the azole drugs voriconazole and posaconazole for first-line treatment and prophylaxis, respectively, in most cases (18). Despite being the preferred therapeutic option, azoles are also associated with serious side-effects, such as hepatotoxicity, visual disturbances, rash, photosensitivity, psychosis and prolonged QT interval – and are susceptible to a number of clinically significant drug-drug interactions involving cytochrome P450 metabolism (11, 15, 16, 19). Most alarming is the emergence of resistance to azole antifungals.

Azole-resistant *A. fumigatus* isolates have now been reported worldwide and have been correlated with treatment failure and high mortality rates (50 to 100%) (14). Ongoing monitoring in the Netherlands has shown a rapid increase in the prevalence of azole-resistant *A. fumigatus*, with the first examples emerging in 2000, growing to a prevalence of 10.1% in 2010 (20, 21). A more recent survey of 16 Dutch hospitals reported azole resistance rates of 5 to 10%, with rates up to 30% in particular hematology wards (22). Similarly, a UK study of clinical *A. fumigatus* isolates spanning 1997 to 2007 reported a rapid rise in the frequency of resistance to azoles after 2004; up to 17% in 2007 (23). This rapid emergence in resistance to the main class of drugs used to treat *Aspergillus* infections, increasing incidence of infection, and limitations of currently available antifungals, all highlight the need for the development of new antifungals with novel targets. This requires a detailed knowledge of the basic biology of the organism and the intracellular systems that are essential for its growth and survival in the human host. One such system is the maintenance of intracellular redox homeostasis.

The two main antioxidant systems that are responsible for maintaining cellular redox homeostasis, the glutathione (GSH) and thioredoxin (Trx) systems, are essential for cellular viability (24, 25). The Trx system is present in all domains of life and has a diverse range of functions including: maintaining the intracellular environment in a reducing state to prevent protein aggregation or inactivation due to the formation of deleterious disulfide bonds, acting as an electron donor for various biosynthetic enzymes (for example, ribonucleotide reductase; responsible for production of deoxyribonucleotides for DNA synthesis (26)) or enzymes that catalyze the reduction of reactive oxygen species, the redox regulation of many transcription factors, and allowing correct insertion of native disulfide bonds in proteins entering the endoplasmic reticulum (27-29). These functions are mediated by Trx, a small single domain protein with two adjacent redox-active cysteines that provide the electrons required for reduction of substrate (30, 31). The reducing activity of Trx is dependent on Trx reductase (TrxR), which catalyzes the transfer of electrons from NADPH to the redox active dithiol of Trx (30) (**Fig. 1a**). TrxRs (EC 1.8.1.9) are dimeric flavoenzymes and can be divided into two broad classes: high molecular weight (MW) TrxR and low MW TrxR (28).

High MW TrxRs are present in animals and have a typical subunit MW >55 kDa. In addition to endogenous Trx, mammalian TrxR can efficiently reduce a range of substrates including Trxs from other species, a number of other disulfide and selenocysteine-containing proteins,

and also a variety of small molecules such as peroxides, selenite, selenodiglutathione, vitamin K and 5,5'-dithiobis(2-nitrobenzoic acid) (DTNB) (32). They are structurally homologous to glutathione reductases, with a similar arrangement of FAD and NADPH binding domains, but with an additional flexible C-terminal extension containing a redox-active cysteine-selenocysteine pair (33, 34). The increased reactivity of this selenocysteine at the active site is believed to confer the higher substrate promiscuity of high MW TrxR as compared to low MW TrxR (35).

Low MW TrxRs are present in prokaryotes, plants and fungi and show specificity for their endogenous Trx substrate (36-38), with an overall structure and molecular mechanism that differs considerably from high MW TrxRs. A single subunit is typically 35-40 kDa and is composed of an NADPH domain, a FAD domain, and a CA[T/V]C active site contained within the NADPH domain (39). These active-site cysteine residues provide the redox-active dithiol from which reducing equivalents are transferred to Trx in a thiol-disulfide

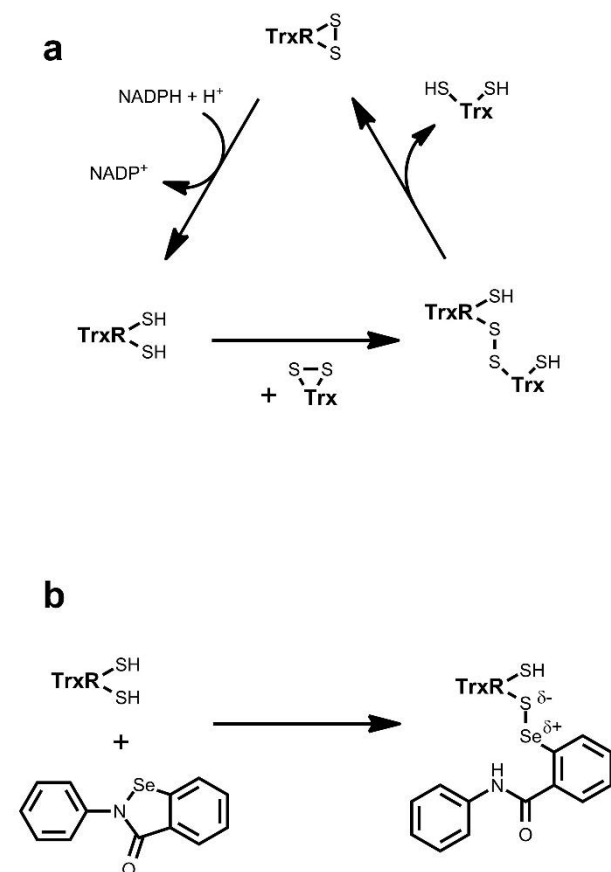


Figure 1 | TrxR reaction mechanism and inhibition by EbSe. (a) TrxR catalyzes the NADPH-dependent reduction of Trx via a dithiol-exchange reaction. (b) Proposed mechanism by which EbSe (bottom left) inhibits low MW TrxR (1).

exchange reaction (40). Two distinct enzyme conformations are required to complete the catalytic cycle, referred to as flavin-oxidizing (FO) or flavin-reducing (FR) conformations (40, 41). A 66° rotation of the NADPH domain relative to the FAD domain is required to alternate between these two conformations (40, 41). In the FR conformation, the bound NADPH molecule is aligned with the embedded FAD cofactor to allow for electron transfer from its nicotinamide group to the flavin group (41). Concurrently, the active site dithiol is exposed to allow for reduction of Trx. In the FO conformation, the flavin group is aligned with the active site to allow reduction of the disulfide to regenerate the active site dithiol (39, 40).

The central role of the Trx system in cellular redox homeostasis, anti-oxidant defense and DNA synthesis has led to the investigation of TrxR as a target for antimicrobials (1, 42-44) as well as drugs for the treatment of cancer (45, 46) and rheumatoid arthritis (47). In addition, the differing structures and molecular mechanisms of high and low MW TrxRs affords the possibility of selectively inhibiting the Trx system of bacterial and fungal pathogens over the human system (1). In fungi, the essential role of TrxR (low MW) has been shown by genetic studies (37, 48-50). The *Saccharomyces cerevisiae* genome contains two TrxR genes, *TRR1* and *TRR2*, encoding for cytosolic and mitochondrial enzymes, respectively (51). Disruption of *TRR1* results in poor viability, hypersensitivity to H₂O₂, methionine auxotrophy, and growth that is slow and temperature-sensitive (49, 50). Similarly, a *TRR2* knockout strain was twice as sensitive to oxidative stress caused by H₂O₂ exposure than wildtype (37). More significantly, a conditional mutant strain of *A. fumigatus* in which *TRR1* expression was repressed exhibited a severe growth defect under normal growth conditions (48), presenting TrxR as a potential target for novel antifungals.

Ebselen (2-phenyl-1,2-benzoselenazol-3(2H)-one; EbSe), a small selenium-containing redox active molecule (**Fig. 1b**), has shown potential as a drug that can target TrxR (1). In humans, EbSe has antioxidant, anti-inflammatory and cytoprotective properties, and a favorable toxicological profile, and is being investigated for the treatment of a range of clinical presentations including stroke (52), bipolar disorder (53), type II diabetes (54), osteoporosis (55) and noise-induced hearing loss (56). In contrast, EbSe has been shown to have antimicrobial activity against a range of bacterial and yeast pathogens (57-60), and is a potent inhibitor of *E. coli* TrxR *in vitro* (1).

Here, we show that EbSe is a nanomolar inhibitor of *A. fumigatus* TrxR (*Af*TrxR), and verified that EbSe has potent antifungal activity against *A. fumigatus* in culture. Inhibition of TrxR is mediated via formation of a covalent complex with a specific active-site cysteine. We also present the crystal structure of *Af*TrxR at 3.2 Å and have used this structural information, along with MS/MS data confirming the EbSe-TrxR interaction, to inform molecular modeling of the protein-inhibitor complex *in silico*, providing further insight into the specific mechanism of inhibition.

RESULTS

AfTrxR enzyme kinetics and inhibition by ebselen. Recombinant AfTrxR, purified to homogeneity, was assessed for its ability to reduce *A. fumigatus* Trx (AfTrx) using the DTNB assay, essentially as described (30, 32, 36, 61). The kinetic parameters of AfTrxR were determined to be comparable to those of low MW TrxRs from other species, with an apparent K_M for AfTrx of $1.2 \pm 0.1 \mu\text{M}$ and k_{cat} of $8.6 \pm 0.2 \text{ sec}^{-1}$ (Table 1). Others have shown that EbSe is a potent inhibitor of *E. coli* TrxR *in vitro*, with a K_i of $0.52 \pm 0.13 \mu\text{M}$ (1). Upon addition of EbSe to our assay, we also observed a significant decrease in AfTrxR activity. At concentrations of EbSe from zero to $0.90 \mu\text{M}$, the data fit a standard model of competitive inhibition (Supplementary Fig. 1) and show that EbSe is an even more potent inhibitor of AfTrxR than for *E. coli* TrxR, with a K_i of $0.22 \pm 0.01 \mu\text{M}$ (Table 1). AfTrxR activity was completely abolished in the presence of $4 \mu\text{M}$ EbSe (data not shown).

Table 1. Kinetic parameters of TrxRs from *A. fumigatus*, *S. cerevisiae* and *E. coli*, with endogenous Trx as substrate. Inhibition constants for EbSe have been determined for AfTrxR and EcTrxR only.

Enzyme	K_M (μM)	k_{cat} (sec^{-1})	EbSe K_i (μM)
AfTrxR ^a	1.2 ± 0.1	8.6 ± 0.2	0.22 ± 0.01
ScTrxR	1.3^b	43.7^b	ND
EcTrxR	2.89^c	22^c	0.52 ± 0.13^d

^a Data for the current study were collected in triplicate, with uncertainty expressed as standard error. ^b Data obtained from Oliveira *et al.*, 2010 (36). ^c Prongay *et al.*, 1989 (62). ^d Lu *et al.*, 2013 (1). ND = Not determined. All data were collected using the DTNB assay under similar experimental conditions.

Ebselen interacts covalently with a catalytic cysteine. EbSe reacts with exposed cysteines to form covalent selenosulfide adducts (63, 64). This is the proposed mechanism by which EbSe inhibits bacterial TrxR, and involves the formation of a covalent bond between the Se atom and the Sy of one of the active site cysteines (1) (Fig. 1b). This is accompanied by the cleavage of the Se-N bond, resulting in the opening of the 1,2-selenazolidin-3-one ring. In contrast, EbSe is efficiently turned over by mammalian (high MW) TrxR to produce EbSe selenol (65). This incongruence can be explained by observing that for high MW TrxR, the increased reactivity of the selenocysteine at the active site results in the formation of a diselenide bond, which is non-polar and therefore attacked readily by the nucleophilic resolving cysteine, allowing for the efficient turnover of EbSe, whereas the selenosulfide bond formed between low MW TrxR and EbSe is polar with a partial negative charge on the S atom, hindering nucleophilic attack by the resolving cysteine. To investigate whether this is the mechanism of inhibition of AfTrxR by EbSe, AfTrxR was subjected to MS/MS analysis after incubation with excess EbSe. The experiment was performed for wild-type AfTrxR and two mutants, AfTrxR(C145S) and AfTrxR(C148S). Peptides covering the active site were detected for all three proteins (Fig. 2; Supplementary Figs. 2 and 3). Only one of these was modified by EbSe, AfTrxR(C145S). The MS/MS data indicate that this peptide was modified at Cys148, with a mass increase corresponding to one EbSe molecule (Fig. 2; Supplementary Fig. 2). The corresponding cysteine residue of *E. coli* TrxR (Cys138) has been shown by biochemical (66) and structural (41) studies to be the attacking thiolate on the redox-active disulfide of Trx. In addition, EbSe was shown to modify Cys138 of *E. coli* TrxR previously (1), consistent with our results.

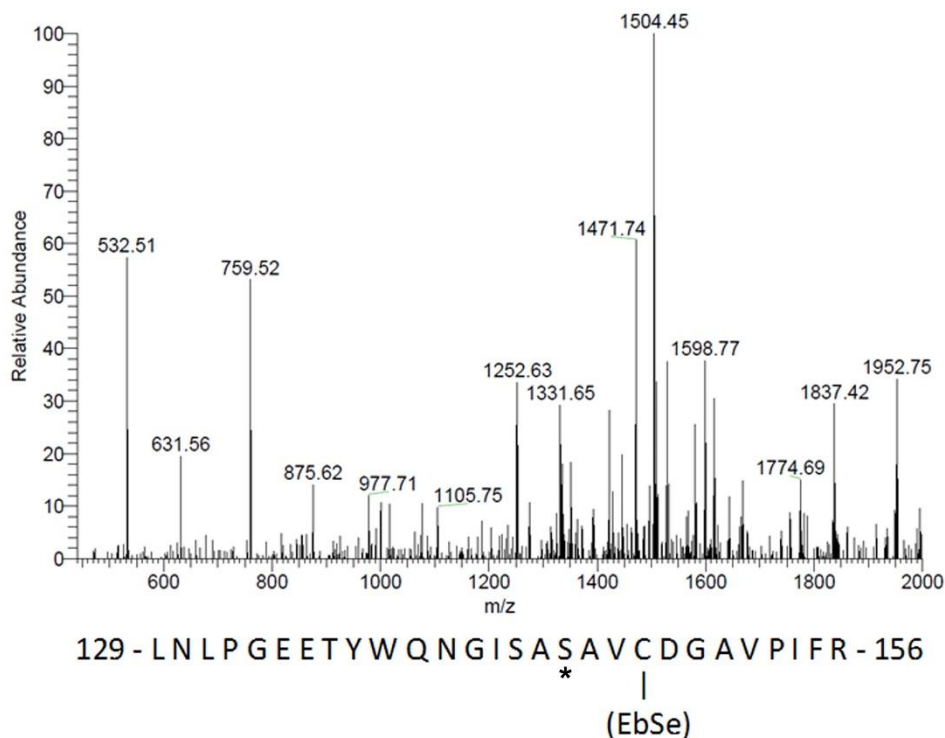


Figure 2 | MS/MS data shows that EbSe forms a covalent bond with Cys148 of *Af*TrxR. Displayed above is the MS/MS data of a peptide with m/z 1642.74 derived from *Af*TrxR(C145S) after incubation with excess EbSe. A mass shift at Cys148 equal to the addition of one EbSe molecule (MW = 274.18) confirms the formation of a covalent bond between EbSe and Cys148. The peptide sequence modified at Cys148 is shown, with the C145S mutation marked by an asterisk. Full peptide annotation along with equivalent non-modified peptides derived from *Af*TrxR wildtype, C145S and C148S proteins is provided in **Supplementary Figs. 2 and 3**.

Ebselen has potent antifungal activity against *A. fumigatus*. To assess whether the observed *in vitro* inhibition of TrxR by EbSe translates to inhibition of fungal growth, the antifungal activity of EbSe against *A. fumigatus* was determined on solid and in liquid media according to Clinical & Laboratory Standards Institute methods. In broth microdilution, EbSe inhibited growth of *A. fumigatus* with an MIC of 1-2 $\mu\text{g/mL}$, comparable to or better than that of other currently available non-azole antifungal drugs (**Table 2**). Similarly, on solid media, a clear zone of inhibition was evident that demonstrated the inhibition of *A. fumigatus* growth by EbSe (**Supplementary Fig. 4**).

Table 2. Antifungal activity of EbSe and other non-azole antifungal drugs against *A. fumigatus* (ATCC MYA 3626) by broth microdilution method after 48 hr incubation.

Compound	MIC value ($\mu\text{g/mL}$)
Ebselen	1-2
Caspofungin	0.125-1
Nystatin	4-8
Amphotericin B	4-8

Crystal Structure of *A. fumigatus* TrxR. The crystal structure of *Af*TrxR in complex with NADPH and FAD was solved in space group $P3_221$ by molecular replacement using data to a resolution of 3.2 Å. Data processing and refinement statistics are listed in **Supplementary Table 1**. The asymmetric unit contains two protein subunits, representing a head-to-tail homodimer (**Fig. 3a**). The tertiary structure of each *Af*TrxR subunit is homologous to yeast, bacteria and plant TrxRs solved previously; when superposed with *E. coli*, *S. cerevisiae* and *A. thaliana* TrxR crystal structures, the resulting RMSD values across all C α s are 2.28 Å, 0.83 Å and 1.35 Å, respectively (**Supplementary Fig. 5**). Electron density allowed model building

of residues 1 through 326 of both polypeptide chains, with the exceptions of Met1 and Gly39 of subunit A, and Ala37 through Gly43 of subunit B. The density is poor for the $\beta 2$ - $\eta 1$ loop (residues 34 to 44) relative to the rest of the structure, suggestive of flexibility in this region. This loop forms a ‘cap’ over the FAD binding pocket, shielding the adenosine rings of FAD from solvent. This FAD cap is conserved in yeast and plant TrxRs, but consists of five fewer residues in the *E. coli* TrxR (**Supplementary Fig. 6**). Its structure has been observed previously for *Entamoeba histolytica* TrxR (44), and, given its position at the Trx binding site, it is very likely to contribute to the species-specific recognition of Trx by low MW TrxRs. The C-terminal 47 residues (327 to 373) of both subunits are unstructured, representing a disordered region. The crystal lattice (not shown) contains wide solvent channels, consistent with the high solvent content and fragility of the crystals, which are probably necessary to accommodate this flexible C-terminus. Interestingly, this C-terminal extension is absent from *E. coli*, *S. cerevisiae* and *A. thaliana* TrxRs (**Supplementary Fig. 6**), and its functional significance is unknown.

Each subunit of *Af*TrxR consists of two domains: an FAD domain and an NADPH domain (**Fig. 3a**). Both domains form Rossmann folds, typical of nucleotide binding domains, with a central five-stranded parallel β -sheet sandwiched between an anti-parallel β -sheet on one side and three α -helices on the other. Regarding both dinucleotides and their respective domains, the adenosine nucleoside is positioned at the C-terminal end of the central parallel β -sheet, and

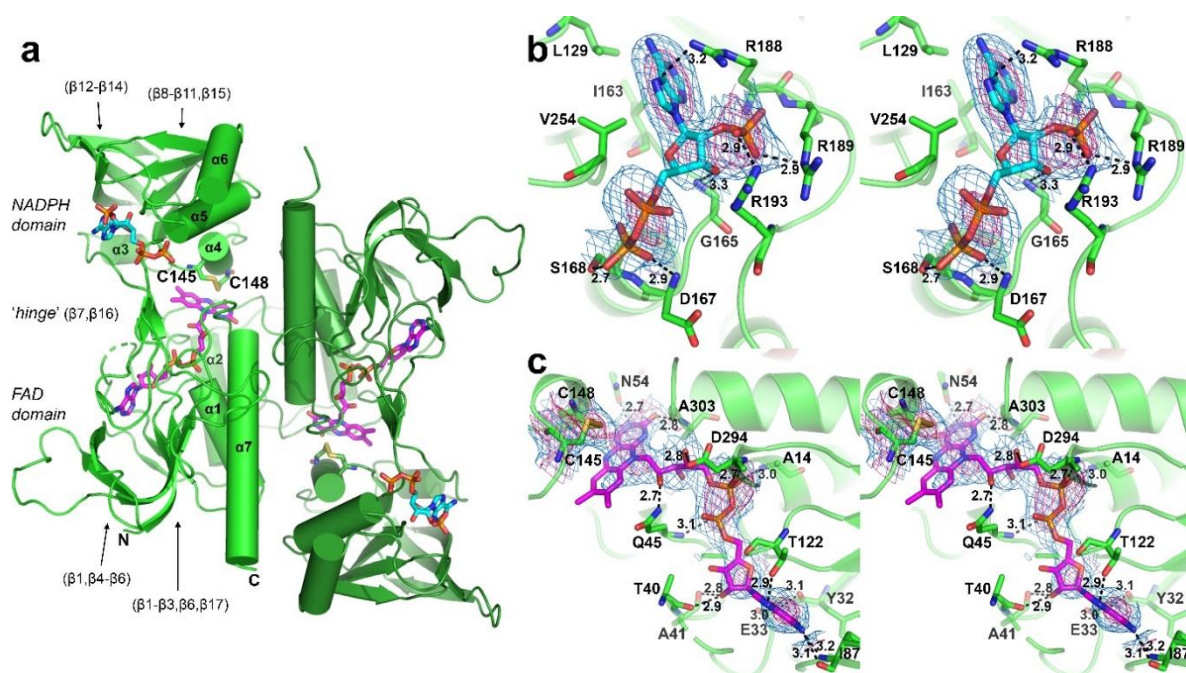


Figure 3 | Crystal structure of *Af*TrxR in flavin-oxidizing conformation at 3.2 Å. The NADPH molecule (cyan), the FAD molecule (magenta) and key residues are shown as sticks. The polypeptide backbone is shown in cartoon representation. A 2mF_o-DF_c composite omit electron density map for the bound dinucleotides and active site cysteines (Cys145 and Cys148) is contoured at 1.0 (blue mesh) and 3.0 (pink mesh) rmsd (right panels only). Lengths of hydrogen bonds (dashes) are shown in Å. (a) The *Af*TrxR homodimer. α -helices (cylinders) and β -stands (arrows) are labeled for one subunit. Each subunit (colored different shades of green) contains an NADPH domain connected to an FAD domain via a short two-stranded ‘hinge’. Each domain is composed of a central parallel β -sheet sandwiched between an antiparallel β -sheet and three α -helices (note that $\beta 1$ and $\beta 6$ contribute to both β -sheets of the FAD domain). (b) Stereo view of the adenosine of NADPH with key binding site residues. Electron density was insufficient to model the nicotinamide riboside. (c) Stereo view of the bound FAD cofactor and key residues. The flavin moiety is poised for electron transfer to the S γ atom of Cys148.

the bridging pyrophosphate is positioned at the N-terminus of the central α -helix. The two domains are connected by a short two-stranded antiparallel β -sheet that serves as the hinge, allowing the domain rotation necessary for completion of the catalytic cycle (41). The dimerization interface area is 2,096 Å², involving 34 hydrogen bonds (2.4 – 3.8 Å) and seven salt-bridges. The three α -helices (α 1, α 2 and α 7) of the FAD domain along with the η 1- α 2 loop contribute most of the residues at the dimer interface. A number of solvent molecules are present at or near the interface.

The adenosine nucleotide of NADPH, including the 3'-phosphate and bridging pyrophosphate, could be modeled in the NADPH binding site of both subunits; however, the nicotinamide riboside was not well ordered and therefore was excluded from the model (**Fig. 3a,b**). The bound NADPH is largely solvent exposed, allowing for rapid exchange of NADP⁺ for NADPH after transfer of reducing equivalents to FAD. Three conserved arginine residues of the β 10- α 6 loop interact favorably with the 3'-phosphoadenosine of the NADPH: Arg189 and Arg193 both form salt-bridges (2.9 Å) to the 3'-phosphate, and Arg188 packs against the adenine rings (~ 3.2 Å). The importance of these electrostatic interactions is highlighted by the strict conservation of these basic residues (**Supplementary Fig. 6**) and the high specificity of TrxR for NADPH over NADH, which lacks the 3'-phosphate (38). The opposite face of the adenine base packs against hydrophobic sidechains of Leu129, Ile163 and Val254. The pyrophosphate is bound at the N-terminus of α 5, with hydrogen bonds to Asp167 (N) (2.9 Å) and Ser168 (OH) (2.7 Å). Modeling of the nicotinamide riboside using the structure of TrxR from *H. pylori* as a template – for which the entire NADPH molecule is well defined (PDB: 2Q0K) – results in a distance of >15 Å between the nicotinamide and the flavin of FAD (not shown). A large domain rotation would thus be required to bring the nicotinamide of the NADPH into proximity to reduce the flavin (and simultaneously expose the active site cysteines – which are buried in the interior of the protein), as previously shown by structural studies on *E. coli* TrxR (41).

Although no exogenous FAD was added during the protein purification or crystallization, electron density at the FAD binding site indicates that it is bound tightly and co-purified; an FAD molecule modeled at this site refined to an occupancy of greater than 85% in each subunit. The FAD is in an extended conformation, with one end (the flavin group) bound near the dimer interface and the other (the adenine base) partially exposed to solvent on the opposite side of the FAD domain (**Fig. 3a,c**). The adenosine is bound in a pocket at the C-terminal ends of β 1, β 2, and β 6. Five hydrogen bonds (2.9–3.2 Å) to peptide backbone atoms of Tyr32, Glu33 and Ile87, and the sidechain hydroxyl of Thr122 stabilize the adenine base, and three hydrogen bonds (2.8–3.0 Å) to peptide backbone atoms of Ser11, Thr40 and Ala41 stabilize the ribose sugar. The negatively charged pyrophosphate is located immediately at N-terminal end of α 1, interacting favorably with the helix dipole, and stabilized by three hydrogen bonds (2.7 – 3.1 Å) to backbone nitrogen atoms of Ala14, Gln45 and Asp294. The flavin moiety is positioned in the interior of the protein at the N-terminal end of α 7. Here, the flavin is very close to the active site disulfide formed by Cys145 and Cys148. This is the flavin-oxidizing conformation of TrxR, with the flavin group poised for electron transfer to the active site cysteines. The C4 atom of the flavin group and the S γ atom of Cys148 are positioned only 3.3 Å from one another, consistent with the reaction cycle proceeding via a covalent adduct formed between these two atoms (39, 62). In contrast, the distance between this C4 atom and Cys145 (S γ) is 5.3 Å. The positive charge provided by the helix dipole of α 7, a very long helix,

would help to stabilize the negatively charged species that occur during electron transfer from the flavin group to Cys148. A hydrogen bond is formed between the O2 carbonyl of the flavin and the backbone nitrogen of Ala303 (2.9 Å), which is the first residue of $\alpha 7$.

The active site cysteine residues, Cys145 and Cys148, are part of a short helix ($\alpha 4$) in the NADPH domain, and are positioned favorably to form a disulfide bond. Indeed, despite the presence of reducing agent (DTT) in the protein buffer, the electron density indicates that they do form a disulfide bond (**Fig. 3c**), with a distance of 2.03 Å between the S γ atoms of each cysteine. This has been observed previously (44) and suggests that the active site cysteines are readily oxidized during crystallization and/or upon exposure to X-ray radiation.

Modeling the Ebselen-*AfTrxR* Interaction. To investigate the interactions involved in the inhibition of *AfTrxR* by EbSe, the crystal structure of *AfTrxR* along with MS/MS data showing the covalent interaction of EbSe with Cys148 were used to inform *in silico* modeling of the complex. As discussed above, *AfTrxR* crystallized in the FO conformation, with the active site cysteines buried in the core of the protein close to the flavin group. In this conformation, there is a narrow cavity between the NADPH domain and FAD domain, leading from the NADPH binding site to the active site. *In silico* docking of EbSe to the *AfTrxR* crystal structure showed that, although an EbSe molecule can occupy this cavity, access to Cys148 is precluded as the cavity narrows to < 3 Å in diameter, too narrow to allow EbSe to react with Cys148 (not shown).

The FR conformation of *AfTrxR* was therefore modeled by rotating the NADPH domain $\sim 66^\circ$ relative to the FAD domain, and modifying the active site to its reduced, dithiol configuration (**Fig. 4a**). This was guided by the structure of *E. coli* TrxR in the FR conformation (41) (PDB ID 1F6M), and followed by global model optimization (see Online Methods). Superposition of the final model on crystal structures of *E. coli* (1F6M) and *Entamoeba histolytica* (4CCQ) TrxRs in FR conformation gives RMSD values across C α s of 1.65 and 2.48 Å, respectively. In this conformation, both active site cysteines are at the protein surface, with Cys145 positioned away from the bulk solvent and Cys148 positioned towards the bulk solvent, consistent with the preferential modification of Cys148 as suggested by the MS/MS analysis.

Docking of EbSe to this model was performed with inclusion of the proposed reaction mechanism (**Fig. 1b**) in the simulation. This involves breaking of the five-membered 1,2-selenazolidin-3-one ring and formation of a covalent bond between the Se atom of EbSe and the S γ atom of Cys148. The ten top docked conformations (poses) could be divided into three groups – A, B and C – based on their general positioning on the surface of the protein (**Supplementary Fig. 7**). A representative example from each group is shown in **Fig. 4b**. Group A includes five of the ten top poses, all with the EbSe molecule positioned in a narrow groove formed by residues 36 to 42 of the $\beta 2$ - $\eta 1$ loop on one side and $\alpha 4$ (residues 146 to 149) on the other. A single hydrogen bond is formed between the carbonyl oxygen of the bridging amide and backbone nitrogen of Ala41. For the example shown in **Fig. 4b** (wheat color), the aniline ring is positioned at the entrance to the large cavity occupied by the FAD and packs against the S γ atom of Cys145. The ortho-selenobenzamide ring at the other end of the molecule makes contacts with Thr47 and Thr48. Group B includes three poses in which EbSe packs exclusively against the NADPH domain. Each pose involves formation of a hydrogen bond via the N atom of the amide group to the sidechain of either Gln139 or Asp149. For one

of these poses (**Fig. 4b**, pink), the EbSe molecule extends up towards a pocket at the surface of the NADPH domain, approximately 7 Å from the active site. One side of the pocket is mostly hydrophobic, formed by sidechain atoms of Asp149, Val152, Ile154 and Phe155; the other side is formed by Gln139 and backbone atoms of residues 141 through 143. The aniline ring of EbSe is positioned at the entrance to this amphipathic pocket, forming extensive van der Waal contacts with Val152. Group C, which includes only two of the top ten poses, has EbSe packing down almost exclusively on the FAD domain, contacting a conserved string of four threonine residues: Thr47 through Thr50 (**Fig. 4b**, cyan).

The docking results demonstrate several insights into the binding mode of EbSe with TrxR. Aside from the newly formed covalent bond, restraining the molecule to the vicinity of the active site, numerous potential interactions are presented by the range of conformations sampled by the molecule. These specific interactions could be exploited in future drug discovery efforts, enhancing its specificity and increasing its potency as a TrxR inhibitor. For example, the amide of Group A invariably forms a hydrogen bond with Ala41 (N), and the aniline

ring is positioned at the entrance to the FAD cavity, which could be exploited by adding substitutions to the ring, filling the cavity. Group B conformations involve a hydrogen bond to either Gln139 or Asp149 and extend the aniline ring to the entrance of the pocket above the active site. Specific interactions could be engineered by addition of substitutions to ortho- or meta- positions of this aromatic ring to fill this pocket. In addition, for most of the docked conformations, the sidechain of Cys148 is rotated away from Cys145, an unfavorable conformation for nucleophilic attack on the selenosulfide bond by Cys145 (S γ). It is anticipated that these considerations will be useful for informing design of drugs that inhibit AfTrxR via this mechanism.

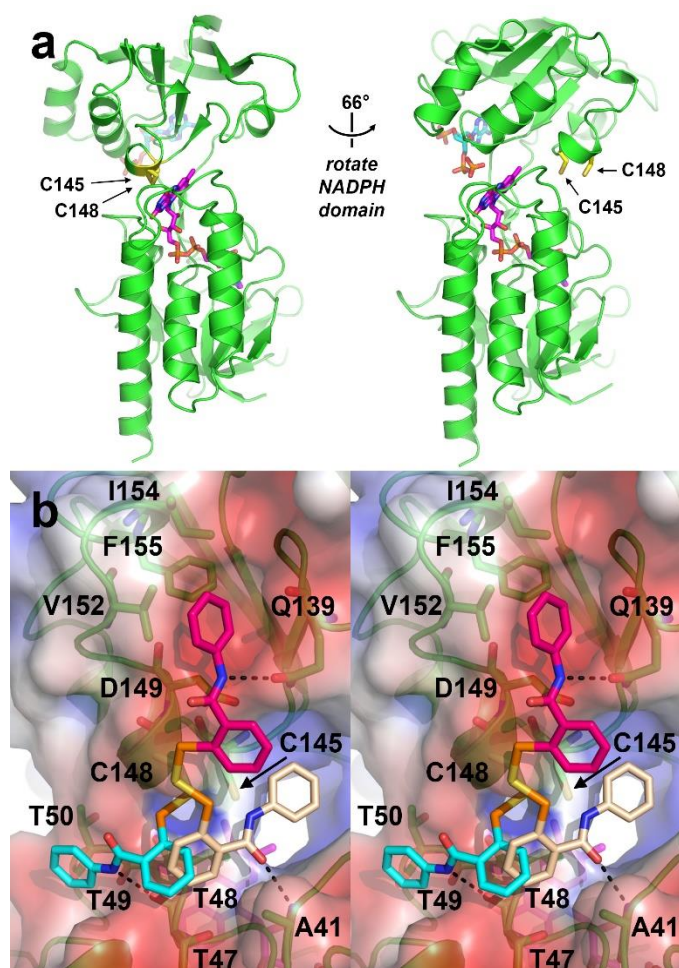


Figure 4 | Modeling of the EbSe–AfTrxR interaction. (a) The flavin-reducing (FR) conformation of AfTrxR was modeled by rotating the NADPH domain by ~66°, exposing the active site cysteines. Cys145 and Cys148 (yellow), FAD (magenta) and NADPH (cyan) are shown as sticks. **(b)** The reaction of EbSe with Cys148 was performed *in silico* using the FR conformation of AfTrxR. The results are shown in stereo view. Representative examples of group A (wheat carbons), group B (pink carbons) and group C (cyan carbons) poses are shown as sticks. Key interacting residues are also shown. A transparent molecular surface representation is shown for the protein, colored by electrostatic potential, -5 kT/e (red) to +5 kT/e (blue). The S γ atom of Cys148 is colored yellow and the Se atom of EbSe is orange. All hydrogen bonds (dashes) are 2.9-3.0 Å in length. The FAD cofactor (magenta) can be seen in the background (bottom of view).

DISCUSSION

The development of new antimicrobials via traditional drug discovery pathways is time and resource expensive, making drug repurposing an attractive option (67, 68). Despite being initially described as a mimic of glutathione peroxidase (69), EbSe has since been shown to strongly stimulate the activity of the mammalian Trx system towards hydrogen peroxide via its ability to act as an efficient substrate for both TrxR (high MW) and Trx, suggesting that its antioxidant activity in mammalian cells is mediated predominantly through its interactions with the Trx system (65, 70). In contrast, EbSe is a potent inhibitor of *E. coli* TrxR (1) and *A. fumigatus* TrxR (this study) – both low MW TrxRs. We also show that EbSe inhibits growth of *A. fumigatus* on solid and in liquid media, with activity comparable to or better than a number of currently available non-azole antifungals (**Table 2**).

The antifungal activity of EbSe against several yeast species has been reported previously (57, 58), and a number of different targets have been proposed. Chan *et al* (58) attributed the fungicidal activity of EbSe against *S. cerevisiae* to its direct inhibition of the plasma membrane H⁺-ATPase, Pma1. The authors also observed, however, that the concentration of EbSe required to inhibit Pma1 was much higher than the concentration at which yeast growth was significantly inhibited, suggesting that the antifungal activity of EbSe may be predominantly mediated by its interaction with a different target. A more recent study by Thangamani *et al* (57) showed that EbSe disrupted redox homeostasis in yeast. Although their study focused on the EbSe-mediated depletion of GSH and increased sensitivity of *GSH1* and *GSH2* deletion mutants to EbSe, *TRR1* and *TRR2* mutants also showed increased sensitivity, suggesting that EbSe probably disrupts redox homeostasis via both GSH and Trx systems. In addition, depletion of intracellular GSH by EbSe has been similarly observed in mammalian cells (71). Therefore, while it is a likely contributor to EbSe toxicity, it does not explain the marked increase in sensitivity of fungal cells to EbSe over mammalian cells.

EbSe reacts with thiol groups (63, 72). It has thus been shown to modulate a range of biological systems, largely via its ability to both inhibit various cysteine-containing enzymes (73) and potentiate cellular antioxidant systems by acting as a mimic of glutathione peroxidase (69) and peroxiredoxin (65) in mammalian cells. The complex interplay between the myriad of pathways that are affected by exposure to EbSe makes it difficult to delineate its major functional targets; however, the stark difference in physiological outcomes on mammalian versus microbial cells provides insight. The fact that EbSe is an efficient substrate for mammalian TrxR (facilitating its antioxidant activity as a peroxiredoxin mimic), but is an inhibitor of bacterial and fungal TrxRs, presents an effective basis for drug selectivity, providing an explanation for why EbSe displays relatively low toxicity to mammalian cells (1, 60) while being a potent inhibitor of fungal cell growth. In addition, there is strong evidence to suggest that inhibition of TrxR by EbSe is a major contributor to its antibacterial activity (1). In light of these observations and the potent inhibition of *AfTrxR* we observe *in vitro* (**Table 1; Supplementary Fig. 1**), we suspect that targeting of TrxR is central to the antifungal activity of EbSe. Significantly, the MIC of EbSe against *A. fumigatus* of 1-2 µg/mL (≈ 4-7 µM) (**Table 2**) corresponds very closely to the concentration that completely inhibited *AfTrxR* activity *in vitro* (~4 µM), consistent with TrxR being a major target.

Our *in silico* analyses suggest that EbSe binds to Cys148, locking *AfTrxR* in a catalytically

non-productive FR conformation. Simulation of the EbSe-Cys148 reaction shows EbSe binding to the surface of *AfTrxR* in an array of conformations, consistent with the binding of a small molecule to the protein surface in a largely non-specific manner while being constrained to the same site by the covalent selenosulfide bond (**Fig. 4b**; **Supplementary Fig. 7**). Categorizing the different docked conformations into groups highlighted potential specific interactions that could facilitate efficient packing of EbSe, and potential EbSe analogs, onto the surface of the protein. Half of the top ten poses showed the EbSe molecule positioned between the β 2- η 1 loop of the FAD domain and α 4 of the NADPH domain, suggesting preferential binding to this groove (**Supplementary Fig. 7**, wheat color). Notably, residues 36 through 40 of the β 2- η 1 loop, which form one side of this groove, are absent from *EcTrxR*. It is tempting to speculate that this may contribute to the enhanced inhibition of *AfTrxR* over *EcTrxR* by EbSe.

Rational design of analogs to exploit specific TrxR-inhibitor interactions, while also positioning Cys148 in an unfavorable conformation for nucleophilic attack by Cys145 (S_y), is expected to increase the specificity and potency of the inhibitor. In particular, the amphipathic pocket near the active site as well as the groove leading to the FAD cavity present as potential inhibitor binding sites, warranting investigation of EbSe analogs that extend into these spaces by the addition of pharmacophores that facilitate specific interactions. In parallel, a detailed description of the *AfTrxR*-*AfTrx* interaction is expected to provide insights useful for inhibitor design. For example, based on observation of the homologous *E. coli* TrxR-Trx complex (PDB ID 1F6M) we hypothesize that a conserved arginine residue of Trx (*AfTrx* Arg76) inserts into the amphipathic pocket above the active site. Addition of similar pharmacophores to the ortho- or meta- positions of the aniline ring (see **Fig. 4b**, pink) could enhance binding of the inhibitor, improving specificity and potency.

During infection of the human host, opportunistic fungal pathogens such as *A. fumigatus* must contend with conditions of high oxidative stress (74, 75). Therefore, given that the Trx system is central to antioxidant defense, it is expected the antifungal activity of EbSe (and analogs) may be enhanced in the context of the host environment. In addition, EbSe can cross the blood-brain barrier (76), making it an attractive option for the treatment of cerebral aspergillosis – a condition associated with particularly high mortality rates (3). The fungicidal activity of EbSe against *Candida* and *Cryptococcus* clinical isolates has been confirmed recently, demonstrating MIC values of 0.5 to 2 μ g/mL (57); concentrations that are in the same range as we have determined here for *A. fumigatus*, warranting further investigation into EbSe and its analogs as novel broad-spectrum antifungals.

MATERIALS AND METHODS

Reagents. All reagents were purchased from Sigma-Aldrich™. PCR primers were from GeneWorks (Thebarton, SA, Australia). NADPH (50 mM) and FAD (10 mM) aqueous stocks were stored at -20°C until required. Ebselen was stored at 4°C in powder form until required. A 9 mM working stock of EbSe was made up fresh in 100% DMSO.

Cloning of *A. fumigatus* TRR1. The entire *TRR1* coding sequence was amplified by PCR from *A. fumigatus* strain Af293 (77) cDNA (a generous gift from Dr. James Fraser, University of Queensland) using primers:

(1) 5' GGGGACAAGTTTGTACAAAAAAGCAGGCTACGAAAACCTGTATTTTCAGG
GAATGGTGCACACAAAAGTTACCA 3' and,

(2) 5' GGGGACCACTTTGTACAAGAAAGCTGGGTATTAGAGAAGAGGGTTCGACT
TGTATT 3',

and cloned into Gateway® pDONR™221 Vector (Invitrogen™) with a Tobacco Etch Virus (TEV) protease cleavage site upstream of the ORF (underlined in primer (1) sequence). This *TEV-TRR1* construct was then subcloned via Gateway® recombination sites into Gateway® Nova pET-57-DEST™ vector for expression of recombinant protein in *E. coli* with an N-terminal NusA and hexahistidine tag and confirmed by sequencing. Here, the *TRR1* transcript we have identified (GenBank accession MG551986) is shorter than the putative sequence previously deposited (GenBank accession XM_746439) (77). The resulting protein product is shorter by 17 amino acids near the N-terminus, with the replacement of 19 amino acids (Thr7 through Val27) with 2 amino acids (Val7-Ile8). Alignment of this protein sequence with thioredoxin reductase sequences from other fungal species including *Aspergillus*, *Penicillium*, *Blastomyces* and *Saccharomyces spp.* provides strong support for our new annotation.

AfTrxR protein expression and purification. Expression of AfTrxR was induced in 2.5 L *E. coli* BL21(λDE3) shake-flask culture for 20 hours at 16°C. Cells were lysed by mechanical disruption in 20 mM Tris-HCl (pH 8.0), 500 mM NaCl, 10 mM imidazole (pH 8.0), 10% glycerol and purified by using two Ni²⁺-NTA columns (Bio-Rad) with a TEV protease digest in between to remove the NusA and his-tag. The protein solution was then made up to 1 M (NH₄)₂SO₄, passed through a HiTrap™ Phenyl FF HS column (GE Healthcare Life Sciences) and eluted using a 1 to 0 M (NH₄)₂SO₄ gradient. Final protein purity was > 95%, as assessed by SDS-PAGE. Protein was dialyzed to 20 mM Tris-HCl (pH 7.5), 50 mM NaCl before being concentrated to ~ 6 mg/mL, flash frozen in liquid nitrogen and stored at -80°C.

AfTrxR extinction coefficient determination. The extinction coefficient of AfTrxR at 280 nm was calculated by determining the concentration of liberated FAD cofactor as described (78). Briefly, purified protein was incubated with excess FAD before removing unbound FAD by gel filtration. Absorbance at 280 nm was measured prior to liberating bound FAD by incubation with 0.2% SDS for 15 min at room temperature. Following this, the concentration of FAD was determined by measuring the absorbance at 450 nm, using the extinction coefficient of 11300 M⁻¹.cm⁻¹ for FAD. Assuming a ratio of one FAD molecule per protein subunit, the extinction coefficient of AfTrxR at 280nm was determined to be 1.57 (mg/mL)⁻¹ using measurements at three different concentrations. This value was used for all further protein concentration determinations, and subsequently validated by comparison with protein

concentration values determined by infrared absorbance using a Direct Detect® spectrometer (Merck).

AfTrxA protein expression and purification. A pET-45b(+) vector containing the coding sequence for *A. fumigatus* thioredoxin, TrxA (GenBank accession XM_748424) with an N-terminal hexahistidine tag was purchased from GenScript® (Piscataway, NJ, USA). Protein expression was induced in 2 L shake-flask culture of *E. coli* BL21(λDE3) for 20 hours at 16°C. Cells were lysed by mechanical disruption in 20 mM Tris-HCl (pH 8.0), 500 mM NaCl, 10 mM imidazole (pH 8.0), 5 mM β-mercaptoethanol, 10% glycerol. His-tagged AfTrxA was purified from lysate using a Ni²⁺-NTA column (Bio-Rad) followed by a HiPrep™ 26/60 Sephacryl™ S-300 HR column (GE) pre-equilibrated in phosphate buffered saline (without reducing agent), flash-frozen in liquid nitrogen and stored at -80°C until required.

Enzyme assay. AfTrxR activity was determined in the absence and presence of EbSe using the DTNB assay, as described (30, 32, 36, 61). Assays were performed in triplicate in 96-well plate format and optimized for buffer pH, salt and NADPH concentration. AfTrxR was first incubated with excess FAD and passed through a size-exclusion column to remove unbound FAD. The reaction was started by addition of 30nM AfTrxR to 100 mM potassium phosphate (pH 7.5), 2 mM EDTA, 1 mM DTNB, 0.2 mM NADPH and 0–10 μM AfTrxA in a final volume of 200 μL. Absorbance at 414 nm was monitored for 20min at 25°C using a Multiskan Ascent spectrophotometer (Thermo Scientific™). Inhibition by EbSe was determined by addition of EbSe at final concentrations 0–0.90 μM to the assay prior to addition of AfTrxR. The final DMSO concentration was 0.5% in all experiments and had no effect on AfTrxR activity. Data from the initial 60 sec was used for calculation of initial reaction velocities. Reduction of DTNB in the absence of AfTrxA was negligible (240-fold slower than V_{max}) and did not increase in the presence of EbSe, indicating that neither DTNB nor EbSe are substrates for AfTrxR (65). Previous studies have shown that the activities of human Trx and *E. coli* Trx2 can be inhibited by oxidation of non-catalytic cysteine residues (30, 79). In addition, EbSe catalyzes the formation of intermolecular and intramolecular disulfide bonds in human Trx (63). It is possible that AfTrxA, which contains an additional non-catalytic cysteine (Cys29), may be oxidized to form Trx dimers linked via intermolecular disulfides. Indeed, we observed a reducible high MW species after purification of recombinant AfTrxA corresponding to a Trx dimer (~ 25 kDa). Therefore, assuming 1 mol of EbSe can inactivate 2 mol of AfTrxA via oxidation and dimer formation, the effective initial concentration of substrate (Trx) in our assay is given by:

$$[\text{Trx}]_{\text{effective}} = [\text{Trx}] - 2x[\text{EbSe}]$$

Our assay data were adjusted accordingly and the resulting plots fit well to the standard model of competitive inhibition (**Supplementary Fig. 1**). Non-linear regression analysis was performed using GraphPad Prism (v7).

Mass spectrometry. Sample preparation. AfTrxR wt, C145S and C148S protein samples were diluted to 12 μM in protein buffer (20 mM Tris pH 7.5, 100 mM NaCl) before being incubated with 20-fold molar excess DTT at 37°C for 1 hr. Samples were washed three times using 10000 MWCO filter spin columns with protein buffer to remove DTT before incubation with 20-fold molar excess EbSe for at least 1 hr. Samples were then digested with a modified filter-aided sample preparation (FASP) method (80) as follows: Samples were mixed with 8 M Urea,

placed onto a Vivacon 500 (Sartorius) filter spin column, and centrifuged at 14 000 x g for 15 minutes. The filter spin columns containing the samples were washed three times with 8 M Urea and then three times with 50 mM ammonium bicarbonate (NH₄HCO₃). Samples were digested overnight at 37°C by placing 100 ng of sequencing grade modified trypsin (Promega) in 5 mM NH₄HCO₃ onto the filter spin columns. (4) Samples were centrifuged at 14000 x g for 15 minutes and the flow through was collected. The volumes of the resulting peptide extracts were reduced by vacuum centrifugation to approximately 1 µL then resuspended with 0.1% TFA in 2% ACN to a total volume of ~20 µL.

Data acquisition by liquid chromatography– electrospray ionization tandem mass spectrometry. Nano-LC–ESI-MS/MS was performed on an Ultimate 3000 RSLC system (Thermo Fisher Scientific) coupled to a LTQ Orbitrap XL ETD MS instrument (Thermo-Fisher Scientific). Peptide samples were pre-concentrated concentrated onto a C18 trapping column (Acclaim PepMap100 C18 75 µm × 20 mm, Thermo-Fisher Scientific) at a flow rate of 5 µL/min in 2% acetonitrile (ACN), 0.1% trifluoroacetic acid (TFA) for 8 minutes. Peptide separation was performed using a 75 µm ID C18 column (Acclaim PepMap100 C18 75 µm × 15 cm, Thermo-Fisher Scientific) at a flow rate of 0.3 µL/min using a linear gradient from 5 to 45% B (A: 5% ACN, 0.1% formic acid (FA); B: 80% FA) over 72 minutes, followed by a 20 minute wash with 90% B, and 20 minute equilibration 5% A. MS scans were acquired in the mass range of 300 to 2000 m/z at a resolution of 60000. The six most intense precursor ions selected for isolation and were subjected to CID fragmentation using a dynamic exclusion of 5 seconds. Dynamic exclusion criteria included a minimum relative signal intensity of 1000, and ≥2+ charge state. An isolation width of 3.0 was used with a normalized collision energy 40.

Data analysis. RAW files were analyzed using the MaxQuant software (version 1.5.2.8) with Andromeda search engine (20) against the non-redundant *Aspergillus* UniProt database with the addition of the mutant sequences. The standard Orbitrap settings in MaxQuant were used with a mass error tolerance of 10 ppm. The variable modifications of oxidation of methionine and EbSe binding to cysteine residues was specified, with the digestion enzyme specified as trypsin. The false discovery rate (FDR) was set to 1% for both proteins and peptides, with a minimum peptide length of 7 amino acids.

Antifungal assays. *Aspergillus fumigatus* (ATCC MYA-3626) was obtained from the National Mycology Reference Centre (South Australian Pathology, Australia). Frozen stocks were thawed, cultured and subcultured on Sabouraud dextrose agar. The standard inoculum was prepared by collecting colonies from 48 hours old culture. This organism was used for both the broth microdilution assay and disk diffusion assay.

Broth microdilution assay. *A. fumigatus* susceptibility tests for EbSe was carried out by broth microdilution in RPMI 1640 broth, as described in accordance with the National Committee for Clinical & Laboratory Science Institute (CLSI) standard method M27-A3. Along with EbSe, standard antifungal reference drugs caspofungin (Selleckchem.com, USA), amphotericin B (Sigma-Aldrich, USA), and nystatin (TOKU-E, USA) were used. Two fold serial dilutions of compounds were performed to cover the concentration range 0.97 µg/mL to 500 µg/mL for EbSe and 0.03 µg/mL to 16 µg/mL for all reference drugs and EbSe. The final concentration of the fungal strains was 5 x 10⁵ CFU/mL. Presence or absence of physical

growth was determined by examining the microdilution wells gradually from optically clear to slightly hazy to prominent decrease in turbidity.

Disk diffusion assay. *A. fumigatus* susceptibility tests for EbSe was carried out by broth disk diffusion assay on solid media, as described by the Clinical & Laboratory Standards Institute document M51-P. Blank Whatman paper (6 mm) antibiotic assay disks were impregnated with 12 µg of the test and reference compounds and allowed to dry at room temperature. A sterile cotton swab was dipped into each adjusted fungal suspension and used to uniformly cover the surface of a Mueller-Hinton with Glucose and Methylene Blue (MHGMB) agar plate. Antifungal disks were placed on the inoculated MHGMB plates used. Control disks without antifungal drugs or sample compounds were also placed on the plate. Discs impregnated with caspofungin (positive control) were used. The plates were incubated for 24 h at 35°C before measuring the diameter of the zone of inhibition in millimeters.

Protein crystallization. Purified recombinant *AfTrxR* at ~ 6 mg/mL was incubated at 25°C for 30 min in the presence of 5 mM NADPH and 20 mM DTT before being subject to crystallization at 16°C by vapor diffusion using the hanging-drop method. Each drop contained 1 µL of well solution and 1 µL of protein solution, over a reservoir volume of 0.5 mL. Crystals grew in 32% Tacsimate (pH 7.0) (Hampton Research) as yellow, pseudo-hexagonal rods to a size of ~ 300 x 200 µm in < 1 week.

X-ray data collection and refinement. Diffraction data were collected at an X-ray energy of 13000 eV at 1° intervals with 1° oscillation at 100 K at the Australian Synchrotron (MX1 beamline), using 70% Tacsimate (pH 7.0) as cryoprotectant. Data were processed using iMosflm (81), solved by molecular replacement using Phaser MR (82); the structure of *S. cerevisiae* cytoplasmic thioredoxin reductase (Trr1) (PDB ID 3D8X) was used for the search model. Atomic coordinates were rebuilt manually using Coot (83) and refined using phenix.refine (84). During refinement, non-crystallographic symmetry (NCS) restraints were applied, X-ray/stereochemistry and X-ray/ADP weights were optimized, and anisotropic B-factor refinement was restricted to torsion-liberation-screw (TLS) groups (85) defined automatically by phenix.refine. Atoms of each FAD or NADPH molecule were grouped for occupancy refinement. The final model exhibited good overall geometry, with 95.28% of peptide bonds in favored regions of the Ramachandran plot and no outliers. Structure factors and atomic coordinates can be accessed at the RCSB Protein Data Bank (<https://www.rcsb.org>), with accession code 6BPY.

In silico modeling and docking. Atomic coordinates for the FAD domain (residues 1-127, 256-326) and NADPH domain (residues 128-255) of the *AfTrxR* crystal structure were structurally aligned separately to the corresponding domains of the crystal structure of *EcTrxR* in FR conformation (PDB ID 1F6M) (41). Chain breaks were mended in Coot (83). ICM Molsoft (v3.8-6a) (86) was then used to add hydrogens and refine the model by global optimization of side chains and annealing of the peptide backbone (20 iterations). Covalent docking of EbSe to Cys148 was then performed using ICM Molsoft (“Thoroughness” was set to 50).

Structure visualization. Chemical structures were drawn using ChemDraw Ultra (v12.0). All molecular graphics images were produced using PyMol™ (v1.8.6.0) (87). Secondary structural elements were assigned using DSSP (88). PISA (89) was used to calculate the dimer

interface area. Electrostatic potential maps were calculated using APBS (90), with atomic charges assigned using the PDB2PQR webserver (v2.1.1) (91).

ACKNOWLEDGEMENTS

X-ray diffraction data collection was undertaken on the MX1 beamline at the Australian Synchrotron, part of ANSTO. We acknowledge Prof Hans Griesser, Future Industries Institute, University of South Australia, for providing laboratories and equipment used in microbiological evaluation.

REFERENCES

1. Lu J, Vlamis-Gardikas A, Kandasamy K, Zhao R, Gustafsson TN, Engstrand L, Hoffner S, Engman L, Holmgren A. 2013. Inhibition of bacterial thioredoxin reductase: an antibiotic mechanism targeting bacteria lacking glutathione. *Faseb j* 27:1394-403.
2. Latge JP. 1999. *Aspergillus fumigatus* and aspergillosis. *Clin Microbiol Rev* 12:310-50.
3. Gallien S, Fournier S, Porcher R, Bottero J, Ribaud P, Sulahian A, Socie G, Molina JM. 2008. Therapeutic outcome and prognostic factors of invasive aspergillosis in an infectious disease department: a review of 34 cases. *Infection* 36:533-8.
4. Thompson GR, 3rd, Patterson TF. 2008. Pulmonary aspergillosis. *Semin Respir Crit Care Med* 29:103-10.
5. Warnock DW. 2007. Trends in the epidemiology of invasive fungal infections. *Nihon Ishinkin Gakkai Zasshi* 48:1-12.
6. Groll AH, Shah PM, Mentzel C, Schneider M, Just-Nuebling G, Huebner K. 1996. Trends in the postmortem epidemiology of invasive fungal infections at a university hospital. *J Infect* 33:23-32.
7. Kontoyiannis DP, Marr KA, Park BJ, Alexander BD, Anaissie EJ, Walsh TJ, Ito J, Andes DR, Baddley JW, Brown JM, Brumble LM, Freifeld AG, Hadley S, Herwaldt LA, Kauffman CA, Knapp K, Lyon GM, Morrison VA, Papanicolaou G, Patterson TF, Perl TM, Schuster MG, Walker R, Wannemuehler KA, Wingard JR, Chiller TM, Pappas PG. 2010. Prospective surveillance for invasive fungal infections in hematopoietic stem cell transplant recipients, 2001-2006: overview of the Transplant-Associated Infection Surveillance Network (TRANSNET) Database. *Clin Infect Dis* 50:1091-100.
8. Espinosa V, Rivera A. 2016. First Line of Defense: Innate Cell-Mediated Control of Pulmonary Aspergillosis. *Front Microbiol* 7:272.
9. Sugui JA, Kwon-Chung KJ, Juvvadi PR, Latge JP, Steinbach WJ. 2015. *Aspergillus fumigatus* and related species. *Cold Spring Harb Perspect Med* 5:a019786.
10. Walsh TJ, Anaissie EJ, Denning DW, Herbrecht R, Kontoyiannis DP, Marr KA, Morrison VA, Segal BH, Steinbach WJ, Stevens DA, van Burik JA, Wingard JR, Patterson TF. 2008. Treatment of aspergillosis: clinical practice guidelines of the Infectious Diseases Society of America. *Clin Infect Dis* 46:327-60.
11. Chowdhry R, Marshall WL. 2008. Antifungal therapies in the intensive care unit. *J Intensive Care Med* 23:151-8.
12. Hadrich I, Makni F, Neji S, Abbes S, Cheikhrouhou F, Trabelsi H, Sellami H, Ayadi A. 2012. Invasive aspergillosis: resistance to antifungal drugs. *Mycopathologia* 174:131-41.
13. Qiao J, Liu W, Li R. 2008. Antifungal resistance mechanisms of *Aspergillus*. *Nihon Ishinkin Gakkai Zasshi* 49:157-63.
14. Verweij PE, Chowdhary A, Melchers WJ, Meis JF. 2016. Azole Resistance in *Aspergillus fumigatus*: Can We Retain the Clinical Use of Mold-Active Antifungal Azoles? *Clin Infect Dis* 62:362-8.
15. Lewis RE. 2011. Current concepts in antifungal pharmacology. *Mayo Clin Proc* 86:805-17.
16. Herbrecht R, Denning DW, Patterson TF, Bennett JE, Greene RE, Oestmann JW, Kern WV, Marr KA, Ribaud P, Lortholary O, Sylvester R, Rubin RH, Wingard JR, Stark P, Durand C, Caillot D, Thiel E, Chandrasekar PH, Hodges MR, Schlamm HT, Troke PF, de Pauw B. 2002. Voriconazole versus amphotericin B for primary therapy of invasive aspergillosis. *N Engl J Med* 347:408-15.
17. Bates DW, Su L, Yu DT, Chertow GM, Seger DL, Gomes DR, Dasbach EJ, Platt R. 2001. Mortality and costs of acute renal failure associated with amphotericin B therapy. *Clin Infect Dis* 32:686-93.
18. Patterson TF, Thompson GR, 3rd, Denning DW, Fishman JA, Hadley S, Herbrecht R, Kontoyiannis DP, Marr KA, Morrison VA, Nguyen MH, Segal BH, Steinbach WJ, Stevens DA, Walsh TJ, Wingard JR, Young JH, Bennett JE. 2016. Practice Guidelines for the Diagnosis and Management of Aspergillosis: 2016 Update by the Infectious Diseases Society of America. *Clin Infect Dis* doi:10.1093/cid/ciw326.

19. Schwartz S, Ruhnke M, Ribaud P, Corey L, Driscoll T, Cornely OA, Schuler U, Lutsar I, Troke P, Thiel E. 2005. Improved outcome in central nervous system aspergillosis, using voriconazole treatment. *Blood* 106:2641-5.
20. D. Versteeg, E. Snelders, T. Rijs, W. Melchers, P. Verweij. 2012. Continued increase of azole resistance in *Aspergillus fumigatus* (Af) in Dutch Hospitals, abstr ICAAC 52nd,
21. Snelders E, van der Lee HA, Kuijpers J, Rijs AJ, Varga J, Samson RA, Mellado E, Donders AR, Melchers WJ, Verweij PE. 2008. Emergence of azole resistance in *Aspergillus fumigatus* and spread of a single resistance mechanism. *PLoS Med* 5:e219.
22. Lestrade PP, Meis JF, Arends JP, van der Beek MT, de Brauwier E, van Dijk K, de Greeff SC, Haas PJ, Hodiament CJ, Kuijper EJ, Leenstra T, Muller AE, Oude Lashof AM, Rijnders BJ, Roelofsen E, Rozemeijer W, Tersmette M, Terveer EM, Verduin CM, Wolfhagen MJ, Melchers WJ, Verweij PE. 2016. Diagnosis and management of aspergillosis in the Netherlands: a national survey. *Mycoses* 59:101-7.
23. Howard SJ, Cerar D, Anderson MJ, Albarrag A, Fisher MC, Pasqualotto AC, Laverdiere M, Arendrup MC, Perlin DS, Denning DW. 2009. Frequency and evolution of Azole resistance in *Aspergillus fumigatus* associated with treatment failure. *Emerg Infect Dis* 15:1068-76.
24. Toledano MB, Delaunay-Moisan A, Outten CE, Igbaria A. 2013. Functions and cellular compartmentation of the thioredoxin and glutathione pathways in yeast. *Antioxid Redox Signal* 18:1699-711.
25. Matsui M, Oshima M, Oshima H, Takaku K, Maruyama T, Yodoi J, Taketo MM. 1996. Early embryonic lethality caused by targeted disruption of the mouse thioredoxin gene. *Dev Biol* 178:179-85.
26. Thelander L, Reichard P. 1979. Reduction of ribonucleotides. *Annu Rev Biochem* 48:133-58.
27. Arner ES, Holmgren A. 2000. Physiological functions of thioredoxin and thioredoxin reductase. *Eur J Biochem* 267:6102-9.
28. Lu J, Holmgren A. 2014. The thioredoxin antioxidant system. *Free Radical Biology and Medicine* 66:75-87.
29. Poet GJ, Oka OB, van Lith M, Cao Z, Robinson PJ, Pringle MA, Arner ES, Bulleid NJ. 2017. Cytosolic thioredoxin reductase 1 is required for correct disulfide formation in the ER. *Embo j* 36:693-702.
30. Holmgren A, Bjornstedt M. 1995. Thioredoxin and thioredoxin reductase. *Methods Enzymol* 252:199-208.
31. Wahl MC, Irmeler A, Hecker B, Schirmer RH, Becker K. 2005. Comparative structural analysis of oxidized and reduced thioredoxin from *Drosophila melanogaster*. *J Mol Biol* 345:1119-30.
32. Arner ES, Zhong L, Holmgren A. 1999. Preparation and assay of mammalian thioredoxin and thioredoxin reductase. *Methods Enzymol* 300:226-39.
33. Sandalova T, Zhong L, Lindqvist Y, Holmgren A, Schneider G. 2001. Three-dimensional structure of a mammalian thioredoxin reductase: implications for mechanism and evolution of a selenocysteine-dependent enzyme. *Proc Natl Acad Sci U S A* 98:9533-8.
34. Fritz-Wolf K, Urig S, Becker K. 2007. The structure of human thioredoxin reductase 1 provides insights into C-terminal rearrangements during catalysis. *J Mol Biol* 370:116-27.
35. Zhong L, Holmgren A. 2000. Essential role of selenium in the catalytic activities of mammalian thioredoxin reductase revealed by characterization of recombinant enzymes with selenocysteine mutations. *J Biol Chem* 275:18121-8.
36. Oliveira MA, Discola KF, Alves SV, Medrano FJ, Guimaraes BG, Netto LE. 2010. Insights into the specificity of thioredoxin reductase-thioredoxin interactions. A structural and functional investigation of the yeast thioredoxin system. *Biochemistry* 49:3317-26.
37. Pedrajas JR, Kosmidou E, Miranda-Vizuete A, Gustafsson JA, Wright AP, Spyrou G. 1999. Identification and functional characterization of a novel mitochondrial thioredoxin system in *Saccharomyces cerevisiae*. *J Biol Chem* 274:6366-73.
38. Baker LM, Raudonikiene A, Hoffman PS, Poole LB. 2001. Essential thioredoxin-dependent peroxiredoxin system from *Helicobacter pylori*: genetic and kinetic characterization. *J Bacteriol* 183:1961-73.
39. Waksman G, Krishna TS, Williams CH, Jr., Kuriyan J. 1994. Crystal structure of *Escherichia coli* thioredoxin reductase refined at 2 Å resolution. Implications for a large conformational change during catalysis. *J Mol Biol* 236:800-16.
40. Williams CH, Jr. 1995. Mechanism and structure of thioredoxin reductase from *Escherichia coli*. *Faseb j* 9:1267-76.
41. Lennon BW, Williams CH, Jr., Ludwig ML. 2000. Twists in catalysis: alternating conformations of *Escherichia coli* thioredoxin reductase. *Science* 289:1190-4.
42. Theobald AJ, Caballero I, Coma I, Colmenarejo G, Cid C, Gamo FJ, Hibbs MJ, Bass AL, Thomas DA. 2012. Discovery and biochemical characterization of *Plasmodium* thioredoxin reductase inhibitors from an antimalarial set. *Biochemistry* 51:4764-71.
43. Fritz-Wolf K, Jortzik E, Stumpf M, Preuss J, Iozef R, Rahlfs S, Becker K. 2013. Crystal Structure of the *Plasmodium falciparum* Thioredoxin Reductase–Thioredoxin Complex. *Journal of Molecular Biology* 425:3446-3460.
44. Parsonage D, Sheng F, Hirata K, Debnath A, McKerrow JH, Reed SL, Abagyan R, Poole LB, Podust LM. 2016. X-ray structures of thioredoxin and thioredoxin reductase from *Entamoeba histolytica* and prevailing hypothesis of the mechanism of Auranofin action. *J Struct Biol* 194:180-90.

45. Zhang D, Xu Z, Yuan J, Zhao YX, Qiao ZY, Gao YJ, Yu GA, Li J, Wang H. 2014. Synthesis and molecular recognition studies on small-molecule inhibitors for thioredoxin reductase. *J Med Chem* 57:8132-9.
46. Liu Y, Duan D, Yao J, Zhang B, Peng S, Ma H, Song Y, Fang J. 2014. Dithiaarsanes Induce Oxidative Stress-Mediated Apoptosis in HL-60 Cells by Selectively Targeting Thioredoxin Reductase. *J Med Chem* 57:5203-11.
47. James LR, Xu ZQ, Sluyter R, Hawksworth EL, Kelso C, Lai B, Paterson DJ, de Jonge MD, Dixon NE, Beck JL, Ralph SF, Dillon CT. 2015. An investigation into the interactions of gold nanoparticles and anti-arthritis drugs with macrophages, and their reactivity towards thioredoxin reductase. *J Inorg Biochem* 142:28-38.
48. Hu W, Sillaots S, Lemieux S, Davison J, Kauffman S, Breton A, Linteau A, Xin C, Bowman J, Becker J, Jiang B, Roemer T. 2007. Essential gene identification and drug target prioritization in *Aspergillus fumigatus*. *PLoS Pathog* 3:e24.
49. Machado AK, Morgan BA, Merrill GF. 1997. Thioredoxin reductase-dependent inhibition of MCB cell cycle box activity in *Saccharomyces cerevisiae*. *J Biol Chem* 272:17045-54.
50. Pearson GD, Merrill GF. 1998. Deletion of the *Saccharomyces cerevisiae* TRR1 gene encoding thioredoxin reductase inhibits p53-dependent reporter gene expression. *J Biol Chem* 273:5431-4.
51. Grant CM. 2001. Role of the glutathione/glutaredoxin and thioredoxin systems in yeast growth and response to stress conditions. *Mol Microbiol* 39:533-41.
52. Parnham M, Sies H. 2000. Ebselen: prospective therapy for cerebral ischaemia. *Expert Opin Investig Drugs* 9:607-19.
53. Singh N, Sharpley AL, Emir UE, Masaki C, Herzallah MM, Gluck MA, Sharp T, Harmer CJ, Vasudevan SR, Cowen PJ, Churchill GC. 2016. Effect of the Putative Lithium Mimetic Ebselen on Brain Myo-Inositol, Sleep, and Emotional Processing in Humans. *Neuropsychopharmacology* 41:1768-78.
54. Mahadevan J, Parazzoli S, Oseid E, Hertzell AV, Bernlohr DA, Vallerie SN, Liu CQ, Lopez M, Harmon JS, Robertson RP. 2013. Ebselen treatment prevents islet apoptosis, maintains intranuclear Pdx-1 and MafA levels, and preserves beta-cell mass and function in ZDF rats. *Diabetes* 62:3582-8.
55. Baek JM, Kim JY, Yoon KH, Oh J, Lee MS. 2016. Ebselen Is a Potential Anti-Osteoporosis Agent by Suppressing Receptor Activator of Nuclear Factor Kappa-B Ligand-Induced Osteoclast Differentiation In vitro and Lipopolysaccharide-Induced Inflammatory Bone Destruction In vivo. *Int J Biol Sci* 12:478-88.
56. Kil J, Lobarinas E, Spankovich C, Griffiths SK, Antonelli PJ, Lynch ED, Le Prell CG. 2017. Safety and efficacy of ebselen for the prevention of noise-induced hearing loss: a randomised, double-blind, placebo-controlled, phase 2 trial. *Lancet* doi:10.1016/s0140-6736(17)31791-9.
57. Thangamani S, Eldesouky HE, Mohammad H, Pascuzzi PE, Avramova L, Hazbun TR, Seleem MN. 2017. Ebselen exerts antifungal activity by regulating glutathione (GSH) and reactive oxygen species (ROS) production in fungal cells. *Biochim Biophys Acta* 1861:3002-3010.
58. Chan G, Hardej D, Santoro M, Lau-Cam C, Billack B. 2007. Evaluation of the antimicrobial activity of ebselen: role of the yeast plasma membrane H⁺-ATPase. *J Biochem Mol Toxicol* 21:252-64.
59. Bender KO, Garland M, Ferreyra JA, Hryckowian AJ, Child MA, Puri AW, Solow-Cordero DE, Higginbottom SK, Segal E, Banaei N, Shen A, Sonnenburg JL, Bogyo M. 2015. A small-molecule antivirulence agent for treating *Clostridium difficile* infection. *Sci Transl Med* 7:306ra148.
60. Thangamani S, Younis W, Seleem MN. 2015. Repurposing ebselen for treatment of multidrug-resistant staphylococcal infections. *Sci Rep* 5:11596.
61. Zhang Z, Bao R, Zhang Y, Yu J, Zhou CZ, Chen Y. 2009. Crystal structure of *Saccharomyces cerevisiae* cytoplasmic thioredoxin reductase Trr1 reveals the structural basis for species-specific recognition of thioredoxin. *Biochim Biophys Acta* 1794:124-8.
62. Prongay AJ, Engelke DR, Williams CH, Jr. 1989. Characterization of two active site mutations of thioredoxin reductase from *Escherichia coli*. *J Biol Chem* 264:2656-64.
63. Sakurai T, Kanayama M, Shibata T, Itoh K, Kobayashi A, Yamamoto M, Uchida K. 2006. Ebselen, a seleno-organic antioxidant, as an electrophile. *Chem Res Toxicol* 19:1196-204.
64. Favrot L, Lajiness DH, Ronning DR. 2014. Inactivation of the *Mycobacterium tuberculosis* antigen 85 complex by covalent, allosteric inhibitors. *J Biol Chem* 289:25031-40.
65. Zhao R, Masayasu H, Holmgren A. 2002. Ebselen: a substrate for human thioredoxin reductase strongly stimulating its hydroperoxide reductase activity and a superfast thioredoxin oxidant. *Proc Natl Acad Sci U S A* 99:8579-84.
66. Veine DM, Mulrooney SB, Wang PF, Williams CH, Jr. 1998. Formation and properties of mixed disulfides between thioredoxin reductase from *Escherichia coli* and thioredoxin: evidence that cysteine-138 functions to initiate dithiol-disulfide interchange and to accept the reducing equivalent from reduced flavin. *Protein Sci* 7:1441-50.
67. Butts A, Krysan DJ. 2012. Antifungal drug discovery: something old and something new. *PLoS Pathog* 8:e1002870.
68. Thangamani S, Mohammad H, Younis W, Seleem MN. 2015. Drug repurposing for the treatment of staphylococcal infections. *Curr Pharm Des* 21:2089-100.

69. Sies H. 1993. Ebselen, a selenoorganic compound as glutathione peroxidase mimic. *Free Radic Biol Med* 14:313-23.
70. Zhao R, Holmgren A. 2002. A novel antioxidant mechanism of ebselen involving ebselen diselenide, a substrate of mammalian thioredoxin and thioredoxin reductase. *J Biol Chem* 277:39456-62.
71. Yang CF, Shen HM, Ong CN. 2000. Ebselen induces apoptosis in HepG(2) cells through rapid depletion of intracellular thiols. *Arch Biochem Biophys* 374:142-52.
72. Kade IJ, Balogun BD, Rocha JB. 2013. In vitro glutathione peroxidase mimicry of ebselen is linked to its oxidation of critical thiols on key cerebral suphydryl proteins - A novel component of its GPx-mimic antioxidant mechanism emerging from its thiol-modulated toxicology and pharmacology. *Chem Biol Interact* 206:27-36.
73. Azad GK, Tomar RS. 2014. Ebselen, a promising antioxidant drug: mechanisms of action and targets of biological pathways. *Mol Biol Rep* 41:4865-79.
74. Abad A, Fernandez-Molina JV, Bikandi J, Ramirez A, Margareto J, Sendino J, Hernando FL, Ponton J, Garaizar J, Rementeria A. 2010. What makes *Aspergillus fumigatus* a successful pathogen? Genes and molecules involved in invasive aspergillosis. *Rev Iberoam Micol* 27:155-82.
75. Philippe B, Ibrahim-Granet O, Prevost MC, Gougerot-Pocidallo MA, Sanchez Perez M, Van der Meer A, Latge JP. 2003. Killing of *Aspergillus fumigatus* by alveolar macrophages is mediated by reactive oxidant intermediates. *Infect Immun* 71:3034-42.
76. Singh N, Halliday AC, Thomas JM, Kuznetsova OV, Baldwin R, Woon EC, Aley PK, Antoniadou I, Sharp T, Vasudevan SR, Churchill GC. 2013. A safe lithium mimetic for bipolar disorder. *Nat Commun* 4:1332.
77. Nierman WC, Pain A, Anderson MJ, Wortman JR, Kim HS, Arroyo J, Berriman M, Abe K, Archer DB, Bermejo C, Bennett J, Bowyer P, Chen D, Collins M, Coulsen R, Davies R, Dyer PS, Farman M, Fedorova N, Fedorova N, Feldblyum TV, Fischer R, Fosker N, Fraser A, Garcia JL, Garcia MJ, Goble A, Goldman GH, Gomi K, Griffith-Jones S, Gwilliam R, Haas B, Haas H, Harris D, Horiuchi H, Huang J, Humphray S, Jimenez J, Keller N, Khouri H, Kitamoto K, Kobayashi T, Konzack S, Kulkarni R, Kumagai T, Lafon A, Latge JP, Li W, Lord A, Lu C, et al. 2005. Genomic sequence of the pathogenic and allergenic filamentous fungus *Aspergillus fumigatus*. *Nature* 438:1151-6.
78. Aliverti A, Curti B, Vanoni MA. 1999. Identifying and quantitating FAD and FMN in simple and in iron-sulfur-containing flavoproteins. *Methods Mol Biol* 131:9-23.
79. Miranda-Vizuete A, Damdimopoulos AE, Gustafsson J, Spyrou G. 1997. Cloning, expression, and characterization of a novel *Escherichia coli* thioredoxin. *J Biol Chem* 272:30841-7.
80. Wisniewski JR, Zougman A, Nagaraj N, Mann M. 2009. Universal sample preparation method for proteome analysis. *Nat Methods* 6:359-62.
81. Leslie AGW, Powell HR. 2007. Processing Diffraction Data with Mosflm, p 41–51. *In* Read RJ, Sussman JL (ed), *Evolving Methods for Macromolecular Crystallography*, vol 245. Springer, Dordrecht, The Netherlands.
82. McCoy AJ, Grosse-Kunstleve RW, Adams PD, Winn MD, Storoni LC, Read RJ. 2007. Phaser crystallographic software. *J Appl Crystallogr* 40:658-674.
83. Emsley P, Lohkamp B, Scott WG, Cowtan K. 2010. Features and development of Coot. *Acta Crystallographica Section D-Biological Crystallography* 66:486-501.
84. Afonine PV, Grosse-Kunstleve RW, Echols N, Headd JJ, Moriarty NW, Mustyakimov M, Terwilliger TC, Urzhumtsev A, Zwart PH, Adams PD. 2012. Towards automated crystallographic structure refinement with phenix.refine. *Acta Crystallogr D Biol Crystallogr* 68:352-67.
85. Winn MD, Isupov MN, Murshudov GN. 2001. Use of TLS parameters to model anisotropic displacements in macromolecular refinement. *Acta Crystallogr D Biol Crystallogr* 57:122-33.
86. Abagyan R, Totrov M, Kuznetsov D. 1994. ICM - A new method for protein modeling and design - applications to docking and structure prediction from the distorted native conformation. *Journal of Computational Chemistry* 15:488-506.
87. Schrodinger, LLC. 2015. The PyMOL Molecular Graphics System, Version 1.8.
88. Touw WG, Baakman C, Black J, te Beek TA, Krieger E, Joosten RP, Vriend G. 2015. A series of PDB-related databanks for everyday needs. *Nucleic Acids Res* 43:D364-8.
89. Krissinel E, Henrick K. 2007. Inference of macromolecular assemblies from crystalline state. *J Mol Biol* 372:774-97.
90. Baker NA, Sept D, Joseph S, Holst MJ, McCammon JA. 2001. Electrostatics of nanosystems: Application to microtubules and the ribosome. *Proceedings of the National Academy of Sciences of the United States of America* 98:10037-10041.
91. Dolinsky TJ, Nielsen JE, McCammon JA, Baker NA. 2004. PDB2PQR: an automated pipeline for the setup of Poisson-Boltzmann electrostatics calculations. *Nucleic Acids Research* 32:W665-W667.

Supplementary Information

Aspergillus fumigatus thioredoxin reductase: structure, mechanism, and inhibition

**Andrew C. Marshall¹, Mohammed A. Hossain², Georgia Arentz⁴, Peter Hoffman⁴,
Bryan R. Coad^{2,3}, and John B. Bruning^{1,*}**

¹Institute for Photonics and Advanced Sensing (IPAS), School of Biological Sciences, The University of Adelaide, Adelaide, South Australia 5005, Australia.

²Future Industries Institute, University of South Australia, Mawson Lakes, South Australia 5095, Australia.

³School of Agriculture, Food & Wine, The University of Adelaide, Adelaide, South Australia 5005, Australia.

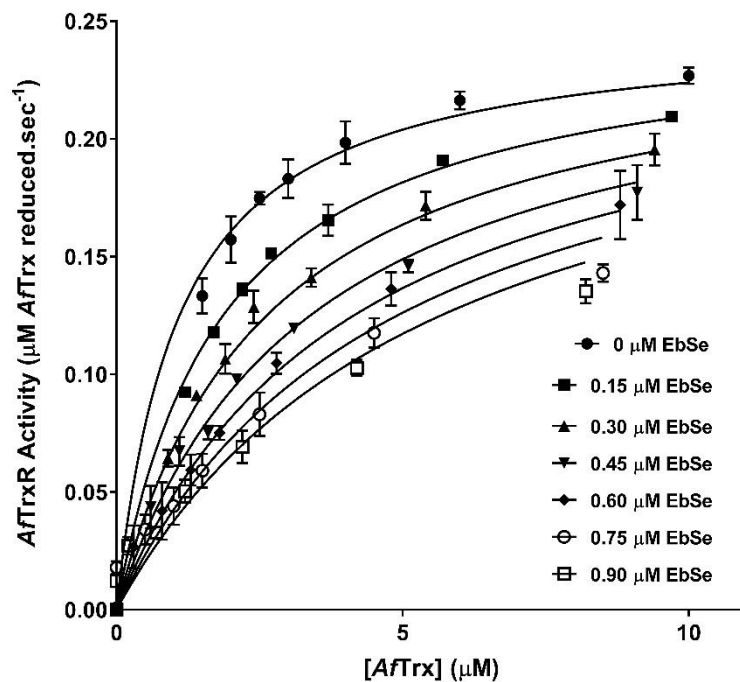
⁴Adelaide Proteomics Centre, School of Biological Sciences, University of Adelaide, Adelaide, South Australia 5005, Australia; Institute for Photonics and Advanced Sensing (IPAS), University of Adelaide, Adelaide, South Australia 5005, Australia.

*To whom correspondence should be addressed. John B. Bruning, School of Biological Sciences, Adelaide, South Australia, Australia, Tel.: +61 (08) 8313-5218; Fax: +61 (08) 8313-4362; E-mail: john.bruning@adelaide.edu.au

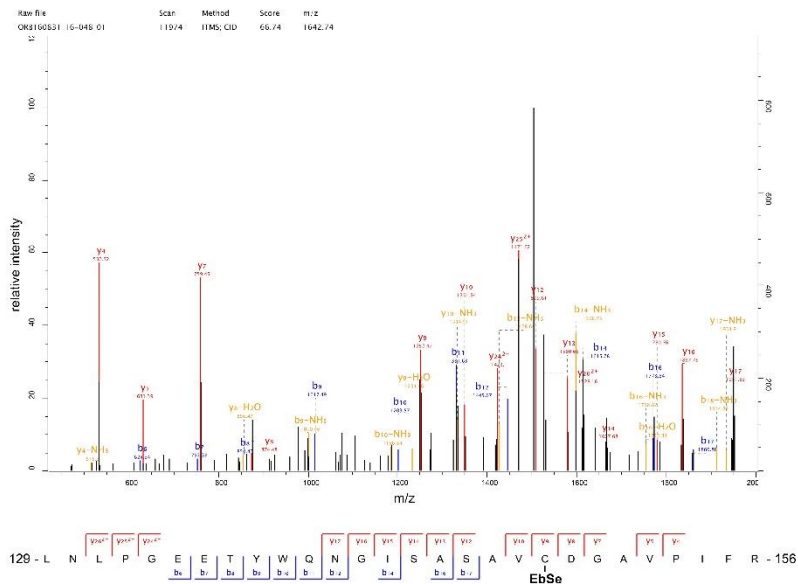
Supplementary Table 1. X-ray diffraction data collection and refinement statistics.

AfTrxR (PDB: 6BPY)	
Data collection^a	
Space group	<i>P</i> 3 ₂ 21
Cell dimensions	
<i>a</i> , <i>b</i> , <i>c</i> (Å)	159.22, 159.22, 121.37
α , β , γ (°)	90.00, 90.00, 120.00
Wavelength (Å)	0.9537
Resolution (Å)	30.0 – 3.20 (3.39 – 3.20) ^b
<i>R</i> _{merge}	0.191 (2.309)
<i>R</i> _{pim}	0.055 (0.792)
<i>CC</i> (1/2)	0.994 (0.441)
<i>I</i> / σ <i>I</i>	9.4 (0.8)
Completeness (%)	95.9 (88.9)
Redundancy	12.3 (8.2)
Refinement	
Resolution (Å)	30.0 – 3.20
No. reflections	28215
<i>R</i> _{work} / <i>R</i> _{free}	0.2310 / 0.2613
No. atoms	
Protein	4721
Ligand ^c	237
Water	45
Average <i>B</i> -factors (Å ²)	
Protein	104.1
Ligand/ion	144.5
Water	76.2
RMS deviations	
Bond lengths (Å)	0.002
Bond angles (°)	0.53

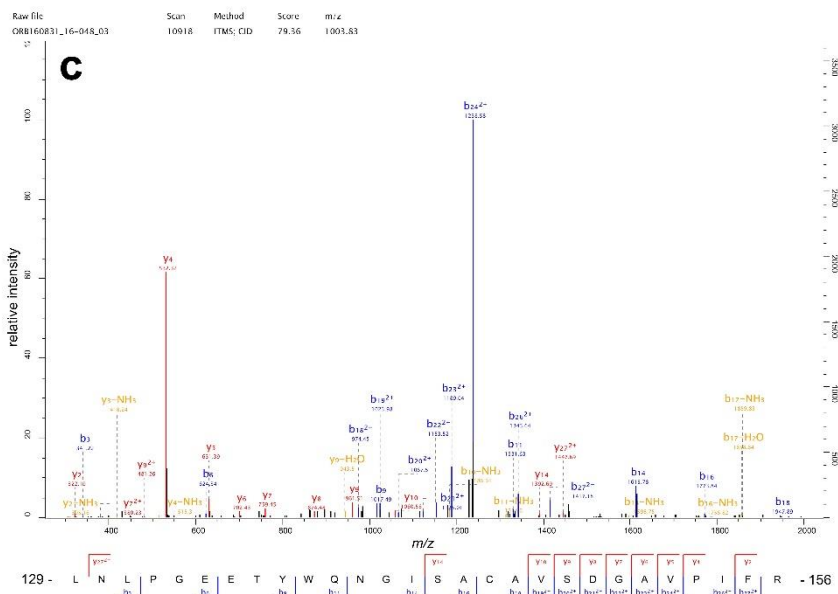
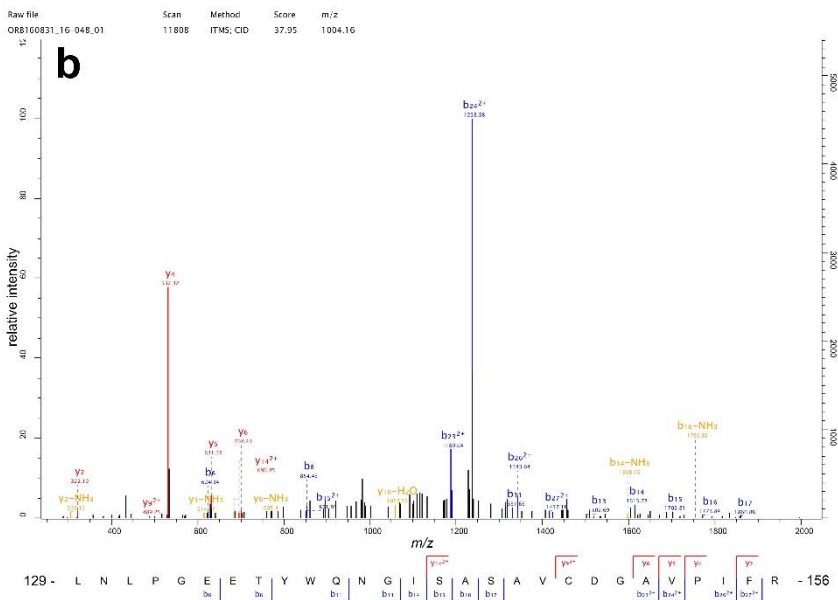
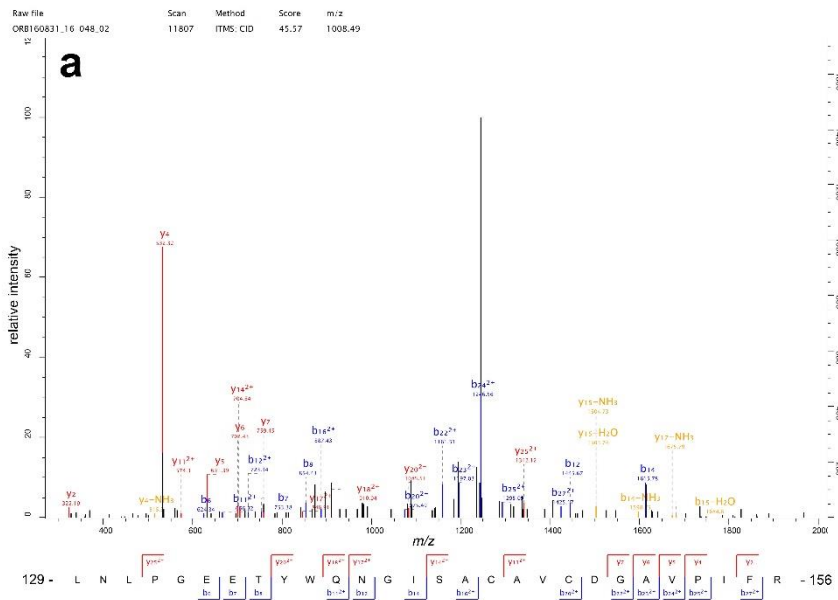
^a Data was collected from a single crystal. ^b Values in parentheses are for highest-resolution shell. ^c “Ligand/ion” includes atoms of two FAD and two NADP(H) (adenosine only) molecules, as well as seven formate, five malonate, one malate and one acetate ion.



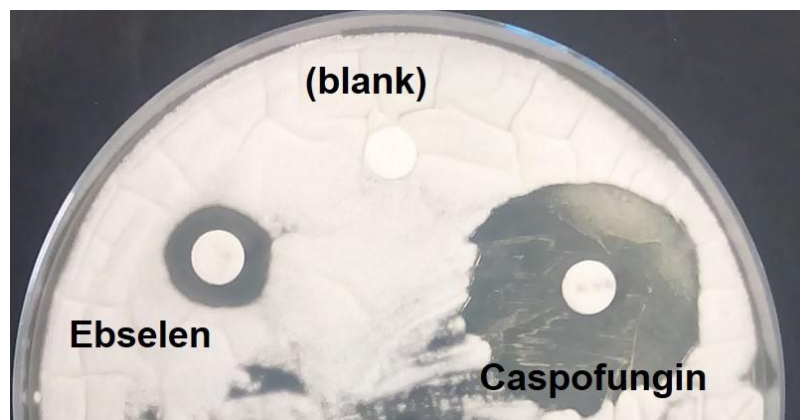
Supplementary Figure 1 | *In vitro* inhibition of AfTrxR by EbSe. Data were collected in triplicate. Error bars represent standard deviation. The standard model of competitive inhibition was fit by non-linear regression (GraphPad Prism).



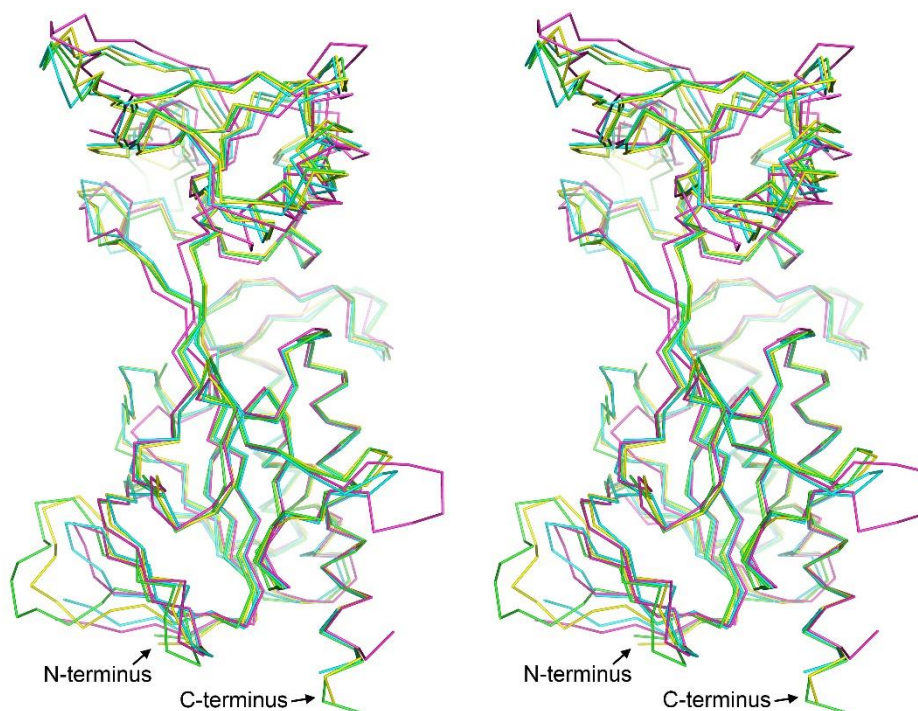
Supplementary Figure 2 | EbSe interacts covalently with Cys148 of AfTrxR. Full MS/MS data annotation of peptide isolated from AfTrxR(C145S) after incubation with excess EbSe (see Figure 2). The peptide sequence, modified by EbSe at Cys148, is shown below.



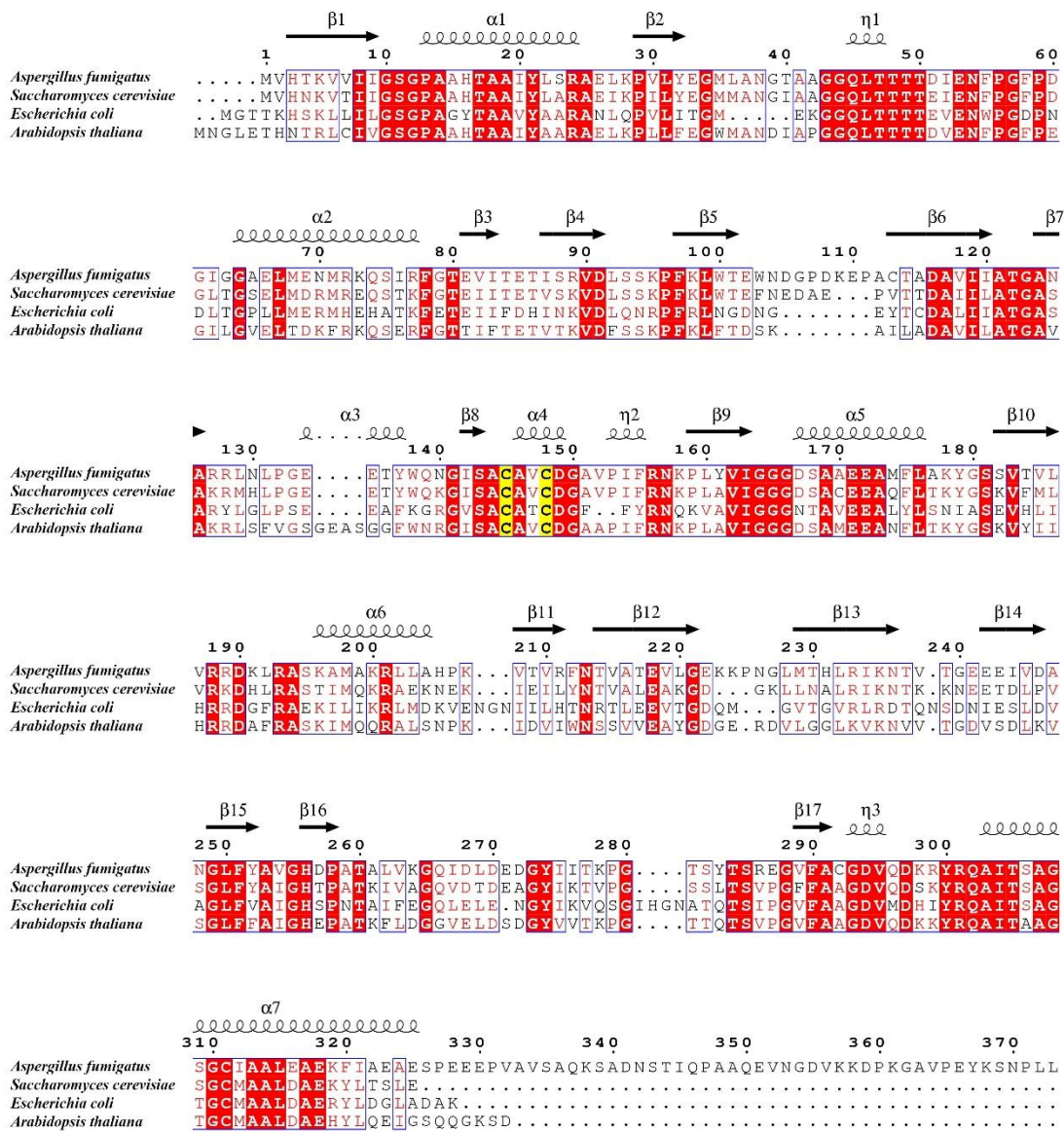
Supplementary Figure 3 (previous page) | Annotated MS/MS data for non-modified wildtype, C145S and C148S peptides. Active site peptides isolated from (a) wildtype, (b) C145S or (c) C148S *Af*TrxR proteins after incubation with excess EbSe, for which bound EbSe could not be detected. The annotated sequence for each peptide is shown below each respective spectrum.



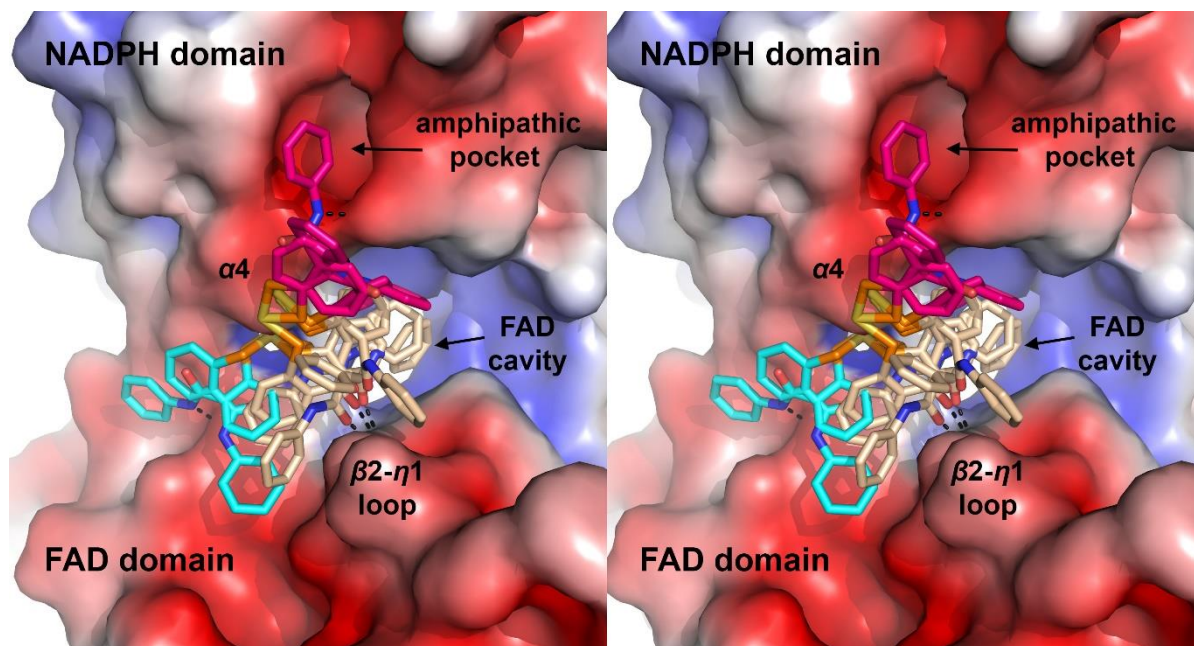
Supplementary Figure 4 | Antifungal activity of EbSe against *A. fumigatus* on solid media. Disc diffusion assay for the antifungal susceptibility testing of EbSe and caspofungin against *A. fumigatus* (ATCC MYA-3626) after 24 hours.



Supplementary Figure 5 | Superposition of low MW TrxR crystal structures shown in cross-eyed stereo view. The tertiary structures of TrxR monomers from *A. fumigatus* (green; PDB ID 6BPY), *S. cerevisiae* (yellow; PDB ID 3D8X), *E. coli* (magenta; PDB ID 1TDF) and *A. thaliana* (cyan; PDB ID 1VDC) are highly conserved, with RMSD values across all C-alphas of < 2.3 Å.



Supplementary Figure 6 | Alignment of low MW TrxR protein sequences from fungi, bacteria and plant. Conserved residues are outlined by blue boxes; those that are 100% conserved are in white text on red background; and those that are 75% conserved, or conservative substitutions, are in red text. Catalytic residues are highlighted yellow. Secondary structural features (top) refer to the *Af*TrxR crystal structure: β -strands = arrows, α -helices = large coils, 3_{10} -helices = tight coils. All four sequences have associated crystal structures (see **Supplementary Fig. 5**). The sequence alignment was calculated using Clustal omega and presented using the ESprict 3.0 web server¹. Database references: *A. fumigatus* – GenBank MG551986, *S. cerevisiae* – UniProt P29509, *E. coli* – UniProt P0A9P4, *A. thaliana* – UniProt Q39243. The N-terminal mitochondrial target peptide of *A. thaliana* TrxR (residues 1 through 42) was excluded from the alignment for clarity.



Supplementary Figure 7 | EbSe–*Af*TrxR docking results. EbSe was reacted with Cys148 *in silico*. The top ten docked poses (shown as sticks) were grouped according to their position on the surface of the protein. Group A poses (wheat) bind in the groove formed by $\alpha 4$ and the $\beta 2$ - $\eta 1$ loop leading to the FAD cavity. Group B (pink) bind exclusively to the NADPH-domain, and reach to the amphipathic pocket above the active site. Group C (cyan) bind exclusively to the FAD domain. The molecular surface of the protein is colored by electrostatic potential, -5 kT/e (red) to +5 kT/e (blue). All hydrogen bonds (black dashes) have lengths of 2.7-3.1 Å.

References for Supplementary Information

1. Robert, X. & Gouet, P. Deciphering key features in protein structures with the new ENDscript server. *Nucleic Acids Res* **42**, W320-4 (2014).

Chapter 7:

Discussion and Future Directions

7.1. Structural Characterisation of Promising Targets for New Antifungals

Resistance of pathogens to antimicrobial drugs has emerged as one of the greatest challenges of the 21st century (Butts and Krysan, 2012; Campoy and Adrio, 2017; Lewis, 2013; Ventola, 2015). Despite a large international push towards the discovery and development of new antibiotics, the need for the development of new antifungals is an area that is often overlooked. It is estimated that fungal infections affect approximately 1.2 billion people worldwide, causing between 1.5 and 2 million deaths annually (Denning and Bromley, 2015) (also see www.gaffi.org). In general, targets that lack a human homologue have traditionally been the focus for antifungal development, as reflected by the fact that most current drugs target components that are unique to fungi. More recently however, consideration of proteins with human orthologues as drug targets has broadened the scope for possible new antifungals (Butts and Krysan, 2012). High-resolution structural information is invaluable, not only for elucidating basic molecular mechanisms that are fundamental to important biological processes, but also for informing drug design, particularly in cases where the existence of human homologues presents a challenge to achieving an acceptable toxicity profile.

X-ray crystallography is the primary technique used for the determination of three-dimensional structures of proteins; however, protein structure solution is commonly hindered by the inherent difficulty of protein crystallisation (Smyth and Martin, 2000; Zheng et al., 2015). Here, by employing a high-throughput Structural Genomics-style approach at the outset, useful structural information on three proteins involved in different critical biological processes has been obtained within a relatively short timeframe. Following from successful initial screening, X-ray crystal structures have been solved and further biochemical and/or biophysical analyses have been performed on *A. fumigatus* cytosolic thiolase (afCT), proliferating cell nuclear antigen (AfumPCNA), and thioredoxin reductase (AfTrxR) – gaining a greater understanding of the basic biology of the organism and uncovering avenues for the development of new potential antifungals.

7.2. Future Directions for Three Targets that were the Focus of the Current Study

7.2.1. Cytosolic Thiolase

Ergosterol biosynthesis is well validated as a viable drug target, with three different classes of approved antifungal agents targeting different enzymes in the pathway (Campoy and Adrio, 2017). This is in addition to polyenes, which target ergosterol directly. Therefore, detailed descriptions of other enzymes involved in the ergosterol synthesis pathway could uncover further avenues for antifungal development. afCT is essential for the growth of *A. fumigatus*, catalysing the first step in ergosterol synthesis. In **Chapter 4**, the exact geometry of two previously-unobserved reaction intermediates in the thiolase catalytic site is reported. Inhibitors of acetyl-transferase enzymes that mimic tetrahedral intermediates that occur during acetyl-transfer between CoA and the enzyme have been investigated in the past (Martin et al., 1994). The crystal structures presented herein are expected to be invaluable for informing inhibitor design, leading to potential drug leads. In addition, the differences between afCT and hCT regarding particular residues surrounding their active site, their activation by monovalent cations, and their possible substrate specificities are all factors that should be considered for designing specificity into thiolase-targeting drugs.

7.2.2. Proliferating Cell Nuclear Antigen

PCNA is a central hub for a myriad of proteins including cell-cycle regulators and enzymes essential for DNA replication and repair (Moldovan et al., 2007), and therefore similarly presents as a promising drug target (see **Chapter 5**). The structural study on AfumPCNA presented herein strongly suggests that the mechanism by which DNA sliding-clamps interact with their partner proteins is largely conserved between humans and filamentous fungi. However, key structural differences at the PIP-box binding site – uncovered by the crystal structure of AfumPCNA and accompanying molecular dynamics simulation – provide a foundation for the future design of peptides and peptide mimetics that exhibit the necessary selectivity for AfumPCNA over human PCNA to serve as antifungal therapeutics. Future work should endeavour to establish the key determinants that confer high affinity of a peptide for AfumPCNA. Therefore, the next obvious step towards a peptide-based AfumPCNA inhibitor would be to first determine a PIP-box consensus sequence for *A. fumigatus*, before selecting for peptides that have the highest affinity for the protein. Given the availability of the entire *A. fumigatus* genomic sequence, it is expected that a bioinformatic analysis would be sufficient to determine an approximate PIP-box consensus. Based on the results of previous bioinformatics analysis of fungal PCNA interaction networks, this is likely to be similar to the human PIP-box consensus (Zamir et al., 2012). Various biophysical and biochemical techniques such as phage-display, fluorescence polarisation, surface plasmon resonance (SPR) and/or isothermal titration calorimetry (ITC) could be used in parallel with X-ray crystallography to select for and determine the interactions that contribute most to the affinity of a peptide for AfumPCNA.

7.2.3. Thioredoxin Reductase

An attractive approach to expedite the antifungal development process is to repurpose drugs that have already been shown to be safe for use in humans (Butts and Krysan, 2012). The repurposing of ebselen (EbSe) for the treatment of various drug-resistant bacterial pathogens has been recently investigated (Thangamani et al., 2015). The potent antifungal activity of EbSe against *A. fumigatus* demonstrated herein (see **Chapter 6**), along with its previously demonstrated activity against a number of yeast species (Chan et al., 2007; Thangamani et al., 2017), underscores this small molecule as a promising antifungal candidate. It is expected that the *in vivo* efficacy of EbSe for the treatment of fungal infections will be established in the near future. In addition, the use of EbSe in combination with other currently available antifungals should be investigated. It is suggested herein that the primary fungal target of EbSe is TrxR; however, additional research is required to provide further validation. This could include genetic and microbiological experiments such as target over-expression, isolation of mutations that confer resistance, or mass spectrometry-based proteomics.

A crystal structure of AfTrxR in complex with EbSe would allow visualisation of key drug-protein interactions. During the timeframe of the current study, extensive screening of crystallisation conditions and numerous rounds of optimisation resulted in the ability to produce large crystals of AfTrxR(C145S) protein (truncated at the C-terminus) after incubation with excess EbSe, in a reproducible manner (see Appendix 4). Unfortunately, these crystals did not diffract X-rays to sufficient resolution to allow for structure solution. A sharp decline in the intensity of reflections at a resolution of approximately 5 to 10 Å was typical. It is possible that the large domain rotation inherent to the function of TrxR promotes a degree of

flexibility within the crystal lattice that is hindering high-resolution diffraction. This is consistent with the marked decrease in the R_{free} value observed when implementing TLS parameters during refinement of the *AfTrxR* structure (without EbSe), for which the highest resolution diffraction data obtained was still modest (3.2 Å). Further attempts at crystal optimisation could include: the addition of detergents and other additives, limited proteolysis to remove flexible regions and determine the optimal construct, and crystal seeding to uncover new conditions in which nucleation is impossible but crystal growth can occur.

In lieu of a crystal structure, *in silico* modelling experiments suggest that, although the major contribution to the EbSe-*AfTrxR* interaction is the covalent bond formed to Cys148, a number of secondary interactions may be exploited by possible EbSe analogues to enhance affinity and specificity. Employing other biophysical analyses, such as ITC and SPR, to determine the binding affinities of EbSe and EbSe analogues to stable TrxR mutants lacking the active site cysteines would allow determination of the relative contribution of the covalent and non-covalent interactions to the inhibition of TrxR by EbSe.

7.3. Additional Targets for Future Investigation

In addition to the three proteins that were the focus of this study, a number of other initial targets showed promising preliminary results. In particular, IreA, enzymes of the β -oxidation pathway, and chitin synthases present as good candidates for further investigation.

7.3.1 The Master Regulator of the UPR: IreA

Perturbations in endoplasmic reticulum (ER) homeostasis (ER stress) may lead to the accumulation of unfolded proteins; therefore, maintenance of ER homeostasis is essential for cell survival. The unfolded protein response (UPR) is comprised of the signalling pathways that are activated in eukaryotic cells in response to ER stress, and collectively prevent the folding capacity of the ER from being overwhelmed. When activated, the UPR acts to increase protein folding machinery and total ER volume, stimulate degradation of misfolded proteins, and attenuate overall protein synthesis (Kaufman, 2002; Liu and Kaufman, 2003; Ron and Hubbard, 2008). Higher eukaryotes possess three distinct but overlapping pathways that constitute the UPR, regulated by three ER-localised transmembrane receptors: Ire1, PERK and ATF6. Each of these has a luminal domain that detects ER stress and a cytoplasmic effector domain that passes the signal on to downstream components (Ron and Hubbard, 2008). Ire1 mediates the most conserved UPR pathway, present in all eukaryotes, whereas ATF6 and PERK pathways are not conserved in lower eukaryotes (Liu and Kaufman, 2003). Ire1 is a single pass transmembrane protein and has been extensively studied in *Saccharomyces cerevisiae*. Ire1 oligomerises in response to accumulation of unfolded proteins in the ER, leading to trans-autophosphorylation of its cytosolic Ser/Thr kinase domain. This activates its C-terminal RNase domain, which processes the *HAC1* mRNA allowing it to be translated, producing HAC1; a potent transcription factor that activates expression of many UPR-inducible genes (Kaufman, 2002; Shamu and Walter, 1996). The *A. fumigatus* Ire1 homologue, IreA, is the master regulator of the UPR. A recent study showed that, in addition to UPR activation in response to acute ER stress, IreA is essential for growth and maintenance of homeostasis in changing or adverse environmental conditions. IreA was shown to be an

important contributor to growth at mammalian body temperature, growth on complex media, iron acquisition, growth under hypoxic conditions and cell wall homeostasis. Together, HacA (the HAC1 homologue) and IreA were shown to influence expression of greater than 13% of all *A. fumigatus* ORFs (Feng et al., 2011; Krishnan and Askew, 2014). Significantly, deletion of IreA resulted in a mutant that was completely avirulent in a mouse model of IA. In addition, *A. fumigatus* mutants defective in UPR activation showed a significant increase in caspofungin, itraconazole, voriconazole and amphotericin B susceptibilities (Feng et al., 2011; Richie et al., 2009). The role of IreA as a master regulator of gene expression in combination with its multidomain structure presents it as a promising target for novel anti-fungal therapies. Drugs that target any of the three functional domains of IreA are conceivable. In addition, the three overlapping UPR pathways that are possessed by higher eukaryotes may make human cells more resilient to effects produced by cross-reactivity of inhibitors with human Ire1, reducing side-effects associated with future antifungals that target IreA.

The crystal structure of the luminal domain of yeast Ire1 has been solved previously (Credle et al., 2005). Mutations in putative interaction interfaces suggested that both dimerisation and oligomerisation of the luminal domain are essential for UPR activation, a finding that is consistent with previous studies (Liu et al., 2000; Liu et al., 2002; Shamu and Walter, 1996). In addition, it exhibits a deep groove, formed by parallel α -helices supported by an antiparallel β -sheet platform; reminiscent of the peptide binding region of Major Histocompatibility Complex (MHC) proteins. Sequence and mutational analysis of residues involved in forming the base of this groove demonstrated that they are highly conserved and important for UPR activation by Ire1. This supports the hypothesis that the luminal domain is able to directly bind to linear peptides, and that this may be a mechanism by which it senses unfolded proteins in the ER (Credle et al., 2005). The luminal domain of IreA may therefore present as a promising novel target for anti-*Aspergillus* peptide-mimetic drugs. A crystal structure of the *A. fumigatus* IreA luminal domain would be invaluable for further investigating this hypothesis.

So far, a large homogenous sample of the luminal domain of *A. fumigatus* IreA as recombinant soluble protein has been successfully obtained, and screening for crystallisation conditions has commenced (see **Appendix 3**). Further work is needed to produce diffraction-quality crystals. In addition, investigation of the peptide binding properties of this domain would be useful for informing inhibitor design, and shed light on its molecular mechanism and biological function. A protocol used previously to isolate endogenous peptides bound to a human class I MHC molecule (Jardetzky et al., 1991) could be used to identify peptides that are bound by IreA. Briefly, purified recombinant IreA luminal domain would be mixed with soluble *A. fumigatus* extract, purified a second time to remove non-interacting peptides, and washed in denaturing conditions by centrifugal filtration. Recovered peptides could then be identified by mass spectrometry. Furthermore, a co-crystal structure of IreA with a bound peptide is expected to shed light on key peptide binding interactions – valuable information for informing the design of future synthetic or peptide-based inhibitors.

7.3.2. Chitin Synthases

Chitin, a homopolymer of $\beta(1,4)$ -linked N-acetylglucosamine, is an essential structural component of the fungal cell wall (Lenardon et al., 2010; Roncero, 2002). Its essentiality to fungal survival and its absence in mammalian cells make it an attractive target for antifungal drugs (Campoy and Adrio, 2017). Chitin synthases (ChS) synthesise chitin from UDP-N-

acetylglucosamine. Despite being the second most abundant biopolymer on the planet, the details of the regulation and mechanism of chitin synthesis are lacking. All ChSs contain a signature motif (QRRRW), essential for catalytic activity, and most are zymogenic and plasma-membrane bound (Roncero, 2002). Based on phylogenetic analysis, ChSs can be divided into seven classes and two distinct families. Family 1 consists of classes I – III and family 2 consists of classes IV – VII (Muszkieta et al., 2014; Roncero, 2002). *A. fumigatus* has eight ChS genes that encompass all seven classes. Enzymes from family 1 are: ChSA (Class I), ChSB (Class II), ChSC (Class III) and ChSG (Class III); family 2 are: ChSF (Class IV), CSMA (previously annotated as ChSE) (Class V), ChSD (Class VI) and CSMB (Class VII) (Jimenez-Ortigosa et al., 2012; Muszkieta et al., 2014). There exist complex and poorly defined relationships between the activities of these different ChSs, and between ChS activity and the overall content of different polysaccharides in the fungal cell wall. This, along with the large number of genes and a possible level of redundancy, makes assigning functions to specific ChSs very difficult (Muszkieta et al., 2014). It has been hypothesised that chitin may be structured in different ways in the cell wall by different ChSs, rather than existing as a simple homogenous polymer, although the functional significance of this remains unknown. Extensive mutagenesis studies have largely failed to establish a clear morphogenetic trend, and results are often difficult to interpret. Single and multiple gene deletions of ChSA, ChSB, ChSC, ChSD or ChSF have resulted in minor or no changes in phenotype, with no observable effect on growth rate or virulence, suggesting that there exists a level of redundancy (Mellado et al., 1996; Muszkieta et al., 2014; Rogg et al., 2011). Deletion of ChSG resulted in a significant growth defect on solid media, with a radial colony growth rate of approximately 30% of the wild-type strain, and a more branched hyphal morphology. Conidial cell walls appeared less organised when compared to wild-type, with the melanin layer only loosely attached to the surface. In addition, total mycelial ChS activity was reduced by 90% compared to the parental strain, suggesting that ChSG is the main contributor to ChS activity (Mellado et al., 1996; Muszkieta et al., 2014). Notably, a $\Delta ChSC/\Delta ChSG$ double deletion mutant exhibited poor conidiation and decreased virulence in a murine model of pulmonary aspergillosis (Mellado et al., 1996). Deletion of CSMA results in poor conidiation and periodic hyphal swelling (Aufauvre-Brown et al., 1997), and reductions in colony growth rate, total ChS activity (30% of wild-type activity) and conidial cell wall chitin content (20% of wild-type) (Muszkieta et al., 2014). CSMA and CSMB have both been shown to be essential for proper conidia cell surface modelling, with gene knockouts resulting in a loss of conidia surface hydrophobicity associated with malformation of the surface rodlet layer and an easily detachable melanin layer, an increase in exposed immunostimulatory polysaccharides leading to a more effective immune response in vitro, and much larger swollen conidia, suggesting that the cell wall is softer and more fragile under external stress (Alsteens et al., 2013; Jimenez-Ortigosa et al., 2012; Muszkieta et al., 2014). In addition, $\Delta CSMA$ and $\Delta CSMB$ mutants exhibited alterations in hyphal morphology associated with irregular distribution of chitin in the mycelial cell wall, and much shorter chitin fibrils. Notably, these mutants displayed decreased sensitivity to Nikkomycin Z (a chitin synthesis inhibitor), but a significant increase in susceptibility to echinocandins (β -glucan synthesis inhibitors) (Jimenez-Ortigosa et al., 2012; Muszkieta et al., 2014). This is consistent with the apparent compensatory reaction that occurs between cell wall β -glucan synthesis and chitin synthesis when either process is inhibited independently, and also the strong antifungal synergy observed between Nikkomycin Z and echinocandins when used in combination (Chiou et al., 2001; Stevens, 2000; Verwer et

al., 2012). Deletion of all four family 2 genes resulted in a significant reduction in virulence in an immunocompromised mouse model (Muszkieta et al., 2014). This mutant was completely avirulent in mice undergoing caspofungin-treatment, whereas the wild-type strain caused 100% mortality after 5 days. Interestingly, a family 2 triple mutant ($\Delta CSMA/CSMB/CHSF$) showed no growth at 50°C, but was rescued by further deletion of *CHSD*. This, along with the observation that a simple $\Delta CHSD$ mutant had higher mycelial cell wall chitin levels, suggests that ChSD may act as a negative regulator of chitin synthesis (Muszkieta et al., 2014). The most severe morphological defects were observed when ChS genes were deleted from both families in a single strain, suggesting the presence of a level of cooperation between members of the two families. A $\Delta CSMA/CHSG$ double mutant showed decreased ChS activity, cell wall chitin levels, colonial growth rate and conidiation, in addition to highly branched and swollen hyphae (Mellado et al., 2003). Further deletion of *CSMB* and *CHSF* ($\Delta CSMA/CSMB/CHSF/CHSG$) resulted in severe hyphal swelling and branching, significant alterations in cell wall polysaccharide composition, a complete inability to produce conidia, and a drastic reduction in growth rate at 37°C (less than 16% of wild-type growth) (Muszkieta et al., 2014).

Despite its obvious potential as a target for novel antifungals, fundamental details of chitin biosynthesis and regulation are poorly understood. Solving the structure of even one ChS would be a significant step toward a detailed understanding of the molecular mechanisms that underlie the synthesis and regulation of this important structural polymer.

The results presented in **Chapter 3** show the successful recovery of partially purified samples of the putative catalytic domains of *A. fumigatus* CSMA and ChSF, which appear to be soluble when fused to MBP (see **Chapter 3, Figure 5**). If large-scale purification is successful, screening for crystallisation conditions will commence. Alternatively, other expression systems may be employed, such as *Pichia pastoris* (Ahmad et al., 2014). Here, genes codon-optimised for *P. pastoris* expression would be cloned into appropriate vectors and tested for methanol-induced expression of recombinant protein. Using a yeast expression system provides the option of incorporating a tag for protein secretion, which often simplifies the protein purification process as it renders cell lysis unnecessary; thus, all intracellular proteins are simply removed when cells are separated from the growth media.

The putative catalytic domain of a ChS from *Botrytis cinerea* has been successfully purified as recombinant protein previously (Magellan et al., 2010). Despite showing favourable affinity for substrate, this construct was catalytically inactive. This suggests that other domains, transmembrane segments and/or loops may be essential for catalysis and processivity. Establishing a protocol for the purification of a full length ChS would be a significant step forward in the investigation chitin synthesis.

7.3.3. The β -Oxidation Pathway

The use of fatty acids as a source of energy involves four steps, each catalysed by a different enzyme, to convert acyl-CoA substrates into acetyl-CoA and an acyl-CoA molecule shortened by two carbon atoms, which is available to undergo subsequent β -oxidation cycles (Kunau et al., 1995). The importance of β -oxidation for the virulence of fungal pathogens, particularly those for which the lung is the primary site of infection, has been indicated previously (Kretschmer et al., 2012; Ramirez and Lorenz, 2009). The fungal kingdom exhibits a huge

diversity of β -oxidation pathways (Shen and Burger, 2009) and very little is known about the details of this pathway in specific species. The preliminary results presented in **Chapter 3** show that the recovery of soluble MBP-fusion proteins for all four *A. fumigatus* β -oxidation enzymes is possible using the protocol contained herein (see **Chapter 3**, **Figure 5**, and **Appendix 2**). Subsequent large-scale purification and screening for crystallisation conditions is currently being undertaken. Crystallographic analysis of all four β -oxidation enzymes, along with biochemical studies to determine kinetic parameters and substrate length preference, will be valuable for gaining a better understanding of an important process fundamental to the basic biology of *A. fumigatus*.

7.4. Concluding Remarks

The current project has shown that applying a standardised high-throughput methodology within the context of a small research laboratory is an efficient approach to gain a wealth of new information useful for uncovering biological mechanisms and informing future development of drugs. Powerful structural biology methodologies – most notably X-ray crystallography (Zheng et al., 2015), nuclear magnetic resonance spectroscopy (Li and Kang, 2017) and the recent advent of near atomic resolution cryo-electron microscopy (Cheng et al., 2017) – continue to emerge and develop, improving our understanding of macromolecular structures and their interactions. As these technologies become more standardised, it is anticipated that increasing numbers of smaller research groups will be able to readily apply these methods, contributing to our understanding of the basic processes that underlie biological functions, and providing a secure foundation for the development of therapeutics to combat existing and emerging diseases.

Appendices

Appendix 1 – PCR Primer Sequences for Preliminary Targets

All sequences are typed 5' to 3'. Gateway® recombination sites are underlined; coding sequence for TEV protease cleavage site is in bold; coding sequence for protein of interest is in capitals.

ECH_F: ggggacaagttgtacaaaaagcaggctat**gaaaacctgtatttcagggga**ATGCCCTCAATACATCCCC
ECH_R: ggggaccactttgtacaagaaagctgggtaTTACAACCTTGCTGTCCACCC
ACD_F: ggggacaagttgtacaaaaagcaggctac**gaaaacctgtatttcagggga**ATGGCATCTATCGCCCGT
ACD_R: ggggaccactttgtacaagaaagctgggtaCTATTTAGTGTACTGCTTTTGCAGGA
3HACD_F: ggggacaagttgtacaaaaagcaggctac**gaaaacctgtatttcagggga**ATGGCTCAATTCATCCCAC
3HACD_R: ggggaccactttgtacaagaaagctgggtaCTATTGAGCCCAATCCATGC
KAT1_F: ggggacaagttgtacaaaaagcaggctac**gaaaacctgtatttcagggga**ATGGCCGAGATCGCCTA
KAT1_R: ggggaccactttgtacaagaaagctgggtaTTAAACCTGCTCGTTCACAAACAAAC
TRR1_F: ggggacaagttgtacaaaaagcaggctac**gaaaacctgtatttcagggga**ATGGTGCACACAAAAGTTACCA
TRR1_R: ggggaccactttgtacaagaaagctgggtaTTAGAGAAGAGGGTTCGACTTGTATT
GFA1_F: ggggacaagttgtacaaaaagcaggctac**gaaaacctgtatttcagggga**ATGTGCGGTATCTTCGGCTA
GFA1_R: ggggaccactttgtacaagaaagctgggtaTTATTCAACGGTGACCGATTT
HEM15_F: ggggacaagttgtacaaaaagcaggctac**gaaaacctgtatttcagggga**ATGGCTCTCCGCCGGCCATTA
HEM15_R: ggggaccactttgtacaagaaagctgggtaCTAAACTACAAGAGAAGAAAATCGGTGCGC
ERG10_F: ggggacaagttgtacaaaaagcaggctac**gaaaacctgtatttcagggga**ATGTCTTCGCTTCCAGCTGT
ERG10_R: ggggaccactttgtacaagaaagctgggtaCTAAAGTAGCTCAACCACCAGAGC
IREA_101F: ggggacaagttgtacaaaaagcaggctat**gaaaacctgtatttcagggga**GCGCGGTCTCTGCAG
IREA_453R: ggggaccactttgtacaagaaagctgggttaGCCATTCAGCGAGTGAAC
IREA_702F: ggggacaagttgtacaaaaagcaggctat**gaaaacctgtatttcagggga**GGTGTCTTCAAATTGGTCGTC
IREA_1165R: ggggaccactttgtacaagaaagctgggttaCTCAACCGGAGTAAAATATCGTTTG
CHSA_163F: ggggacaagttgtacaaaaagcaggctat**gaaaacctgtatttcagggga**CACGGTAACCTGGTCCTGG
CHSA_545R: ggggaccactttgtacaagaaagctgggtattaACTTCCGTTTCAGCCATCTG
CHSB_281F: ggggacaagttgtacaaaaagcaggctat**gaaaacctgtatttcagggga**GCTCCTGAAAAGCAAAGTCG
CHSB_703R: ggggaccactttgtacaagaaagctgggtattaAGAGTGGTCGGTCTTCCAAG
CHSC_160F: ggggacaagttgtacaaaaagcaggctat**gaaaacctgtatttcagggga**CATGAAGAATTCACGCATATGC
CHSC_525R: ggggaccactttgtacaagaaagctgggtattaGGAGCCATTGAGCCATCG
CHSD_100F: ggggacaagttgtacaaaaagcaggctat**gaaaacctgtatttcagggga**ACCGCTCCCAAACAGTTG
CHSD_396R: ggggaccactttgtacaagaaagctgggtattaGCGCTTCAAAGCCGC
CHSF_635F: ggggacaagttgtacaaaaagcaggctat**gaaaacctgtatttcagggga**CACGAAGCGGTTGTCCC
CHSF_1019R: ggggaccactttgtacaagaaagctgggtattaTGTACCGCAAAGATCCCG

CHSG_141F: ggggacaagttgtacaaaaagcaggctatgaaaacctgtatttcaggggGCTACAAGAAAGGTCAAGTTGG

CHSG_562R: ggggaccactttgtacaagaaagctgggtattaTCCA CTCTTG TACATCCGACC

CSMA_1231F:

ggggacaagttgtacaaaaagcaggctatgaaaacctgtatttcaggggTTGGATAAGTTCATCATCTGTCAAG

CSMA_1564R: ggggaccactttgtacaagaaagctgggtattaGGAGTTGATCCACCGACG

CSMB_1054F:

ggggacaagttgtacaaaaagcaggctatgaaaacctgtatttcaggggCAAGATAAGTTTGTCAATTTGTCTCG

CSMB_1405R: ggggaccactttgtacaagaaagctgggtattaGCCACACAGGTCCTTCAGAG

PCR products were incorporated into appropriate Gateway® vectors using BP and LR Clonase enzyme mixes (ThermoFisher Scientific) according to the manufacturer's protocol.

Appendix 2 – Small-Scale Protein Expression and Solubility Testing Protocol

Expression of heterologous protein was induced in *E. coli* BL21(λ DE3) cells in 10 mL Luria-Bertani (LB) broth by the addition of 0.5 mM isopropyl β -D-1-thiogalactopyranoside (IPTG) to log-phase cultures (when OD₆₀₀ reached approx. 0.5), before incubation with shaking at 16°C overnight. The next morning cultures were harvested, resuspended in 1 mL of the initial purification buffer (0.5 M NaCl, 20 mM Tris pH 8.0, 10% glycerol, 10 mM imidazole, 5 mM β -mercaptoethanol (BME)), and stored at -80°C until required. Cells were lysed by vortexing with 0.1 mm glass beads for 5 min at 4°C. Following clarification of cell lysate by centrifugation, protein was recovered by batch purification with Ni-NTA resin, eluted with buffer containing 500 mM imidazole, and analysed by SDS-PAGE (see **Chapter 3, Figure 5**).

Appendix 3 – Protein Purification and Preliminary Crystallisation Screening for the *A. fumigatus* IreA Luminal Domain

Purification of the IreA luminal domain (IreA.LD) was made difficult due to the inefficiency of the TEV protease digest, and subsequent inability to isolate the cleaved protein from MBP – which has a very similar molecular weight to IreA.LD – and the remaining MBP-IreA.LD fusion. This truncation was subsequently re-cloned into a vector for its expression as a 6xhis-NusA-tagged fusion (pET-57-DEST), and expression of recombinant H6-NusA-IreA.LD was induced in a 4 L *E. coli* BL21(λDE3) culture overnight at 16°C. Cells were resuspended in buffer (0.5 M NaCl, 20 mM Tris pH 8.0, 10% glycerol, 10 mM imidazole, 5 mM BME) and lysed by mechanical disruption before insoluble cell debris was removed by centrifugation. Cell lysate was subject to Ni-affinity chromatography using a 5 mL Ni-NTA column (Bio-Rad), with sequential 10 and 25 mM imidazole wash steps, followed by elution of his-tagged protein with buffer containing 250 mM imidazole. Fractions containing H6-NusA-IreA.LD were pooled and dialysed to 0.5 M NaCl, 20 mM Tris pH 8.0, 10% glycerol, 1 mM imidazole, 5 mM BME, in the presence of TEV protease at an approximate 4:1 ratio of protein:TEV by mass. Dialysis was at room temperature for 30 min, then 16°C overnight. Dialysed protein was passed through the Ni-IMAC column again to remove the H6-NusA tag, with cleaved IreA.LD present in the flow-through. This was dialysed to 20 mM NaCl, 20 mM Tris pH 8.0, 10% glycerol, 1 mM DTT, loaded onto a 1 mL ENrichQ column (Bio-Rad), and eluted using a 20–700 mM NaCl gradient. Fractions containing IreA.LD were pooled (3 mL), diluted to 10 mL with 50 mM NaCl, 20 mM Tris pH 7.5, 1 mM DTT and passed through an SEC Sephacryl 26/60 S-300 column (GE) (**Figure A2**). Fractions containing IreA.LD were pooled and concentrated to approximately 10 mg/mL. Final protein yield was 12 mg (from 4 L culture). This sample was immediately subject to crystallisation screening using the sitting drop vapour-diffusion method, with a 75 μL reservoir volume under 2 μL drops (1 μL protein sample + 1 μL reservoir solution). A range of commercial sparse matrix screens in 96-well format (Hampton Research, Molecular Dimensions) were employed. Only very small, non-diffracting crystals have been obtained thus far (not shown).

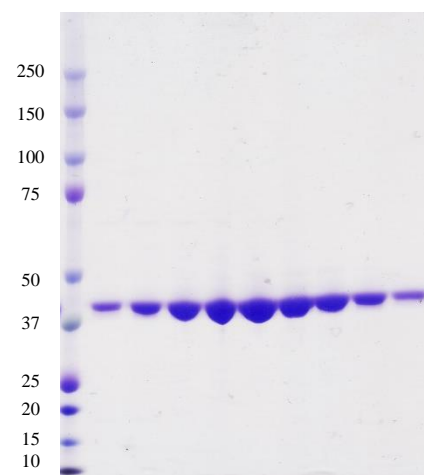


Figure A2. SDS-PAGE analysis of consecutive size-exclusion chromatography fractions containing recombinant IreA.LD protein (retention = 0.5 to 0.6 column volumes). Protein standards are shown (left) with masses indicated in kDa.

Appendix 4 – Co-crystallisation of AfTrxR in Complex with EbSe: Preliminary Results

Crystallisation of AfTrxR in complex with EbSe was attempted by both crystal soaking and co-crystallisation. However, it was observed that AfTrxR (apo) crystallised in FO conformation, whereas the *in silico* experiments strongly suggest that EbSe binds to AfTrxR in FR conformation (see **Chapter 6**). This makes it highly unlikely that EbSe can access the AfTrxR active site in the current crystallisation condition, and has prompted a focus on co-crystallisation of the AfTrxR-EbSe complex. For this, Cys145 of AfTrxR was mutated to serine, and residues 328 through 373 at the C-terminus removed (disordered region in crystal structure; see **Chapter 6**), to result in AfTrxR(C145S)trunc. This was over-expressed with a TEV-cleavable N-terminal 6xhis and NusA tag in *E. coli* BL21(λ DE3) from a pET-57-DEST vector. Protein was initially purified from lysate essentially as described for H6-NusA-IreA.LD (see **Appendix 3**) – involving two stages of Ni-affinity chromatography with a TEV protease digest in between to remove the H6-NusA tag. AfTrxR(C145S)trunc was further purified by hydrophobic interaction chromatography (HIC) using a 5 mL HiPrep Phenyl column (GE Healthcare) equilibrated in 0.75 M $(\text{NH}_4)_2\text{SO}_4$, 0.5 M NaCl, 20 mM Tris pH 8.0, and eluted using a gradient to a buffer containing 20 mM Tris pH 8.0 only. Fractions containing AfTrxR(C145S)trunc were concentrated to approx. 10 mL, incubated with 5x molar excess FAD for 45 min at room temperature in the dark, and passed through an SEC Sephacryl 26/60 S-300 column (GE) equilibrated in 20 mM Tris pH 7.5, 50 mM NaCl. Protein was concentrated to 24 mL and incubated with 1 molar equivalent FAD, 5x molar excess NADPH and 40x molar excess EbSe for 5 hr at room temperature in the dark. This sample was then passed through the SEC Sephacryl 26/60 S-300 column (GE) equilibrated in 20 mM Tris pH 7.5, 100 mM NaCl. Fractions containing AfTrxR(C145S)trunc were concentrated to approx. 10 mg/mL and subject to crystallisation trials immediately using the hanging drop vapour-diffusion method, with 500 μL reservoir volumes and 2 to 10 μL drop sizes containing 2:1, 1:1 or 2:3 ratios of reservoir:protein sample. Large crystals grew in conditions containing PEG3350 and NH_4NO_3 or CsCl after 3 days (**Figure A3**). The best of these diffracted X-rays to approx. 5 Å at the MX1 Beamline at the Australian Synchrotron (data not shown).

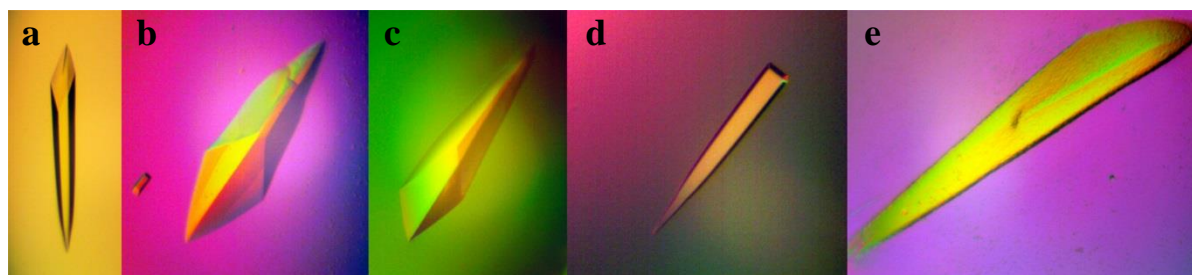


Figure A3. Crystals of AfTrxR(C145S)trunc protein co-purified with EbSe. The bound FAD cofactor gives them a yellow colour. These crystals have lengths (maximum dimension) of between 0.3 and 1 mm, and grew in (a) 15% PEG3350, 75 mM KCl; (b) 16.5% PEG3350, 130 mM CsCl, 10 mM KCl; (c) 14% PEG3350, 70 mM NH_4NO_3 ; (d) 15% PEG3350, 60 mM NH_4NO_3 ; (e) 18% PEG3350, 120 mM NH_4NO_3 .

Bibliography

This includes references for publications cited in Chapters 1, 2, 3 and 7. Bibliographies for Chapters 4, 5 and 6 are included at the end of each chapter.

Abad, A., Fernandez-Molina, J.V., Bikandi, J., Ramirez, A., Margareto, J., Sendino, J., Hernando, F.L., Ponton, J., Garaizar, J., and Rementeria, A. (2010). What makes *Aspergillus fumigatus* a successful pathogen? Genes and molecules involved in invasive aspergillosis. *Revista iberoamericana de micologia* 27, 155-182.

Ahmad, M., Hirz, M., Pichler, H., and Schwab, H. (2014). Protein expression in *Pichia pastoris*: recent achievements and perspectives for heterologous protein production. *Applied microbiology and biotechnology*.

Alcazar-Fuoli, L., and Mellado, E. (2012). Ergosterol biosynthesis in *Aspergillus fumigatus*: its relevance as an antifungal target and role in antifungal drug resistance. *Frontiers in microbiology* 3, 439.

Ali, M.M., Bagratuni, T., Davenport, E.L., Nowak, P.R., Silva-Santisteban, M.C., Hardcastle, A., McAndrews, C., Rowlands, M.G., Morgan, G.J., Aherne, W., et al. (2011). Structure of the Ire1 autophosphorylation complex and implications for the unfolded protein response. *The EMBO journal* 30, 894-905.

Alsteens, D., Aimaniananda, V., Hegde, P., Pire, S., Beau, R., Bayry, J., Latge, J.P., and Dufrene, Y.F. (2013). Unraveling the nanoscale surface properties of chitin synthase mutants of *Aspergillus fumigatus* and their biological implications. *Biophysical journal* 105, 320-327.

Anderson, W.F. (2009). Structural genomics and drug discovery for infectious diseases. *Infectious disorders drug targets* 9, 507-517.

Arendrup, M.C., Garcia-Effron, G., Buzina, W., Mortensen, K.L., Reiter, N., Lundin, C., Jensen, H.E., Lass-Flörl, C., Perlin, D.S., and Bruun, B. (2009). Breakthrough *Aspergillus fumigatus* and *Candida albicans* double infection during caspofungin treatment: laboratory characteristics and implication for susceptibility testing. *Antimicrobial agents and chemotherapy* 53, 1185-1193.

Arendrup, M.C., Perkhofer, S., Howard, S.J., Garcia-Effron, G., Vishukumar, A., Perlin, D., and Lass-Flörl, C. (2008). Establishing in vitro-in vivo correlations for *Aspergillus fumigatus*: the challenge of azoles versus echinocandins. *Antimicrobial agents and chemotherapy* 52, 3504-3511.

Arora, A., Chandra, N.R., Das, A., Gopal, B., Mande, S.C., Prakash, B., Ramachandran, R., Sankaranarayanan, R., Sekar, K., Suguna, K., et al. (2011). Structural biology of *Mycobacterium tuberculosis* proteins: the Indian efforts. *Tuberculosis (Edinburgh, Scotland)* 91, 456-468.

Aufauvre-Brown, A., Mellado, E., Gow, N.A., and Holden, D.W. (1997). *Aspergillus fumigatus* chsE: a gene related to CHS3 of *Saccharomyces cerevisiae* and important for hyphal growth and conidiophore development but not pathogenicity. *Fungal genetics and biology: FG & B* 21, 141-152.

Balajee, S.A., Weaver, M., Imhof, A., Gribskov, J., and Marr, K.A. (2004). *Aspergillus fumigatus* variant with decreased susceptibility to multiple antifungals. *Antimicrobial agents and chemotherapy* 48, 1197-1203.

- Bates, D.W., Su, L., Yu, D.T., Chertow, G.M., Seger, D.L., Gomes, D.R., Dasbach, E.J., and Platt, R. (2001). Mortality and costs of acute renal failure associated with amphotericin B therapy. *Clinical infectious diseases: an official publication of the Infectious Diseases Society of America* 32, 686-693.
- Bolard, J. (1986). How do the polyene macrolide antibiotics affect the cellular membrane properties? *Biochimica et biophysica acta* 864, 257-304.
- Butts, A., and Krysan, D.J. (2012). Antifungal drug discovery: something old and something new. *PLoS pathogens* 8, e1002870.
- Campoy, S., and Adrio, J.L. (2017). Antifungals. *Biochemical pharmacology* 133, 86-96.
- Chan, G., Hardej, D., Santoro, M., Lau-Cam, C., and Billack, B. (2007). Evaluation of the antimicrobial activity of ebselen: role of the yeast plasma membrane H⁺-ATPase. *Journal of biochemical and molecular toxicology* 21, 252-264.
- Chen, C.H., Ho, C., Liu, H.C., Tsung, T.T., and Hung, T.T. (2011). Spontaneous empyema necessitatis caused by *Aspergillus fumigatus* in an immunocompetent patient. *JRSM short reports* 2, 25.
- Cheng, Y., Glaeser, R.M., and Nogales, E. (2017). How Cryo-EM Became so Hot. *Cell* 171, 1229-1231.
- Chim, N., Habel, J.E., Johnston, J.M., Krieger, I., Miallau, L., Sankaranarayanan, R., Morse, R.P., Bruning, J., Swanson, S., Kim, H., et al. (2011). The TB Structural Genomics Consortium: a decade of progress. *Tuberculosis (Edinburgh, Scotland)* 91, 155-172.
- Chiou, C.C., Mavrogiorgos, N., Tillem, E., Hector, R., and Walsh, T.J. (2001). Synergy, pharmacodynamics, and time-sequenced ultrastructural changes of the interaction between nikkomycin Z and the echinocandin FK463 against *Aspergillus fumigatus*. *Antimicrobial agents and chemotherapy* 45, 3310-3321.
- Chowdhry, R., and Marshall, W.L. (2008). Antifungal therapies in the intensive care unit. *Journal of intensive care medicine* 23, 151-158.
- Chryssanthou, E. (1997). In vitro susceptibility of respiratory isolates of *Aspergillus* species to itraconazole and amphotericin B. acquired resistance to itraconazole. *Scandinavian journal of infectious diseases* 29, 509-512.
- Credle, J.J., Finer-Moore, J.S., Papa, F.R., Stroud, R.M., and Walter, P. (2005). On the mechanism of sensing unfolded protein in the endoplasmic reticulum. *Proceedings of the National Academy of Sciences of the United States of America* 102, 18773-18784.
- D. Versteeg, E. Snelders, T. Rijs, W. Melchers, and P. Verweij (2012). Continued increase of azole resistance in *Aspergillus fumigatus* (Af) in Dutch Hospitals. In ICAAC 52nd.
- Denning, D.W., and Bromley, M.J. (2015). Infectious Disease. How to bolster the antifungal pipeline. *Science (New York, NY)* 347, 1414-1416.
- Denning, D.W., Radford, S.A., Oakley, K.L., Hall, L., Johnson, E.M., and Warnock, D.W. (1997a). Correlation between in-vitro susceptibility testing to itraconazole and in-vivo

- outcome of *Aspergillus fumigatus* infection. The Journal of antimicrobial chemotherapy 40, 401-414.
- Denning, D.W., Venkateswarlu, K., Oakley, K.L., Anderson, M.J., Manning, N.J., Stevens, D.A., Warnock, D.W., and Kelly, S.L. (1997b). Itraconazole resistance in *Aspergillus fumigatus*. Antimicrobial agents and chemotherapy 41, 1364-1368.
- Ehebauer, M.T., and Wilmanns, M. (2011). The progress made in determining the *Mycobacterium tuberculosis* structural proteome. Proteomics 11, 3128-3133.
- Ennifar, E. (2013). X-ray crystallography as a tool for mechanism-of-action studies and drug discovery. Current pharmaceutical biotechnology 14, 537-550.
- Espinosa, V., and Rivera, A. (2016). First Line of Defense: Innate Cell-Mediated Control of Pulmonary Aspergillosis. Frontiers in microbiology 7, 272.
- Feng, X., Krishnan, K., Richie, D.L., Amanianda, V., Hartl, L., Grahl, N., Powers-Fletcher, M.V., Zhang, M., Fuller, K.K., Nierman, W.C., et al. (2011). HacA-independent functions of the ER stress sensor IreA synergize with the canonical UPR to influence virulence traits in *Aspergillus fumigatus*. PLoS pathogens 7, e1002330.
- Gallien, S., Fournier, S., Porcher, R., Bottero, J., Ribaud, P., Sulahian, A., Socie, G., and Molina, J.M. (2008). Therapeutic outcome and prognostic factors of invasive aspergillosis in an infectious disease department: a review of 34 cases. Infection 36, 533-538.
- Grabowski, M., Niedzialkowska, E., Zimmerman, M.D., and Minor, W. (2016). The impact of structural genomics: the first quinquennial. Journal of structural and functional genomics 17, 1-16.
- Gray, K.C., Palacios, D.S., Dailey, I., Endo, M.M., Uno, B.E., Wilcock, B.C., and Burke, M.D. (2012). Amphotericin primarily kills yeast by simply binding ergosterol. Proceedings of the National Academy of Sciences of the United States of America 109, 2234-2239.
- Hadrich, I., Makni, F., Neji, S., Abbes, S., Cheikhrouhou, F., Trabelsi, H., Sellami, H., and Ayadi, A. (2012). Invasive aspergillosis: resistance to antifungal drugs. Mycopathologia 174, 131-141.
- Herbrecht, R., Denning, D.W., Patterson, T.F., Bennett, J.E., Greene, R.E., Oestmann, J.W., Kern, W.V., Marr, K.A., Ribaud, P., Lortholary, O., et al. (2002). Voriconazole versus amphotericin B for primary therapy of invasive aspergillosis. The New England journal of medicine 347, 408-415.
- Hiser, L., Basson, M.E., and Rine, J. (1994). ERG10 from *Saccharomyces cerevisiae* encodes acetoacetyl-CoA thiolase. The Journal of biological chemistry 269, 31383-31389.
- Howard, S.J., Cerar, D., Anderson, M.J., Albarrag, A., Fisher, M.C., Pasqualotto, A.C., Laverdiere, M., Arendrup, M.C., Perlin, D.S., and Denning, D.W. (2009). Frequency and evolution of Azole resistance in *Aspergillus fumigatus* associated with treatment failure. Emerging infectious diseases 15, 1068-1076.

- Hu, W., Sillaots, S., Lemieux, S., Davison, J., Kauffman, S., Breton, A., Linteau, A., Xin, C., Bowman, J., Becker, J., et al. (2007). Essential gene identification and drug target prioritization in *Aspergillus fumigatus*. *PLoS pathogens* 3, e24.
- Ioerger, T.R., and Sacchettini, J.C. (2009). Structural genomics approach to drug discovery for *Mycobacterium tuberculosis*. *Current opinion in microbiology* 12, 318-325.
- Jardetzky, T.S., Lane, W.S., Robinson, R.A., Madden, D.R., and Wiley, D.C. (1991). Identification of self peptides bound to purified HLA-B27. *Nature* 353, 326-329.
- Jimenez-Ortigosa, C., Aïmanianda, V., Muszkieta, L., Mouyna, I., Alsteens, D., Pire, S., Beau, R., Krappmann, S., Beauvais, A., Dufrene, Y.F., et al. (2012). Chitin synthases with a myosin motor-like domain control the resistance of *Aspergillus fumigatus* to echinocandins. *Antimicrobial agents and chemotherapy* 56, 6121-6131.
- Kaufman, R.J. (2002). Orchestrating the unfolded protein response in health and disease. *The Journal of clinical investigation* 110, 1389-1398.
- Kelley, L.A., and Sternberg, M.J. (2009). Protein structure prediction on the Web: a case study using the Phyre server. *Nature protocols* 4, 363-371.
- Kretschmer, M., Wang, J., and Kronstad, J.W. (2012). Peroxisomal and mitochondrial beta-oxidation pathways influence the virulence of the pathogenic fungus *Cryptococcus neoformans*. *Eukaryotic cell* 11, 1042-1054.
- Krishnan, K., and Askew, D.S. (2014). The fungal UPR: A regulatory hub for virulence traits in the mold pathogen *Aspergillus fumigatus*. *Virulence* 5, 334-340.
- Kunau, W.H., Dommès, V., and Schulz, H. (1995). beta-oxidation of fatty acids in mitochondria, peroxisomes, and bacteria: a century of continued progress. *Progress in lipid research* 34, 267-342.
- Latge, J.P. (1999). *Aspergillus fumigatus* and aspergillosis. *Clinical microbiology reviews* 12, 310-350.
- Latge, J.P. (2001). The pathobiology of *Aspergillus fumigatus*. *Trends in microbiology* 9, 382-389.
- Lee, K.P., Dey, M., Neculai, D., Cao, C., Dever, T.E., and Sicheri, F. (2008). Structure of the dual enzyme Ire1 reveals the basis for catalysis and regulation in nonconventional RNA splicing. *Cell* 132, 89-100.
- Lelièvre, L., Groh, M., Angebault, C., Maherault, A.C., Didier, E., and Bougnoux, M.E. (2013). Azole resistant *Aspergillus fumigatus*: An emerging problem. *Médecine et Maladies Infectieuses* 43, 139-145.
- Lenardon, M.D., Munro, C.A., and Gow, N.A. (2010). Chitin synthesis and fungal pathogenesis. *Current opinion in microbiology* 13, 416-423.
- Lewis, K. (2013). Platforms for antibiotic discovery. *Nature reviews Drug discovery* 12, 371-387.

- Li, L., Nan, J., Li, D., Brostromer, E., Wang, Z., Liu, C., Hou, Q., Fan, X., Ye, Z., and Su, X.D. (2014). Structural genomics studies of human caries pathogen *Streptococcus mutans*. Journal of structural and functional genomics.
- Li, Y., and Kang, C. (2017). Solution NMR Spectroscopy in Target-Based Drug Discovery. Molecules (Basel, Switzerland) 22.
- Lin, S.J., Schranz, J., and Teutsch, S.M. (2001). Aspergillosis case-fatality rate: systematic review of the literature. Clinical infectious diseases: an official publication of the Infectious Diseases Society of America 32, 358-366.
- Lin, T.W., Melgar, M.M., Kurth, D., Swamidass, S.J., Purdon, J., Tseng, T., Gago, G., Baldi, P., Gramajo, H., and Tsai, S.C. (2006). Structure-based inhibitor design of AccD5, an essential acyl-CoA carboxylase carboxyltransferase domain of *Mycobacterium tuberculosis*. Proceedings of the National Academy of Sciences of the United States of America 103, 3072-3077.
- Liu, C.Y., and Kaufman, R.J. (2003). The unfolded protein response. Journal of cell science 116, 1861-1862.
- Liu, C.Y., Schroder, M., and Kaufman, R.J. (2000). Ligand-independent dimerization activates the stress response kinases IRE1 and PERK in the lumen of the endoplasmic reticulum. The Journal of biological chemistry 275, 24881-24885.
- Liu, C.Y., Wong, H.N., Schauerte, J.A., and Kaufman, R.J. (2002). The protein kinase/endoribonuclease IRE1alpha that signals the unfolded protein response has a luminal N-terminal ligand-independent dimerization domain. The Journal of biological chemistry 277, 18346-18356.
- Madureira, A., Bergeron, A., Lacroix, C., Robin, M., Rocha, V., de Latour, R.P., Ferry, C., Devergie, A., Lapalu, J., Gluckmana, E., et al. (2007). Breakthrough invasive aspergillosis in allogeneic haematopoietic stem cell transplant recipients treated with caspofungin. International journal of antimicrobial agents 30, 551-554.
- Magellan, H., Drujon, T., Thellend, A., Piffeteau, A., and Becker, H.F. (2010). Expression in *E. coli* and characterization of the catalytic domain of Botrytis cinerea chitin synthase. BMC research notes 3, 299.
- Martin, D.P., Bibart, R.T., and Druceckhammer, D.G. (1994). Synthesis of novel analogs of acetyl-coenzyme A - mimics of enzyme reaction intermediates. Journal of the American Chemical Society 116, 4660-4668.
- McCormick, A., Loeffler, J., and Ebel, F. (2010). *Aspergillus fumigatus*: contours of an opportunistic human pathogen. Cellular microbiology 12, 1535-1543.
- Mellado, E., Aufauvre-Brown, A., Gow, N.A., and Holden, D.W. (1996). The *Aspergillus fumigatus* chsC and chsG genes encode class III chitin synthases with different functions. Mol Microbiol 20, 667-679.
- Mellado, E., Dubreucq, G., Mol, P., Sarfati, J., Paris, S., Diaquin, M., Holden, D.W., Rodriguez-Tudela, J.L., and Latge, J.P. (2003). Cell wall biogenesis in a double chitin synthase

- mutant (chsG-/chsE-) of *Aspergillus fumigatus*. Fungal genetics and biology : FG & B 38, 98-109.
- Moldovan, G.L., Pfander, B., and Jentsch, S. (2007). PCNA, the maestro of the replication fork. *Cell* 129, 665-679.
- Musa, T.L., Ioerger, T.R., and Sacchettini, J.C. (2009). The tuberculosis structural genomics consortium: a structural genomics approach to drug discovery. *Advances in protein chemistry and structural biology* 77, 41-76.
- Muszkietta, L., Aimaganianda, V., Mellado, E., Gribaldo, S., Alcazar-Fuoli, L., Szewczyk, E., Prevost, M.C., and Latge, J.P. (2014). Deciphering the role of the chitin synthase families 1 and 2 in the in vivo and in vitro growth of *Aspergillus fumigatus* by multiple gene targeting deletion. *Cellular microbiology*.
- Nierman, W.C., Pain, A., Anderson, M.J., Wortman, J.R., Kim, H.S., Arroyo, J., Berriman, M., Abe, K., Archer, D.B., Bermejo, C., et al. (2005). Genomic sequence of the pathogenic and allergenic filamentous fungus *Aspergillus fumigatus*. *Nature* 438, 1151-1156.
- Patterson, T.F., Thompson, G.R., 3rd, Denning, D.W., Fishman, J.A., Hadley, S., Herbrecht, R., Kontoyiannis, D.P., Marr, K.A., Morrison, V.A., Nguyen, M.H., et al. (2016). Practice Guidelines for the Diagnosis and Management of Aspergillosis: 2016 Update by the Infectious Diseases Society of America. *Clinical infectious diseases: an official publication of the Infectious Diseases Society of America*.
- Qiao, J., Liu, W., and Li, R. (2008). Antifungal resistance mechanisms of *Aspergillus*. *Nihon Ishinkin Gakkai zasshi = Japanese journal of medical mycology* 49, 157-163.
- Ramirez, M.A., and Lorenz, M.C. (2009). The transcription factor homolog CTF1 regulates beta-oxidation in *Candida albicans*. *Eukaryotic cell* 8, 1604-1614.
- Richie, D.L., Hartl, L., Aimaganianda, V., Winters, M.S., Fuller, K.K., Miley, M.D., White, S., McCarthy, J.W., Latge, J.P., Feldmesser, M., et al. (2009). A role for the unfolded protein response (UPR) in virulence and antifungal susceptibility in *Aspergillus fumigatus*. *PLoS pathogens* 5, e1000258.
- Rocha, E.M., Garcia-Effron, G., Park, S., and Perlin, D.S. (2007). A Ser678Pro substitution in Fks1p confers resistance to echinocandin drugs in *Aspergillus fumigatus*. *Antimicrobial agents and chemotherapy* 51, 4174-4176.
- Rocha, E.M., Gardiner, R.E., Park, S., Martinez-Rossi, N.M., and Perlin, D.S. (2006). A Phe389Leu substitution in ergA confers terbinafine resistance in *Aspergillus fumigatus*. *Antimicrobial agents and chemotherapy* 50, 2533-2536.
- Rogg, L.E., Fortwendel, J.R., Juvvadi, P.R., Lilley, A., and Steinbach, W.J. (2011). The chitin synthase genes chsA and chsC are not required for cell wall stress responses in the human pathogen *Aspergillus fumigatus*. *Biochemical and biophysical research communications* 411, 549-554.
- Ron, D., and Hubbard, S.R. (2008). How IRE1 reacts to ER stress. *Cell* 132, 24-26.

- Roncero, C. (2002). The genetic complexity of chitin synthesis in fungi. *Current genetics* 41, 367-378.
- Ryder, N.S. (1992). Terbinafine: mode of action and properties of the squalene epoxidase inhibition. *The British journal of dermatology* 126 Suppl 39, 2-7.
- Schwartz, S., Ruhnke, M., Ribaud, P., Corey, L., Driscoll, T., Cornely, O.A., Schuler, U., Lutsar, I., Troke, P., and Thiel, E. (2005). Improved outcome in central nervous system aspergillosis, using voriconazole treatment. *Blood* 106, 2641-2645.
- Shamu, C.E., and Walter, P. (1996). Oligomerization and phosphorylation of the Ire1p kinase during intracellular signaling from the endoplasmic reticulum to the nucleus. *The EMBO journal* 15, 3028-3039.
- Shen, Y.Q., and Burger, G. (2009). Plasticity of a key metabolic pathway in fungi. *Functional & integrative genomics* 9, 145-151.
- Singh, N., and Paterson, D.L. (2005). *Aspergillus* infections in transplant recipients. *Clinical microbiology reviews* 18, 44-69.
- Smyth, M.S., and Martin, J.H. (2000). x Ray crystallography. *Journal of Clinical Pathology: Molecular pathology* 53, 8-14.
- Snelders, E., Huis In 't Veld, R.A., Rijs, A.J., Kema, G.H., Melchers, W.J., and Verweij, P.E. (2009). Possible environmental origin of resistance of *Aspergillus fumigatus* to medical triazoles. *Applied and environmental microbiology* 75, 4053-4057.
- Steinbach, W.J. (2013). Are we there yet? Recent progress in the molecular diagnosis and novel antifungal targeting of *Aspergillus fumigatus* and invasive aspergillosis. *PLoS pathogens* 9, e1003642.
- Stevens, D.A. (2000). Drug interaction studies of a glucan synthase inhibitor (LY 303366) and a chitin synthase inhibitor (Nikkomycin Z) for inhibition and killing of fungal pathogens. *Antimicrobial agents and chemotherapy* 44, 2547-2548.
- Thangamani, S., Eldesouky, H.E., Mohammad, H., Pascuzzi, P.E., Avramova, L., Hazbun, T.R., and Seleem, M.N. (2017). Ebselen exerts antifungal activity by regulating glutathione (GSH) and reactive oxygen species (ROS) production in fungal cells. *Biochimica et biophysica acta* 1861, 3002-3010.
- Thangamani, S., Younis, W., and Seleem, M.N. (2015). Repurposing Clinical Molecule Ebselen to Combat Drug Resistant Pathogens. *PloS one* 10, e0133877.
- Upton, A., Kirby, K.A., Carpenter, P., Boeckh, M., and Marr, K.A. (2007). Invasive aspergillosis following hematopoietic cell transplantation: outcomes and prognostic factors associated with mortality. *Clinical infectious diseases: an official publication of the Infectious Diseases Society of America* 44, 531-540.
- van der Linden, J.W., Snelders, E., Kampinga, G.A., Rijnders, B.J., Mattsson, E., Debets-Ossenkopp, Y.J., Kuijper, E.J., Van Tiel, F.H., Melchers, W.J., and Verweij, P.E. (2011). Clinical implications of azole resistance in *Aspergillus fumigatus*, The Netherlands, 2007-2009. *Emerging infectious diseases* 17, 1846-1854.

- Ventola, C.L. (2015). The antibiotic resistance crisis: part 1: causes and threats. *P & T : a peer-reviewed journal for formulary management* 40, 277-283.
- Vermeulen, E., Lagrou, K., and Verweij, P.E. (2013). Azole resistance in *Aspergillus fumigatus*: a growing public health concern. *Current opinion in infectious diseases* 26, 493-500.
- Verweij, P.E., Chowdhary, A., Melchers, W.J., and Meis, J.F. (2016). Azole Resistance in *Aspergillus fumigatus*: Can We Retain the Clinical Use of Mold-Active Antifungal Azoles? *Clinical infectious diseases: an official publication of the Infectious Diseases Society of America* 62, 362-368.
- Verwer, P.E., van Duijn, M.L., Tavakol, M., Bakker-Woudenberg, I.A., and van de Sande, W.W. (2012). Reshuffling of *Aspergillus fumigatus* cell wall components chitin and beta-glucan under the influence of caspofungin or nikkomycin Z alone or in combination. *Antimicrobial agents and chemotherapy* 56, 1595-1598.
- Walsh, T.J., Anaissie, E.J., Denning, D.W., Herbrecht, R., Kontoyiannis, D.P., Marr, K.A., Morrison, V.A., Segal, B.H., Steinbach, W.J., Stevens, D.A., et al. (2008). Treatment of aspergillosis: clinical practice guidelines of the Infectious Diseases Society of America. *Clinical infectious diseases: an official publication of the Infectious Diseases Society of America* 46, 327-360.
- Warnock, D.W. (2007). Trends in the epidemiology of invasive fungal infections. *Nihon Ishinkin Gakkai zasshi = Japanese journal of medical mycology* 48, 1-12.
- Weigelt, J. (2010). Structural genomics-impact on biomedicine and drug discovery. *Experimental cell research* 316, 1332-1338.
- Zamir, L., Zaretsky, M., Fridman, Y., Ner-Gaon, H., Rubin, E., and Aharoni, A. (2012). Tight coevolution of proliferating cell nuclear antigen (PCNA)-partner interaction networks in fungi leads to interspecies network incompatibility. *Proceedings of the National Academy of Sciences of the United States of America* 109, E406-414.
- Zheng, H., Handing, K.B., Zimmerman, M.D., Shabalin, I.G., Almo, S.C., and Minor, W. (2015). X-ray crystallography over the past decade for novel drug discovery - where are we heading next? *Expert opinion on drug discovery* 10, 975-989.
- Zhou, J., Liu, C.Y., Back, S.H., Clark, R.L., Peisach, D., Xu, Z., and Kaufman, R.J. (2006). The crystal structure of human IRE1 luminal domain reveals a conserved dimerization interface required for activation of the unfolded protein response. *Proceedings of the National Academy of Sciences of the United States of America* 103, 14343-14348.